TECHNISCHE
UNIVERSITÄT
WIEN
Vienna University of Technology

Dissertation

Ligand-engineered zeolite imidazole frameworks for environmental and energy applications

ausgeführt zum Zwecke der Erlangung des akademischen Grades einer Doktorin der
Naturwissenschaften unter der Leitung von

Univ. Prof. Dr. Dominik Eder

E165
Institut für Materialchemie

eingereicht an der Technischen Universität Wien
Fakultät für Technische Chemie

von

Zheao Huang

12131829

Wien, am 28, January 2025

Contents

Abstract

Zeolitic imidazolate frameworks (ZIFs) are a subset of metal-organic frameworks (MOFs), typically formed by the coordination of divalent metal ions with nitrogen atoms in imidazole organic ligands, resulting in neutral open-framework structures with zeolite-like topologies. ZIFs exhibit high crystallinity, tuned porosity, high specific surface area, and chemical stability, making them highly promising for environmental and energy applications. These features enable ZIFs to efficiently provide clean water through water purification and generate clean fuel through water electrolysis, addressing the needs for carbon neutrality and solving energy and environmental crises. However, as research progresses, most MOFs/ZIFs face main challenges such as a lack of mesoscale cavities, saturated metal sites, poor stability in catalytic environments, and low electrical conductivity. Therefore, this thesis focuses on the ligand engineering of ZIF frameworks with sodalite topology (ZIF-8 and ZIF-67) through mixed ligand and selective ligand removal (SeLiRe) strategies to overcome these critical challenges.

In the first project in this thesis, I employed the SeLiRe strategy to engineer hierarchically porous ZIFs. This novel method entails synthesizing mixed-ligand ZIFs with various ratios of two ligands and subsequently applying controlled thermal treatments to selectively remove the thermolabile secondary linker. This process results in a dual-pore structure comprising both micropores and newly introduced mesopores. The size, distribution, and shape of the newly mesopores are notably influenced by the mixing ratio of the secondary ligand and the heating parameters. For application, hierarchically porous ZIF exhibits a 40-fold enhancement in adsorption capacity for various organic dyes in aqueous solutions, with significantly faster adsorption rates, owing to the increased pore volume that facilitates the rapid diffusion of dye molecules to active adsorption sites.

In the second project in this thesis, I further extended the SeLiRe strategy to confirm that the engineered open metal sites (OMS) were successfully incorporated into the ZIF framework. Advanced characterization techniques were used to evaluate their role in the hydrogen evolution reaction (HER) and to investigate their altered structural and electronic modifications under electrocatalytic conditions. In-situ electrochemical analysis and X-ray absorption spectroscopy revealed that, at a specific potential, the unsaturated $Zn-N_2$ sites chemisorbed hydroxide ions from the electrolyte, forming high-valence $HO-Zn-N_2$ active sites. The optimal OMS-ZIF achieved an exceptionally low overpotential of 0.41 V, enabling a sustained current density of 1.0 A cm^{-2} with 120-hour stability. Theoretical simulations further demonstrated that high-valence $HO-Zn-N_2$ active sites significantly enhance water molecule activation kinetics, thereby improving the efficiency of the Volmer step.

In the third experimental project in this thesis, I utilized the mixed ligand strategy to bolster the activity and stability of (photo)electrocatalytically active MOFs. Four mixed-ligand variants of zeolitic imidazolate framework-67 (ZIF-67) were synthesized, enabling an in-depth analysis of the impact of the secondary ligand on the reconstruction of the ZIF framework during the electrocatalytic oxygen evolution reaction (OER). Some secondary ligands retained the fundamental framework while inducing surface reconstruction to form an in-situ cobalt (oxy)hydroxide layer, in stark contrast to the complete reconstruction observed in single-ligand ZIFs. The cobalt (oxy)hydroxide layer, along with its interfacial synergistic effects, enhanced conductivity and catalytic performance, while also improving (photo)electrochemical stability.

These results indicate that the ligand engineering strategy is a powerful tool to design advanced functional frameworks with enhanced activity, selectivity and durability in environmental and energy applications.

Introduction

1.1 Porous materials

Inspired by many natural materials such as charcoal, sponges, and pumice, which feature empty spaces and pores ranging from nano- to centimeters in diameter, porous materials composed of either inorganic or organic compounds have been synthesized [1]. These materials now play a vital role in our daily activities and the industrial sector, including zeolites, mesoporous silica, carbon, metal oxides, and polymers [2-4].

Among them, zeolites are typically crystalline aluminosilicates composed of tetrahedral atoms (Si or Al) forming an open framework structure [5]. Due to their outstanding stability and well-defined pore sizes, they are widely used in industrial applications, such as the ZSM-5 zeolite. However, their fixed and relatively small pore sizes limit their use in advanced applications requiring larger or more tunable pore architectures.

Mesoporous silica materials, on the other hand, feature high surface areas, larger pores and are well-suited for catalytic reactions involving large reactant molecules. While mesoporous silica exhibits the long-range order in its pore structure, the surrounding walls are amorphous [6]. This non-crystalline nature means their stability and catalytic activity are inherently lower compared to other porous materials.

Recently, a new class of porous materials has been extensively studied and reported: metal-organic frameworks (MOFs). Their synthesis has evolved from zeolite chemistry, focusing on the assembly of organic and inorganic building units to form porous structures. Unlike purely inorganic materials, MOFs allow for much greater flexibility in combining metal nodes and organic ligands through reticular chemistry, resulting in thousands of unique framework structures [7]. This flexibility provides MOFs with tunable pore sizes, adjustable chemical functionalities, and a variety of structural topologies.

Generally, advanced applications require porous materials that offer greater tunability in terms of pore structures and chemistries, which has driven the development of next-generation porous materials like MOFs (including covalent organic frameworks and zeolitic imidazolate frameworks) [8]. This thesis will focus on showcasing these novel MOF materials and their applications in environmental and energy fields, highlighting their unique advantages over traditional porous materials.

1.1.1 Metal-organic frameworks (MOFs)

Metal-organic Frameworks (MOFs) are crystalline structures formed via the self-assembly of metal nodes (or metal cluster) and organic ligands, often creating a periodic porous network framework. Their concept was introduced by Yaghi and co-authors in 1995 [9-10]. The self-assembly process of MOFs is heavily influenced by the coordination tendencies of the secondary building units (SBUs), alongside the characteristics of the organic ligands, such as their functional groups, length, and rigidity (Figure 1.1) [11]. These unique hybrid structures exhibit several defining characteristic features that set them apart from traditional materials:

1. **Molecular nature**: Both organic and inorganic components of MOFs are molecular or small atomic clusters. This distinct composition results in discrete energy levels in their electronic structures, unlike the band structures of solid materials.
2. **Exceptional surface area**: The molecular nature ensures that every atom is essentially "surface," leading to some of the highest specific surface areas.
3. **Flexible chemistry**: The organic and inorganic components of MOFs exhibit molecular-like chemistries, enabling straightforward functionalization or doping. This versatility is difficult to achieve in traditional solid materials.
4. **Adjustable pore structure**: MOFs feature tunable pore diameters, structures, and connectivity through reticular chemistry, including variations in ligand type and length. This precise control facilitates the adsorption, diffusion, and catalytic turnover of specific molecules.
5. **Structural versatility**: Depending on the nature of the organic linkers, MOFs can exhibit flexibility (e.g., breathing upon gas adsorption) or rigidity, further broadening their applicability.
6. **Localized properties at interfaces**: The interfaces between the inorganic and organic components in MOFs can generate localized electric fields or metal-semiconductor junctions, making them ideal for charge transfer and redox applications.
7. **Periodicity and crystallinity**: MOFs can be either crystalline or glass-like, with periodic arrangements of metal nodes providing uniform and abundant active sites, enhancing the reaction activity.

These features make MOFs highly versatile materials with applications in catalysis [12-13], gas storage and separation [14-15], energy conversion and storage [16], pollutant purification [17-18], and chemical sensors [19]. Based on the Hard and Soft Acids and Bases (HSAB) theory, various multifunctional MOFs with well-defined topologies have been reported, cementing their status as a research hotspot in recent years.

However, MOFs also face challenges that limit their broader application.

1). Ensuring structural integrity and stability under various conditions, such as humidity, temperature, and pH, remains a critical hurdle.

2). Achieving efficient utilization of adsorption and catalytic sites can be complex due to diffusion limitations or structural constraints.

3). Design and synthesis of MOFs require careful control over component combinations and reaction conditions, adding to their chemical complexity.

4). Identifying the optimal organic and inorganic components for specific applications is a non-trivial challenge, necessitating a balance between functionality and stability.

This thesis addresses these limitations through the ligand engineering strategy in MOFs, opening new pathways for their practical applications in diverse scientific and industrial domains.

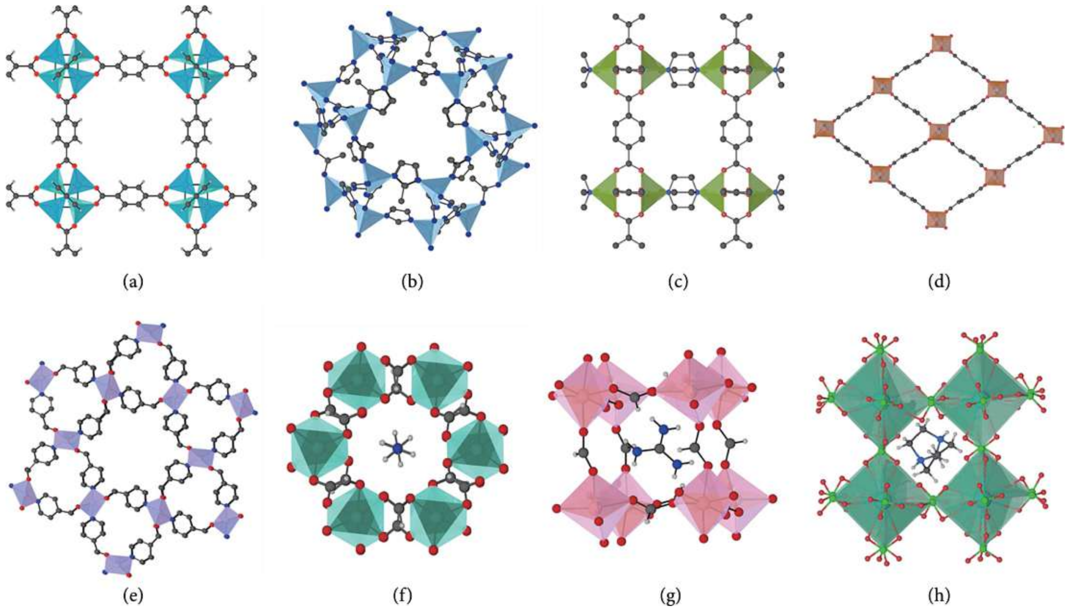

Figure 1.1: Crystal structures of some prototypical MOFs. From (a) to (h): MOF-5, ZIF-8, DMOF-1, MIL-53(Ga), QMOF-1, $NH_4ZnH(COO)_3$, $GuaZn(HCOO)_3$, and $DABCOH_2K(ClO_4)_3$. Reprinted with permission from Research-SPJ [20].

1.1.2 Zeolitic imidazolate frameworks (ZIFs)

Zeolitic imidazolate frameworks (ZIFs) are a subset of Metal-organic frameworks (MOFs), typically formed by the coordination of divalent metal ions (e.g., Zn^{2+} or Co^{2+}) with nitrogen atoms in imidazole organic ligands (e.g., 2-methylimidazole), resulting in neutral open-framework structures with zeolite-like topologies (Figure 1.2) [21]. The name "Zeolitic Imidazolate Frameworks" is derived from the similarity of the 145° metal–imidazole–metal bond angles to the Si-O-Si angles in (alumina)silicate zeolites.

The first ZIFs were synthesized by Yaghi and co-authors in 2006 and 2008, where they produced 12 and an additional 25 ZIFs, respectively, some of these ZIFs exhibited remarkable thermal and chemical stability [22-23]. Based on the interaction modes between ligands, ZIFs can form various topological structures such as ANA, GME, GIS, BCT, RHO, MER, and SOD [24]. While ZIFs not only exhibit physical and chemical properties comparable to those MOFs mentioned above but also provide the added advantages of zeolites, such as superior thermal and chemical stability, along with a wide variety of structural topologies.

Compared to traditional zeolites, which have surface areas less than 1000 m^2 g^{-1}, typical ZIFs boast much higher surface areas exceeding 1000 m^2 g^{-1} [25]. In terms of porosity, unlike zeolites, ZIFs allow precise control over pore size, shape, and surface chemistry. Zeolites often struggle to achieve uniform and well-ordered pore structures during the synthesis process [21]. Some review articles suggest that another notable advantage of ZIFs is their superior thermal and chemical stability under harsh conditions, whereas traditional zeolites generally have limited stability under strongly acidic or basic environments [21, 26]. However, based on my experience and research, I remain cautious about fully endorsing this claimed stability advantage.

Therefore, in this thesis, I focus on the commonly used sodalite (SOD) topology ZIFs, specifically ZIF-8 (zinc-based) and ZIF-67 (cobalt-based), as precursors for ligand engineering strategy to enhance activity and stability in various environmental and energy applications.

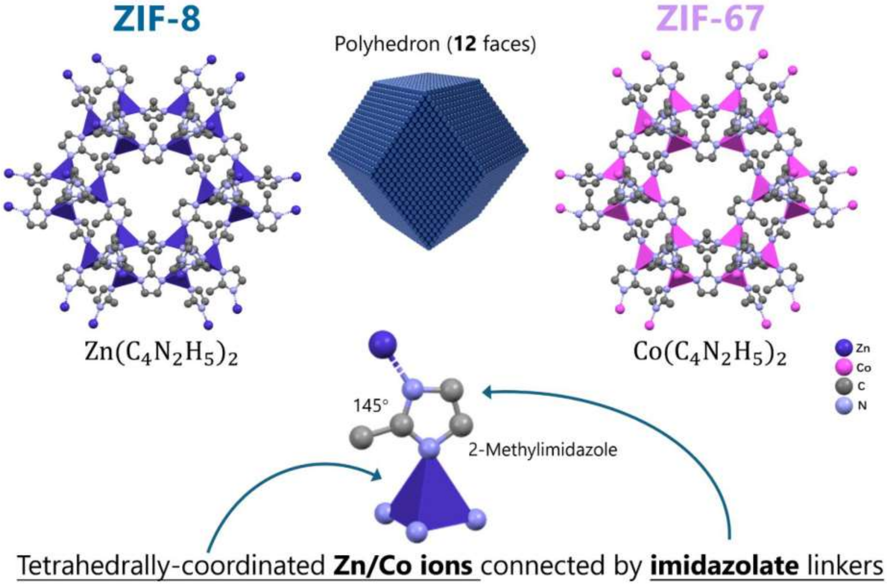

Figure 1.2: Morphology and framework structure of sodalite topology ZIF-8 (left) and ZIF-67 (right).

1.2 Ligand engineering strategy

With the continuous expansion of organic chemistry and coordination chemistry, an increasing number of structurally complex organic ligands with unique functional groups are being synthesized [27]. This has led to a corresponding increase in the variety and number of MOFs/ZIFs. Based on the HSAB theory, it has become simpler to achieve structural stabilization using a wide array of ligands available as options. Crucially, these organic ligands largely determine the framework structure and chemical properties of MOFs/ZIFs [9]. For instance, by altering the types of functional groups or metal salts on the ligands, one can adjust the topological structure [28], pore size [29], and selective functionalities [30] of MOFs/ZIFs. This strategy is commonly referred to as ligand engineering.

1.2.1 Ligand modification strategy

Ligand modification of the primary ligand in MOFs/ZIFs is a common strategy to introduce new functional properties. This involves synthesizing MOFs/ZIFs using primary ligands with additional functional groups, such as amino (–NH_2), sulfonyl (–SO_3H), hydroxyl (–OH), or carbonyl (C=O) groups [31]. Among these, amino-functionalized ligands are the most frequently employed, accounting for about 90% of such modifications, due to their electron-withdrawing properties. Examples include NH_2-UIO-66, NH_2-MIL-125, NH_2-ZIF-8 and so on. These functional groups allow for tuning the inherent optical, electronic, and porous properties of MOFs/ZIFs. For instance, the addition of amino groups can extend the light absorption range of MIL-125 from UV to visible light, significantly enhancing its photocatalytic potential under visible light irradiation [32].

Another ligand modification strategy involves ligand extension to create larger pores facilitating the adsorption of macromolecules or enhancing π–π interactions. Eddaoudi et al. [33] were pioneers in employing this strategy to functionalize MOF-5, demonstrating that pore size could be expanded using long molecular struts like biphenyl, tetrahydropyrene, pyrene, and terphenyl. Additionally, they incorporated organic groups such as –Br, –NH_2, –OC_3H_7, –OC_5H_{11}, –C_2H_4, and –C_4H_4. This approach led to the synthesis of a series of MOF-5 structures with identical topologies but homogeneous periodic pores ranging from 3.8 to 28.8 Å. The optimized sample exhibited high methane storage capacity.

Deng et al. [34] further advanced this strategy by combining short and very long ligands, synthesizing an isoreticular series of MOF-74 structures with pore channels up to 10 nanometers in diameter and great chemical/thermal stability, enabling natural proteins to pass through the large pores and directly enter the MOF-74 framework. Endo et al. [35] developed metal-organic-covalent-organic frameworks (MOCOFs) through double extension of metal-organic and covalent organic ligands. These MOCOFs feature large surface areas, high crystallinity, excellent chemical and thermal stability, and chiral networks.

In catalysis, extending the length of dicarboxylate ligands has been used to strengthen π–π interactions between ligands, as demonstrated by Ma et al. [36] and Yuan et al [37]. This enhancement improves MOF stability in alkaline solutions and boosts electrocatalytic activity through hydroxide transformation.

However, this ligand extension strategy comes with challenges. First, the pore space can be easily occupied by guest molecules, making it difficult to achieve permanent porosity [38]. Additionally, removing these guest molecules may lead to structural collapse. Second, excessively long ligands can result in interpenetrating networks, hindering the formation of highly crystalline periodic frameworks.

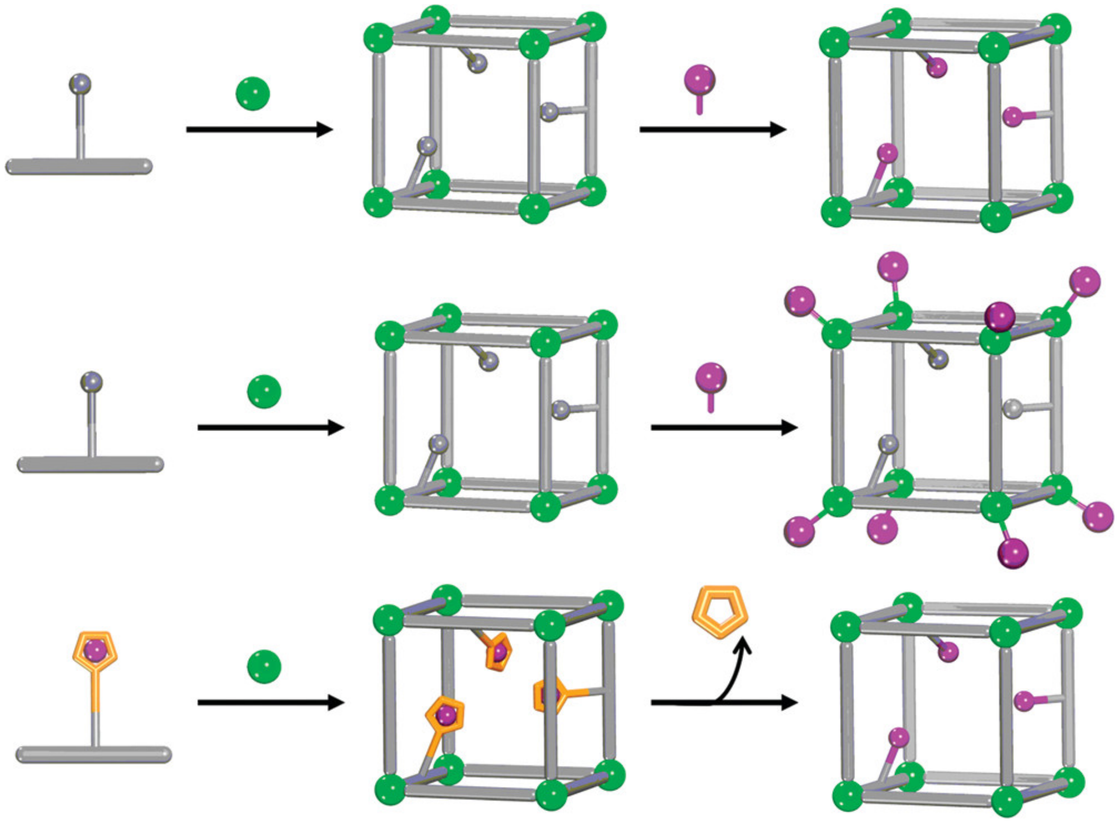

Figure 1.3: Generic schemes for ligand modification strategy. Reprinted with permission from ACS Publications [39].

1.2.2 Mixed-ligand strategy

Generally, MOFs/ZIFs are formed by the combination of a single ligand and metal ions. However, as research advances, there is growing interest in further refining the surface, functionality, and porosity of MOFs/ZIFs [40]. These properties largely depend on the configuration and functional groups of the ligands [41]. Consequently, the strategy of employing dual or multiple ligands, known as mixed-ligand engineering, has garnered significant interest (Figure 1.4).

In mixed-ligand strategy, the ligand selection is crucial for determining the properties of the synthesized MOFs/ZIFs. For instance, a secondary ligand can introduce specific desired organic functional groups into the MOFs/ZIFs structure, enabling the incorporation of multiple functional groups within the same framework [42 43]. Additionally, potential synergistic effects between multiple functional groups can enhance the functional properties of MOFs/ZIFs, creating a "1 + 1 > 2" effect, thus increasing their practical value [9] .

In earlier research, Deng et al. [43] successfully developed 18 types of mixed-ligand MOF-5 by combining multiple functional groups, which significantly enhanced their adsorption capacities for H_2, CO, and CO_2 compared to single-ligand MOFs. ZIF-62, synthesized using a mixture of two ligands—benzimidazole and imidazole—demonstrated excellent thermal stability and the ability to melt prior to decomposition, making it a key material for quenching processes to create unique MOF glasses [44-46]. Others, Wang et al. [47] and Wu et al., [48] designed a range of MOF@MOF composites using ligand engineering, yielding stable and highly efficient photocatalysts.

Despite these advances, verifying the distribution of new or secondary ligands within the framework remains extremely challenging. Characterization techniques such as nuclear magnetic resonance (NMR) and infrared (IR) spectroscopy are often used to confirm the presence of ligands and their corresponding functional groups, but determining the exact spatial distribution of ligands requires advanced atomic-resolution electron microscopy. Unfortunately, most MOFs/ZIFs are electron-beam-sensitive materials, which struggle to maintain their morphology and structure under prolonged exposure to high electron doses [49]. While atomic-resolution imaging requires higher electron doses to achieve sufficient clarity, the fragile nature of these materials demands specialized electron microscopy, such as cryo-electron or low-dose electron microscopy [50]. Consequently, there are significant technical limitations in characterizing these mixed-ligand MOFs/ZIFs.

In terms of synthesis, the feasibility of producing mixed-ligand MOFs/ZIFs often relies on the use of hydrothermal methods to achieve uniform mixing of ligands and facilitate crystal growth; however, this process typically requires higher energy input (such as elevated temperatures and pressures) than single-ligand samples, leading to increased resource consumption [51]. Microwave-assisted synthesis provides further potential to optimize these processes by allowing better control over parameters such as reactor pressure, temperature, and reaction time. During crystal nucleation and growth, the application of controlled microwave power and stirring ensures a more homogeneous distribution of secondary ligands while significantly reducing synthesis time. This is particularly advantageous for ZIF crystals. Therefore, all ZIF syntheses in this thesis were conducted using microwave-assisted reactors. Other importantly, the presence of multiple organic ligands can lead to coordination competition during the synthesis, which may expose more defects on the positive side but can negatively affect the crystallinity and morphology of the structure [52].

In summary, the mixed-ligand strategy primarily involves introducing additional ligands with key functional groups into the MOFs/ZIFs structure, thereby altering the coordination structure and chemical properties to meet diverse application needs. Limitations in characterization techniques and synthesis challenges underscore the need for further research and innovation in this field. In Article #3 (Chapter 3), using the mixed-ligand strategy, I synthesized a series of SOD-type ZIFs with mixed ligands, achieving enhanced electrocatalytic activity and stability through in-situ surface reconstruction.

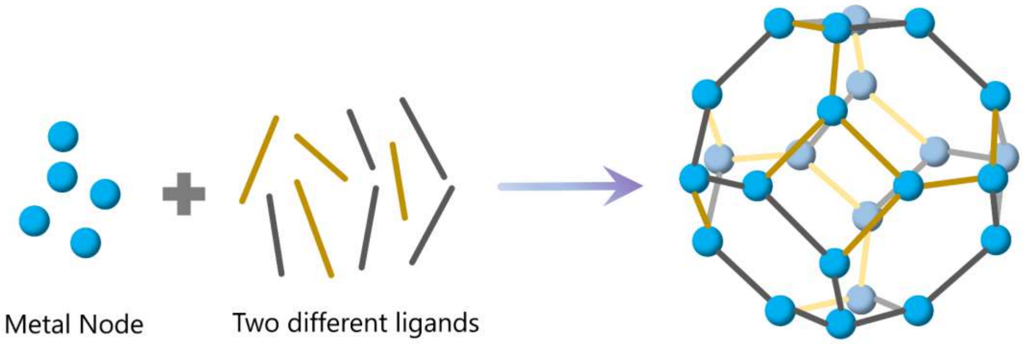

Figure 1.4: Schematic diagram of two different ligands mixed into a ZIF framework of the same topology.

1.2.3 Selective ligand removal (SeLiRe) strategy

Recent years have been a growing attempt to design hierarchically porous MOFs/ZIFs materials composed of micro- and mesopores, typically featuring interconnected channels and structural defects [38]. The inclusion of mesoscale cavities and open metal sites broadens the scope of their potential applications. Selective ligand removal (SeLiRe) is a powerful strategy for creating structural defects and hierarchical porosity in MOFs/ZIFs, compared to traditional templating methods [8]. This strategy combines mixed-ligand method and labile ligand decomposition (Figure 1.5). Initially, both stable and labile ligands are mixed during synthesis, followed by the labile ligands are selectively removed by certain means, leaving behind an abundance of missing ligand/cluster defects.

For example, during the SeLiRe process with thermolabile ligands, the bonds formed between the thermolabile ligand and the metal nodes typically cleave preferentially at high temperatures [53]. This is accompanied by the detachment and pyrolysis of the thermolabile ligand, while the thermostable primary ligand remains largely unaffected. This selective removal allows for the construction of new pore structures and missing ligand/cluster defects, which can often be fine-tuned to some extent by adjusting the thermolabile ligand ratio and the heating parameters.

To date, commonly reported methods include thermolysis [53-54], hydrolysis [55], ozonolysis [56], and laser photolysis [57], which can selectively remove labile ligands by consuming high energy. For example, Zhou et al. [53] selectively removed thermolabile ligands in multivariate MOFs (MTV-MOFs) to transform micropores into hierarchical pores. Naghdi et al. [29] applied the thermal SeLiRe strategy to selectively eliminate the secondary ligand in MIL-125-Ti, resulting in the formation of two unique mesoporous structures—large cavities and branching fractures—which significantly improved photocatalytic hydrogen generation. Zhou et al. [57] further utilized developed a controlled advanced laser photolysis to remove photolabile ligands, generating mesopores and more complicated patterns within the microporous UiO-66-Zr in mere tens of milliseconds.

It is worth noting that, similar to the challenges faced in mixed-ligand strategy (Section 1.2.2), controlling the ratio of labile ligands or the balance between labile and primary ligands during synthesis can be challenging. The real spatial distribution and local arrangement of labile ligands in mixed-ligand MOFs/ZIFs often remain difficult to adjust precisely, resulting in additional pores or defects with unpredictable structures after processing [11]. Additionally, an excessive ratio of labile ligands with bulky organic functional groups may interfere with the nucleation process of MOFs/ZIFs, particularly those with imidazole or extended stacked aromatic carbon ring ligands. Moreover, the removal process itself requires careful handling, as the decomposition of labile ligands is often accompanied by a decrease in crystallinity, and harsh removal environments (e.g., high temperatures or aqueous conditions) can damage the morphology and parts of the framework structure. Therefore, the careful selection of mild removal methods and easily removable ligands as the secondary ligand is crucial for the SeLiRe strategy. Despite these challenges, compared to traditional templating methods, the SeLiRe strategy retains an advantage in maintaining the crystallinity of MOF/ZIF while effectively allowing for some degree of control over the distribution of additional pores and/or defects.

To further validate the distribution of additional pores and/or defects, as previously discussed for the mixed-ligand strategy, advanced characterization techniques such as high-resolution TEM/STEM and synchrotron-based XAS are considered highly effective [51]. For instance, using novel low-dose electron microscopy—which can prevent damage to the framework caused by high-energy electron beams—Liu et al. [58] and Wang et al. [59] successfully observe the missing ligand/cluster defects in defective UiO-66, showing distinct spatial distributions of defects coexisting with the ordered framework structure. These were evident from the contrast differences in HRTEM images compared to pristine UiO-66. While I could not access such advanced low-dose EM techniques, in Article #1 (Chapter 3) of this thesis, TEM images of SeLiRe_ZIF-8 revealed uniformly distributed bright spots at the center of nanoparticles, which were inferred to indicate the presence of additional pore structures through the SeLiRe strategy. Similarly, synchrotron XAS is another powerful technique to probe the local defect structures in MOFs/ZIFs. In Article #2, I utilized synchrotron XAS to analyze the coordination parameters of Zn sites in SeLiRe_ZIF-8, verifying the presence of localized and unsaturated Zn–N$_2$ sites and their derivative HO–Zn–N$_2$ sites. This is in stark contrast to the saturated Zn–N$_4$ sites observed in standard ZIF-8, further confirming the creation of missing ligand/cluster defects and corresponding open metal sites via the SeLiRe strategy. Similarly, Xue et al. [60] used Fourier-transformed XAS to demonstrate that introducing missing ligand defects can generate unsaturated Co^{2+} sites in Co-BDC MOFs.

In addition to advanced techniques, common characterizations such as IR (to verify bond cleavage), NMR (to confirm ligand removal), and TGA (to analyze the thermal decomposition of thermolabile ligands) are discussed/used in Article #1 (see Chapter 3 for details). Despite the combination of various techniques enabling the effective characterization of most SeLiRe-induced local structural defects in MOFs/ZIFs, achieving in-situ characterization of the SeLiRe process under real reaction or application conditions remains highly challenging [51].

In summary, the SeLiRe strategy is a post-synthetic method widely applicable to MOFs/ZIFs materials. The removal of labile ligands leads to the formation of additional porous structures (e.g., channels and cavities) and missing ligand/cluster defects, providing additional active sites and creating more pore space, which is beneficial for potential applications. Article #1 has a detailed study on utilizing the SeLiRe strategy to construct the hierarchically micro- and mesoporous ZIF-8, ultimately enhancing its adsorption capacity for methylene blue.

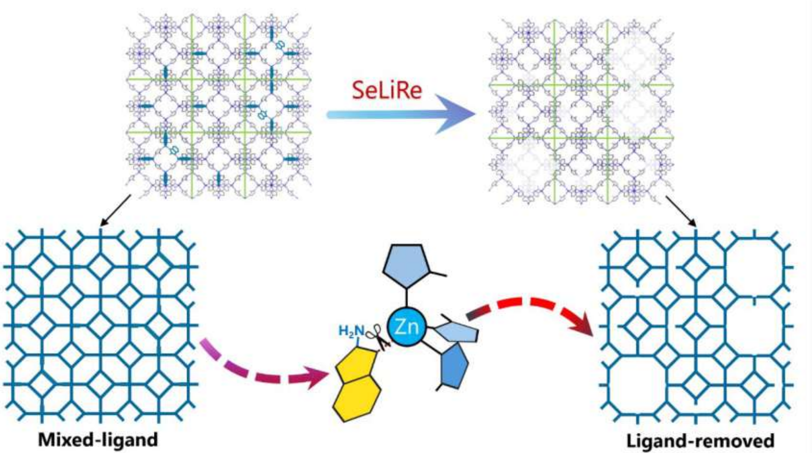

Figure 1.5: Schematic diagram of the selective ligand 2-aminobenzimidazole removal process for the mixed-ligand ZIF-8

1.3 Open metal sites and single-atom catalysts

MOFs/ZIFs possess abundant and well-ordered metal nodes, making them one of the most effective precursors for developing materials with open metal sites or single-atom catalysts. Due to the unique properties of open metal sites, such as isolated and dispersed metal atoms, fully exposed active sites, and distinct electronic structures, the materials with these sites have been widely applied in various catalytic reactions, demonstrating significantly higher catalytic activity compared to traditional nano-catalysts [61].

In MOFs/ZIFs, the coordination interactions between the periodically arranged ligands can act as fences, facilitating the atomic dispersion of target metal atoms. Moreover, the ligands themselves provide abundant nitrogen and carbon elements, which effectively anchor single metal atoms within the MOF framework. For example, ZIF-8, a commonly studied SOD topological structure, has been extensively utilized to anchor Fe, Mn, and even noble metal like Pt and Au onto nitrogen-doped carbon (NC) derived from ZIF-8 pyrolysis, resulting in the formation of M-N_x/NC structures (Figure 1.6) [62-64]. The widespread research on such active sites/structures has become overly abundant, so specific examples will not be listed here [65-66].

While this approach has yielded good catalytic performance, it has certain limitations or issues that could be considered counterproductive:

1. **Loss of framework structure and crystallinity**: The periodic framework structure and crystallinity of MOFs/ZIFs, often regarded as their hallmark properties, are entirely sacrificed during high-temperature pyrolysis in inert gas atmospheres. The elaborate effort put into identifying suitable metal nodes and ligands to synthesize MOF/ZIF structures ends up being wasted when these materials are merely used as precursors for anchoring target metal atoms.
2. **Dependence on introduced metal atoms**: The enhancement in catalytic activity primarily stems from the introduced target metal atoms, which serve as the real active sites, rather than from the inherent metal atoms within the MOFs/ZIFs. For instance, in Fe-N_x/NC, the real active site is the Fe atom, while the abundant Zn atoms originally present in ZIF-8 are evaporated at temperatures above 900°C in an inert atmosphere [67] to enable the metal dispersion and isolation of single Fe atoms.
3. **Low yield and energy inefficiency**: Thermolysis, the commonly used and straightforward treatment method, results in the evaporation of most of the original metal and ligand components from MOFs/ZIFs. Typically, the yield after high-temperature pyrolysis does not exceed 5%, making industrial-scale production or batch synthesis nearly impossible. Moreover, high-temperature

and inert gas protection require substantial energy and resources, leading to further inefficiencies.

In this thesis, I advocate for approaches that preserve the intrinsic framework structure and crystallinity of MOFs/ZIFs while constructing suitable and stable open metal sites or single-atom sites without introducing new metals. In Article #2 (Chapter 3), the Zn atoms originally present in ZIF-8 were used as the target metal sites. Using the SeLiRe strategy, I engineered the high-valence HO–Zn–N_2 sites to serve as real active sites for enhancing catalytic activity, and the SOD topology of ZIF-8 was successfully retained.

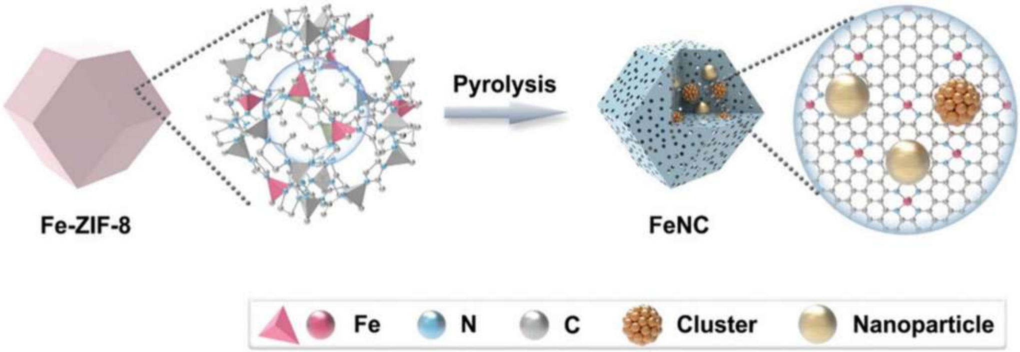

Figure 1.6: Schematic illustration of the synthesis of the Fe-NC electrocatalyst. Reprinted with permission from Wiley-VCH [68].

1.4 Environmental and energy applications

Over the past 20 years, at particularly relevant in the context of achieving carbon neutrality and addressing escalating environmental issues, novel MOF materials have garnered significant interest in the energy and environmental applications due to their inherent and characteristic features [69]. MOFs/ZIFs are extensively researched and applied in areas such as wastewater treatment/purification and other energy storage/conversion applications. Their high surface area and adjustable porous structures allow for selective adsorption/separation based on molecular size and polarity, such as gases, metal ions, and organic pollutants, which is of great significance for environmental remediation [70-71]. The abundance of metal active sites , combined with potential ligand defects, renders MOFs/ZIFs and their derivatives highly effective catalysts for a range of electrochemical processes, such as the hydrogen evolution reaction (HER), oxygen evolution reaction (OER), and oxygen reduction reaction (ORR) [72-75]. Similarly, in energy storage applications, MOFs/ZIFs can be used as electrodes in batteries and supercapacitors, where strategies such as multiple hydrogen bonding and π-π stacking can effectively enhance the energy/power density of the devices [76-78].

1.4.1 Water purification

Water scarcity and pollution are pressing global issues that humanity faces both now and in the future, efficiently purifying industrial and domestic wastewater into potable water is a crucial solution to this problem [79]. The high surface area, chemical properties and adjustable porosity of MOFs/ZIFs have attracted significant attention in the field of water purification, particularly for the adsorption and degradation of pollutants (e.g., dye and heavy metals) in aqueous solutions [80-81]. Their high surface area provides abundant adsorption sites for organic pollutants, while their tunable porous structures allow for selective diffusion of molecules within the cavities.

Common adsorption mechanisms of MOFs and their derived materials include electrostatic attraction [82-83], π-π interactions [84], hydrogen bonding [85], Lewis acid-base interactions [86], and physisorption [87]. The adsorption properties can be further enhanced by introducing ligand defects with additional mesopores, changing the surface charge, synthesizing composites, or through the mentioned above strategies. For example, Wang et al. [88] synthesized a series of amino-functionalized MOFs (including MIL-101-NH_2, MIL-53-NH_2, UiO-66-NH_2, and MOF-5-NH_2) though the mixed-ligand strategy, which showed significant potential for removing heavy metals. Zhang et al. [89] introduced different functional groups (-NH_2, -NO_2, and -Br) into MIL-53-Fe to achieve efficient adsorption of tetracycline (TCN) from aqueous solutions. Naghdi et al. [90] employed the SeLiRe strategy to obtain hierarchically porous MIL-125-Ti for the adsorption of glyphosate from aqueous solutions, with the additional mesopores increasing the adsorption capacity by nearly threefold. Similarly, Jhung et al. [91] enhanced the adsorption capacity of PCN-222-Fe for removing most cationic dyes from aqueous solutions by introducing mesopores.

For the adsorption kinetics curves obtained from experimental data were common fitted to pseudo-first-order (PFO) and pseudo-second-order (PSO) models [92], defined as follows Eq 1.4.1-2:

$$Q_t = Q_e(1 - e^{-K_1 t}) \tag{1.4.1}$$

$$Q_t = \frac{K_2 Q_e^2 t}{1 + K_2 Q_e t} \tag{1.4.2}$$

Here, K_1 (min^{-1}) and K_2 ($g\ mg^{-1}\ min^{-1}$) are the rate constants associated with the PFO and PSO models, respectively. Some reports suggest that the PFO model tends to describe physisorption occurring on the sample surface, while the PSO model is indicative of chemisorption [93]. However, this should be analyzed on a case-by-case basis and combined with characterization of the sample post-reaction to determine if new bonds have formed.

For adsorption isotherms, the experimental data were common fitted to Langmuir and Freundlich isotherm models [94], defined as follows Eq 1.4.3-4:

$$Q_e = \frac{Q_{max} K_L C_e}{1 + K_L C_e} \tag{1.4.3}$$

$$Q_e = K_F {C_e}^{1/n} \tag{1.4.4}$$

Here, Q_{max} (mg g^{-1}) represents the maximum adsorption capacity. K_L (L mg^{-1}) and K_F (mg g^{-1}) (mg L^{-1}) $^{-n}$ are the constants of the Langmuir and Freundlich models, representing adsorption capacity and the strength of the adsorbate-adsorbent interaction, respectively. The parameter n describes adsorption intensity and reflects the energy distribution and heterogeneity of the adsorption sites [95]. The Langmuir model typically describes monolayer adsorption on homogeneous surface, whereas the Freundlich model typically describes multilayer adsorption on heterogeneous surface [96].

Similarly, MOFs/ZIFs can achieve water purification through the catalytic degradation of organic pollutants. For instance, in photocatalysis, some MOFs with semiconductor properties can generate electron-hole pairs under light irradiation. The photoexcited electrons can react with O_2 to form reactive superoxide radicals ($O_2^{\bullet-}$), while the positively charged holes can attack hydroxide ions or water molecules to generate highly reactive hydroxyl radicals (•OH) [81]. These two radicals possess high oxidation potentials, enabling them to degrade organic pollutants in aqueous solutions through advanced oxidation processes (AOPs) within a short time frame [97-99]. Numerous studies have reported the efficient photocatalytic degradation of dyes in aqueous solutions using MOFs, thus achieving the goal of water purification [81, 100-102].

1.4.2 Water electrolysis to produce hydrogen

Water electrolysis is an efficient and rapid method of splitting water molecules (H_2O) into hydrogen (H_2) and oxygen (O_2) [73]. When powered by sustainable clean energy sources, such as solar or wind power, it offers the added benefit of reducing carbon emissions [103]. Hydrogen evolution reaction (HER) primarily occurs at the solid-liquid interface of the electrode and the electrolyte, with different mechanisms for acidic and alkaline electrolytes [104-105], as follows Eq 1.4.5-10:

Acidic:

$$Volmer: H_3O^+ + e^- + M \rightarrow M - H_{ad} + H_2O \qquad 1.4.5$$

$$Heyrovsky: M - H_{ad} + H_3O^+ + e^- \rightarrow M + H_2 + H_2O \qquad 1.4.6$$

$$Tafel: M - H_{ad} + M - H_{ad} \rightarrow 2M + H_2 \qquad 1.4.7$$

Alkaline:

$$Volmer: H_2O + e^- + M \rightarrow M - H_{ad} + OH^- \qquad 1.4.8$$

$$Heyrovsky: M - H_{ad} + H_2O + e^- \rightarrow M + H_2 + OH^- \qquad 1.4.9$$

$$Tafel: M - H_{ad} + M - H_{ad} \rightarrow 2M + H_2 \qquad 1.4.10$$

HER is generally more favorable under acidic conditions, because the energy required to adsorb hydrated protons (H_3O^+) is much lower than that of breaking the H-O-H bond of water molecules under alkaline conditions [106]. To date, noble metals like Pt remain the benchmark HER electrocatalysts due to their fast kinetics and low overpotential (0.1 V at 10 mA cm^{-2}), but the high cost and scarce resources limit the widespread applications [107]. In recent years, MOFs/ZIFs have been extensively researched in the electrocatalysis field due to their inherent advantages, such as:

- Abundant metal nodes that serve as active sites.
- Tunable porosity can expose more unsaturated/defective active sites.
- Micropore structure allows water molecules to rapidly access the active sites.
- High surface area that exposes more reactive sites.

Therefore, effectively tuning the active sites is crucial for enhancing the HER catalytic performance of MOFs/ZIFs. However, MOFs/ZIFs tend to be more "fragile" in electrocatalysis, due to the relatively weaker coordination bonds between metal nodes and organic ligands compared to the stronger ionic bonds found in inorganic solids [108]. This is exacerbated by the high and low pH values of the electrolytes. The unstable structure coupled with potentially lower electrical conductivity of most MOFs/ZIFs prevents their direct use as electrocatalysts. This issue can typically be improved through strategies such as ligand engineering or incorporating additional metal nodes, as detailed below section.

1.4.3 Water electrolysis to produce oxygen

For the anode reaction in water electrolysis, the oxygen evolution reaction (OER) has more complex kinetics and thermodynamic requirements than HER [109]. This is because OER involves four thermodynamically uphill processes, with at least three intermediates, requiring a higher overpotential to complete the reaction [110]. Currently, two recognized OER mechanisms are the traditional adsorbate evolution mechanism (AEM) and the lattice oxygen-mediated mechanism (LOM). The AEM mechanism is mainly discussed here as follows Eq 1.4.11-20 [109]:

Acidic:

$$H_2O + M \rightarrow M - OH_{ad} + H^+ + e^- \tag{1.4.11}$$

$$M - OH_{ad} \rightarrow M - O_{ad} + H^+ + e^- \tag{1.4.12}$$

$$2M - O_{ad} \rightarrow 2M + O_2 \tag{1.4.13}$$

$$M - OH_{ad} + H_2O \rightarrow M - OOH + H^+ + e^- \tag{1.4.14}$$

$$M - OOH_{ad} \rightarrow M + O_2 + H^+ + e^- \tag{1.4.15}$$

Alkaline:

$$OH^- + M \rightarrow M - OH_{ad} + e^- \tag{1.4.16}$$

$$M - OH_{ad} + OH^- \rightarrow M - O_{ad} + H_2O + e^- \tag{1.4.17}$$

$$2M - O \rightarrow 2M + O_2 \tag{1.4.18}$$

$$M - OH_{ad} + OH^- \rightarrow M - OOH_{ad} + e^- \tag{1.4.19}$$

$$M - OOH_{ad} + OH^- \rightarrow M + O_2 + H_2O \tag{1.4.20}$$

Unlike HER, OER is easier to occur in alkaline electrolytes compared to acidic ones. This is because the first step of OER in acidic electrolytes involves the dissociation of water molecules, leading to slower reaction kinetics, whereas in alkaline electrolytes, this step is not involved. Rutile-type RuO$_2$ is often regarded as the benchmark catalyst for OER, typically requiring only 0.3 V to achieve a current density of 10 mA cm^{-2} [111].

Due to the high overpotential required for OER, in-situ characterization techniques should be employed to monitor the electro-oxidation of MOF structures, to prevent them from transforming into metal hydroxides [108]. For example, directly using ZIF-67 in an alkaline environment under cyclic voltammetry can result in the formation of high-valence cobalt (oxy)hydroxide nanosheets [112]. Similarly, Tian et al. [113] demonstrated that upon applying a potential, a 3 nm thick oxyhydroxide layer forms on the MOFs surface, eventually transforming into metal oxyhydroxide nanosheets. For MOFs/ZIFs for electrocatalysis, several strategies can be employed to avoid the electro-oxidation process and to enhance the catalytic activity/stability [73, 114]:

1. **Constructing unsaturated active sites:** Creating ligand defects in MOFs can enhance their catalytic activity by exposing more active sites.
2. **Introducing different functionalized ligands:** Functionalized ligands with various groups can modify the electronic environment and electrical density of metal nodes.
3. **Incorporating multiple metals:** High activity metals doping such as Ni and Cu can regulate the coordination environment and exert additional synergistic effect.
4. **Composite structure:** Heterostructures interface can promote charge transfer and provide more active sites by heterostructures interface.

For example, Zhang et al. [103] significantly enhanced OER activity and alkaline stability by achieving post-synthetic ion exchange from MAF-X27-Cl to MAF-X27-OH. Li et al. [60] introduced missing ligand defects to tune the Co-MOF electronic structure, which exhibited excellent OER performance. Feng et al. [115] reported a low-temperature sulfur treatment method for Fe-MOF, introducing SO_3 terminal ligands, the resulting Fe_{MOFs}-SO_3 exhibited excellent stability and activity, making them highly suitable for large-scale industrial applications. These strategies collectively aim to overcome the kinetic barriers of OER and are also applicable to the previously discussed HER, thereby enhancing the electrocatalytic performance and stability of MOFs/ZIFs.

Despite these advances, these strategies still have limitations. They tend to increase the structural complexity of MOFs/ZIFs, compounding synthesis complexity, cost, and energy consumption. In electrocatalysis, especially for high-potential OER, partial reconstruction and electro-oxidation are almost unavoidable, particularly in high-pH alkaline electrolytes (1M KOH) [108, 112], not to mention the irreversible chloride ion (Cl^-) corrosion encountered in seawater electrolysis. Additionally, the inherently low conductivity of MOFs/ZIFs is challenging to improve significantly through these strategies to match that of noble metals (Pt or Au) or carbon materials (graphene and nitrogen-doped carbon). As a result, the catalytic performance of most MOFs/ZIFs and their derivatives rarely reaches optimal levels. Most research focuses instead on understanding structural evolution, catalytic mechanisms, and interfacial reactions of MOFs/ZIFs rather than solely enhancing catalytic activity.

Challenges and aims

As introduced in Chapter 1 of this thesis, metal-organic frameworks (MOFs) and their subfamily of zeolitic imidazolate frameworks (ZIFs) have significant potential in environmental and energy applications due to their unique features. They can meet the demands for carbon neutrality and address energy and environmental crises. Currently, MOFs/ZIFs face following main challenges in water purification and catalytic applications: (1) limited access to active sites due to the lack of mesopores, (2) saturated metal coordination hindering catalytic activity, (3) insufficient stability in (photo)electrochemical environments, and (4) low electrical conductivity reducing catalytic efficiency.

To overcome these critical challenges, this thesis focuses on ligand engineering of sodalite topology ZIFs through mixed ligand (section 1.3.2) and selective ligand removal (sections 1.3.3) strategies to alter their electronic structure and chemical properties. Details on how these challenges are addressed to achieve the desired objectives can be found in the cumulative papers in Chapter 3. Chapter 2 introduces the instruments used for material characterization. Starting from Chapter 3, a cumulative collection of published articles, and a summary of the highlights are as follows:

Article #1 explores a ligand removal strategy of designing hierarchical porous ZIFs with various topologies. Through controlled thermal treatments, the thermolabile ligand can be quantitatively removed, thereby introducing mesopores of uniform size and shape into the ZIF structure for methylene blue adsorption.

Article #2 focuses on the open metal sites in the SeLiRe-ZIF from Article #1 and identifies their contribution to the HER mechanism. Advanced in-situ characterization and computational simulations are used to validate the local structure of these active sites that facilitate the water activation kinetics.

Article #3 continues a mixed ligand strategy by incorporating four distinct heterocycles featuring amino groups as a respective secondary ligand, aiming to construct a series of ligand-engineered ZIFs. A set of cutting-edge in-situ techniques are used to deeply study the new ZIF samples to elucidate structural, electronic, and functional changes during photo- and electrocatalytic OER processes.

Each article's introduction section thoroughly addresses the challenges faced by ZIFs, their current status, and the motivation behind employing specific strategies to tackle these challenges.

Finally, Chapter 4 summarizes the research, discusses the future application prospects and challenges of MOFs/ZIFs materials, and proposes ideas for further improvements.

Characterization and methods

This chapter describes all the characterization equipment used to analyze the electronic structure, chemical properties, and surface morphology of ligand-engineered zeolite imidazole frameworks (ZIFs). Each section briefly provides the introduction to the theoretical background, detailed information about the respective equipment, and the steps for measuring the samples. Computational simulations and detailed information on the sample synthesis are discussed in the corresponding sections of the relevant articles or referred to the articles stored online.

2.1 X-ray spectroscopy techniques

2.1.1 X-ray diffraction

Background:

X-ray diffraction (XRD) is a commonly used, universal, and rapid characterization technique employed by researchers to determine whether MOF materials are crystalline and to provide certain information such as crystal structure and crystal phase of the MOFs/ZIFs. In this thesis, since all materials are primarily in powder form, every sample was tested for its Bragg characteristic peaks and crystallinity using powder XRD. The stability of the samples before and after the reaction can be easily demonstrated by comparing the changes in intensity and shifts of the Bragg peaks obtained from the XRD measurements.

Setup:

The sample holder used is a single crystal silicon, and the sample powder is fixed onto it with a drop of heptane. The XRD instrument used is an ANalytical X'Pert Pro multi-purpose diffractometer (MPD) with Bragg-Brentano geometry. The X-ray source is Cu, operating at a voltage of 45 kV and a current of 40 mA. Additionally, in-situ temperature XRD measurements were utilized; for more details, please refer to Article #1.

2.1.2 X-ray photoelectron spectroscopy

Background:

X-ray photoelectron spectroscopy (XPS) is a commonly used technique for analyzing the electronic structure of the MOF surface near region, providing information on elemental composition, oxidation states, and chemical environments within the

MOFs/ZIFs. In this thesis, XPS was primarily used to analyze the high-valence oxidation states (Articles #2 and #3) of the ZIF powders before and after the reaction, such as the presence of Co^{3+}, Co^{3+} in CoOOH, and HO−Zn bond.

Setup:
The analyses were conducted using a custom-built SPECS XPS spectrometer equipped with a monochromatized Al-Kα X-ray source (μFocus 350) and a hemispherical WAL-150 analyzer (acceptance angle: 60°). For more details on the equipment, sample preparation, and data analysis, please refer to the respective articles.

2.1.3 X-ray absorption fine structure spectroscopy

Background:
X-ray absorption fine structure (XAS) spectroscopy is primarily driven by synchrotron radiation, and is the premier contactless technique for measuring the electronic and atomic structure around metal sites. The XAS spectra of condensed matter are usually divided in two energy regions: X-ray absorption near edge structure (XANES) and extended X-ray absorption fine structure (EXAFS). By selecting specific metal atoms of ZIF sample, it is possible to obtain information on the coordination number (number of neighboring atoms), bond lengths, and local bonding structures. For instance, in Article #2, it was demonstrated that OH groups are chemisorption to Zn atoms, forming $HO-Zn-N_2$ sites.

Setup:
The Zn K-edge XAS data were collected at beamlines 1W1B and 1W2B in the Beijing Synchrotron Radiation Facility (BSRF, operating at 2.5 GeV with a maximum current of 250 mA). The collected XAFS data were then processed using Athena software for background, pre-edge line, and post-edge line calibration, refer Article #2 for the detailed fitting procedure.

2.2 Infrared spectroscopy

Background:
Attenuated total reflection Fourier transform infrared spectroscopy (ATR-IR) is a crucial technique that utilizes infrared radiation to study the vibrational modes of different bonds within MOF/ZIF frameworks. In this thesis, ATR-IR was used for most samples to confirm the presence of organic functional groups within the framework, such as in Article #1 and Article #3, which successfully demonstrated the presence

of $-NH_2$ groups to verify the successful incorporation of 2-aminobenzimidazole (NH_2-bIm) into the ZIF framework.

Setup:
The IR spectra were obtained using a Perkin Elmer Two Spectrum equipped with a $LiTaO_3$ detector.

2.3 Electron microscopy

2.3.1 Scanning electron microscopy

Background:
Scanning electron microscopy (SEM) uses an electron beam that scan through a raster to obtain images of the morphology and structure of MOFs through the interaction of electrons with the sample surface. In this thesis, SEM is commonly used to simply determine the morphology of ZIF nanoparticles and to calculate their particle size. It should be noted that since most MOF/ZIF materials are electron-beam-sensitive and have poor conductivity, an ion beam sputtering equipment is used for gold coating prior to testing. This forms a surface coating that serves as a protective layer and enhances conductivity, allowing for high-quality SEM images.

Setup:
The SEM equipment used is an FEI Quanta 250 (Schottky-)FEG-SEM, provided by the USTEM (University Service Center for Transmission Electron Microscopy) at TU Wien, equipped with an ETD secondary electron detector and an EDAX-AMETEK Octane Elite 55 detector.

2.3.2 Transmission electron microscopy

Background:
Transmission electron microscopy (TEM) involves an electron beam penetrating a very thin sample or a copper grid loaded with MOF nanoparticles. As the electron beam passes through the sample, the interactions between the electrons and the sample produce images with varying brightness. Given that most MOF/ZIF materials are electron beam-sensitive, it's crucial to avoid high-voltage electron beams that can alter the morphology and damage the structure. In this thesis, TEM was successfully used to confirm the presence of mesoporous cavities (Article #1) and outer (oxy)hydroxide layers (Article #3).

Setup:

The TEM equipment used is a Tecnai F20 FEG-TEM, provided by USTEM (University Service Center for Transmission Electron Microscopy) at TU Wien, equipped with an X-FEG and a Gatan Rio16 CCD-camera.

2.4 Ultraviolet-Visible spectroscopy

Background:

Ultraviolet-visible spectroscopy (UV-Vis) is used to determine the light absorption (UV and visible) and reflection capabilities of MOFs, providing information on electronic transitions and solution concentration. In this thesis, the diffuse reflectance spectroscopy (DRS) mode of UV-Vis was utilized to test the powder samples of ZIFs, assessing their ability to absorb visible light and calculate the band gap using appropriate formulas (detailed in Article #3). For liquid samples, the standard mode was employed to measure absorbance. By using the formulas, the concentration of methylene blue (MB) in solution can be determined, which helps calculate the adsorption capacity of the samples (detailed in Article #1).

Setup:

For powder DRS measurements, $MgSO_4$ was used as a baseline, and measurements were conducted using a Jasco V-670 with an Ulbricht-sphere.

2.5 Raman spectroscopy

Background:

Raman spectroscopy is a contactless analytical technique based on the Raman scattering principle, which involves the inelastic scattering of photons to determine the vibrational modes of molecules within the MOF framework. In this thesis, Raman spectra provided characteristic signals corresponding to different vibrational modes of molecules in the ZIF ligands and corresponding organic functional groups. In Article #3, the Raman spectrometer was coupled with an electrochemical cell for in-situ electrochemical measurement. This enabled real-time monitoring of the evolution of MOF structures on the electrode under various time points and applied potentials, such as the transformation from ZIF-67 to $Co(OH)_2$ to CoOOH during the electrocatalytic OER process.

Setup:

The measurements were collected using a HORIBA LabRAM spectrometer with a 532 nm laser.

2.6 Photoluminescence spectroscopy

Background:

Photoluminescence spectroscopy (PL) is a contactless analytical technique used to study the photoelectric properties of MOFs by analyzing the light emitted when excited electrons from the lowest unoccupied molecular orbital (LUMO) to the highest occupied molecular orbital (HOMO). In this thesis, PL spectra was coupled with an electrochemical cell for in-situ electrochemical PL measurement. In Article #3, the PL spectra were used to monitor the intensity and shift of PL characteristic peaks of ZIF samples on the electrode by varying the reaction time and applied potential, providing insight into the degradation of the ZIF framework. For example, during the electrocatalytic OER process, the PL characteristic peaks of ZIF-67 showed a decrease in intensity and a blue shift over time, indicating its structural degradation.

Setup:

The measurements were performed using a PicoQuant FluoTime 300 spectrometer, with the sample electrodes excited at a wavelength of 425 nm. The excitation source was a 300 W xenon arc lamp equipped with a double-grating monochromator. The detection system comprised a PMA Hybrid 07 detector and a high-resolution double monochromator.

2.7 N_2 Physisorption

Background:

N_2 physisorption method is widely used to measure the specific surface area and pore size distribution of various porous materials, and it is especially important for MOF materials. The principle is based on the different gas adsorption characteristics of open pores in the sample surface. By testing the equilibrium adsorption capacity under a certain pressure, the physical adsorption properties of the MOF/ZIF materials can be obtained through the calculation modeling.

Setup:

In this thesis, the specific surface area was determined using the Brunauer-Emmett-Teller (BET) method, and the pore size distribution data were modeled using non-local density functional theory (NLDFT). Prior to analysis, the samples were degassed under vacuum at 150°C for 2-12 hours, followed by measurements at 77 K using a Micromeritics 3Flex analyzer.

2.8 Nuclear magnetic resonance spectroscopy

Background:

Nuclear magnetic resonance spectroscopy (^{1}H NMR) is a widely used technique for detecting organic functional groups in MOF ligands. The principle is based on the magnetic properties of certain atomic nuclei in the ligand molecules, which provide information about their chemical characteristics. In this thesis, ^{1}H NMR was used to detect the successful incorporation of the secondary ligand and its removal process by identifying the characteristic signals of the hydrogen atoms.

Setup:

ZIF samples were tested in a liquid phase environment by digesting them in d_4-acetic acid, and then liquid-phase ^{1}H NMR spectra were recorded using a Bruker ADVANCE 250 (250.13 MHz) instrument.

2.9 Thermogravimetric analysis

Background:

Thermogravimetric analysis (TGA) is a method used to track and measure changes in the mass or weight of MOFs as the temperature increases under different gas atmospheres (air, Ar, or N_2). This method provides information on the thermal stability and decomposition parameters of MOF/ZIF materials. In this thesis, as described in Article #1, TGA was utilized to determine the suitable temperature windows for selectively removing the secondary ligand to create mesopores and defect structures, given that the primary ligand and the secondary ligand in the mixed-ligand ZIF have different decomposition temperatures.

Setup:

Measurements were performed using a PerkinElmer 8000 instrument (Waltham, USA), with samples heated in Al_2O_3 crucibles at a heating rate of 10°C/min in air, Ar, or N_2 flow.

Results and discussion

This thesis is presented in a cumulative form and includes three peer-reviewed articles reprinted with the permission of respective journals [116-118]. The contributed articles are listed as follows:

Article #1:

"Hierarchically Micro- and Mesoporous Zeolitic Imidazolate Frameworks through Selective Ligand Removal"

*Zheao Huang, Jakob Rath, Qiancheng Zhou, Alexey Cherevan, Shaghayegh Naghdi, and Dominik Eder **

Small, **2024**, *20* (21), 2307981

DOI: https://doi.org/10.1002/smll.202307981

Article #2:

"Engineering of HO–Zn–N_2 Active Sites in Zeolitic Imidazolate Frameworks for Enhanced (Photo)Electrocatalytic Hydrogen Evolution"

*Zheao Huang, Zhouzhou Wang, Qiancheng Zhou, Hannah Rabl, Shaghayegh Naghdi, Ze Yang *, and Dominik Eder **

Angewandte Chemie International Edition, 2024, e202419913

DOI: https://doi.org/10.1002/anie.202419913

Article #3:

"Ligand Engineering Enhances (Photo)Electrocatalytic Activity and Stability of Zeolitic Imidazolate Frameworks via In-situ Surface Reconstruction"

*Zheao Huang, Zhouzhou Wang, Hannah Rabl, Shaghayegh Naghdi, Qiancheng Zhou, Sabine Schwarz, Dogukan Hazar Apaydin, Ying Yu *, and Dominik Eder **

Nature Communications, **2024**, *15* (1), 939.

DOI: https://doi.org/10.1038/s41467-024-53385-0

3.1 Summary of contributed articles

This thesis covers three distinct articles, all of which I am the first author of, showcasing the research work of my Ph.D. The fundamental concept of these articles is based on ligand-engineered sodalite topology ZIFs (ZIF-8 and ZIF-67), involving mixed ligand and selective ligand removal (SeLiRe) strategies, and investigation the performance enhancement of these strategies in dye adsorption for water purification, hydrogen evolution reaction (HER), and oxygen evolution reaction (OER) with ZIFs as adsorbents/catalysts.

Article #1:
I utilized the SeLiRe strategy to develop a series of hierarchical micro- and mesopores ZIFs. The first step involves selecting a thermolabile secondary ligand to synthesize mixed-ligand ZIFs with good crystallinity alongside the initial ligand. I partially replaced the original ligand with the more thermolabile 2-aminobenzimidazole (NH_2-bIm) ligand. The second step involved selectively removing NH_2-bIm by carefully cleaving the metal-ligand coordination. A series of in-situ and ex-situ techniques were employed to clearly reveal the ligand removal process, which was unaffected by the atmosphere (air, Ar or N_2). To thoroughly investigate the ligand removal process, a combination of in-situ and ex-situ techniques was utilized, demonstrating that the process remained consistent under different atmospheric conditions (air, Ar or N_2). Compared to unmodified ZIF-8, the ligand-removed ZIF achieved a 40-fold increase in methylene blue adsorption capacity. This remarkable improvement was attributed to the creation of additional mesopores via the SeLiRe strategy, which expanded the pore volume and facilitated faster diffusion of dye molecules to the adsorption sites.

Comments:
As this was my first published paper during my Ph.D. study, the research depth was somewhat limited. Most of the characterization techniques used were basic and conventional. For instance, the detailed process of ligand removal relied heavily on ATR-IR data rather than advanced in-situ temperature-dependent IR spectroscopy. Although I attempted in-situ DRIFT (Diffuse Reflectance Infrared Fourier Transform) experiments, the results were inconsistent with the ex-situ data, likely due to an issue with the heater, and therefore, these results were not included in **Article #1**.

Additionally, as mentioned in Section 1.2.3, the distribution of secondary ligands in mixed-ligand ZIFs is difficult to confirm, which also made it challenging to accurately determine the location and quantity of the ligand-defect/domain-defect after applying the SeLiRe strategy. Advanced atomic-resolution electron microscopy techniques were not utilized to conduct deeper investigations in this study.

Despite these limitations, **Article #1** primarily serves to introduce a method for creating additional mesopores within the ZIF framework and thoroughly validate its feasibility and mechanism — the SeLiRe strategy. This approach also allows for the design of open metal sites within the SOD-type ZIF framework, which connects directly to the catalytic reactions studied in **Article #2**. It provides a pathway for designing high-valence active sites, offering new ideas for enhancing catalytic performance.

Article #2:

To extend the application range of SeLiRe ZIFs in other fields, I engineered well-defined open metal sites ZIF (OMS-ZIF) via the SeLiRe strategy and investigating their role in the HER mechanism. By combining in-situ electrochemical Raman/UV-vis/PL spectroscopy and complementary techniques such as synchrotron X-ray absorption spectroscopy, I verified that the $Zn–N_2$ sites obtained by the SeLiRe strategy preferentially chemisorbed OH anions in presence of alkaline electrolytes to form localized $HO–Zn–N_2$ active sites. These new sites remain stable during electrocatalytic reactions while preserving the original ZIF framework structure. Compared to the saturated $Zn–N_4$ sites in pure ZIF-8, these high-valence active sites provide OMS-ZIF with great electrocatalytic stability, achieving a current density of 10 $mA\,cm^{-2}$ at 0.07 V overpotentials, with stable operation for over 120 hours. Density functional theory (DFT) simulations further validated that the high-valence $HO–Zn–N_2$ active sites promoted water activation kinetics, thereby facilitating the overall HER process. Together, both of the aforementioned **Articles #1** and **#2** involved the SeLiRe strategy on ZIF-8 (Zn), and successfully addressed the challenges in environmental and energy fields.

Comments:

As my third published paper during my Ph.D. study, this paper represents a more focused and concise investigation compared to **Article #1**. It incorporated advanced characterization techniques and extensive computational simulations to predict and validate the catalytic performance of ZIFs. Building on the SeLiRe-ZIF developed in **Article #1**, I employed state-of-the-art synchrotron XAS to confirm critical information about the coordination environment, coordination number, and bond lengths of the $HO–Zn–N_2$ active sites, as well as their transformations under electrocatalytic conditions. I am particularly satisfied with the outcomes of **Article #2**.

However, despite the use of synchrotron XAS, one limitation remains: to achieve more definitive monitoring of the transformations in open metal sites during catalysis, in-situ electrochemical XAS would have been ideal. Unfortunately, as this was my first time using synchrotron techniques and due to the limited availability of beamlines equipped for in-situ electrochemical cell, I could only rely on ex-situ data to validate the presence and behavior of HO–Zn–N_2 active sites in HER process.

The findings of **Article #2** have provided a clear pathway for future research. I plan to engineer HO–M–N_2 active sites, with noble metals such as Pt and Au as the target metals, to further enhance catalytic activity and explore new possibilities in electrocatalysis.

Article #3:

Next, I selected ZIF-67 (Co) which shares the sodalite topology with ZIF-8 (Zn), and successfully incorporated four secondary ligands featuring aromatic carbon rings and -NH_2 groups through a mixed ligand strategy. These secondary ligands were uniformly microwave synthesized with the primary imidazole ligand to construct a series of ligand-engineered ZIFs (LE-ZIFs) with high crystallinity, aiming to enhancing electrochemical OER activity and stability. To investigate the reconstruction occurring during (photo)electrocatalytic reactions, I combined continuous cyclic voltammetry, in-situ UV-Vis absorption, in-situ Raman, and in-situ photoluminescence (PL) spectroscopy. I observed that the addition of the secondary ligand hindered the complete reconstruction of the LE-ZIF structure into CoOOH compounds; Instead inducing surface-limited reconstruction by forming an ultra-thin CoOOH protective layer (4 nm), thereby enhancing stability under light irradiation and applied electric fields to unprecedented values. Theoretical calculations underscored the crucial role of the synergistic effect of the secondary ligand, which reduced the Gibbs free energy, making the LE-ZIF more stable while accelerating electron transfer to reactants, ultimately enhancing overall OER activity. Additionally, the SeLiRe strategy for ZIF-67 failed due to the difficulty in finding a suitable secondary ligand to create a thermal decomposition window for the original ligand, detailed in the Supporting Information of **Article #1**.

Comments:

As my second published paper during my Ph.D. study, this paper marked my first research focusing on electrocatalysis, specifically for OER applications. Since I was initially unfamiliar with electrocatalytic OER, I spent a considerable amount of time studying this process. Compared to the HER in **Article #2**, OER requires a higher applied potential, making traditional ZIFs more prone to complete reconstruction and electro-oxidation. I utilized three different in-situ electrochemical spectroscopy techniques to monitor the electrocatalytic OER process. Furthermore, this paper reported a series of five new mixed-ligand ZIFs, performing identical performance tests and characterizations on all samples to identify the best catalytic candidate and demonstrate the differing structural evolution trends during OER. This work required a significantly larger effort compared to **Articles #1** and **#2**.

While incorporating a secondary ligand partially mitigated the electro-oxidation process and improved electrical conductivity, it could not completely prevent surface reconstruction, which ultimately led to the formation of core-shell structures in ZIF particles. Two main limitations of this study are: 1) I did not use the atomic-resolution electron microscopy to observe the atomic arrangement at the core-shell interface, and nor monitor the growth of the CoOOH shell and the structural evolution of the mixed-ligand ZIF during the electrocatalytic process using in-situ electrochemical electron microscopy. 2) Although a synergistic effect or electronic transfer between the CoOOH shell and the SOD-type ZIF core likely contributed to the enhanced catalytic activity, I lacked the appropriate characterization tools to substantiate this hypothesis and had to rely solely on computational simulations to infer the existence of the synergistic effect.

Despite these limitations, I consider **Article #3** to be my best publication during my Ph.D. It offers a mixed-ligand strategy to enhance the catalytic stability and activity, providing valuable insights for my research and for other researchers exploring SOD-type ZIFs. This work also opens new avenues for studying other topological MOFs/ZIFs using similar strategies, further expanding the scope of catalyst design.

Overall, in this thesis, the modifications in porosity, electronic structure, and chemical properties of sodalite topology ZIF-8 (Zn) and ZIF-67 (Co) are investigated through mixed ligand and selective ligand removal strategies, providing a detailed analysis of their applications in environmental and energy fields. The results of this thesis have broad implications, offering new design principles for developing multifunctional MOFs/ZIFs tailored for environmental and energy applications. Furthermore, it highlights the potential for expanding these strategies to other topological frameworks, paving the way for future advancements in the MOFs field.

3.2 Published articles

3.2.1 Article #1

"Hierarchically Micro- and Mesoporous Zeolitic Imidazolate Frameworks through Selective Ligand Removal"

*Zheao Huang, Jakob Rath, Qiancheng Zhou, Alexey Cherevan, Shaghayegh Naghdi, and Dominik Eder **

Small, **2024**, *20* (21), 2307981

DOI: https://doi.org/10.1002/smll.202307981

As the first author of these articles, I led the entire research process, provided the original idea, conducted most of the testing, and wrote the manuscript. The corresponding Supplement Information can be found on pages 43-97.

Reprinted with permission from *Small* [116].

Hierarchically Micro- and Mesoporous Zeolitic Imidazolate Frameworks Through Selective Ligand Removal

*Zheao Huang, Jakob Rath, Qiancheng Zhou, Alexey Cherevan, Shaghayegh Naghdi, and Dominik Eder**

A new method to engineer hierarchically porous zeolitic imidazolate frameworks (ZIFs) through selective ligand removal (SeLiRe) is presented. This innovative approach involves crafting mixed-ligand ZIFs (ML-ZIFs) with varying proportions of 2-aminobenzimidazole (NH$_2$-bIm) and 2-methylimidazole (2-mIm), followed by controlled thermal treatments. This process creates a dual-pore system, incorporating both micropores and additional mesopores, suggesting selective cleavage of metal-ligand coordination bonds. Achieving this delicate balance requires adjustment of heating conditions for each mixed-ligand ratio, enabling the targeted removal of NH$_2$-bIm from a variety of ML-ZIFs while preserving their inherent microporous framework. Furthermore, the distribution of the initial thermolabile ligand plays a pivotal role in determining the resulting mesopore architecture. The efficacy of this methodology is aptly demonstrated through the assessment of hierarchically porous ZIFs for their potential in adsorbing diverse organic dyes in aqueous environments. Particularly striking is the performance of the 10%NH$_2$-ZIF-2 h, which showcases an astonishing 40-fold increase in methylene blue adsorption capacity compared to ZIF-8, attributed to larger pore volumes that accelerate the diffusion of dye molecules to adsorption sites. This versatile technique opens new avenues for designing micro/mesoporous ZIFs, particularly suited for liquid media scenarios necessitating efficient active site access and optimal diffusion kinetics, such as purification, catalysis, and sensing.

1. Introduction

Zeolitic imidazolate frameworks (ZIFs) are a special sub-class of metal-organic frameworks (MOFs) constructed from tetrahedral metal ions (e.g. Zn, Co) bridged by imidazolate (IM) ligands.[1] ZIF-8 is a popular representative that is composed of tetrahedrally coordinated zinc ions based on zeolitic sodalite topology.[2] The presence of microporosity (pore size < 2 nm) has allowed ZIF-8 to be extensively researched in adsorption,[3] catalysis,[4] drug release[5] and hydrogen storage.[6] ZIFs were initially regarded as structurally ideal materials with tunable micropores. However, as research has progressed, the lack of mesoscale cavities has shown to impede the diffusion/adsorption of macromolecules (e.g. enzymes, drugs and particulate matter),[7–10] which severely restricts the expansion of ZIFs' application. Thus, the incorporation of mesopores (2–50 nm) in parent ZIFs is crucial in order to meet the requirements of modern applications.

Recent years have seen an increasing number of attempts at designing hierarchically porous MOFs (HP-MOFs), which consist of both micro- and mesopores, often with interconnected channels.[11,12] HP-MOFs are able to retain the advantages of intrinsic micropores, yet the presence of additional mesoscale cavities expands their potential applications. In addition to reducing the restriction of macromolecule diffusion, the existence of hierarchical pores also exposes coordinatively unsaturated sites, facilitating enhanced catalysis and adsorption performance.[10,12,13] Consequently, many synthetic strategies have been developed to design and construct HP-MOFs such as commonly used templating,[14] defect formation strategy,[15] and etching technique.[16] While mesoporous structures can originate from the development of defects, excessively random defects make it difficult to precisely tailor the mesoporous features in terms of molecular size. Furthermore, the template removal and etching processes often result in morphological or structural collapse, which can have detrimental effect on the crystal structure and relevant properties.[17] In addition to these bottlenecks, it remains a challenge to control size and spatial arrangement of the hierarchical pores, not only

---

Z. Huang, J. Rath, A. Cherevan, S. Naghdi, D. Eder
Institute of Material Chemistry
Vienna University of Technology
Vienna 1060, Austria
E-mail: dominik.eder@tuwien.ac.at

Q. Zhou
Institute of Nanoscience and Nanotechnology
College of Physical Science and Technology
Central China Normal University
Wuhan 430079, China

The ORCID identification number(s) for the author(s) of this article can be found under https://doi.org/10.1002/smll.202307981

DOI: 10.1002/smll.202307981

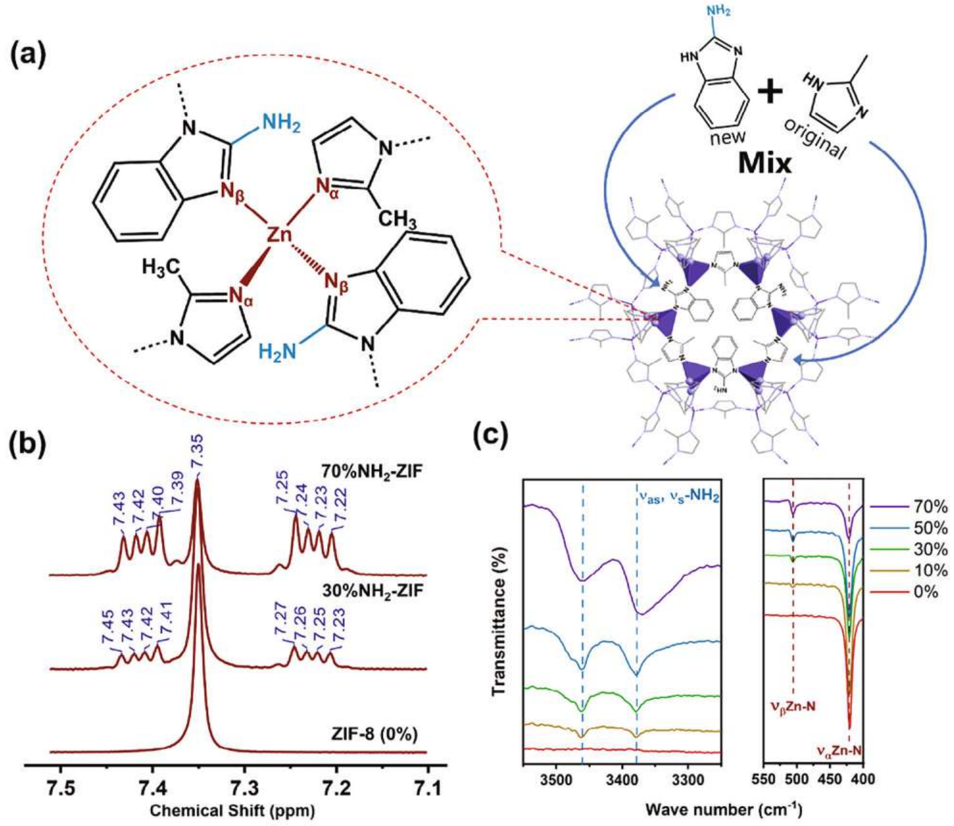

Figure 1. Structural characterization of mixed-ligand ZIFs. Schematic diagram of the ZnN_4 cluster and unit cell a) of the 50%NH_2-ZIF. ^1H NMR spectroscopy of pure ZIF-8, 30%NH_2-ZIF and 70%NH_2-ZIF b), from the entire ^1H NMR in Figure S1 (Supporting Information). All samples were digested using d^4-acetic acid and then tested by ^1H NMR. Ex situ ATR-IR spectra of 0–70%NH_2-ZIFs, presented for the IR range at 400–550 cm^{-1} and 3250–3550 cm^{-1} respectively c), from the entire IR spectra in Figure S2a (Supporting Information).

for the stability of the overall MOF framework, but likewise for maintaining the integrity of the mesoscale cavities.[18–20]

A more promising strategy toward HP-MOFs was recently reported by Feng et al.[21] and Naghdi et al.[13]] and is based on the selective ligand removal (SeLiRe) from mixed-ligand MOFs through thermolysis. This strategy is a post-synthetic method, which makes it applicable to a wider range of MOFs. Moreover, the removal of the thermolabile ligand can result in the formation of different mesoporous architecture, e.g. channels and cavities, making it easier to control the porosity of HP-MOFs while maintaining the intrinsic crystal structure. So far, however, the construction of hierarchical pores via SeLiRe has not been achieved with ZIFs.

Herein, we utilize the SeLiRe strategy for the first time to construct ZIFs with controlled hierarchical micro/mesopores. Distinct functional groups are known to cause considerable differences in the ligand's resistance to thermal treatments[21,22] Therefore, the first step involves the synthesis of mixed-ligand ZIFs (ML-ZIFs) with suitably distinct thermal stability. In this work, we replaced different fractions of the original 2-mIm ligand with the more thermolabile amino-functionalized NH_2-bIm ligand. The second step involves the selective removal of NH_2-bIm through careful cleavage of the metal-ligand coordination. In contrast to the aforementioned MOF examples, the SeLiRe process with ZIFs requires a more careful fine-tuning of various process conditions including temperature, atmosphere and reaction time. The process was monitored through various in situ techniques, and the ligand removal was quantified through ATR-IR and ^1H NMR spectroscopies. In the third step, ligand-removed ZIFs (LR-ZIFs) were assessed to have controlled micro/mesoporosity by N_2 physisorption. Ultimately, we show that the hierarchically porous structure of the new LR-ZIFs can significantly enhance the adsorption capacity of various organic dyes in water.

2. Results and Discussion

2.1. Structural Characterization of Mixed-Ligand ZIFs

ZIF-8 is formed by the tetrahedral coordination of zinc ions linked to the ligand 2-mIm.[23,24] Mixing in the thermolabile ligand, NH_2-bIm (**Figure** 1a), is a typical method for introducing amino groups.[25] We synthesized a series of R%NH_2-ZIFs through solvent-assisted ligand exchange (SALE), where R% represents the synthetic mass of the NH_2-bIm ligand (0–70%). In the ^1H nuclear magnetic resonance (^1H NMR) of Figure 1b, the ML-ZIFs (30% and 70%) exhibit the typical spectral features of both 2-mIm and NH_2-bIm (characteristic quartets on sides of 7.35 ppm), compared to pure ZIF-8. The quartets increase with increasing R%, which allows quantification of the actual mixed-ligand composition by ^1H NMR. Figure S1 and Table S1 (Supporting Information) show that the respective contents are in good agreement with the nominal values.

Attenuated total reflection infrared spectroscopy (ATR-IR) reveals the successful embedding of NH_2-bIm ligands within the ML-ZIF framework. Notably, an increase in the mixing ratio of NH_2-bIm is associated with elevated $\nu(\text{-}NH_2)$ modes (symmetrical at 3380 cm^{-1} and asymmetric at 3460 cm^{-1}, as seen in Figure 1c; Figure S2a, Supporting Information), indicating homogeneous incorporation of NH_2-bIm.[25,26] Additionally, a new band emerges at 506 cm^{-1} (Figure 1c), intensifying with higher NH_2-bIm fractions within the structure. Correspondingly, the original ν(Zn—N) mode (at 421 cm^{-1}) associated with metal-IM bonds diminishes. Importantly, the 506 cm^{-1} band is independent of NH_2-bIm itself (Figure S2b, Supporting Information) and closely resembles the Zn—N band observed in ZIF-7 synthesized using a benzimidazole ligand (bIm) with a structure akin to NH_2-bIm.[27,28]

The data therefore suggest that the new band is generated by the new Zn—N bonding vibration between Zn and N on the fused-imidazole ring on NH_2-bIm (hence, the original Zn—N is named Zn-N_α and the new one is named Zn-N_β). Note that the original tetrahedral coordination of Zn^{2+} is maintained (Figure 1a). The decrease in ν(Zn-N_α) band and the increase in ν(Zn-N_β) band are consistent with the increasing mixed-ligand ratio, thus reflecting the competitive coordination between 2-mIm and NH_2-bIm (Figure S2c,d, Supporting Information).

The X-ray diffraction (XRD) patterns of the ML-ZIFs exhibit a close resemblance to those of ZIF-8, characterized by multiple Bragg peaks, indicating well-preserved intrinsic structure and good crystallinity (Figure S3a, Supporting Information). As the ligand ratio increases, the intensity of the crystalline (011) peak diminishes, accompanied by an increase in its full-width at half-maximum (FWHM). This indicates the presence of structural distortion due to the competitive coordination between the new amino ligand and the original ligand, resulting in a weakening of the crystallinity (Figure S3b, Supporting Information).[29,30] Consequently, this phenomenon introduces some degree of disorder, impacting the morphology and the "optimal" particle size, causing the ZIFs to exhibit less stable growth compared to the prior state (as observed in scanning electron microscopy, SEM, in Figure S4, Supporting Information).

2.2. Influence of Temperature and Time on Selective Ligand Removal

The thermal stability of the samples ranging from 0% to 70% of NH_2-bIm content was examined through thermogravimetric analysis (TGA) under air atmosphere, heating up to 600 °C. The TGA curves reveal distinct mass losses for the ML-ZIFs within the temperature range of 200–400 °C (Figure S5a, Supporting Information). In the case of the 0–50% samples, the initial mass loss ≈200 °C appears relatively consistent, but a noticeable divergence becomes apparent ≈350 °C compared to the pure ZIF-8 (0%). This divergence becomes more pronounced in the 70% sample, where the mass loss is more substantial and initiates at lower temperatures. This heightened mass loss is attributed to the poorer thermal stability (200 °C) and excessive water evaporation (25 °C).[29,31]

The significant reduction in mass observed at temperatures exceeding 400 °C corresponds to the structural breakdown of the ZIFs framework due to ligand oxidation. Additionally, TGA analysis under isothermal heating conditions provides a clearer depiction, illustrating that the mass loss of ML-ZIFs at 300 °C progressively rises with increasing NH_2-bIm content (Figure S5b,c, Supporting Information). This observation suggests a quantitative correlation between the extent of mass loss during heating and the concentration of the NH_2-bIm ligand incorporated in the corresponding ML-ZIF structure.

Further analysis was conducted on all samples using ATR-IR after subjecting them to varying temperatures and durations of thermal treatment (details summarized in Figures S6–S8, Supporting Information). Changes in intensity for bands associated with NH_2-bIm, including $\nu_s(\text{-}NH_2)$ and $\nu_{as}(\text{-}NH_2)$, as well as ν(Zn-N_β), were observed, as shown in **Figure** 2a,b. Notably, in samples ranging from 10% to 50%, these bands exhibit reduction between 250 and 290 °C, while for the 70% samples, the reduction occurs already within the range of 240 to 260 °C. In all the cases, however, the bands such as ν(Zn-N_α), corresponding to 2-mIm, remain intact within these temperature ranges, indicating its higher thermal stability compared to NH_2-bIm (IR spectra in Figure 2c).

Consistent with observations in ^{1}H NMR spectroscopy, the distinctive quartets of NH_2-bIm experience significant reduction following ligand thermolysis, with their chemical shifts becoming barely discernible after 2 h (Figure S9, Supporting Information). Since the amino group is unique to NH_2-bIm, the decline in $\nu(\text{-}NH_2)$ due to temperature can be attributed exclusively to the removal of NH_2-bIm. Likewise, the decrease in ν(Zn-N_β) with increasing heating temperature and duration confirms the quantitative removal of NH_2-bIm from the organic framework through thermolysis, involving cleavage of the Zn-N_β bond.

The intricate interplay between calcination temperature and duration is visually depicted through 2D contour plots, aiding in the identification of specific parameters for achieving quantitative selective ligand removal (Figure 2d; Figure S10, Supporting Information). For instance, in the case of the 30% sample, either a prolonged exposure at lower temperature (e.g. 260 °C for 8 h) or a shorter duration at higher temperature (e.g., 290 °C for 2 h) is effective in selectively removing the NH_2-bIm ligand. In samples with higher ratios (e.g., 70%), even lower heating conditions suffice (Figures S11,S12, Supporting Information). However, it is important to note that while thermolysis effectively removes NH_2-bIm, it may also compromise the inherent framework structure of ZIF-8. This non-desirable impact on the metal-organic framework underscores the need for meticulous precision when defining the heating parameters.

The influence of ligand removal on framework alterations was explored through in situ X-ray diffraction (in situ XRD). The comprehensive diffraction patterns for all samples are summarized in Figures S13 and S14 (Supporting Information). Figure 2e highlights the dynamic changes in the intensity of the (011) peak for the 30% sample at different temperatures and durations. The data indicate that no observable changes occur at heating temperatures and durations below 290 °C and 2 h. Beyond these thresholds, the inherent structure and crystallinity of ZIF-8 progressively deteriorate, eventually resulting in the emergence of peaks corresponding to hexagonal wurtzite ZnO. Similar obser-

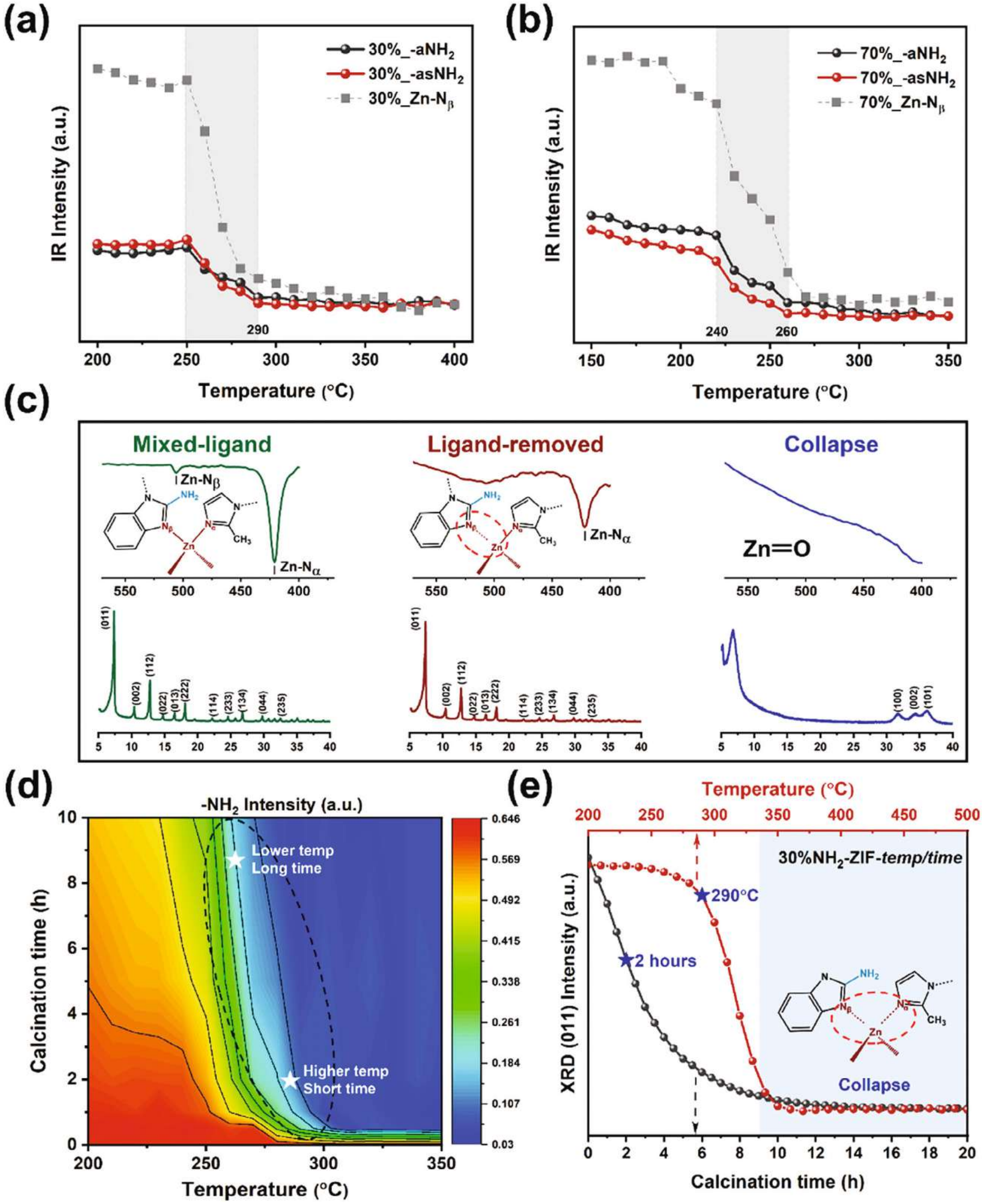

Figure 2. The effects of heating temperature and duration on selective ligand removal. Evolution of the ν(-NH$_2$) and ν(Zn-N$_\beta$) bands extracted from ex-situ AIR-IR for 30%NH$_2$-ZIF a) and 70%NH$_2$-ZIF b) upon heating in air, monitoring the selective removal of NH$_2$-bIm. Ex situ ATR-IR spectra and in situ XRD of 30%NH$_2$-ZIF at room temperature, 290 and 400 °C c). 2D contour plot of ν(-NH$_2$) intensity in ML-ZIFs versus calcination temperature and duration d). Data are extracted from the IR spectra in Figures S6–S8 (Supporting Information) at 3250–3550 cm^{-1} for ν(-NH$_2$), 400–550 cm^{-1} for ν(Zn—N). Evolution intensity plot of (011) peak with calcination temperature/duration in the in-situ XRD of 30%NH$_2$-ZIF e) in air. Data are extracted from the XRD patterns in Figures S13 and S14 (Supporting Information).

vations can be extended from the 2D/3D contour plots of other ML-ZIFs, with the vanishing of the (011) peak accelerating as the proportion of thermolabile NH_2-bIm increases, signifying a diminishing thermal stability of ML-ZIFs (Figure S15, Supporting Information).

It's noteworthy that the effective temperature ranges for achieving selective ligand removal in ML-ZIFs are relatively narrow, spanning ≈40–50 °C. This range contrasts with the broader window of ≈150 °C found in traditional MOFs containing amino-terephthalic acid ligands (e.g., NH_2-MIL-125 and NH_2-UiO-66).[13,21,32] The narrow thermolysis temperature window for both ligands, makes it challenging to selectively remove a particular ligand in this system. For instance, in the case of ZIF-67, which is a cobalt-based analog of ZIF-8, our attempts were unsuccessful primarily due to the low thermal stability of the Co—N bond within ZIF-67 (Figures S16–S18 and Section S2, Supporting Information).

Hence, the collective findings from TGA, ATR-IR, ^{1}H NMR, and XRD analyses validate that subjecting the ML-ZIFs to a 2 h thermal process at 260 °C (for 70% composition) and 290 °C (for 10–50% compositions) achieves the precise elimination of NH_2-bIm while maintaining the integrity of the framework structure.

2.3. Characterization of Pore Structures in LR-ZIFs

The impact of varying calcination conditions and mixed-ligand ratios on the pore structure of ligand-removed ZIFs (LR-ZIFs) was assessed through N_2 physisorption at 77 K. Pure ZIF-8, heated ZIF-8 (290 °C for 2 h) and ML-ZIF exhibit type-I isotherms with no pores exceeding diameters of 2 nm, characteristic of typical microporous materials (**Figures 3**; Figures S19 and S20, Supporting Information). The situation is different with the LR-ZIFs. Utilizing nonlocal density functional theory (NLDFT), we observed that the distinct peak centered at 1.2 nm, representative of intrinsic micropores, is largely preserved independent of the initial mixed-ligand ratio. However, the LR-ZIFs exhibit additional pores in the range from 2 to 30 nm (Figure 3). Moreover, the volume ratio of micro- to mesopores and the size distribution of mesopores are both contingent on the heating duration and initial ligand composition of the samples.

Let us focus first on the influence of heating duration. Figure 3a illustrates that the sample 30%NH_2-ZIF (ML-ZIF) lacks mesopores initially, yet following a 0.5-h thermolysis, a discernible mesopore emerges measuring ≈2.8 nm in diameter, accompanied by a decrease in micropore volume. Subsequently, the volume and dimensions of the mesopores grow from 0.5 to 2 h, culminating at 2 h with a diameter of ≈3.5 nm and a maximum mesopore volume of 0.067 cm^3 g^{-1}. Importantly, the micropore volume and specific surface area exhibit no pronounced reduction trend during this period, signifying a stable hierarchical structure at the 2 h mark of heating (Figure 3b; Figure S20, Supporting Information). In contrast to this, following a 5-h calcination, both the specific surface area and micro/mesopore volume experience a notable decline (Table S2, Supporting Information), attributed to partial framework collapse, as confirmed by XRD and IR analyses.

Continuing, we examine the influence of the initial ligand ratio, specifically focusing on a 2-h thermolysis duration (0–50% at 290 °C, 70% at 260 °C). The findings reveal a significant augmentation in the size distribution of mesopores with escalating NH_2-bIm content, spanning from 3–4 nm in the 10% sample to ≈4–25 nm in the 70% sample. This size expansion is concomitant with a reduction in micropore volume ratio (Figure 3c,d). Intriguingly, a more intricate bimodal meso-porosity distribution is noticeable at 50% (featuring an additional peak ≈6 nm), along with a multimodal distribution at 70%. Furthermore, the 70% sample seems to have lost all the microporous structures, retaining only mesopores distributed within the range of 4–25 nm. These observations imply that the transition of the mesoporous structure tends to be gradual and is influenced by the initial ligand ratio.

Transmission electron microscopy (TEM) images of the 30% sample before and after ligand thermolysis further verify the presence of hierarchical pores (Figure 3e,f). The illuminated regions denote the existence of mesoscale voids that are uniformly arranged throughout the particles, resulting in a sponge-like porous configuration. The size of these mesopores observed in the TEM images mainly ranges from 3 to 4 nm, further supporting the porosity distribution diagram obtained from N_2 physisorption. Notably, these illuminated patches are more pronounced at higher ML ligand ratios, underscoring the augmented mesopore dimensions compared to lower ML ratios (Figure S21, Supporting Information). Importantly, these changes caused by SeLiRe do not affect the chemical state and elemental composition of the surface, which is well illustrated by the fact that Zn 2p and N 1s edges are not significantly shifted in the XPS of ZIFs before and after SeLiRe process (Figure S22, Supporting Information). After two hours of heat treatment, analyses of N 1s peaks clearly show a decrease of the C—N/Zn—N ratio from 49.8% to 38.4% for the sample 30%, and from 70.3% to 53.9% for the sample 70%. This direct evidence further confirms the occurrence of SeLiRe process in ML-ZIFs during the heat treatment.[21]

2.4. Mechanism of Hierarchical Pore Formation

Our research has unveiled a molecular-scale mechanism governing the formation of hierarchical pores that is intricately linked to the mixed-ligand ratios (**Figure 4**). In the context of mixed-ligand ZIF-8, it is established that lower concentrations of the thermolabile ligand generally lead to the creation of smaller nanodomains with a random disposition.[33] Conversely, at higher NH_2-bIm concentrations, the thermolabile ligand has a propensity to aggregate around ZnN_4 clusters, giving rise to larger domains.[33,34]

Upon elevation of temperature, the thermolabile NH_2-bIm undergoes direct decomposition through cleavage of the Zn—N_β bonds, marking the initiation of a one-step SeLiRe process. Simultaneously, the evaporation of small molecules like NO_x, CO_2, and H_2O occurs,[21,35] often accompanied by an intensification of the sample's color (Figure S23, Supporting Information). This process contrasts with the SeLiRe mechanism observed in MOFs featuring the amino-terephthalic acid ligands, where a two-step cleavage occurs, and ligand decomposition results solely from the second (delayed) cleavage.[13,21] Moreover, in contrast to MOFs, we observed that the SeLiRe process in inert gases (Ar and N_2) can also be achieved in the case of ML-ZIFs (Figures S24–S32 and Section S4, Supporting Information), underscoring that the

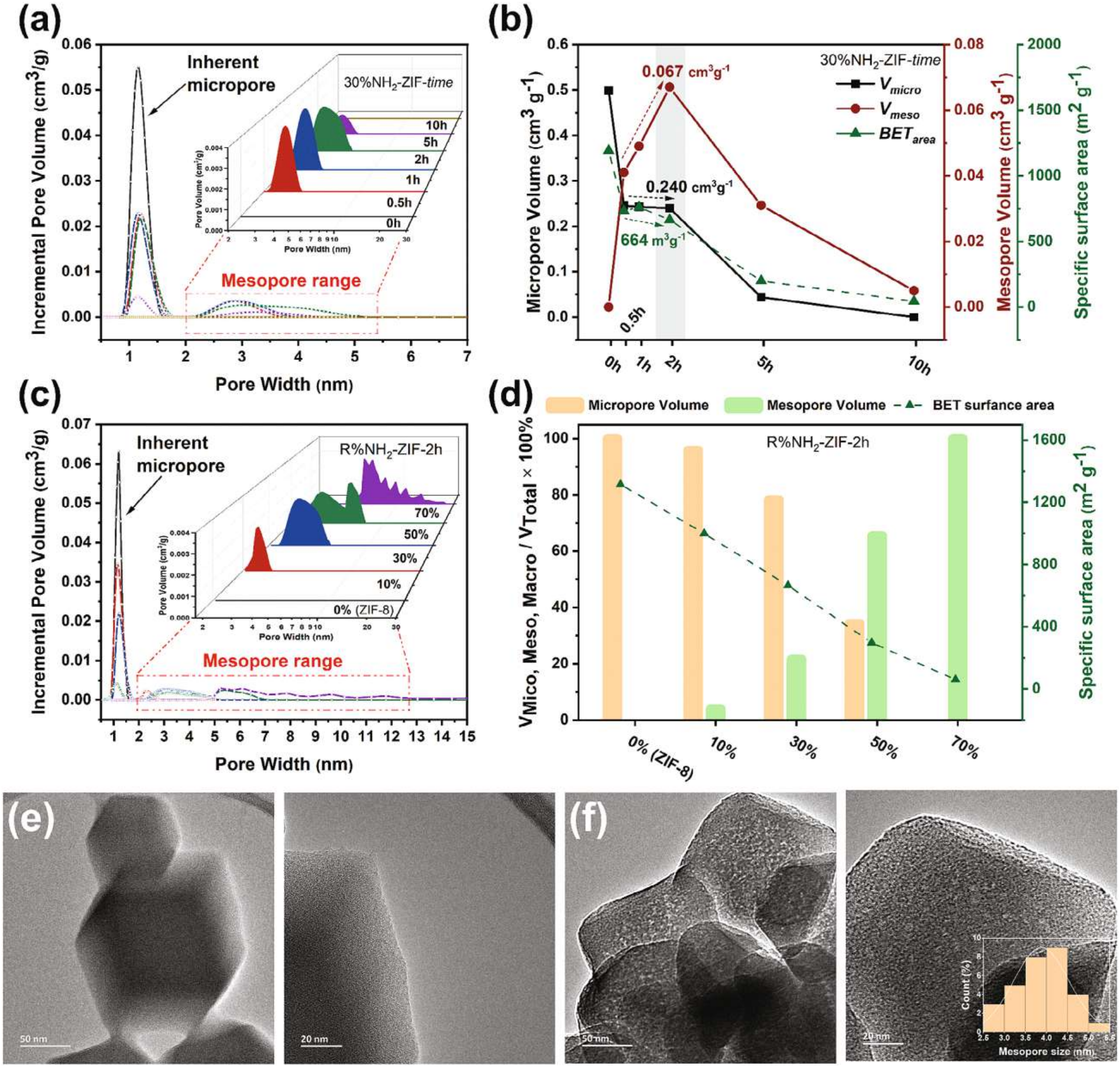

Figure 3. Hierarchical pores in LR-ZIFs. NLDFT porosity distributions of 30%NH$_2$-ZIF-time a) and R%NH$_2$-ZIF-2 h c). Time-dependent plot showing the change of micro-, mesopore volume and BET specific surface area with calcination time from 0–10 h b). Ligand-dependent histogram showing the change of pore volume ratio and BET specific surface area with mixed-ligand ratio d). TEM images of 30%NH$_2$-ZIF before e) and after f) calcination 2 h. The distribution of mesopore size is plotted inside (f).

decomposition of NH$_2$-bIm is not ascribable to oxidation and can transpire independently.

In accordance with existing literature findings,[36,37] the breaking of Zn—N bonds tends to occur more readily upon heating compared to the breakdown of the imidazole ring structure. As the ligand connections gradually weaken, the count of ZnN$_4$ tetrahedral clusters linked to nitrogen starts diminishing (as indicated by the decline curve in Zn-N$_\beta$ in the IR spectrum). Drawing from our observations, it is reasonable to deduce that these disengaged ZnN$_4$ clusters, in conjunction with the adjacent absent ligands, coalesce to form cluster-defects and additional Zn sites within the frameworks.[38] Computational simulations by Zhang et al. provide further support for the thermodynamic feasibility of metal and ligand vacancy formation within the ZIF-8 framework.[39]

To validate the structural integrity under this mechanism, we employed density functional theory (DFT) calculations on the LR-ZIFs framework structure, simulating the removal of various ligand-clusters. Figures S33 and S34 (Supporting Information) depict the LR-ZIFs unit cell post the elimination of one, two, and four Zn-N$_4$ clusters, alongside their associated ligands (Section S5, Supporting Information). The outcomes confirm that the fundamental framework structures remain largely intact upon the introduction of mesopores at the molecular level. Furthermore, the similarity in terms of formation energy values of framework with various number of Zn-N$_4$ clusters removed demon-

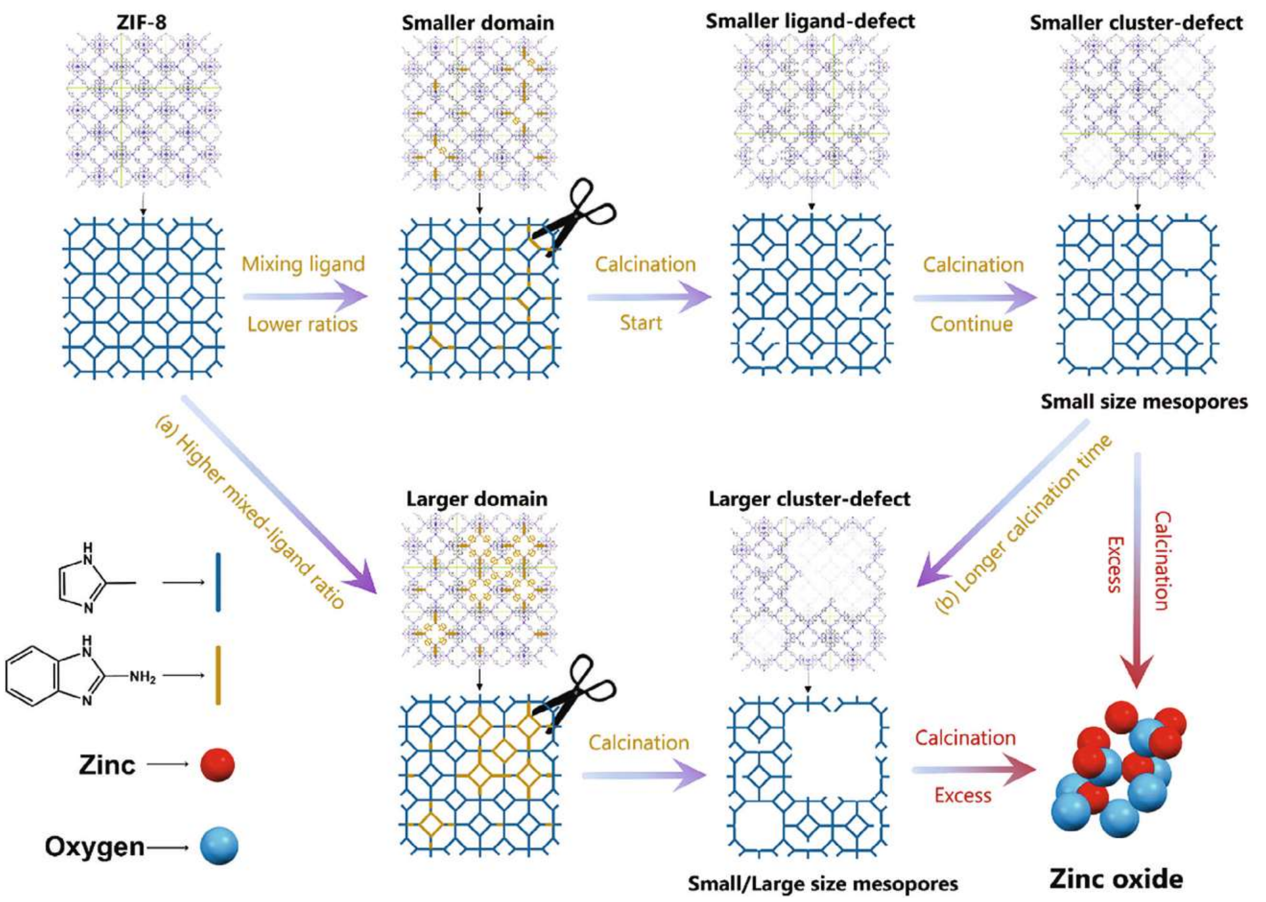

Figure 4. Schematic diagram of the proposed mechanism for the SeLiRe process. The formation of mesopores is guided by the initial distribution of the NH$_2$-bIm ligand that classifies the formation of defects into small and large domains as well as by the chosen conditions for thermolysis. The blue units represent the ligand 2-mIm, and the yellow units represent the ligand NH$_2$-bIm.

strates the thermodynamic stability of cluster-defect configurations (Table S3, Supporting Information). The collective findings from XRD, XPS, SEM, TEM, and ATR-IR underscore that the SeLiRe process exerts minimal impact on the structural integrity, affirming that the LR-ZIFs effectively retain the intrinsic framework architecture of ZIF-8.

The classification of the resulting cluster-defects as either smaller or larger is contingent upon the domain distribution originating from the ligand ratio during synthesis. The formation of these cluster-defects fundamentally influences the mesoporous structure, and their classification is intricately linked to the initial distribution of the thermolabile linker. This mesopore transition is characterized by its continuous nature, signifying that the mesopore structure of LR-ZIFs undergoes a gradual evolution with escalating ligand ratios. This stands in contrast to the discrete dual-pore features, comprising channels and cavities, observed in MIL-125-Ti, which necessitates distinct synthetic pathways.[13]

2.5. Enhancing Dye Adsorption in Water Purification

In order to assess the enhanced efficacy of the LR-ZIFs, we conducted tests to evaluate the samples' ability to adsorb significant organic pollutants from water. Our previous work showcased the substantial improvement in glyphosate molecule adsorption by incorporating larger mesopores into MIL-125-Ti.[40] This enhancement was attributed to the facilitated diffusion of glyphosate molecules into the MOF framework and the provision of new adsorption sites following ligand removal. These sites were ideally suited for glyphosate adsorption through phosphonate coordination.

In this study, we examined how the introduction of hierarchical pores in ZIF-8 impacts the adsorption of various dyes, including methylene blue (MB), methyl orange (MO), and Rhodamine B. The results are presented in Figures S35–S38 (see Section S6, Supporting Information).[41] As summarized in **Figure 5**a, the selective removal of ligands leads to a significant increase in the adsorption capacity for MB. Notably, the 10%NH$_2$-ZIF-2 h sample exhibits the highest MB adsorption capacity, achieving an enhancement of ≈40 times compared to ZIF-8 (Figure 5a,b).

The inherent pore channels of ZIF-8 and ML-ZIFs (with dimensions of 3.4 Å)[42] appear to hinder the diffusion of MB molecules (with dimensions of 17.0 × 7.6 × 3.3 Å)[43] into the central cavities with dimensions of 11.6 Å (see NLDFT Section 2.3 and),[42] thus limiting the utilization of Zn centers as adsorption sites. In contrast, the creation of hierarchical micro/mesopores through ligand thermolysis eliminates this dif-

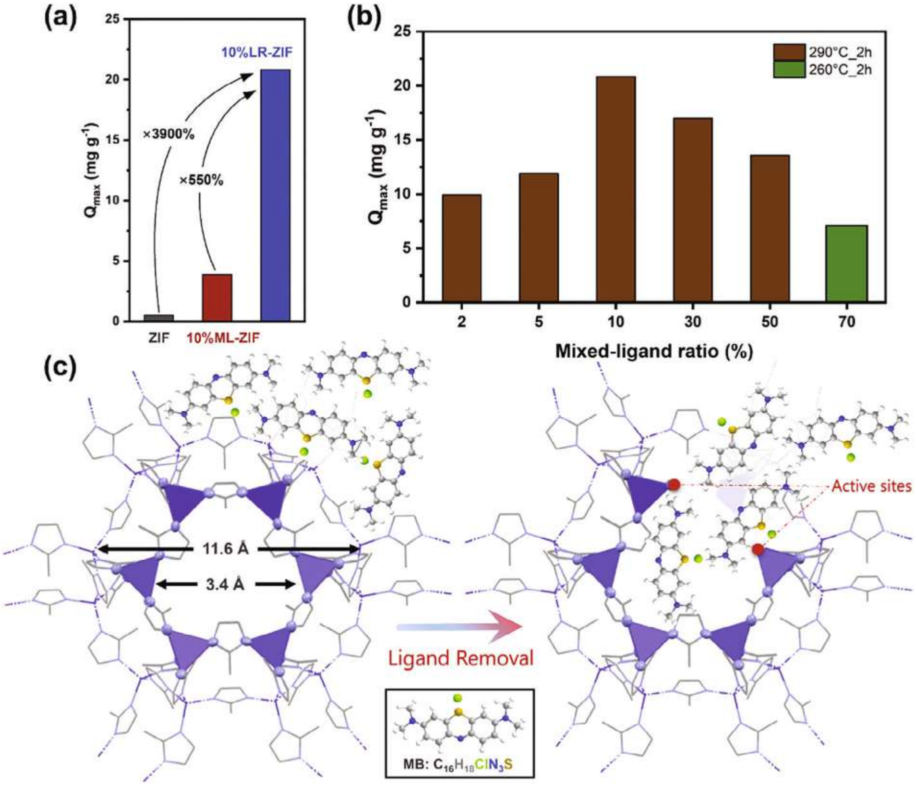

Figure 5. Adsorption of Methylene blue. Maximum adsorption capacity (Q_{max}) of ZIF-8, 10%NH_2-ZIF and 10%NH_2-ZIF-2 h, revealing that the introduction of mesopores greatly enhances the adsorption of MB a). Q_{max} of LR-ZIFs with different mixed-ligand ratio b). Adsorption mechanism in unit cell of ZIF-8 and LR-ZIF; the MB molecule approximately has the dimensions 17.0 × 7.6 × 3.3 Å and fits well within the newly created mesoscale cavities c).

fusion constraint, resulting in an amplified adsorption capacity (Figure 5c).

Similar trends are observed with the anionic methyl orange and the cationic rhodamine B (Figure S37a,b, Supporting Information), indicating that electrostatic interactions have a minor role in dye adsorption. Interestingly, the adsorption capacity of 10%ML-ZIF is also enhanced by ≈5 times compared to pure ZIF-8. While this enhancement is usually attributed to additional electrostatic adsorption between the sulfonic groups of MB and the -NH_2 group on the surface,[25,44] the absence of significant electrostatic interactions in LR-ZIFs point to a different mechanism. This suggests that diffusion plays a more crucial role than attractive electrostatic interactions.

The adsorption kinetics and isotherms data exhibit the closest agreement with the Pseudo-second-order (PSO) and Langmuir models, as summarized in Tables S4 and S5 (Supporting Information). This observation suggests that the adsorption reactions likely involve chemisorption and monolayer molecular adsorption, in line with previous research.[45,46] However, it is important to highlight that although the PSO model provides the best fit, this does not necessitate chemisorption within the ZIFs.[47] It is essential to integrate findings from other analytical techniques and thoroughly investigate the chemical nature of the adsorbent surface.

For a more precise understanding of the adsorption process, we performed a comparative analysis of IR bands and XRD patterns before and after the adsorption of MB/MO. The post-adsorption spectra exhibit no emergence of new bands or significant shifts in the existing bands. However, the IR bands from the dye references are distinctly visible and unchanged (refer to Figure S38a,b, Supporting Information). This confirms that the predominant mode of dye adsorption by the LR-ZIF samples, irrespective of the dye's charge (anionic or cationic), is physisorption. Furthermore, our evaluation of powder XRD data and cyclic tests conducted before and after MB adsorption demonstrates that LR-ZIFs serve as effective and enduring adsorbents (refer to Figure S38c,d, Supporting Information).

Certainly, the enhanced adsorption of dyes can be attributed to a combination of key factors. Primarily, the increased availability of space, particularly the higher pore volume facilitated by the mesopore cavities, plays a pivotal role in achieving a larger adsorption capacity. This augmented pore volume offers additional active sites within the adsorbent material where dyes can be effectively accommodated.

Equally important is the improved accessibility of these pore cavities. When the pores are easily accessible, dyes can seamlessly diffuse into the adsorbent matrix, resulting in a heightened adsorption efficiency. This improved accessibility ensures that dyes can engage effectively with the active sites present within the adsorbent structure, thus facilitating a more efficient adsorption process. It's important to note that this mechanism differs from the glyphosate adsorption process observed in MIL-125-Ti, which involves phosphonate coordination with unsaturated Ti sites combined with hydrogen bond formation.[40]

In essence, the synergistic effect of increased pore volume and enhanced accessibility to pore cavities significantly contributes to the overall heightened dye adsorption observed within the material.

3. Conclusion

Zeolitic imidazolate frameworks (ZIFs) represent a class of microporous materials comprising metal ions interconnected by imidazolate linkers. Despite their demonstrated potential in numerous applications, the absence of mesoscale cavities in most ZIFs can hinder specific functionalities that demand rapid and unimpeded access to active adsorption sites. Such functionalities encompass catalysis, sensing, and the adsorption of substantial molecules in both air and aqueous environments.

To surmount this limitation, we have pioneered an innovative approach by fabricating mixed-ligand ML-ZIFs, utilizing varying proportions of NH_2-bIm (2-aminobenzimidazole) and 2-mIm (2-methylimidazole). Through precisely controlled thermal treatments, we achieve the quantitative elimination of the thermolabile ligand NH_2-bIm, thus introducing uniform mesopores with consistent size and structure within the ZIF matrix.

Our comprehensive investigation, leveraging an array of ex situ and in situ techniques such as XRD, SEM, TEM, ATR-IR, TGA, and ^{1}H NMR, has elucidated the mechanism of ligand removal, unaffected by the ambient atmosphere (air, Ar, or N_2). This indicates that the removal process ensues via the selective cleavage of metal-ligand coordination, rather than oxidation. However, the close temperature proximity between NH_2-bIm and 2-mIm presents a challenge in achieving precise ligand removal, necessitating meticulous calibration of heating temperature and duration for each mixed-ligand composition. Such careful calibration is imperative to achieve the complete elimination of NH_2-bIm, the introduction of uniform mesopores, the prevention of ZnO nanoparticle formation, and the preservation of the inherent microporous framework of the ZIF.

Furthermore, our observations underscore the pivotal role played by the initial distribution of the thermolabile ligand in the as-synthesized ML samples, influencing the resulting configuration of the mesopores. This emphasizes the critical importance of stringent control during the synthesis process.

To demonstrate the versatility and broad applicability of our selective ligand thermolysis, we have evaluated the resulting hierarchically porous ZIF specimens for the adsorption of organic dyes in aqueous media. Impressively, the adsorption capacity for methylene blue (MB) in the case of 10%NH_2-ZIF-2 h exhibited an ≈40-fold increase compared to conventional ZIF-8. Moreover, the 10%NH_2-ZIF-2 h sample showcased recyclability and stability in MB adsorption. This substantial enhancement in adsorption performance is attributed to the incorporation of additional mesopores through the Selective Ligand Removal (SeLiRe) process, which provides larger pore volumes for dye molecules and facilitates expedited transport of these molecules to adsorption sites.

In essence, our work introduces a promising avenue for designing hierarchically micro/mesoporous ZIFs with diverse topologies, thereby unveiling fresh possibilities for a range of applications.

4. Experimental Section

Chemicals: Zinc nitrate hexahydrate ($Zn(NO_3)_2{\cdot}6H_2O$, 98%, ACROS), Cobalt nitrate hexahydrate ($Co(NO_3)_2{\cdot}6H_2O$, 99%, STREM) 2-methylimidazole (2-mIm, $C_4H_6N_2$, 99%, Sigma–Aldrich), 2-aminobenzimidazole (NH_2-bIm, $C_7H_7N_3$, 97%, Sigma–Aldrich), Methanol (MeOH, 99.9%, HiPerSolv CHROMANORM, VWR), Potassium bromide for IR spectroscopy (99%, Fisher scientific, Austria), Sulfuric acid (H_2SO_4, 99.9%, Sigma–Aldrich), Methylene blue (MB, $C_{16}H_{18}ClN_3S{\cdot}xH_2O$, high purity, biological stain, Alfa Aesar), Methyl orange (MO, $C_{14}H_{14}N_3NaO_3S$, 90%, Sigma–Aldrich), Rhodamine B (RhB, $C_{28}H_{31}ClN_2O_3$, pure, 99%, ACROS), d_4-acetic acid for NMR (CD_3CO_2D, 99.4%, Thermo scientific).

Ligand-Removed ZIF-8: LR-ZIF-8 or R%NH_2-ZIF-time/temp refers to the ZIF-8 samples obtained by thermolysis of ML-ZIF-8 at specific temperatures for specific time periods (Section S7, Supporting Information). The heating process was conducted using a muffle furnace (LT 5/12 Nabertherm, Germany) in an air atmosphere, ramp rate of 10 °C min^{-1}. Or a tube furnace (HTM Reetz LK-1100, Germany) with argon/nitrogen flow at a ramp rate of 10 °C min^{-1}. The final temperature was allowed to cool naturally to room temperature. For air atmosphere, the calcination temperature is 290 °C for 0–50%NH_2-ZIFs and 260 °C for 70%. For argon/nitrogen flow, the calcination temperature was 500 °C for 30%NH_2-ZIF and 400 °C for 70%NH_2-ZIF. The samples were labeled as R%NH_2-ZIF-time/temp (or R%-time/temp), where R% indicates the mixing ratio of various NH_2-bIm, time is the calcination time, and temp indicates the special calcination temperature.

Characterization: Powder XRD measurements were performed using PANalytical X'Pert Pro multi-purpose diffractometer (MPD) with Bragg Brentano geometry with Cu anode at 45 kV, 40 mA, equipped with a BBHD Mirror and an X-Celerator multichannel detector. In situ XRD is used with the addition of the Anton Paar HTK 1200 temperature control system, with a heating rate of 5 °C min^{-1}. The sample was heated with a flow rate of 0.5 mL min^{-1} of air, argon, and nitrogen. ATR-IR spectra were obtained with Perkinelmer Spectrum two FT-IR spectrometer, with the $LiTaO_3$ (lithium tantalate) MIR detector. N_2 Physisorption measurements were conducted at a temperature of 77 K, on a 3Flex instrument by Micromeritics. SEM images were recorded on a FEI Quanta 250 (Schottky-)FEG-SEM, TEM measurements displayed in this paper were performed on a Tecnai F20 FEG-TEM, facilitated by USTEM (university service center for transmission electron microscopy) at TU Wien. Raman spectroscopy measurements were carried out using the WITec alpha 300 RSA. UV–Vis and DRS were obtained at 660–670 nm by Jasco V-670. Liquid phase ^{1}H NMR spectra were measured using the Bruker ADVANCE 250 (250.13 MHz) instrument, which is equipped with a 5 mm inverse-broad probe head and z-gradient unit. TGA measurements were carried out using PerkinElmer 8000 (Waltham, USA) with the sample heated in of Al_2O_3 crucible DFT calculations were performed by using the Vienna ab initio program package (VASP). More details are in the Supporting Information..

Supporting Information

Supporting Information is available from the Wiley Online Library or from the author.

Acknowledgements

The first author of this study, Z.H., was financially supported by China Scholarship Council (Nos. 202106770017). S.N. acknowledges the support of the Austrian Science Fund (FWF, I 5413-N). Q.Z. was financially supported by the National Key Research and Development Program of China (2022YFB3803600), National Natural Science Foundation of China (No. U20A20246), and the Fundamental Research Funds for the Central Universities. XRD was supported by Werner Artner of the TU Wien X-ray Center. USTEM was supported by the University Service for Transmission Electron Microscopy – TU Wien. Raman spectroscopy was supported by

Bernhard Fickl. TGA auxiliary measurements and repairs were supported and assisted by Stephen Nagaraju Myakala.

Conflict of Interest

The authors declare no conflict of interest.

Author Contributions

Z.H. carried out most of the experiments and analysis and wrote the initial manuscript. J.R. conducted SEM and TEM, Q.Z. performed DFT simulations. A.C. reviewed and edited the manuscript. S.N. conducted N_2 physisorption and ^{1}H NMR, reviewed and edited the manuscript. D.E. outlined and supervised the project, reviewed and edited the final manuscript.

Data Availability Statement

The data that support the findings of this study are available in the supplementary material of this article.

Keywords

cluster defects, hierarchically porous ZIF, mesopores, selective ligand removal, water purification

Received: September 12, 2023
Revised: December 4, 2023

[1] A. Phan, C. J. Doonan, F. J. Uribe-Romo, C. B. Knobler, M. O'keeffe, O. M. Yaghi, *Acc. Chem. Res.* **2010**, *43*, 58.
[2] B. R. Pimentel, A. Parulkar, E.-K. Zhou, N. A. Brunelli, R. P. Lively, *ChemSusChem* **2014**, *7*, 3202.
[3] M.-M. Chen, H.-L. Hao, W. Zhao, X. Zhao, H.-Y. Chen, J.-J. Xu, *Chem. Sci.* **2021**, *12*, 10848.
[4] Z. Huang, Q. Zhou, J. Wang, Y. Yu, *J. Mater. Sci. Technol.* **2022**, *112*, 68.
[5] M. D. J. Velásquez-Hernández, R. Ricco, F. Carraro, F. T. Limpoco, M. Linares-Moreau, E. Leitner, H. Wiltsche, J. Rattenberger, H. Schröttner, P. Frühwirt, E. M. Stadler, G. Gescheidt, H. Amenitsch, C. J. Doonan, P. Falcaro, *CrystEngComm* **2019**, *21*, 4538.
[6] P. Cheng, Y. H. Hu, *J. Phys. Chem. C* **2014**, *118*, 21866.
[7] A. J. Howarth, Y. Liu, P. Li, Z. Li, T. C. Wang, J. T. Hupp, O. K. Farha, *Nat. Rev. Mater.* **2016**, *1*, 15018.
[8] Y. Wang, J. Yan, N. Wen, H. Xiong, S. Cai, Q. He, Y. Hu, D. Peng, Z. Liu, Y. Liu, *Biomaterials* **2020**, *230*, 119619.
[9] D. K. Yoo, H. C. Woo, S. H. Jhung, *ACS Appl. Mater. Interfaces* **2021**, *13*, 35214.
[10] S. Naghdi, E. Brown, M. Zendehbad, A. Duong, W. Ipsmiller, S. Biswas, M. C. Toroker, H. Kazemian, D. Eder, *Adv. Funct. Mater.* **2023**, *33*, 2213862.
[11] Y. Yao, X. Zhao, G. Chang, X. Yang, B. Chen, *Small Struct.* **2023**, *4*, 2200187.
[12] Y. Yang, X. Arqué, T. Patiño, V. Guillerm, P.-R. Blersch, J. Pérez-Carvajal, I. Imaz, D. Maspoch, S. Sánchez, *J. Am. Chem. Soc.* **2020**, *142*, 20962.
[13] S. Naghdi, A. Cherevan, A. Giesriegl, R. Guillet-Nicolas, S. Biswas, T. Gupta, J. Wang, T. Haunold, B. C. Bayer, G. Rupprechter, M. C. Toroker, F. Kleitz, D. Eder, *Nat. Commun.* **2022**, *13*, 282.
[14] K. Shen, L. Zhang, X. Chen, L. Liu, D. Zhang, Y. Han, J. Chen, J. Long, R. Luque, Y. Li, B. Chen, *Science* **2018**, *359*, 206.
[15] G. Cai, H.-L. Jiang, *Angew. Chem., Int. Ed.* **2017**, *56*, 563.
[16] P. Yang, F. Mao, Y. Li, Q. Zhuang, J. Gu, *Chemistry* **2018**, *24*, 2962.
[17] M. K. Albolkany, C. Liu, Y. Wang, C.-H. Chen, C. Zhu, X. Chen, B. Liu, *Angew. Chem., Int. Ed.* **2021**, *60*, 14601.
[18] Q. Xiong, Y. Chen, D. Yang, K. Wang, Y. Wang, J. Yang, L. Li, J. Li, *Mater. Chem. Front.* **2022**, *6*, 2944.
[19] K.-Y. Wang, L. Feng, T.-H. Yan, S. Wu, E. A. Joseph, H.-C. Zhou, *Angew. Chem., Int. Ed.* **2020**, *59*, 11349.
[20] Y. Yang, P. Fernández-SeriñáN, I. Imaz, F. Gándara, M. Handke, B. Ortín-Rubio, J. Juanhuix, D. Maspoch, *J. Am. Chem. Soc.* **2023**, *145*, 17398.
[21] L. Feng, S. Yuan, L.-L. Zhang, K. Tan, J.-L. Li, A. Kirchon, L.-M. Liu, P. Zhang, Y. Han, Y. J. Chabal, H.-C. Zhou, *J. Am. Chem. Soc.* **2018**, *140*, 2363.
[22] M. Kandiah, M. H. Nilsen, S. Usseglio, S. Jakobsen, U. Olsbye, M. Tilset, C. Larabi, E. A. Quadrelli, F. Bonino, K. P. Lillerud, *Chem. Mater.* **2010**, *22*, 6632.
[23] V. Nozari, C. Calahoo, J. M. Tuffnell, D. A. Keen, T. D. Bennett, L. Wondraczek, *Nat. Commun.* **2021**, *12*, 5703.
[24] L. León-Alcaide, J. López-Cabrelles, M. Esteve-Rochina, E. Ortí, J. Calbo, B. A. H. Huisman, M. Sessolo, J. C. Waerenborgh, B. J. C. Vieira, G. Mínguez Espallargas, *J. Am. Chem. Soc.* **2023**, *145*, 23249.
[25] L. Xiang, L. Sheng, C. Wang, L. Zhang, Y. Pan, Y. Li, *Adv. Mater.* **2017**, *29*, 1606999.
[26] S. Yu, S. Li, S. Huang, Z. Zeng, S. Cui, Y. Liu, *J. Membr. Sci.* **2017**, *540*, 155.
[27] J. Mor, P. Utpalla, J. Bahadur, S. K. Sharma, *Langmuir* **2022**, *38*, 15694.
[28] F. Hillman, J. M. Zimmerman, S.-M. Paek, M. R. A. Hamid, W. T. Lim, H.-K. Jeong, *J. Mater. Chem. A* **2017**, *5*, 6090.
[29] Y. Xiong, N. Deng, X. Wu, Q. Zhang, S. Liu, G. Sun, *Sep. Purif. Technol.* **2022**, *285*, 120321.
[30] R. Ding, W. Zheng, K. Yang, Y. Dai, X. Ruan, X. Yan, G. He, *Sep. Purif. Technol.* **2020**, *236*, 116209.
[31] F. Xie, Y. Wang, L. Zhuo, D. Ning, N. Yan, J. Li, S. Chen, Z. Lu, *J. Hazard. Mater.* **2021**, *412*, 125260.
[32] R. Xu, Q. Ji, P. Zhao, M. Jian, C. Xiang, C. Hu, G. Zhang, C. Tang, R. Liu, X. Zhang, J. Qu, *J. Mater. Chem. A* **2020**, *8*, 7870.
[33] O. Karagiaridi, M. B. Lalonde, W. Bury, A. A. Sarjeant, O. K. Farha, J. T. Hupp, *J. Am. Chem. Soc.* **2012**, *134*, 18790.
[34] H. Sun, H. Jiang, R. Kong, D. Ren, D. Wang, J. Tan, D. Wu, W. Zhu, B. Shen, *Ind. Eng. Chem. Res.* **2019**, *58*, 13274.
[35] J. Tang, R. R. Salunkhe, J. Liu, N. L. Torad, M. Imura, S. Furukawa, Y. Yamauchi, *J. Am. Chem. Soc.* **2015**, *137*, 1572.
[36] S. Gadipelli, W. Travis, W. Zhou, Z. Guo, *Energy Environ. Sci.* **2014**, *7*, 2232.
[37] C. Wu, D. Xie, Y. Mei, Z. Xiu, K. M. Poduska, D. Li, B. Xu, D. Sun, *Phys. Chem. Chem. Phys.* **2019**, *21*, 17571.
[38] M. Li, Y. Liu, F. Li, C. Shen, Y. V. Kaneti, Y. Yamauchi, B. Yuliarto, B. Chen, C.-C. Wang, *Environ. Sci. Technol.* **2021**, *55*, 13209.
[39] C. Zhang, C. Han, D. S. Sholl, J. R. Schmidt, *J. Phys. Chem. Lett.* **2016**, *7*, 459.
[40] S. Naghdi, E. Brown, M. Zendehbad, A. Duong, W. Ipsmiller, S. Biswas, M. C. Toroker, H. Kazemian, D. Eder, *Adv. Funct. Mater.* **2023**, *33*, 2213862.
[41] Y. Yue, P. F. Fulvio, S. Dai, *Acc. Chem. Res.* **2015**, *48*, 3044.
[42] K. S. Park, Z. Ni, A. P. Côté, J. Y. Choi, R. Huang, F. J. Uribe-Romo, H. K. Chae, M. O'Keeffe, O. M. Yaghi, *Stem Cells Int* **2006**, *103*, 10186.
[43] M. Arias, E. López, A. Nuñez, D. Rubinos, B. Soto, M. T. Barral, F. Díaz-Fierros, in *Effect of Mineral-Organic-Microorganism Interactions*

on Soil and Freshwater Environments (Eds: J. Berthelin, P. M. Huang, J. M. Bollag, F. Andreux), Springer US, Boston, MA **1999**, 361.

[44] Z. Jia, X. Dai, B. Liu, Y. Li, C. Bo, *Colloids Surf., A* **2022**, *639*, 128312.

[45] J.-P. Simonin, *Chem. Eng. J.* **2016**, *300*, 254.

[46] R. Kaur, A. Kaur, A. Umar, W. A. Anderson, S. K. Kansal, *Mater. Res. Bull.* **2019**, *109*, 124.

[47] H. N. Tran, S.-J. You, A. Hosseini-Bandegharaei, H.-P. Chao, *Water Res.* **2017**, *120*, 88.

NANO · MICRO
small

Supporting Information

for *Small*, DOI 10.1002/smll.202307981

Hierarchically Micro- and Mesoporous Zeolitic Imidazolate Frameworks Through Selective Ligand Removal

*Zheao Huang, Jakob Rath, Qiancheng Zhou, Alexey Cherevan, Shaghayegh Naghdi and Dominik Eder**

WILEY-VCH

Supporting Information

Hierarchically Micro- and Mesoporous Zeolitic Imidazolate Frameworks through Selective Ligand Removal

Zheao Huang[1], *Jakob Rath*[1], *Qiancheng Zhou*[2], *Alexey Cherevan*[1], *Shaghayegh Naghdi*[1], *and Dominik Eder*[*,1]

[1] Institute of Material Chemistry, Vienna University of Technology, 1060, Vienna, Austria

[2] Institute of Nanoscience and Nanotechnology, College of Physical Science and Technology, Central China Normal University, 430079, Wuhan, China

* Corresponding author. Email: dominik.eder@tuwien.ac.at.

Contect

S1. Ligand NH_2-bIm mixing and removal process

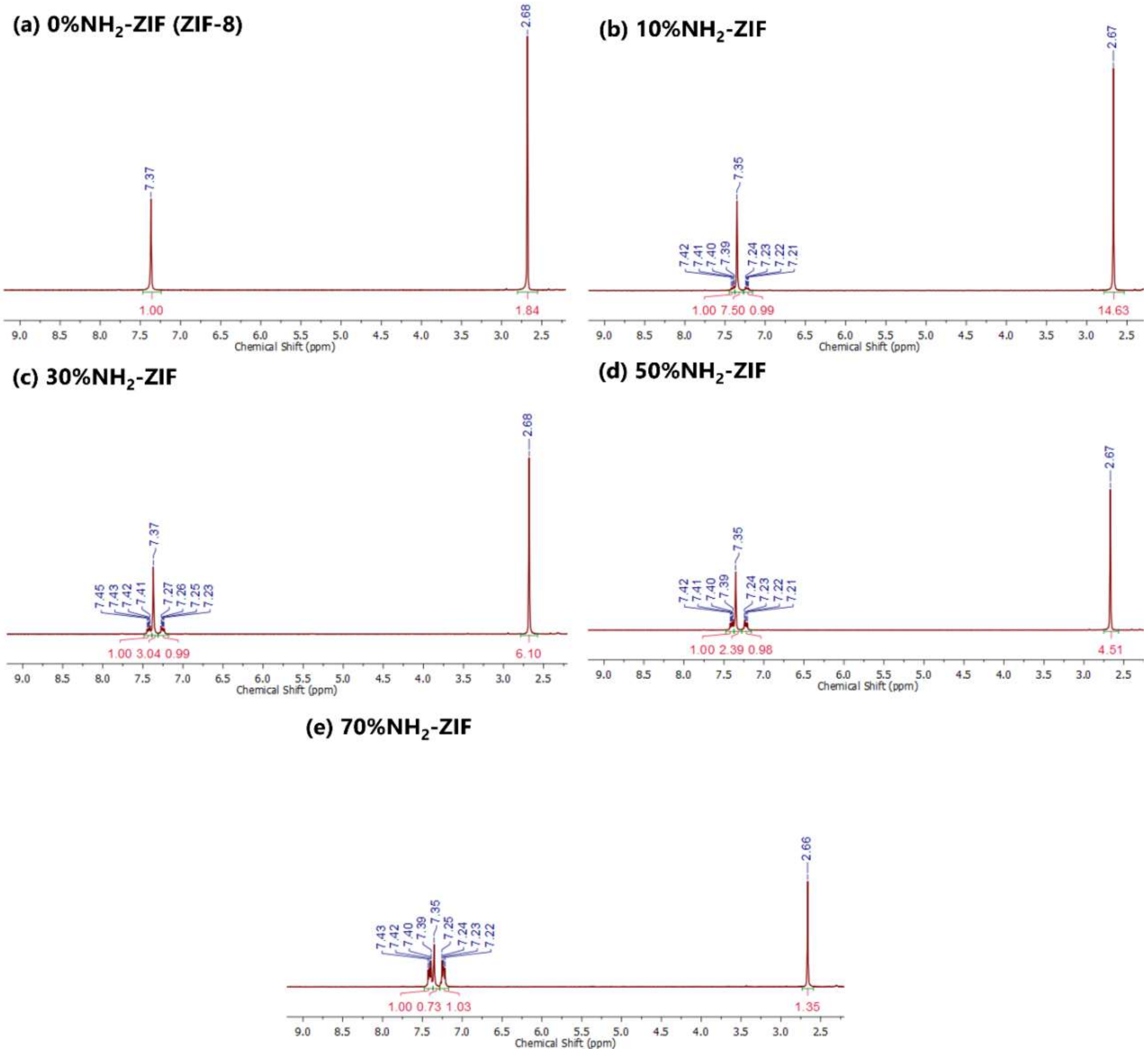

Figure S1. ^{1}H NMR spectroscopy of 0-70%NH_2-ZIFs (a, 0%NH_2-ZIF; b, 10%NH_2-ZIF; c, 30%NH_2-ZIF; d, 50%NH_2-ZIF; e, 70%NH_2-ZIF). The actual ratios of NH_2-bIm can be obtained in **Table S1**.

0%NH_2-ZIF: *^{1}H NMR (250 MHz, Acetic Acid-d_4) δ 2.55 – 2.80 (s, 2H), 7.24 – 7.47 (s, 1H).* 10%NH_2-ZIF: *^{1}H NMR (250 MHz, Acetic Acid-d_4) δ 2.54 – 2.79 (s, 15H), 7.16 – 7.27 (dd, J = 3.2, 6.0 Hz, 1H), 7.27 – 7.38 (s, 7H), 7.38 – 7.45 (dd, J = 3.2, 6.0 Hz, 1H).* 30%NH_2-ZIF: *^{1}H NMR (250 MHz, Acetic Acid-d_4) δ 2.57 – 2.79 (s, 6H), 7.18 – 7.31 (dd, J = 3.2, 6.0 Hz, 1H), 7.31 – 7.39 (s, 3H), 7.39 – 7.48 (dd, J = 3.2, 5.9 Hz, 1H).* 50%NH_2-ZIF: *^{1}H NMR (250 MHz, Acetic Acid-d_4) δ 2.57 – 2.75 (s, 5H), 7.16 – 7.28 (dd, J = 3.2, 6.0 Hz, 1H), 7.28 – 7.37 (s, 2H), 7.37 – 7.47 (dd, J = 3.2, 6.0 Hz, 1H).* 70%NH_2-ZIF: *^{1}H NMR (250 MHz, Acetic Acid-d_4) δ 2.59 – 2.73 (s, 1H), 7.17 – 7.28 (dd, J = 3.2, 6.0 Hz, 1H), 7.28 – 7.37 (s, 1H), 7.37 – 7.48 (dd, J = 3.2, 5.9 Hz, 1H).*

Table S1. Calculation of the NH_2-bIm ratio in ML-ZIFs by ^1H NMR.

Samples **Synthetic mass of NH_2-bIM/2-mIm (g/g)**	**10%NH_2-ZIF**	**30%NH_2-ZIF**	**50%NH_2-ZIF**	**70%NH_2-ZIF**
	0.2/1.8	0.6/1.4	1/1	1.4/0.6
Synthetic ratio of NH_2-bIm (mol%)	6.4%	20.9%	38.2%	60.0%
Actual ratio of NH_2-bIm (mol%)	8.2%	17.9%	22.3%	49.4%

Due to the competitive coordination between the two ligands, the actual ratio gradually deviates from the synthetic ratio as the ratio of NH_2-bIm increases. In thermodynamics, the Zn metal center has a higher affinity for 2-mIm than NH_2-bIm [1, 2]. Moreover, the NH_2-bIm possesses the redundant benzene ring and is excessively bloated for the formation of new Zn-N_β bonds.

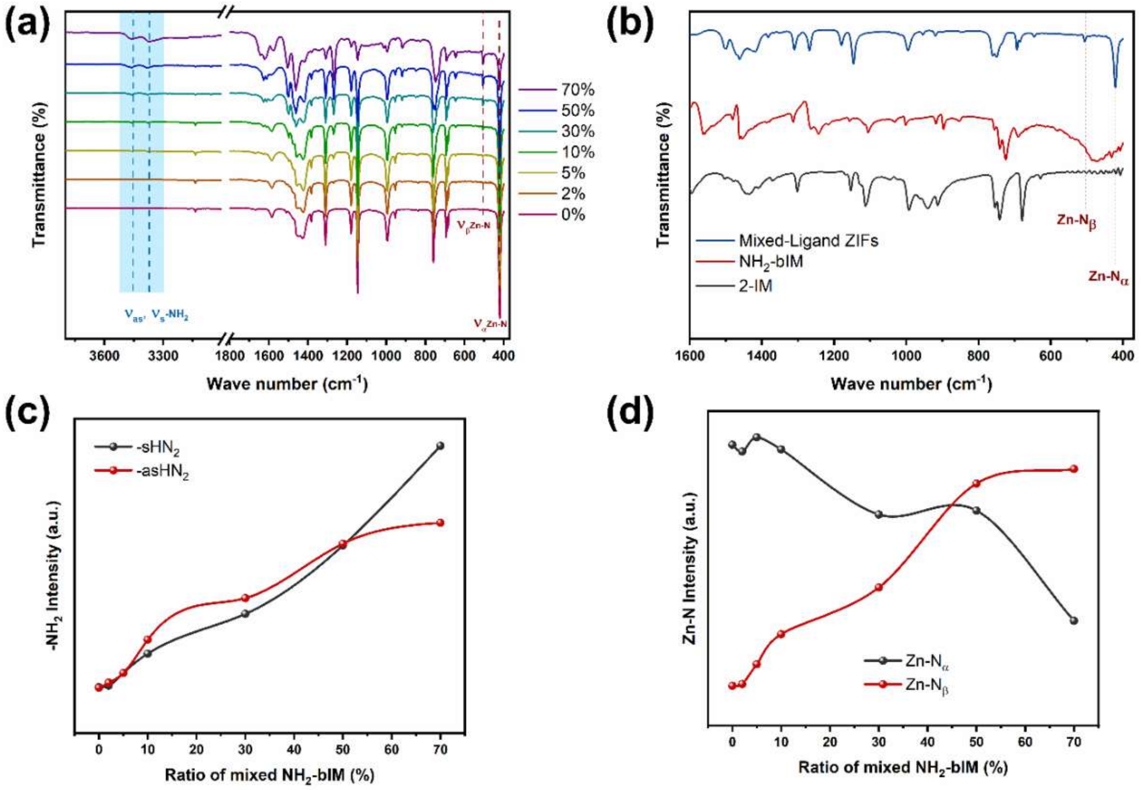

Figure S2. ATR-IR spectra of 0-70%NH$_2$-ZIFs (a). ATR-IR spectra of 2-mIm, NH$_2$-bIm and 50%NH$_2$-ZIF (b). Intensity plot of ν_s(-NH$_2$) intensity (c) and ν(Zn-N) intensity (d) with the mixed-ligand ratio.

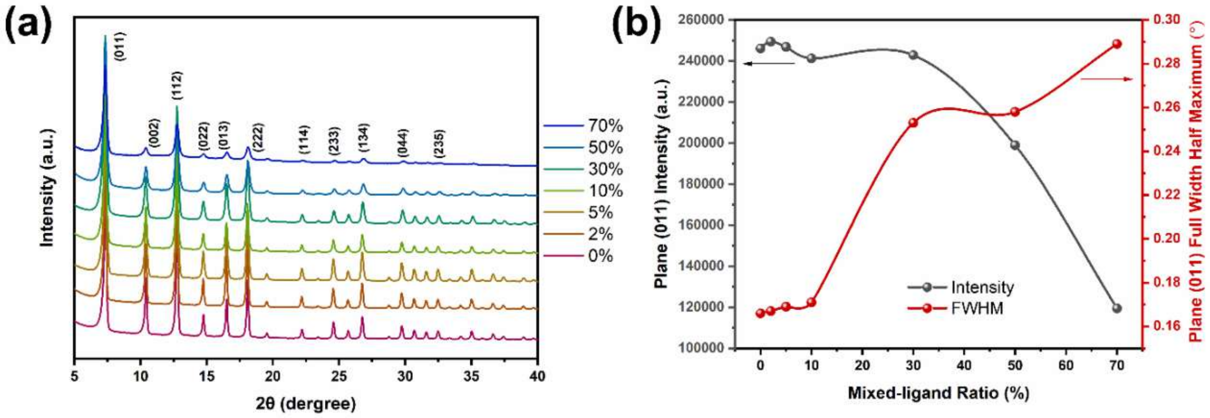

Figure S3. XRD patterns of 0-70%NH_2-ZIFs (a). Evolution plots of the (011) intensity and FWHM with the mixed-ligand ratio (b). XRD patterns of the NH_2-ZIFs are essentially indistinguishable from the simulated ZIF-8. As the ratio of NH_2-bIm increases, the low-angle peaks, particularly the unit lattice constants of (011) changed, show changes in the form of reduced crystallinity and increased FWHM.

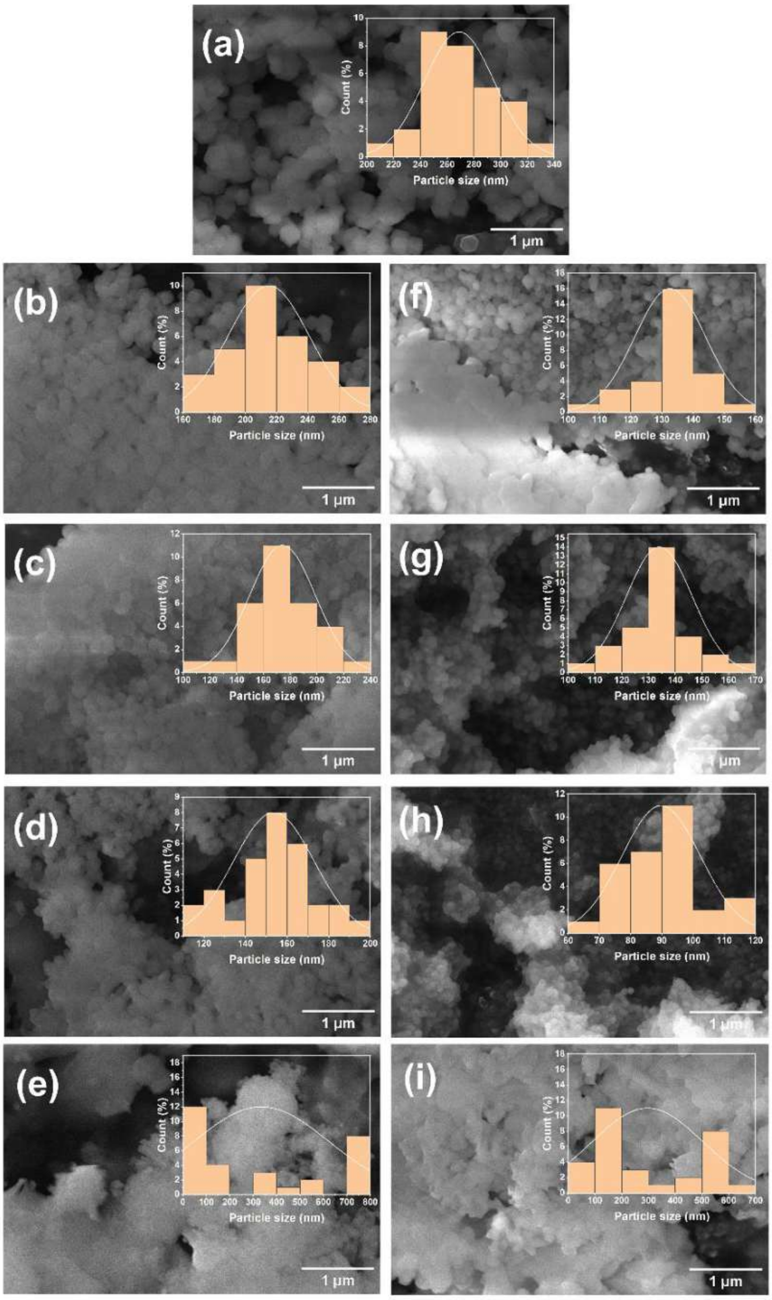

Figure S4. SEM images of 0-70%NH_2-ZIFs (a, 0%NH_2-ZIF; b, 10%NH_2-ZIF; c, 30%NH_2-ZIF; d, 50%NH_2-ZIF; e, 70%NH_2-ZIF) and 10-70%NH_2-ZIF-2h (f, 10%NH_2-ZIF-2h; g, 30%NH_2-ZIF-2h; h, 50%NH_2-ZIF-2h; i, 70%NH_2-ZIF-2h). Noted that the particle sizes of LR-ZIFs were slightly reduced due to oxidation reactions. An ImageJ program was used to select 30 particles from each sample.

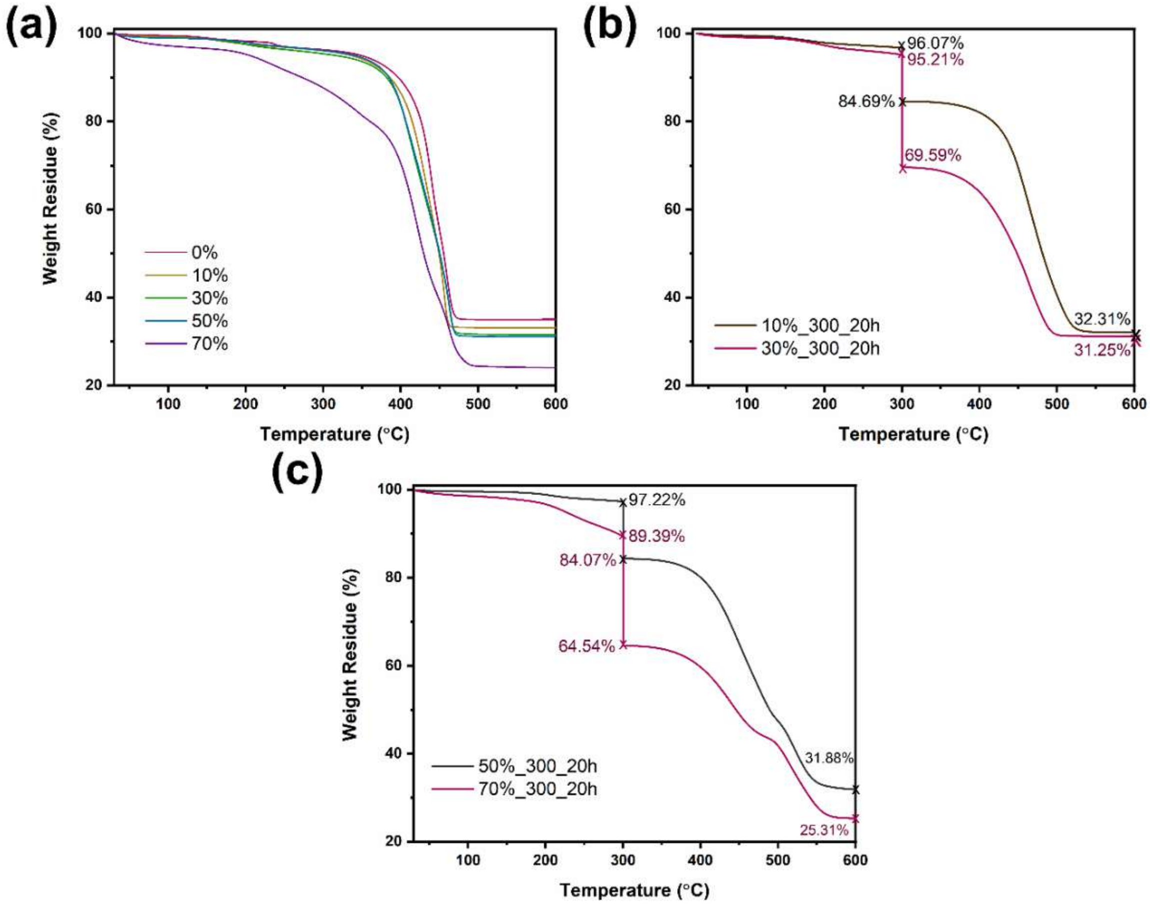

Figure S5. TGA curves of 0-70%NH_2-ZIFs (a). Isothermally heated TGA curves of 10/30%NH_2-ZIF (b) and 50/70%NH_2-ZIF (c) that hold continuously at 300°C for 20 hours. The sudden weight loss is attributed to the prolonged isothermal TGA testing, a departure from the typical TGA setup where the temperature and time are continuously increasing. All TGA tests were all carried out in air atmosphere.

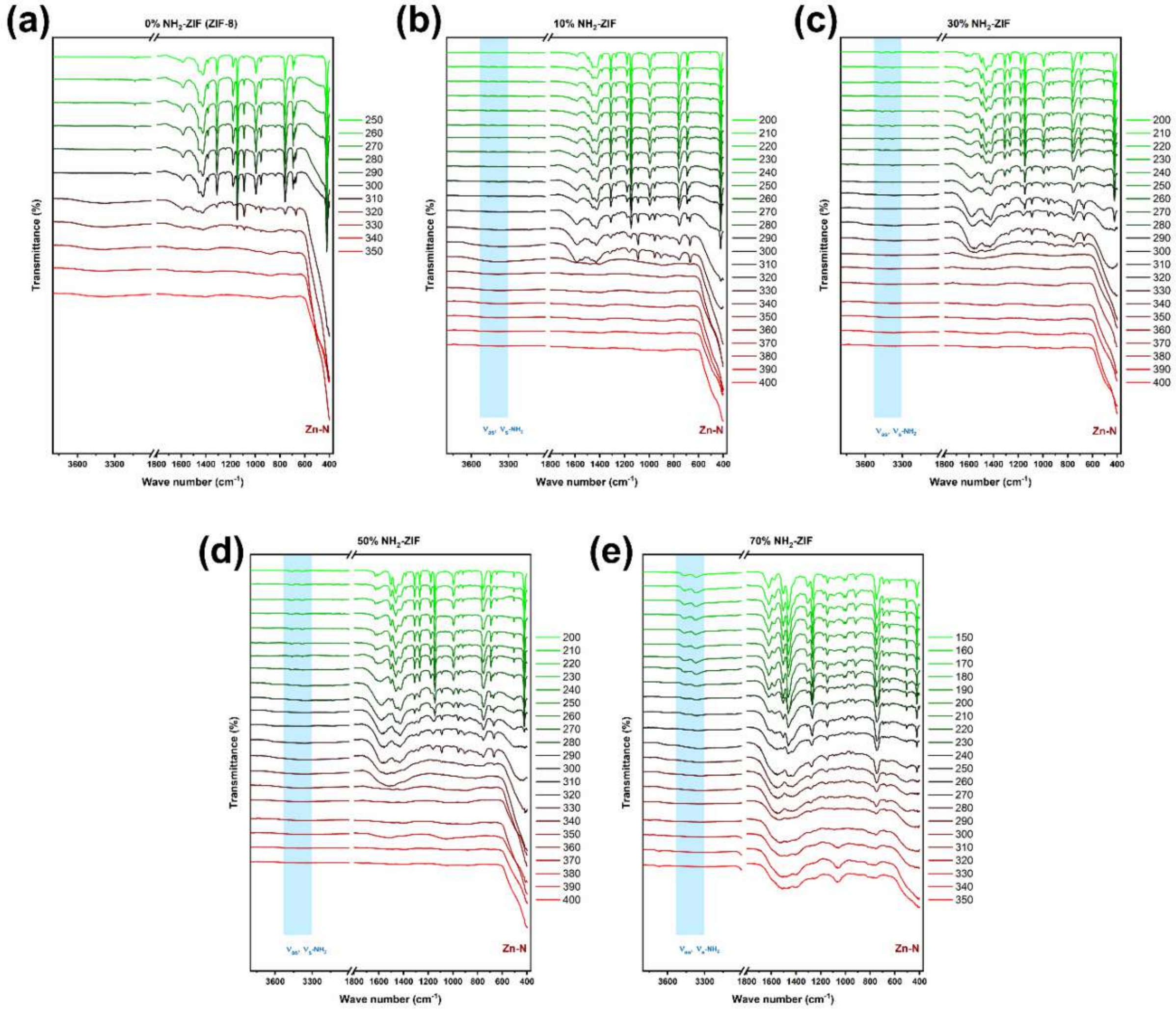

Figure S6. Ex-situ ATR-IR spectra of 0-70%NH_2-ZIFs (a, 0%NH_2-ZIF; b, 10%NH_2-ZIF; c, 30%NH_2-ZIF; d, 50%NH_2-ZIF; e, 70%NH_2-ZIF) at different temperatures. All ML-ZIFs were calcined in a muffle furnace, in air atmosphere, for a period of 2 hours and then cooled naturally to room temperature.

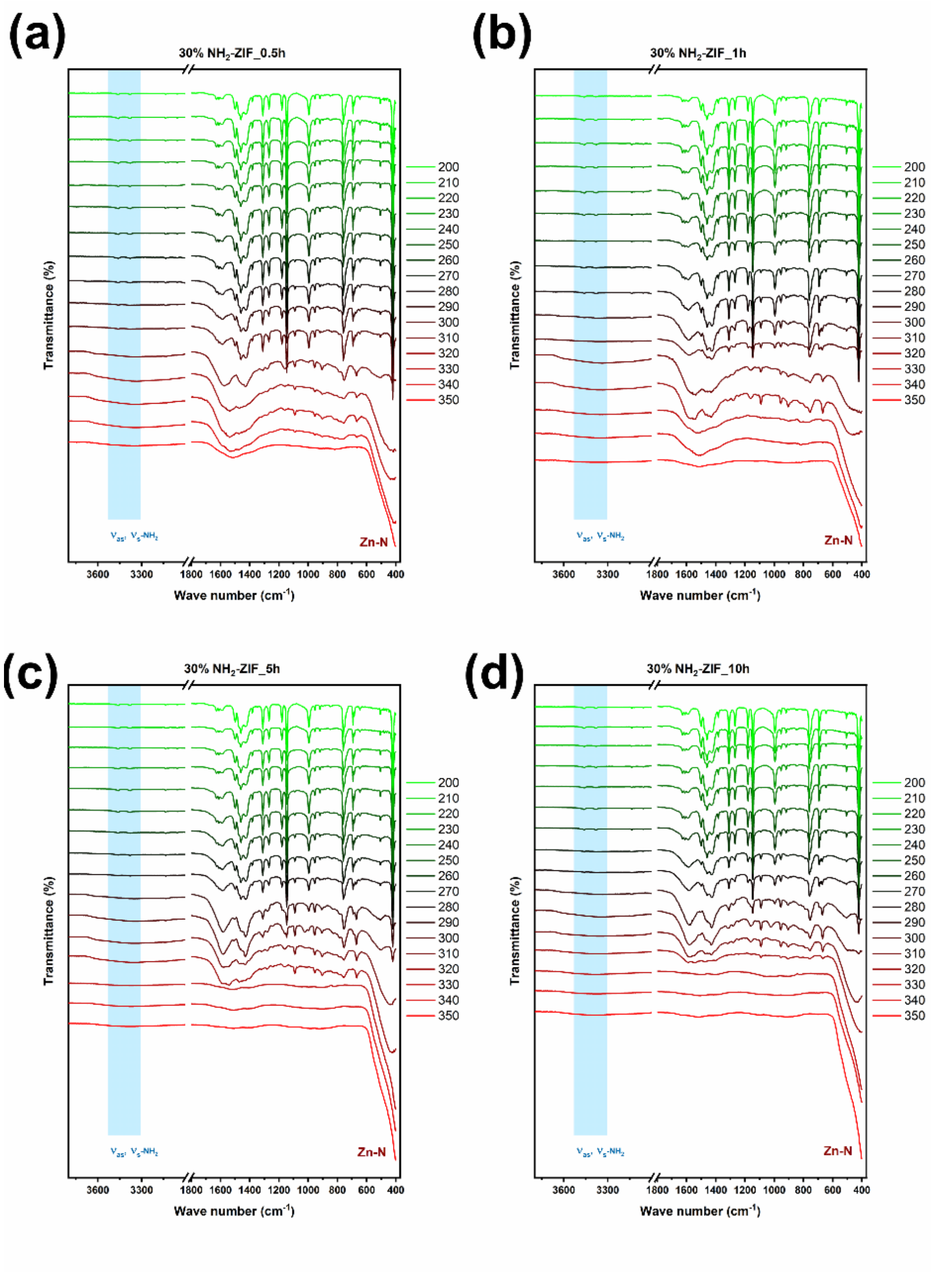

Figure S7. Ex-situ ATR-IR spectra of 30%NH$_2$-ZIFs at different calcination times (a, 0.5 hours; b, 1 hour; c, 5 hours; d, 10 hours). 30%NH$_2$-ZIFs were calcined in a muffle furnace in air atmosphere at 290°C. The data for calcination for 2 hours is included in **Figure S6c**.

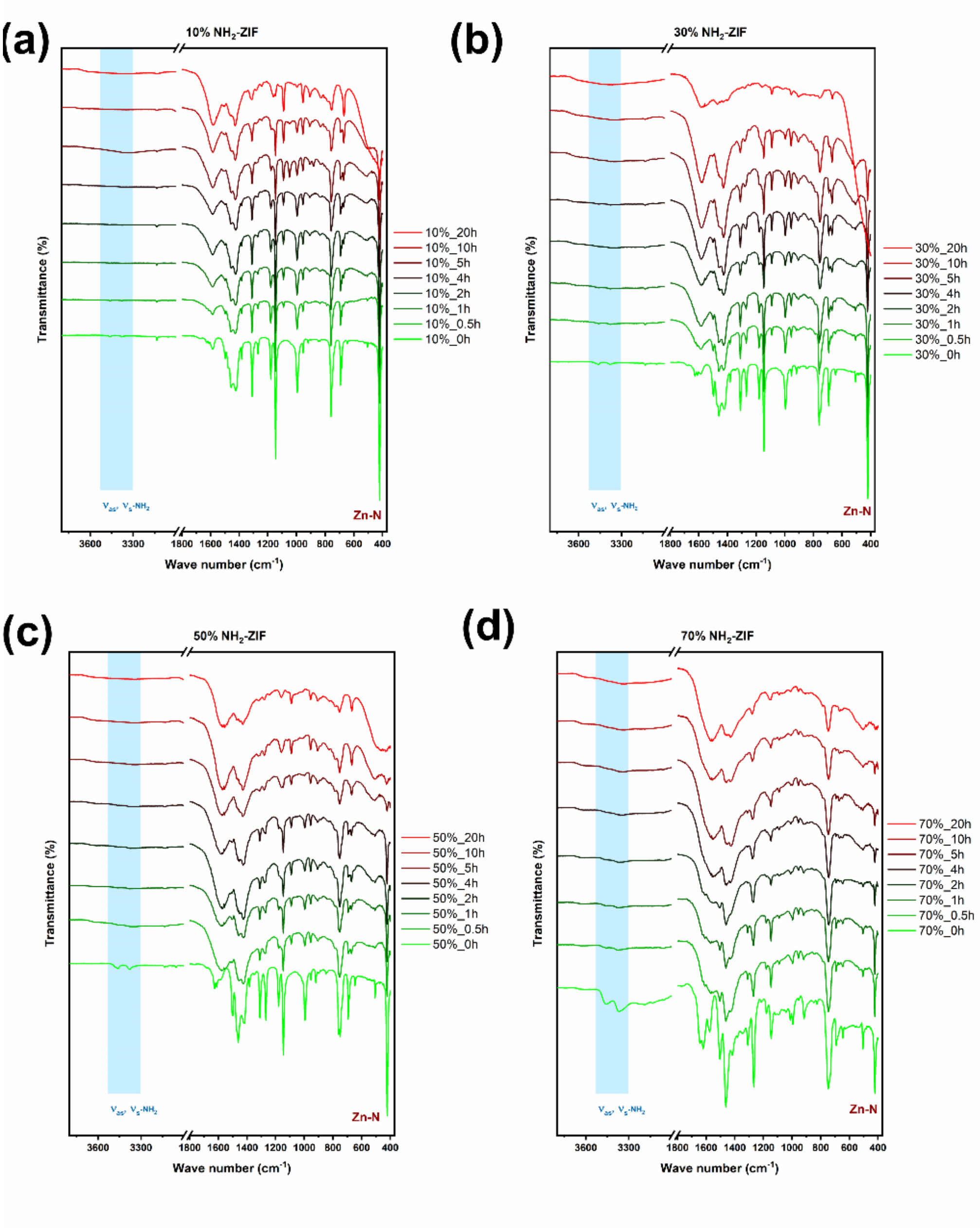

Figure S8. Isothermal ex-situ ATR-IR spectra of 10-70%NH_2-ZIFs (a, 10% NH_2-ZIF; b, 30% NH_2-ZIF; c, 50%NH_2-ZIF; d, 70%NH_2-ZIF) at different calcination times. All NH_2-ZIFs were calcined in a muffle furnace in the air atmosphere. 10-50% at 290°C and 70% at 260°C.

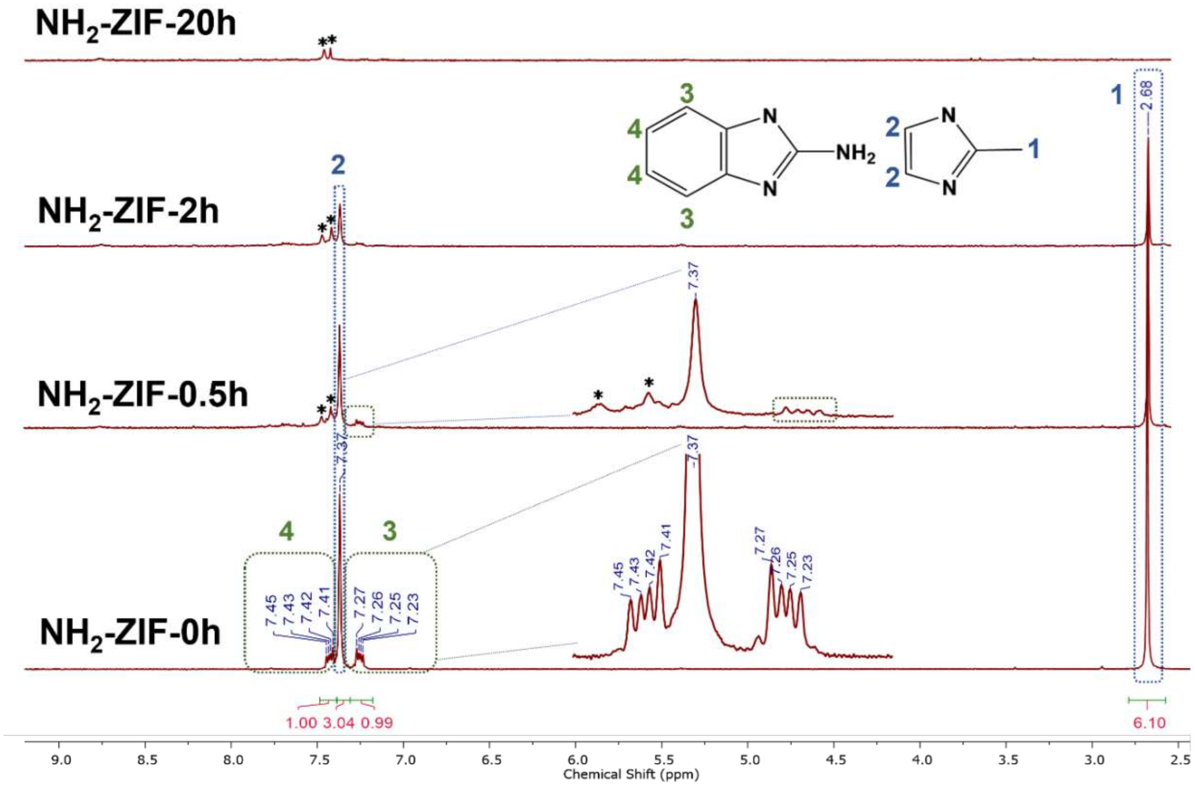

Figure S9. ^{1}H NMR spectroscopy of LR-ZIFs at different calcination times (30%NH_2-ZIF-0h; 30%NH_2-ZIF-0.5h; 30%NH_2-ZIF-2h; 30%NH_2-ZIF-20h). Before heating, the NMR of 30%NH_2-ZIF-0h (ML-ZIF) exhibits typical spectrum features of both 2-mIm and NH_2-bIM. After heating, the characteristic quartets of NH_2-bIm on both sides of 7.35 ppm was markedly reduce and their chemical shifts were barely visible after 2 hours, confirming that the NH_2-bIm can be completely removed by ligand thermolysis strategy. *By-products such as azirine or benzimidazole resulting from the oxidation of the -NH_2 group or ligand NH_2-bIm [3-5], are supported by the cleavage of $\nu_{s, as}$(-NH_2) in ATR-IR (**Figures 2a** and **2b**). After 20 hours, the two ligands were removed and only the *by-products remained, corresponding to the results of isothermal XRD and ATR-IR (**Figures S6-9**, **S13** and **S14**).

30%NH_2-ZIF-0h: *^{1}H NMR (250 MHz, Acetic Acid-d_4) δ 2.57 – 2.79 (s, 6H), 7.18 – 7.31 (dd, J = 3.2, 6.0 Hz, 1H), 7.31 – 7.39 (s, 3H), 7.39 – 7.48 (dd, J = 3.2, 5.9 Hz, 1H).* 30%NH_2-ZIF-0.5h: *^{1}H NMR (250 MHz, Acetic Acid-d_4) δ 2.59 – 2.76 (s, 3H), 7.17 – 7.30 (m, 0H), 7.31 – 7.40 (s, 2H), 7.40 – 7.53 (d, J = 13.5 Hz, 1H).* 30%NH_2-ZIF-2h: *^{1}H NMR (250 MHz, Acetic Acid-d_4) δ 2.62 – 2.74 (s, 2H), 7.21 – 7.29 (s, 0H), 7.32 – 7.40 (s, 1H), 7.40 – 7.52 (d, J = 13.6 Hz, 1H).* 30%NH_2-ZIF-20h:*^{1}H NMR (250 MHz, Acetic Acid-d_4) δ 7.24 – 7.44 (d, J = 9.0 Hz, 1H).*

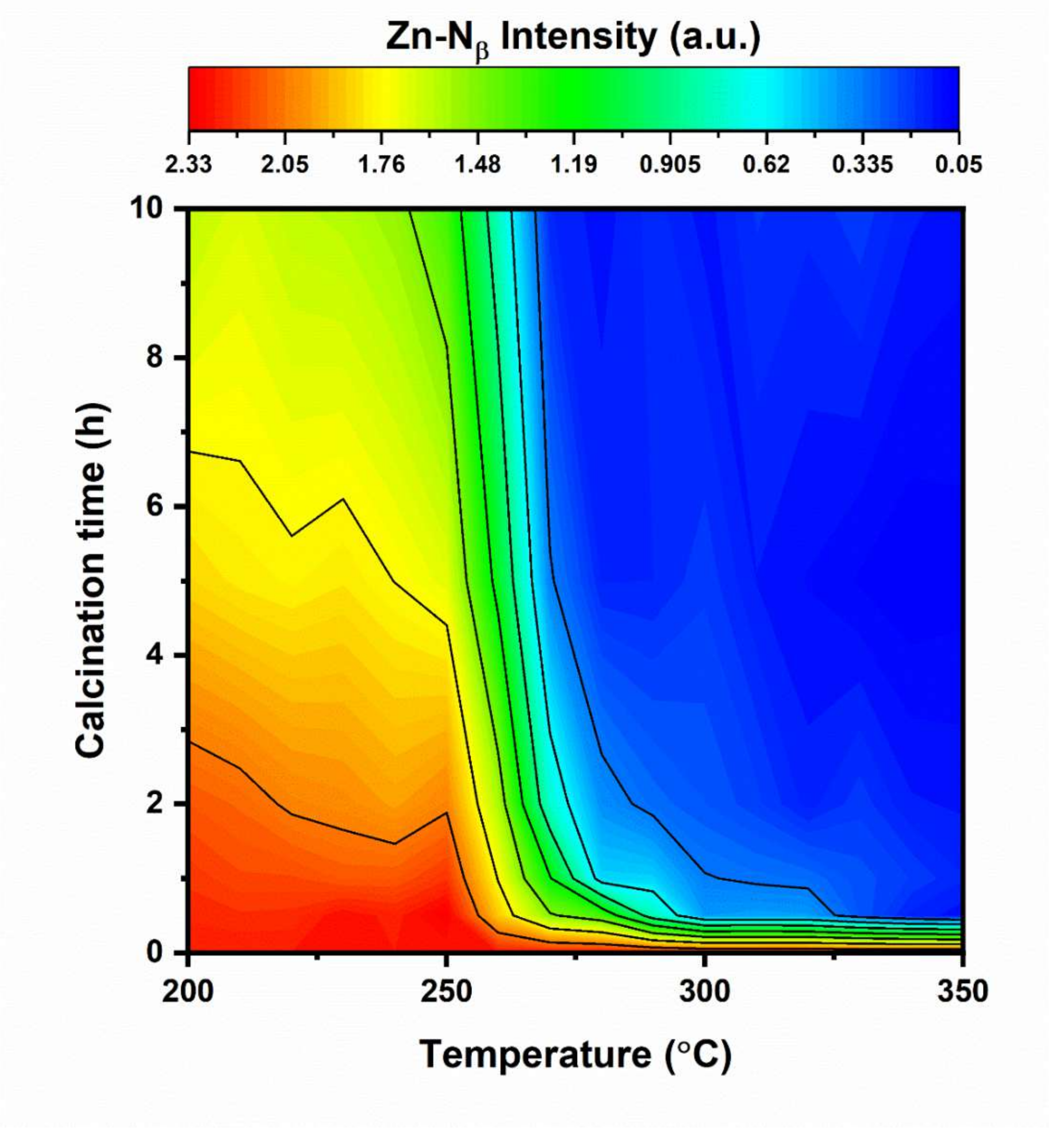

Figure S10. 2D contour plot of ν(Zn-N$_\beta$) intensity in 30%NH$_2$-ZIFs vs. mixed NH$_2$-bIm ratio with calcination temperature. Data are from the IR spectra in **Figures S6** and **S8**.

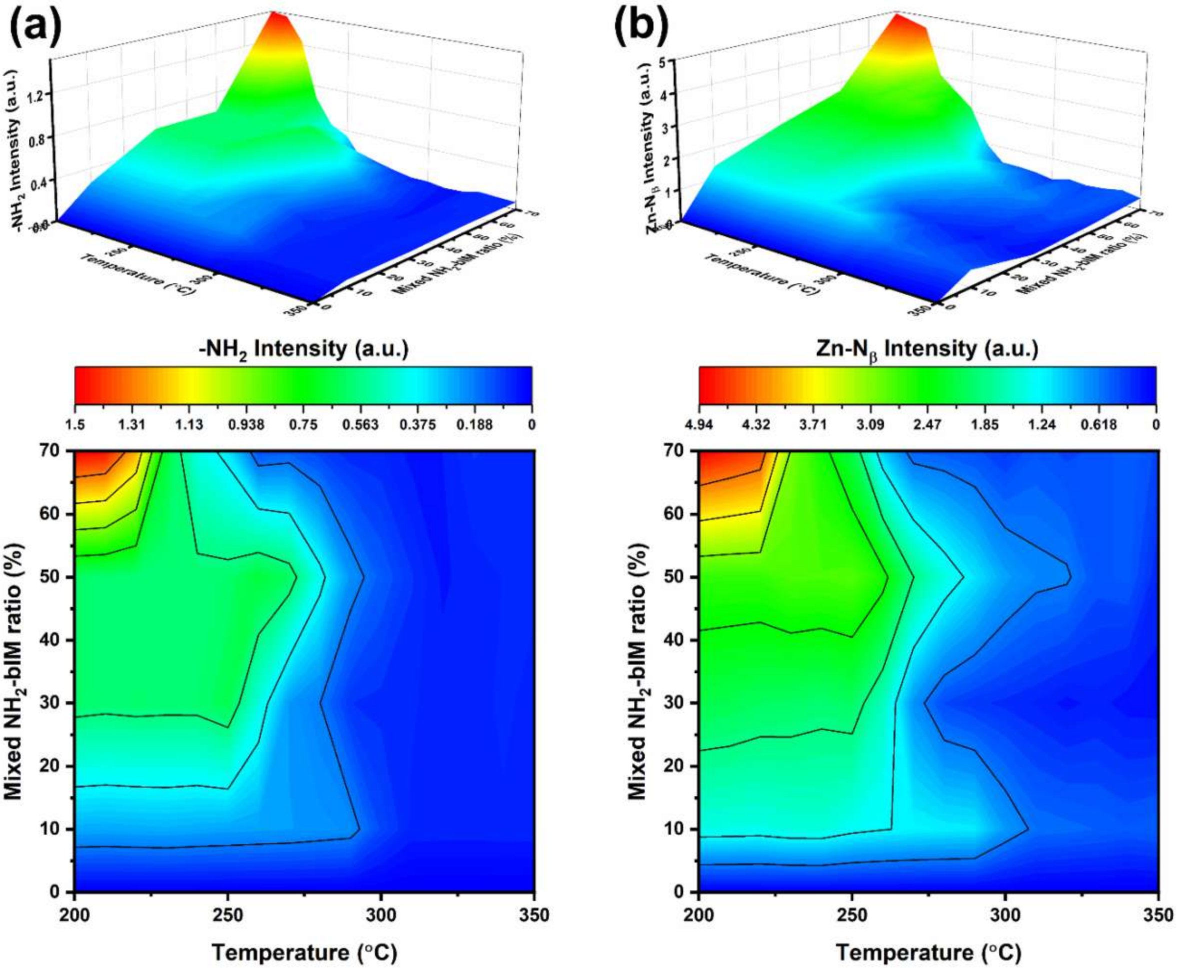

Figure S11. 2D/3D contour plot of ν(-NH$_2$) intensity (a) and ν(Zn-N$_\beta$) intensity (b) in ML-ZIFs vs. mixed NH$_2$-bIm ratio with calcination temperature. Data are from the IR spectra in **Figure S6**.

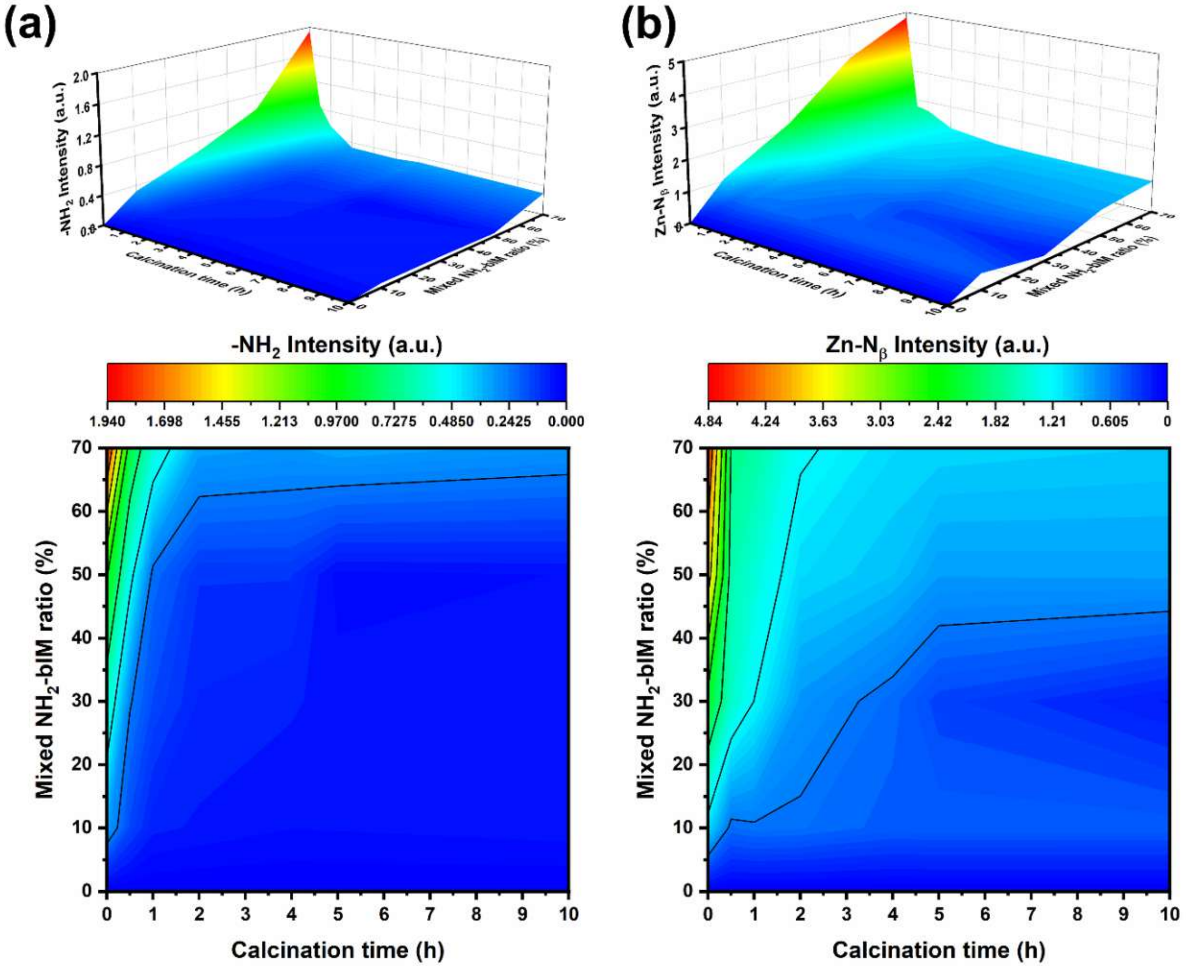

Figure S12. 2D/3D contour plot of ν(-NH$_2$) intensity (a) and ν(Zn-N$_\beta$) intensity (b) in ML-ZIFs vs. mixed NH$_2$-bIm ratio with calcination time. Data are from the IR spectra in **Figure S8**.

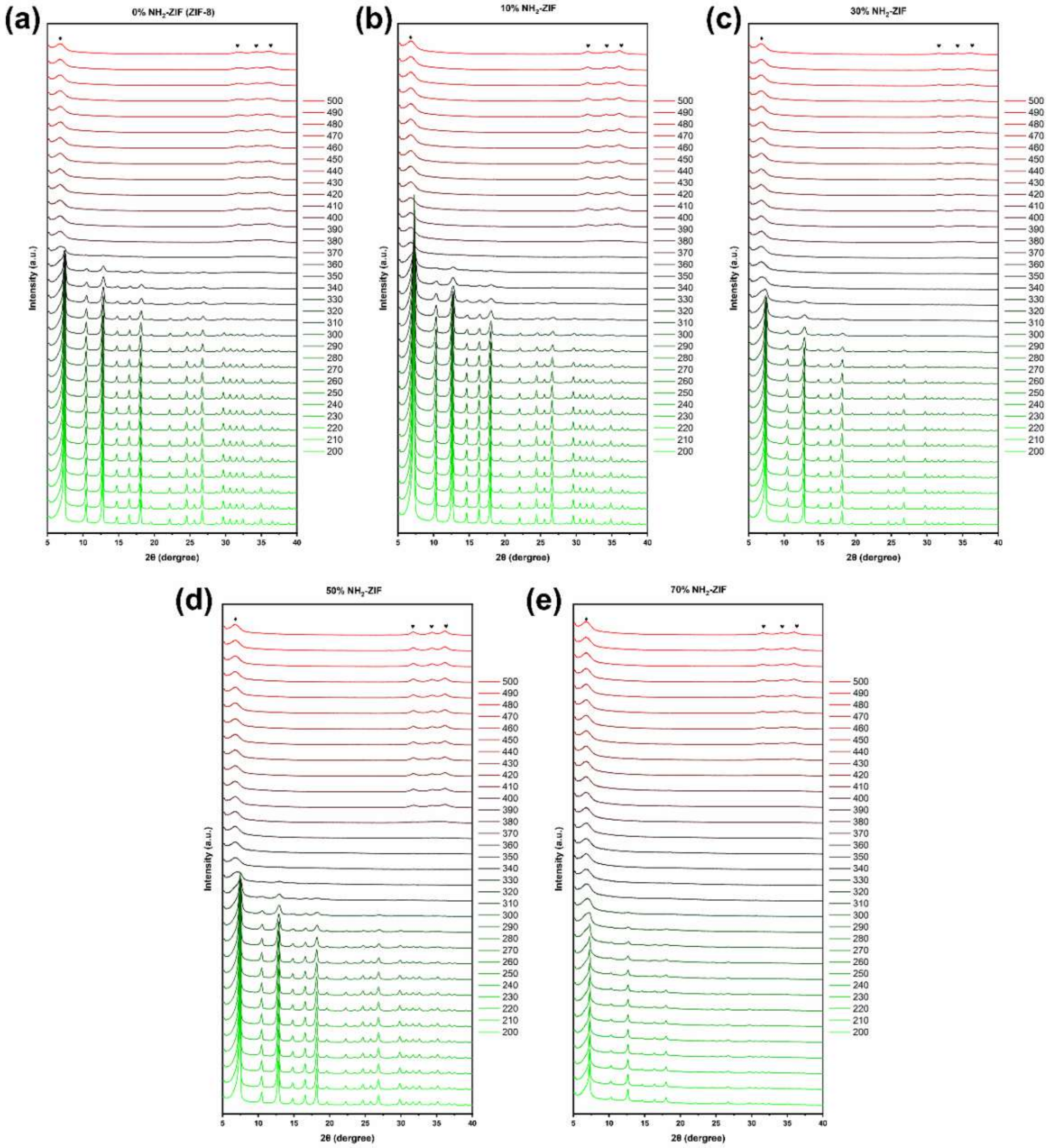

Figure S13. Temperature-programmed in-situ XRD patterns of 0-70%NH_2-ZIFs in air atmosphere (a, 0%NH_2-ZIF; b, 10%NH_2-ZIF; c, 30%NH_2-ZIF; d, 50%NH_2-ZIF; e, 70%NH_2-ZIF). The (011) peak, which is the first peak and has the strongest intensity, is a suitable choice for revealing and studying the transformation of the crystal structure during ligand thermolysis.

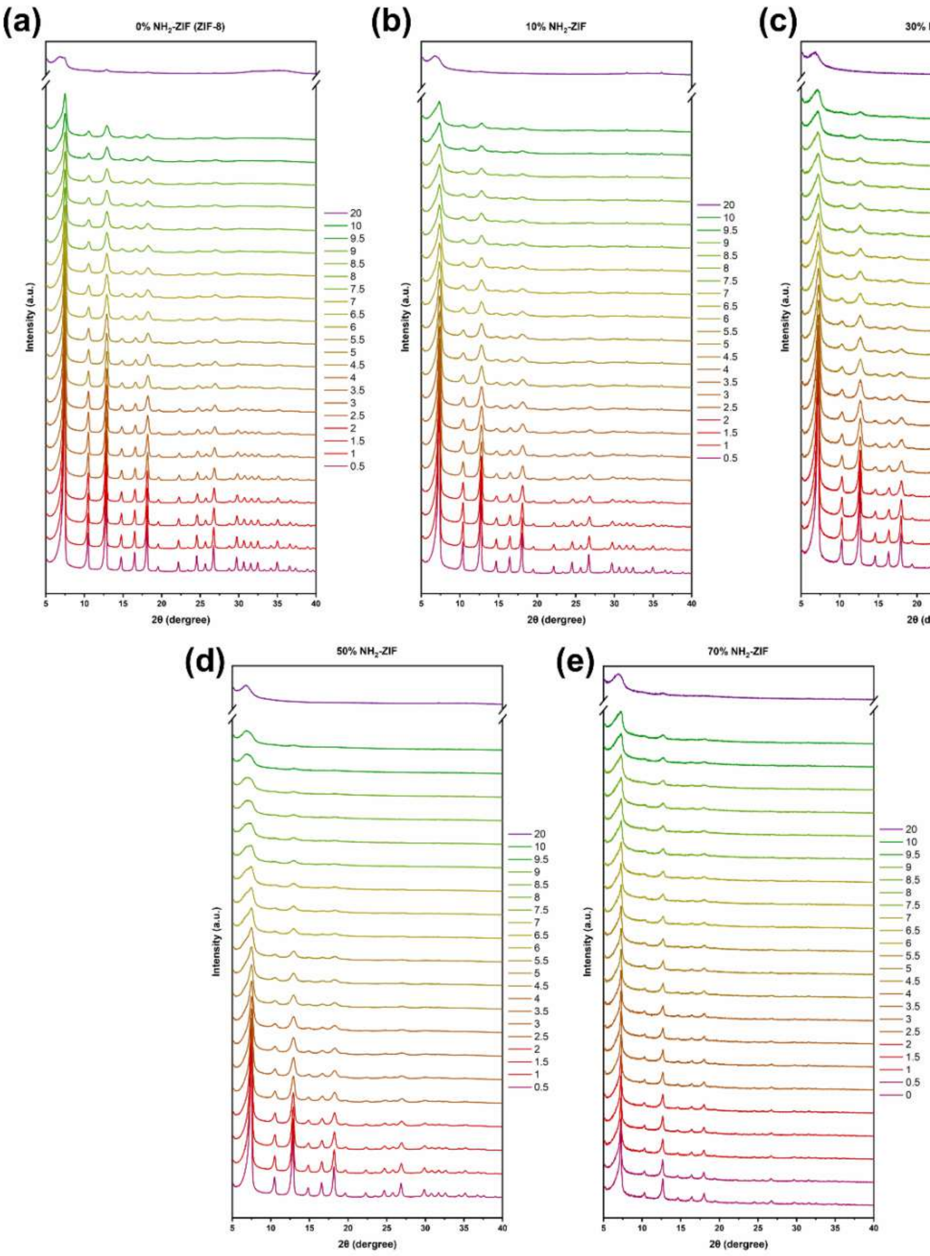

Figure S14. Isothermal in-situ XRD patterns of 0-70%NH$_2$-ZIFs (a, 0%NH$_2$-ZIF; b, 10%NH$_2$-ZIF; c, 30%NH$_2$-ZIF; d, 50%NH$_2$-ZIF; e, 70%NH$_2$-ZIF;) at different calcination times in air atmosphere. 0-50% at 290°C and 70% at 260°C.

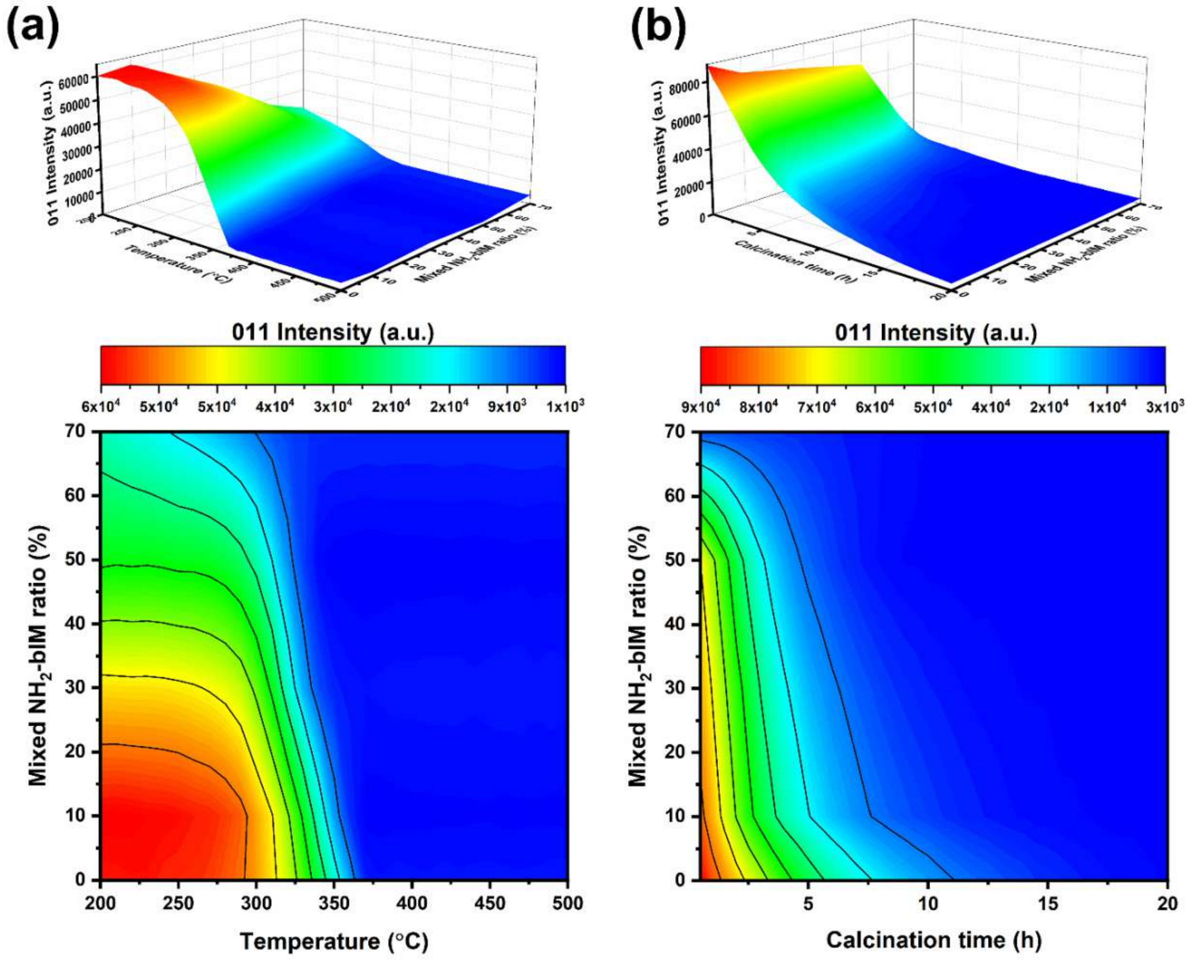

Figure S15. 2D/3D contour plot of (011) intensity in ML-ZIFs vs. mixed NH_2-bIm ratio with temperature (a) and calcination time (b). Data are from the XRD patterns in **Figures S13** and **S14**.

S2. Ligand mixing and removal process for ZIF-67

Mixed-ligand ZIF-67 and its ligand thermolysis process. ZIF-67 and ZIF-8 share the same topology (SOD) in the family of ZIFs [6], with cobalt serving as the metal center. Since, we attempted to mix NH_2-bIminto ZIF-67 and successfully synthesized NH_2-ZIF67 (ML-ZIF-67), as confirmed by presence of $\nu(Co\text{-}N_\beta)$ and $\nu(\text{-}NH_2)$, as well as the XRD patterns (**Figures S16a** and **S16b**). Due to ZIF-67 and ZIF-8 are isostructural with the similar lattice parameters and the same organic ligands, the outcome is almost identical to that of the ML-ZIF-8. However, because coordination differences between Zn-N and Co-N, their thermal stability differs, with the unsaturated Co-N (outer shell is $3d^7 4s^2$) being more susceptible to oxidation than Zn-N (outer shell is $3d^{10} 4s^2$) [7, 8]. A comparison of the TGA curves revealed that the ML-ZIF-67's thermolysis temperature was about 50°C ahead than that of the ML-ZIF-8's (**Figure 2**). Overlapping TGA and intensity plot of (011) peaks illustrate that the mixed-ligand ratio cannot influence the thermolysis temperature of NH_2-ZIF67 (**Figures S16c** and **S16d**). It further demonstrates that NH_2-bImand 2-IM in NH_2-ZIF67 have similar thermolysis temperatures and cannot selectively retain/remove one ligand by temperature.

More detail as observed in the ex-situ ATR-IR spectra (**Figure S17**), crystal structure of NH_2-ZIF67 is rapidly converted to cobalt oxide at 10°C (220-230°C). Prior to oxidation, no significant NH_2-bImremoval process was observed, and both $\nu(Co\text{-}N_\beta)$ and $\nu(\text{-}NH_2)$ were maintained. After switching to inert gas (Ar) calcination, NH_2-ZIF67 was similarly carbonized rapidly between 440-500°C, resulting in the destruction of the ZIF-67 framework. Once again, ligand thermolysis did not occur prior to 450°C in inert gas flow. In conclusion, the temperatures of the two ligands in NH_2-ZIF67 were too near to each other, regardless of the gas atmosphere, to allow the SeLiRe by thermolysis. This removal strategy, in contrast, can be simply applied to the ML-ZIF-8 which has a suitable temperature window of the two ligands.

Currently, we are focusing on finding ligands that can effectively facilitate the mixing and removal of ligands in a specific type of zeolitic imidazolate framework.

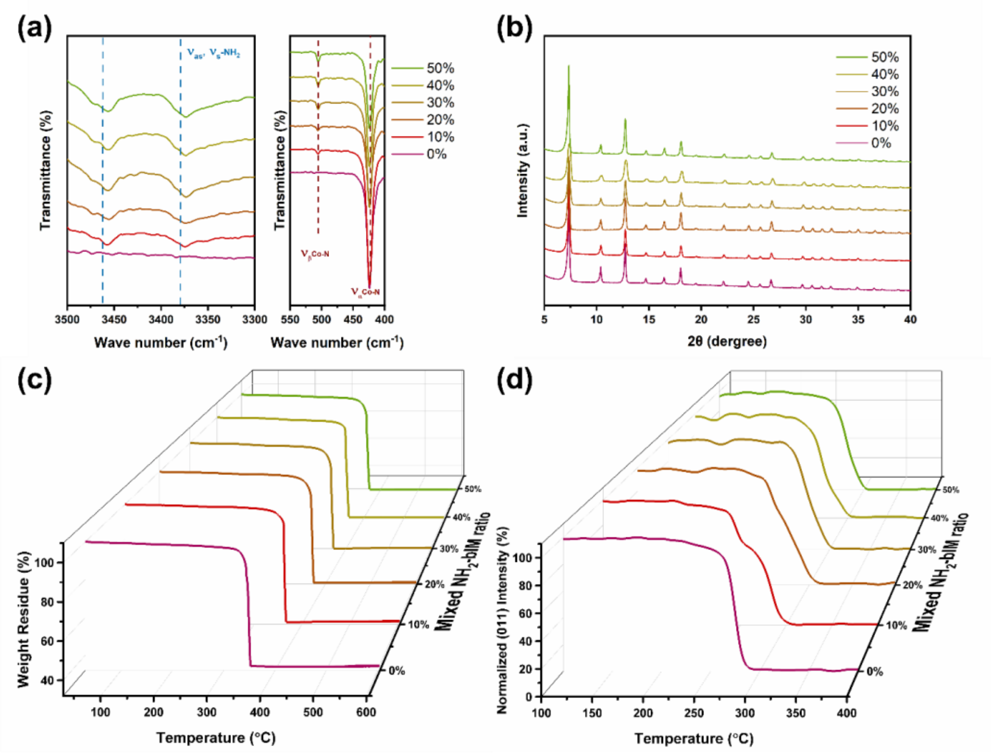

Figure S16. ATR-IR spectra (a) and XRD patterns (b) of 0-50%NH_2-ZIF67. TGA curves of 0-50%NH_2-ZIF67 (c). Intensity evolution plot of (011) peaks in the in-situ XRD with temperature for 0-50%NH_2-ZIF67 (d), data are from the in-situ XRD patterns (**Figure S18**).

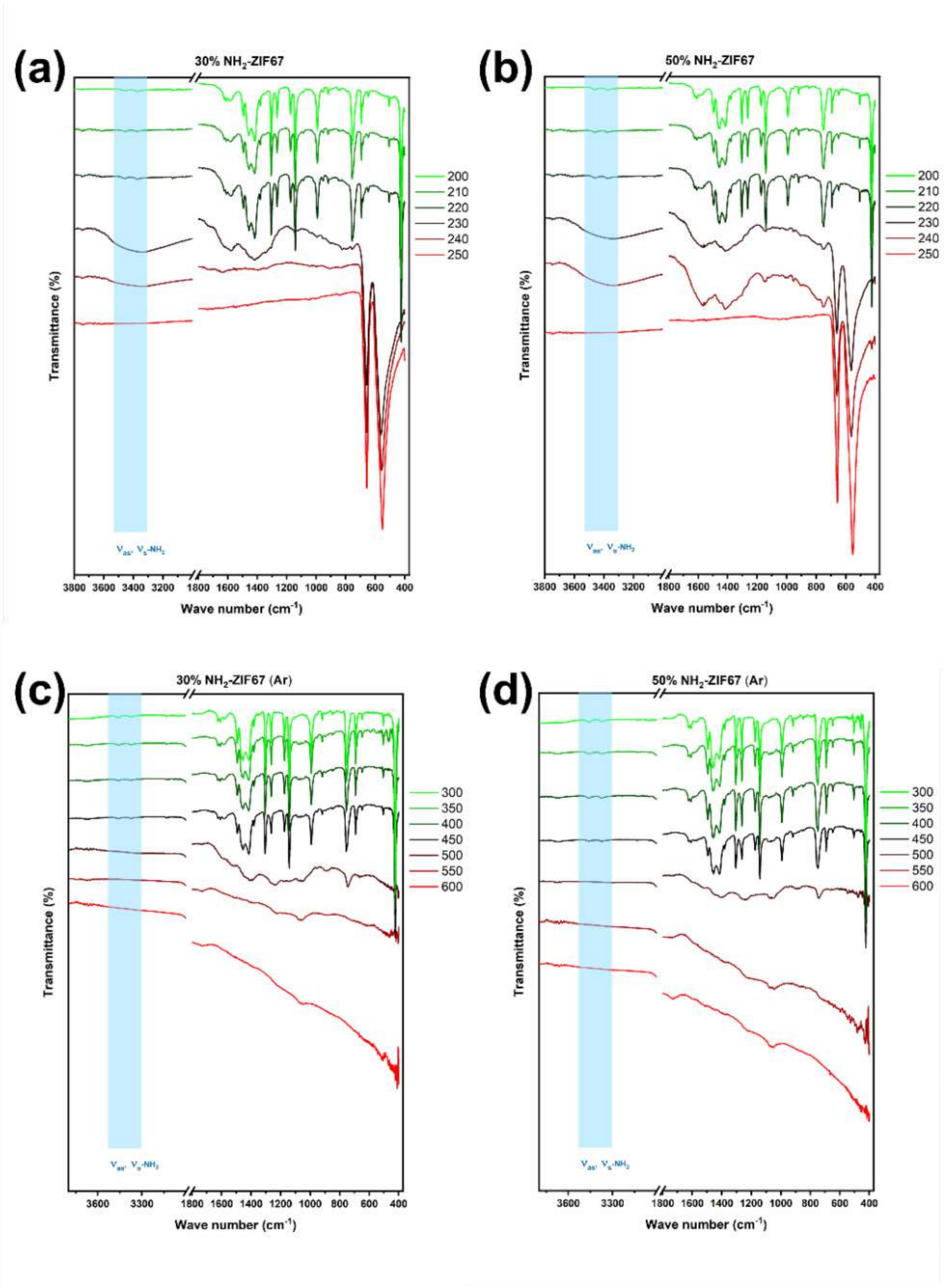

Figure S17. Ex-situ ATR-IR spectra of 30%NH_2-ZIF67 (a, in air; c, in Ar) and 50%NH_2-ZIF67 (b, in air; d, in Ar) at different temperatures. Calcination time of the all NH_2-ZIF67 were two hours, and then cooled naturally to room temperature.

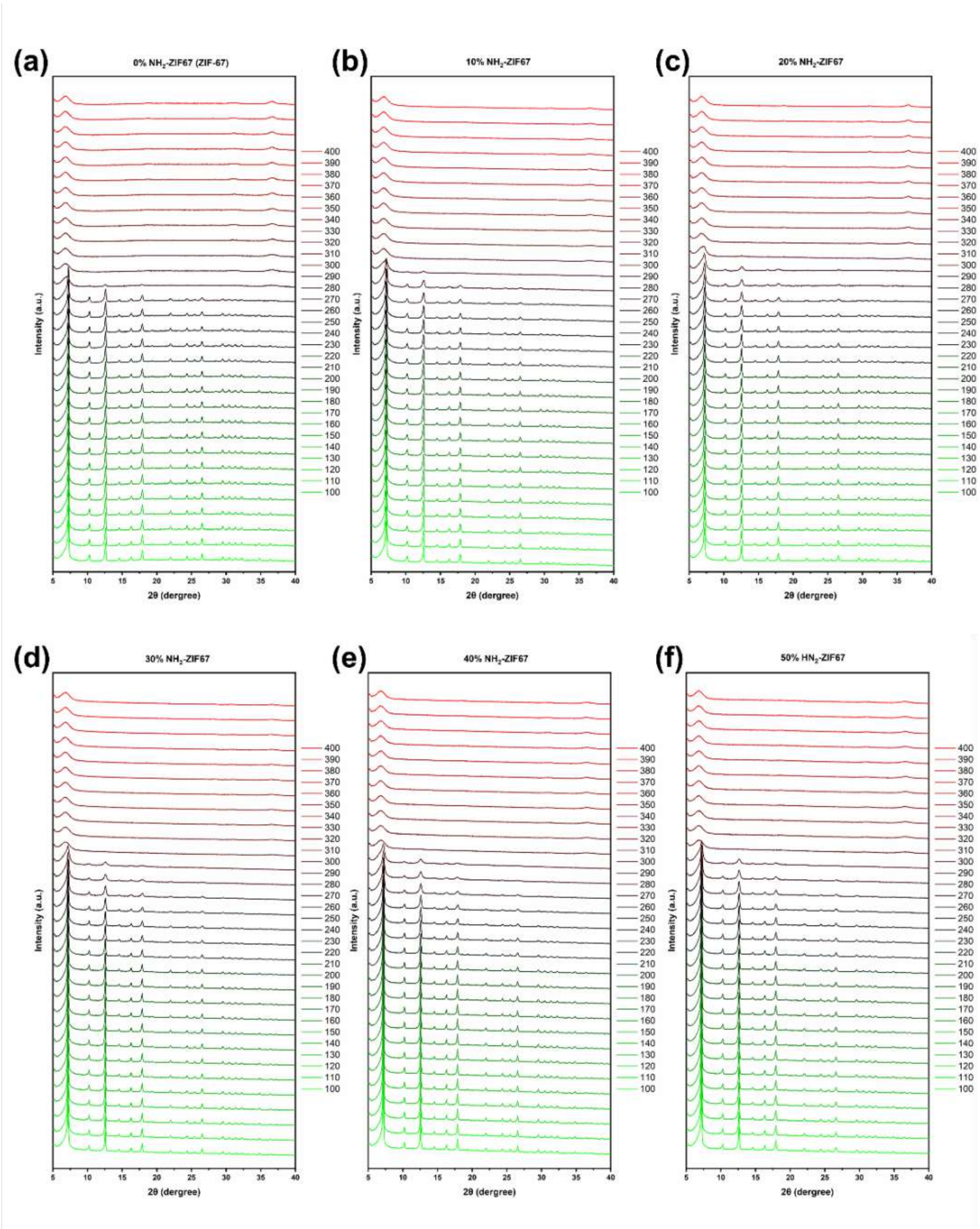

Figure S18. Temperature-programmed in-situ XRD patterns of 0-50%NH_2-ZIF67 in air atmosphere (a, 0%NH_2-ZIF67; b, 10%NH_2-ZIF67; c, 20%NH_2-ZIF67; d, 30%NH_2-ZIF67; e, 40%NH_2-ZIF67; f, 50%NH_2-ZIF67).

S3. Characterization of pore structures

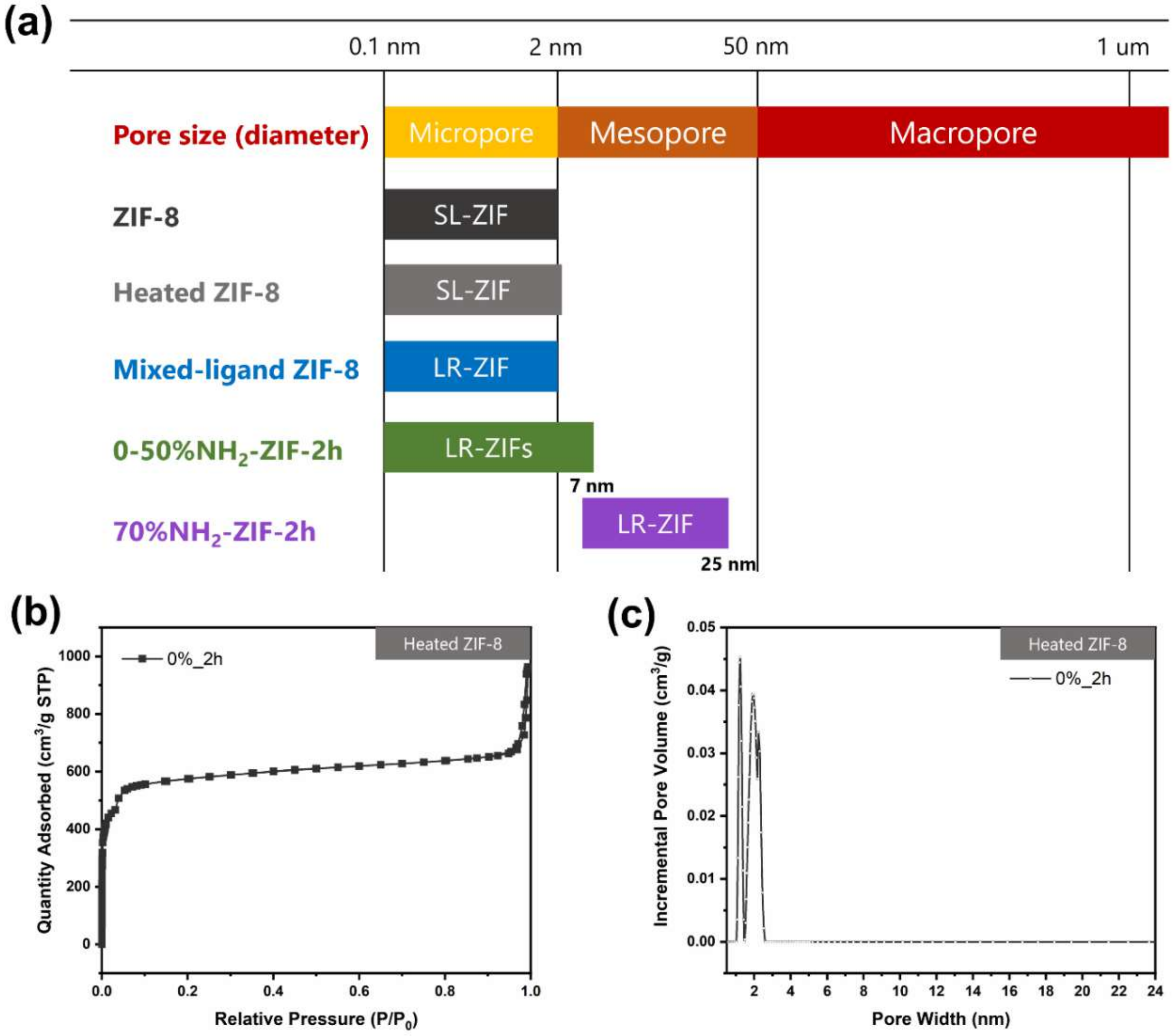

Figure S19. NLDFT porosity distribution diagram of ZIF-8, mixed-ligand ZIF-8, single-ligand ZIF-8 (SL-ZIF) and ligand-removal ZIF-8 (a). Heated ZIF-8 means heating of pure ZIF-8 at 290°C for 2 hours (0%NH_2-ZIF-2h). N_2 sorption isotherm (b) and NLDFT porosity distribution (c) of heated ZIF-8. Despite the impact of heating on the pore distribution of SL-ZIF, it still remains concentrated within the microporous range, indicating the advantage of ML-ZIFs in constructing tuned porous structures through thermolysis.

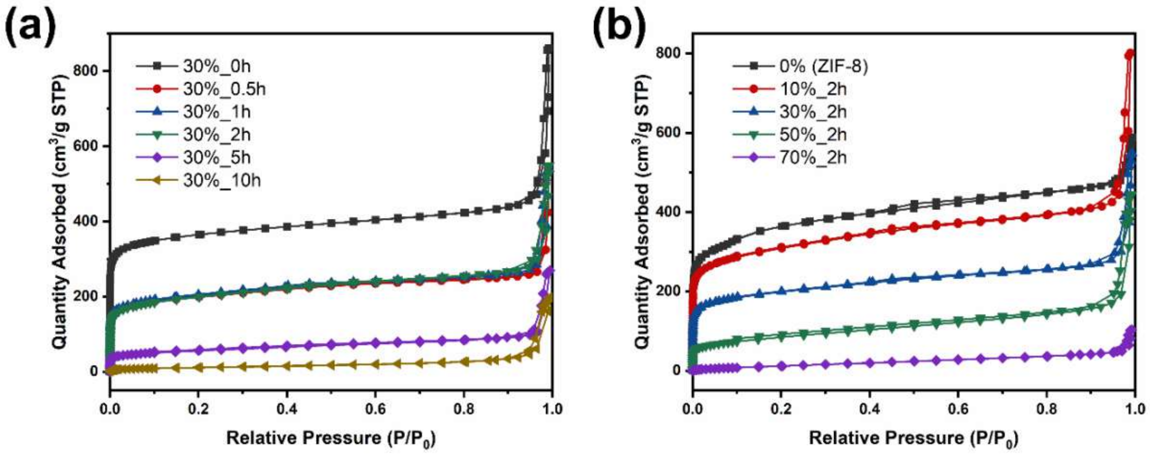

Figure S20. N_2 physisorption isotherms at 77 K of 30%NH_2-ZIF-*time* at 0-10 hours calcination times (a) and R%NH_2-ZIF-2h including ZIF-8 (b).

Table S2. Specific surface area and porosity parameters of ML-ZIFs and LR-ZIFs.

Samples[a]	**Specific surface area**[b] **($m^2\ g^{-1}$)**	**Total Pore Volume ($cm^3\ g^{-1}$)**	**Micropore Volume**[c] **($cm^3\ g^{-1}$)**	**Mesopore Volume**[d] **($cm^3\ g^{-1}$)**
0%NH_2-ZIF-0h (ZIF-8)	1315.0	0.518	0.518	-
10%NH_2-ZIF-2h	999.6	0.392	0.376	0.016
30%NH_2-ZIF-0h	1192.9	0.499	0.499	-
30%NH_2-ZIF-0.5h	733.3	0.287	0.246	0.041
30%NH_2-ZIF-1h	760.9	0.292	0.243	0.049
30%NH_2-ZIF-2h	665.0	0.309	0.240	0.067
30%NH_2-ZIF-5h	199.7	0.075	0.044	0.031
30%NH_2-ZIF-10h	43.5	0.005	-	0.005
50%NH_2-ZIF-2h	296.8	0.131	0.045	0.086
70%NH_2-ZIF-2h	60.1	0.038	-	0.038
30%NH_2-ZIF-Ar-2h	1180.3	0.540	0.342	0.198
70%NH_2-ZIF-Ar-2h	79.5	0.072	-	0.072

[a] In the air atmosphere range, 2-50% heated at 290°C and 70% heated at 260°C. In the Ar flow, 30%NH_2-ZIF heated to 500°C, 70%NH_2-ZIF heated to 400°C.

[b] Brunauer-Emmett-Teller specific surface area.

[c] Cumulative adsorption volume of micropores from 0 to 2 nm in diameter.

[d] Cumulative adsorption volume of mesopores from 2 to 50 nm in diameter according to International Union of Pure and Applied Chemistry (IUPAC) [9].

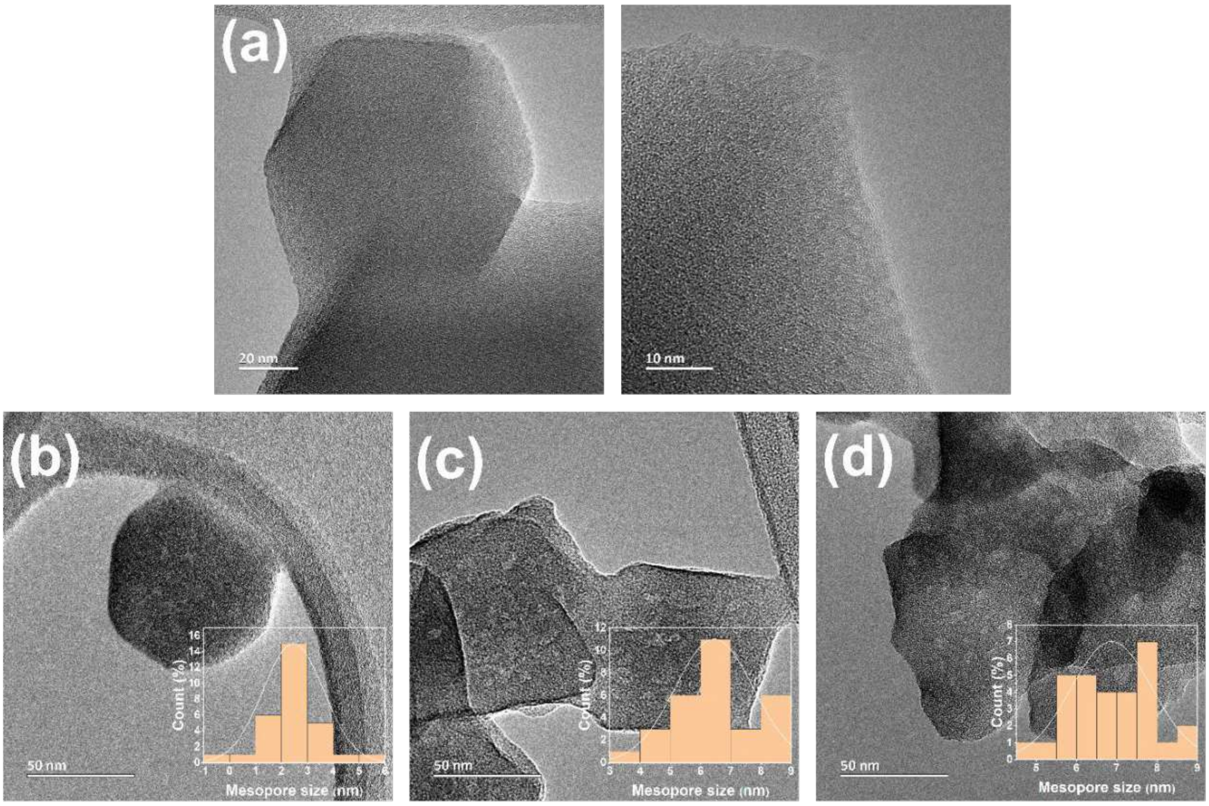

Figure S21. TEM images of pure ZIF-8 (a), 10%NH_2-ZIF-2h (b), 50%NH_2-ZIF-2h (c) and 70%NH_2-ZIF-2h (d). The inside shows the distribution of mesopore size.

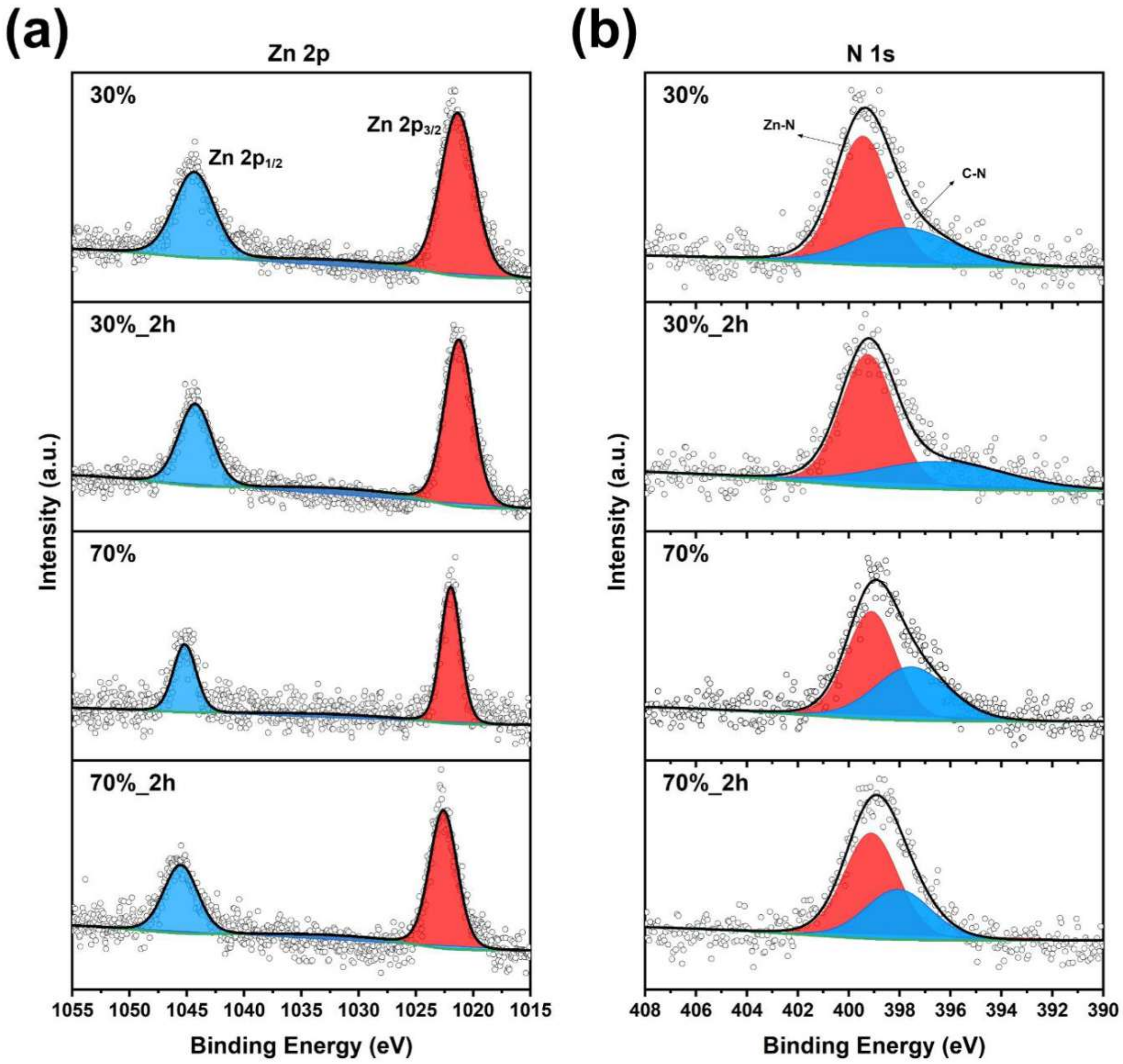

Figure S22. Zn 2p (a) and N 1s (b) spectrum of XPS for 30%NH_2-ZIF, 30%NH_2-ZIF-2h, 70%NH_2-ZIF and 70%NH_2-ZIF-2h. N1 s fitting has two peaks; the first one is assigned to N atom of imidazole linkers at 398.01 eV and the second belongs to nitrogen atom at Zn-N bond at 398.61 eV [10].

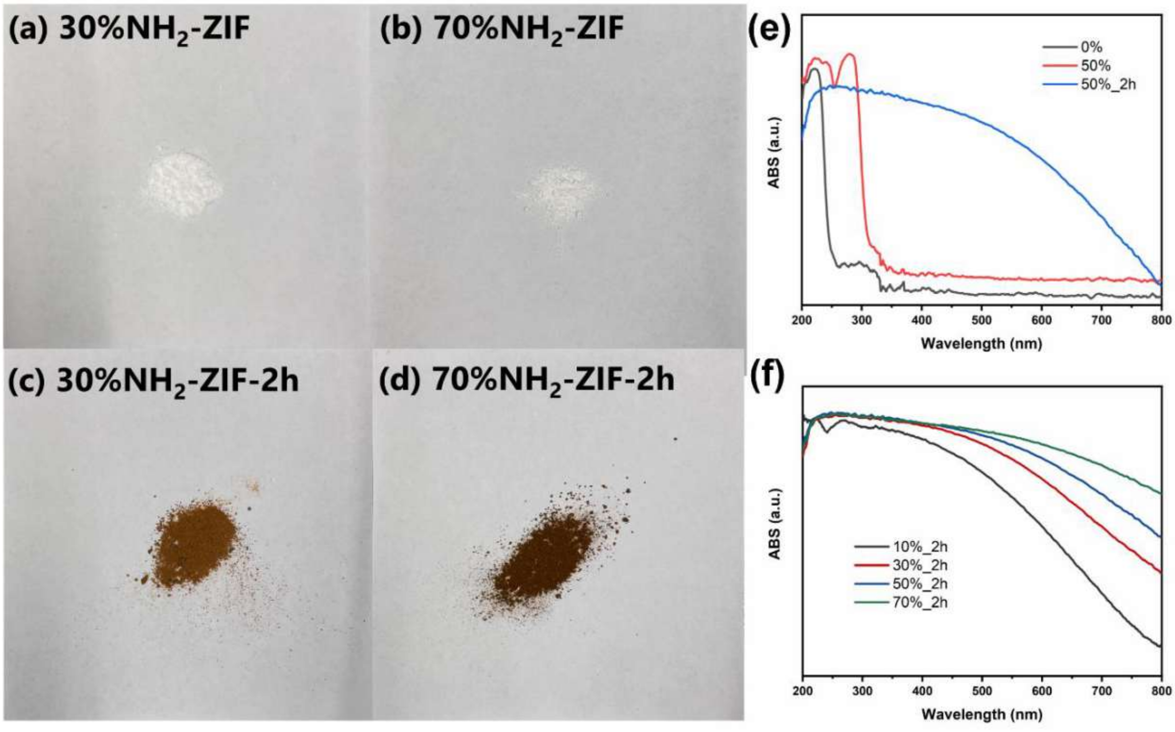

Figure S23. Optical photographs of ML-ZIFs (a, 30%NH2-ZIF; b, 70%NH2-ZIF) and LR-ZIFs (d, 30%NH2-ZIF-2h; e, 70%NH2-ZIF-2h). Powder DRS for 0%NH2-ZIF (ZIF-8), 50%NH2-ZIF-0h and 50%NH2-ZIF-2h (g), and various ratios of ligands 10-70% removal of R%NH2-ZIF-2h (h). As the ratio of NH2-bIm increases, the color of NH2-ZIF-2h gradually deepens (from light brown to dark brown) after ligand thermolysis. This color change can be attributed to the oxidation of the amino group in NH2-bIM; the sample's color often changes to brown when nitrogen-containing compounds are oxidized [3, 11].

S4. Ligand removal in inert gases

Structural characterization of LR-ZIFs. To investigate the effect of inert gas on ligand thermolysis, 30% and 70%NH_2-ZIF were calcined in a tube furnace with an Ar flow. As the temperature rise, the $\nu_{s,\,as}$(-NH_2) and ν(Zn-N_β) of NH_2-ZIF both dropped to 0% in the ex-situ AIR-IR spectra (**Figures S24a** and **S24b**). These bands exhibit reduction between 450-500°C in 30%NH_2-ZIF and 300-450°C in 70%NH_2-ZIF.

In ^{1}H NMR, the thermolabile ligand was almost completely removed from 30%NH_2-ZIF-2h (Ar), while the ligand was only partially removed from 70%NH_2-ZIF-2h (Ar) due to the lower thermolysis temperature (**Figure S25**). Like the thermolysis in air, the characteristic quartets of NH_2-bIm on both sides of 7.35 ppm was markedly reduced. Among them, the NH_2-bIm of 30%NH_2-ZIF-2h (Ar) was more sufficiently removed due to the higher temperature of 500°C, with almost no quadruple peaks remaining. However, due to the excessive mixing of thermolabile ligands in 70%NH_2-ZIF-2h (Ar), it could only maintain its crystallinity at 400°C, resulting in incomplete ligand removal. The *by-products, in contrast to thermolysis in air, from oxidation were not observed.

As well, ligand thermolysis can also be achieved using N_2 flow, with no difference compared to Ar flow. Whether in N_2 or Ar, in-situ XRD illustrates that the crystallinity of ML-ZIF decreased with temperature, while 0%, 30% and 70%NH_2-ZIF collapsed after 450°C, 520°C and 550°C respectively (**Figures S24c** and **S24d**). Similarly, calcination times of >2 hours have the devastating effect on the crystallinity of 30% and 70%NH_2-ZIF (**Figure S28**). If the temperature continues to be raised to 700-900°C, the zinc will evaporate and eventually form the carbon material like nitrogen-doped carbon (NC) or graphitic carbon (GC) [12, 13], which is detrimental for our research. Additionally, the color of LR-ZIF (Ar) tends to be darker due to the additional carbon attached, and the light absorption extends from the UV to the visible region (**Figure S29**).

Hierarchical Pores in LR-ZIFs (Ar). NLDFT porosity distribution and TEM images illustrate the feasibility of constructing sponge-like hierarchical porous ZIFs by SeLiRe process (**Figures S30** and **S31**). Compared to air, 30%NH_2-ZIF-Ar-2h (500°C) exhibits bimodal distribution of mesopores, ranging in size from 2 to 7 nm (close to the 50% in air). In contrast, 70%NH_2-ZIF-Ar-

2h (400°C) obtained by the lower temperature, is almost identical to the calcined sample in air, strongly supporting our hypothesis regarding the SeLiRe mechanism. Note that single-ligand ZIFs also can gradually dislodge the intrinsic metal clusters and thus form the irregular mesopores during high-temperature calcination with inert gases [14, 15]. However, they typically fail to maintain the intrinsic micropores and crystal structure of ZIFs, eventually converting to NC or GC [16]. Moreover, compared with ML-ZIFs, single-ligand ZIFs heating is difficult to regulate the porous channel and spatial arrangement of mesopores through the synthetic condition. Our focus in this work is on the construction of controlled hierarchically porous ZIFs that maintain the intrinsic framework structure, thus making single-ligand ZIFs as a precursor less desirable for our purposes.

Influence of inert gas calcination. Compared to air calcination, the use of inert gas allowed for SeLiRe at higher temperatures, up to 400-500°C, while avoiding the by-products and influence of oxidation reaction on the ML-ZIFs. The surface of the ML-ZIF was the first to be affected by high temperature, tending to carbonize at temperatures over 500°C. The appearance of two bands, D band (1342 cm^{-1}) and G band (1577 cm^{-1}) corresponded to the disordered carbon atoms and the sp^2-hybridised graphite carbon atoms, respectively (**Figure S32d**) [17]. These bands indicate the formation of the graphite/carbon structure resulting from the calcination in inert gas. However, the XRD, ATR-IR, XPS and TGA did not change much, indicating the maintain of the framework structure within ZIF-8 (**Figures S32a-c**). Therefore, the removal of NH$_2$-bIm does not depend on the oxidation reaction, and the SeLiRe process can be achieved in inert gas as well.

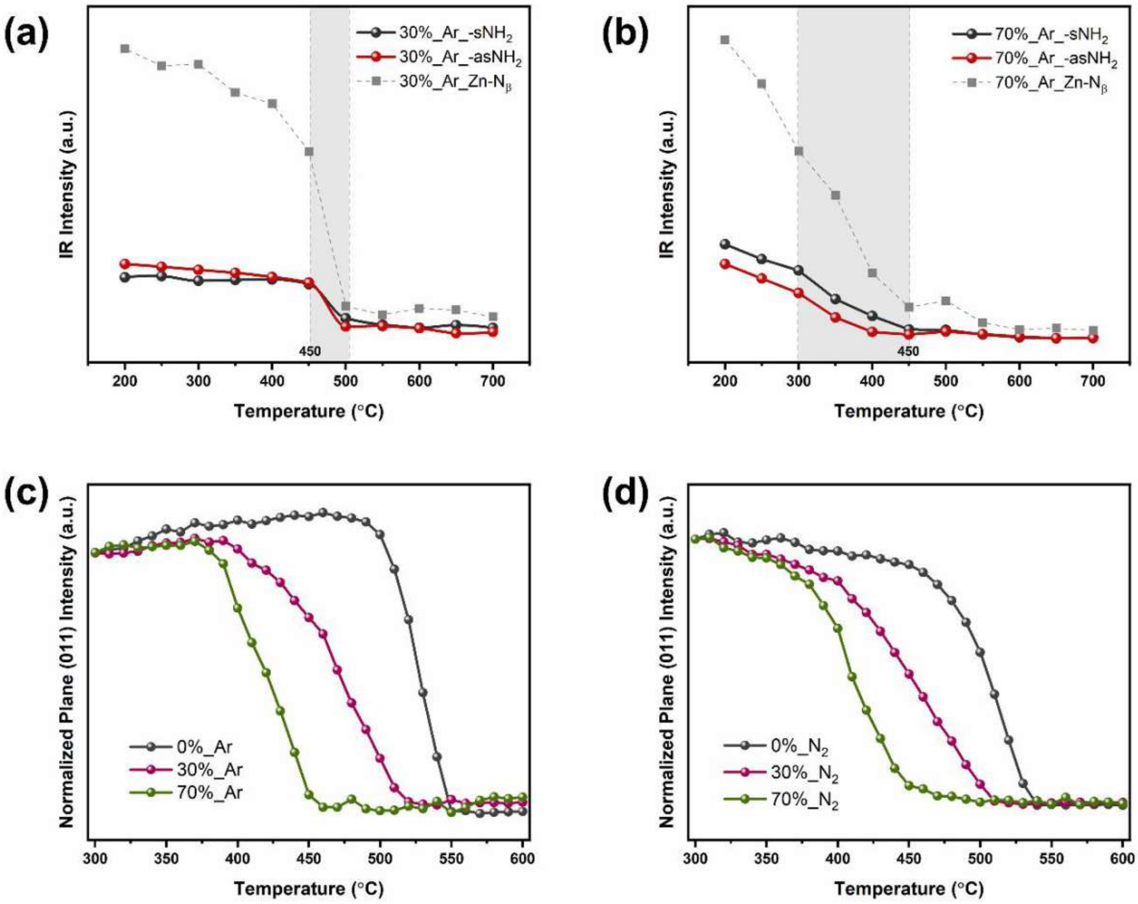

Figure S24. Intensity plot of $\nu_{s,\ as}(\text{-NH}_2)$ and $\nu(\text{Zn-N}_\beta)$ in the ex-situ AIR-IR spectra with temperature for 30% (a) and 70%NH$_2$-ZIF (b) in Ar atmosphere. Data are from the IR spectra in **Figure S26** at 3250-3550 cm^{-1} for $\nu(\text{-NH}_2)$, 400-550 cm^{-1} for $\nu(\text{Zn-N}_\beta)$. Evolution intensity plot of (011) peaks in the in-situ XRD for 0%, 30%, 70%NH$_2$-ZIF in Ar (c) and N$_2$ (d) flow. Data are from the XRD patterns of (011) peaks in **Figure S27**.

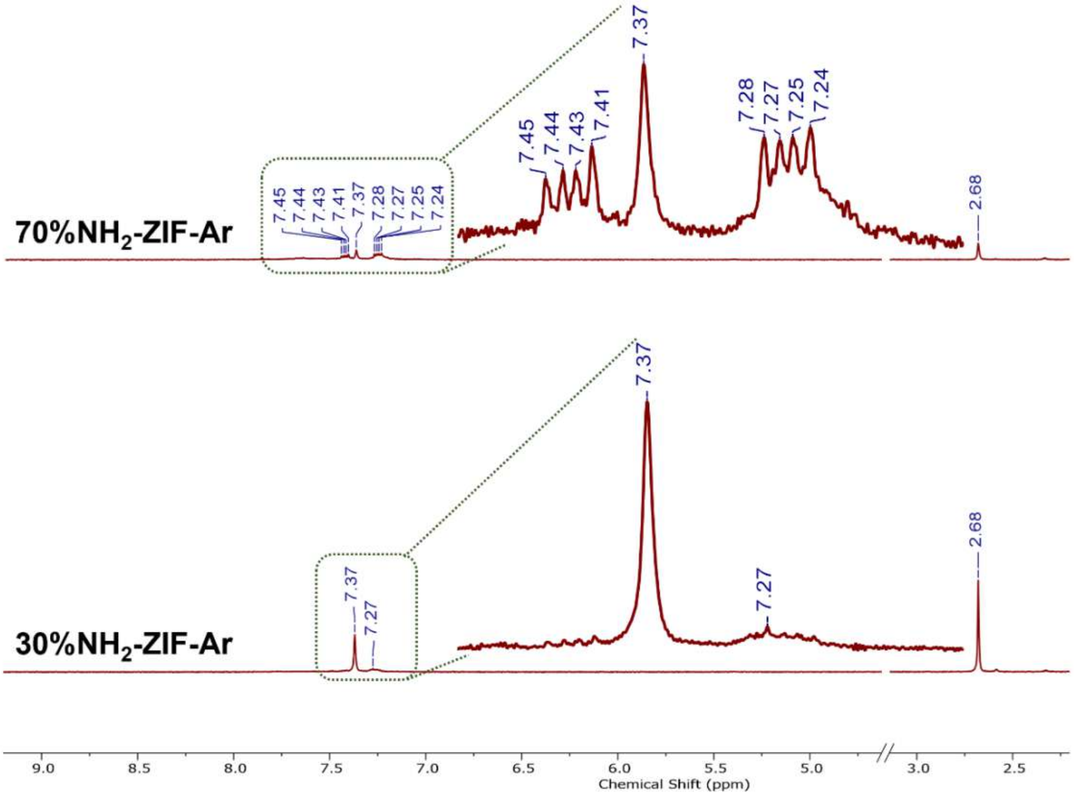

Figure S25. ^{1}H NMR spectroscopy of 30%NH$_2$-ZIF-Ar-2h and 70%NH$_2$-ZIF-Ar-2h in Ar atmosphere.

30%NH$_2$-ZIF-Ar-2h: *^{1}H NMR (250 MHz, Acetic Acid-d$_4$) δ 2.60 – 2.80 (s, 14H), 7.24 – 7.31 (s, 1H), 7.33 – 7.41 (s, 8H).*
70%NH$_2$-ZIF-Ar-2h: *^{1}H NMR (250 MHz, Acetic Acid-d$_4$) δ 2.58 – 2.79 (s, 2H), 7.17 – 7.31 (dd, J = 3.3, 5.9 Hz, 2H), 7.31 – 7.40 (s, 1H), 7.40 – 7.51 (dd, J = 3.3, 5.9 Hz, 1H).*

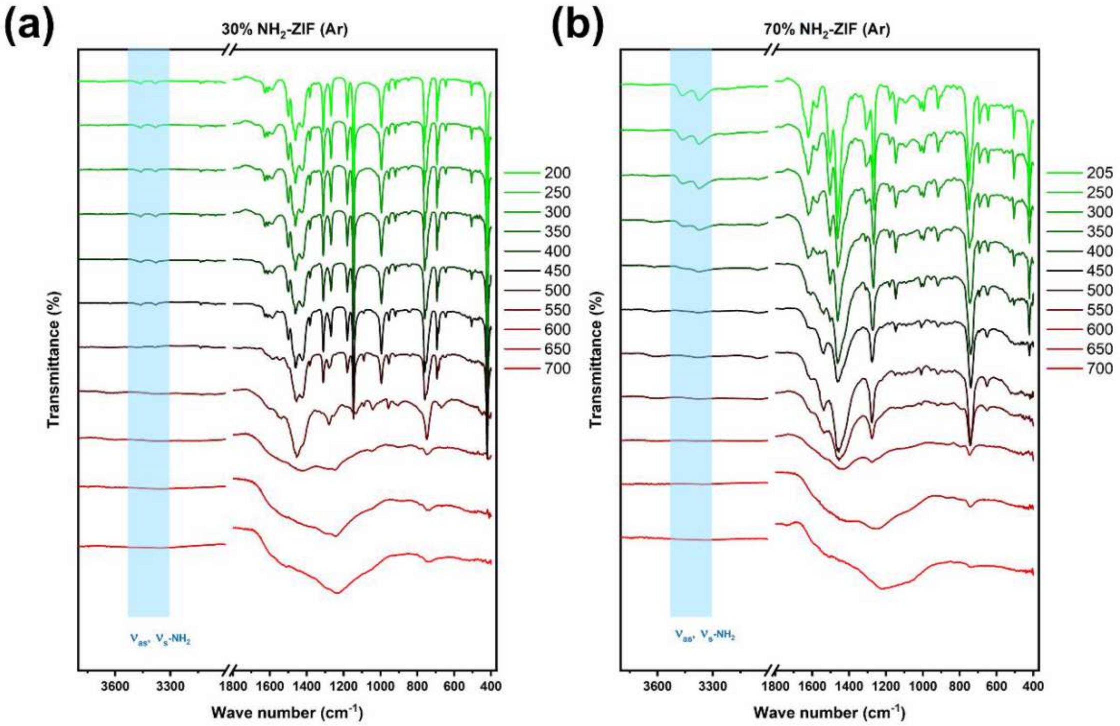

Figure S26. Ex-situ ATR-IR spectra of 30%NH2-ZIF (a) and 70%NH2-ZIF (b) at different temperatures. All ML-ZIFs were calcined in a tube furnace, in Ar atmosphere, for a period of 2 hours and then cooled naturally to room temperature.

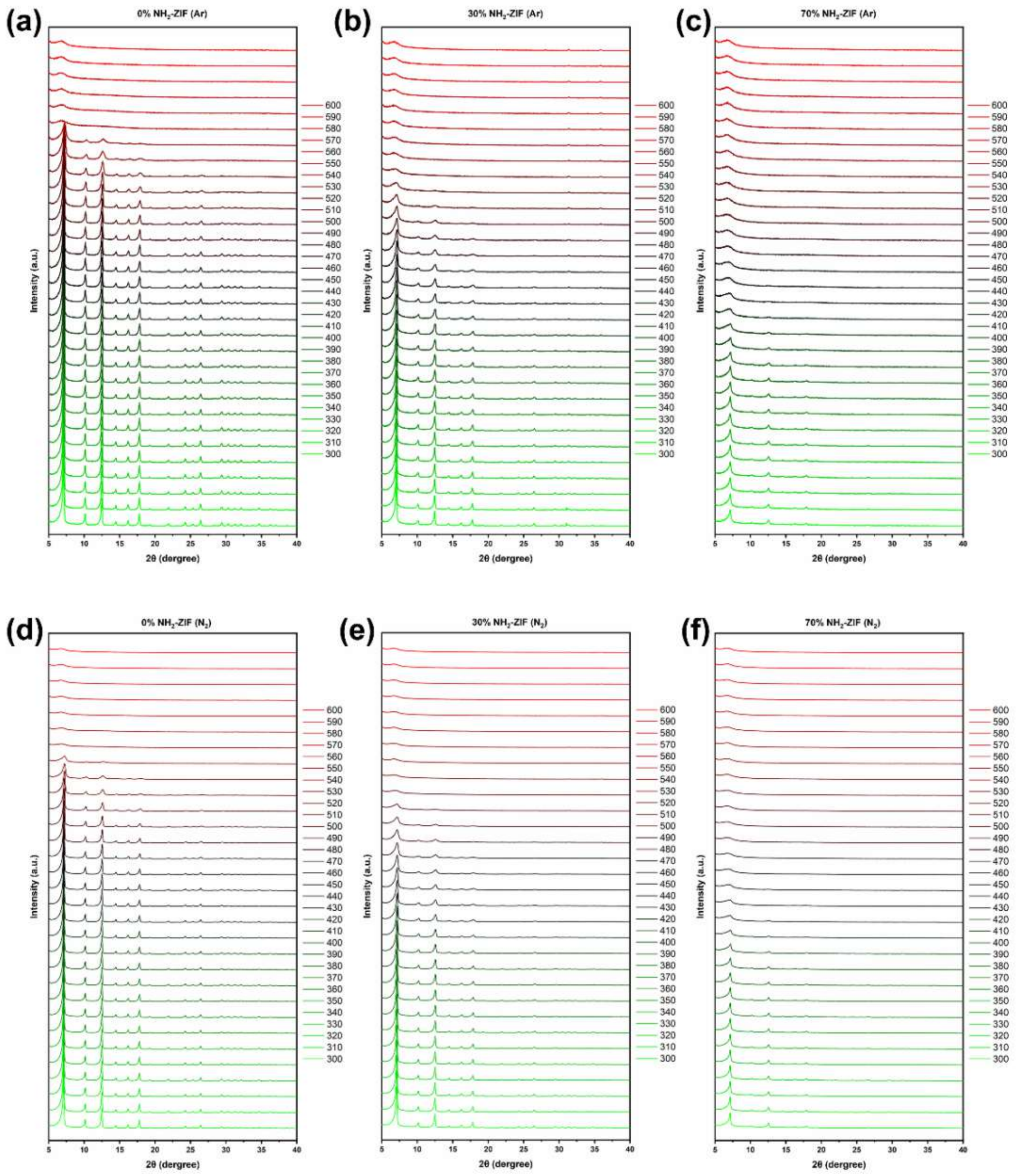

Figure S27. Temperature-programmed in-situ XRD patterns of 0%, 30% and 70%NH$_2$-ZIFs in Ar flow (a, 0%NH$_2$-ZIF; b, 30%NH$_2$-ZIF; c, 70%NH$_2$-ZIF) and in N$_2$ flow (d, 0%NH$_2$-ZIF; e, 30%NH$_2$-ZIF; f, 70%NH$_2$-ZIF).

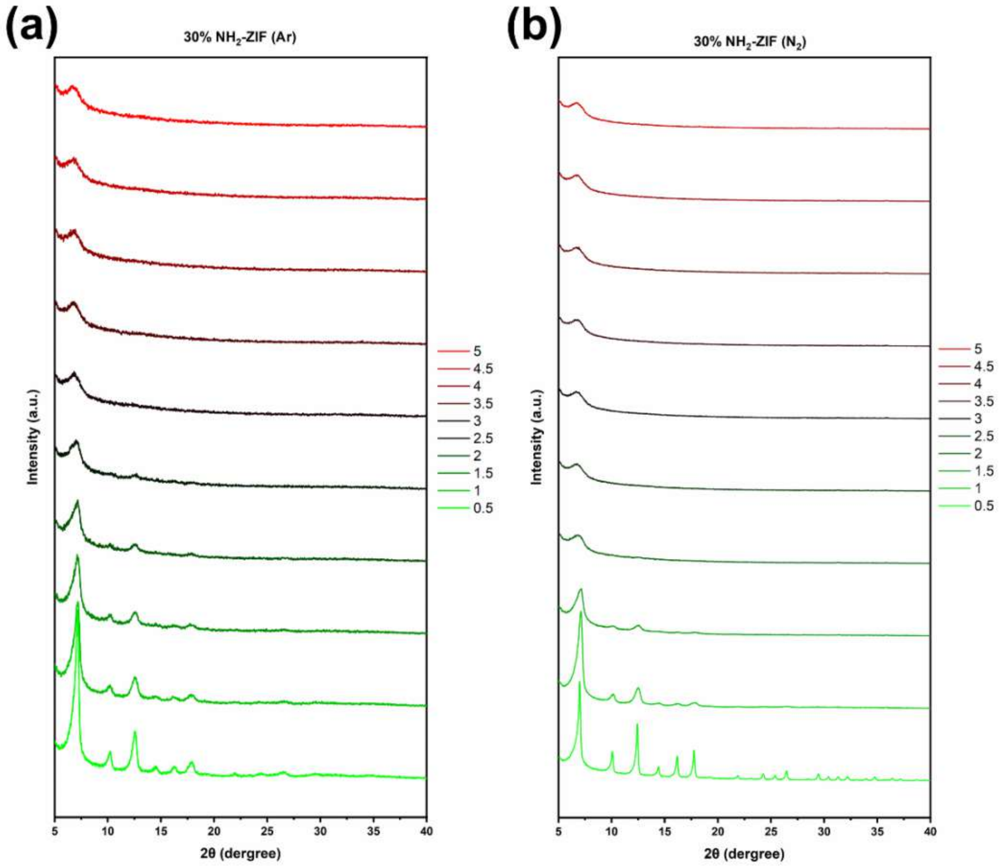

Figure S28. Isothermal in-situ XRD patterns of 30%NH_2-ZIF at different heating times in Ar (a) and N_2 (b) flow at 500°C.

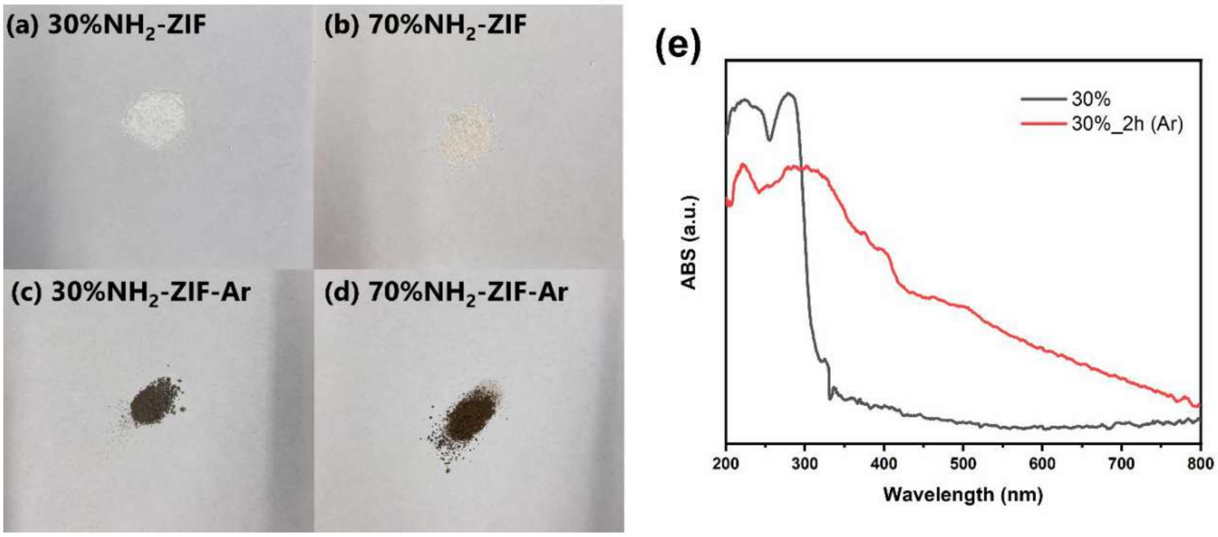

Figure S29. Optical photographs of ML-ZIFs (a, 30%NH$_2$-ZIF; b, 70%NH$_2$-ZIF) and LR-ZIFs (c, 30%NH$_2$-ZIF-Ar-2h; d, 70%NH$_2$-ZIF-Ar-2h). Powder DRS for 30%NH$_2$-ZIF and 30%NH$_2$-ZIF-Ar-2h (e).

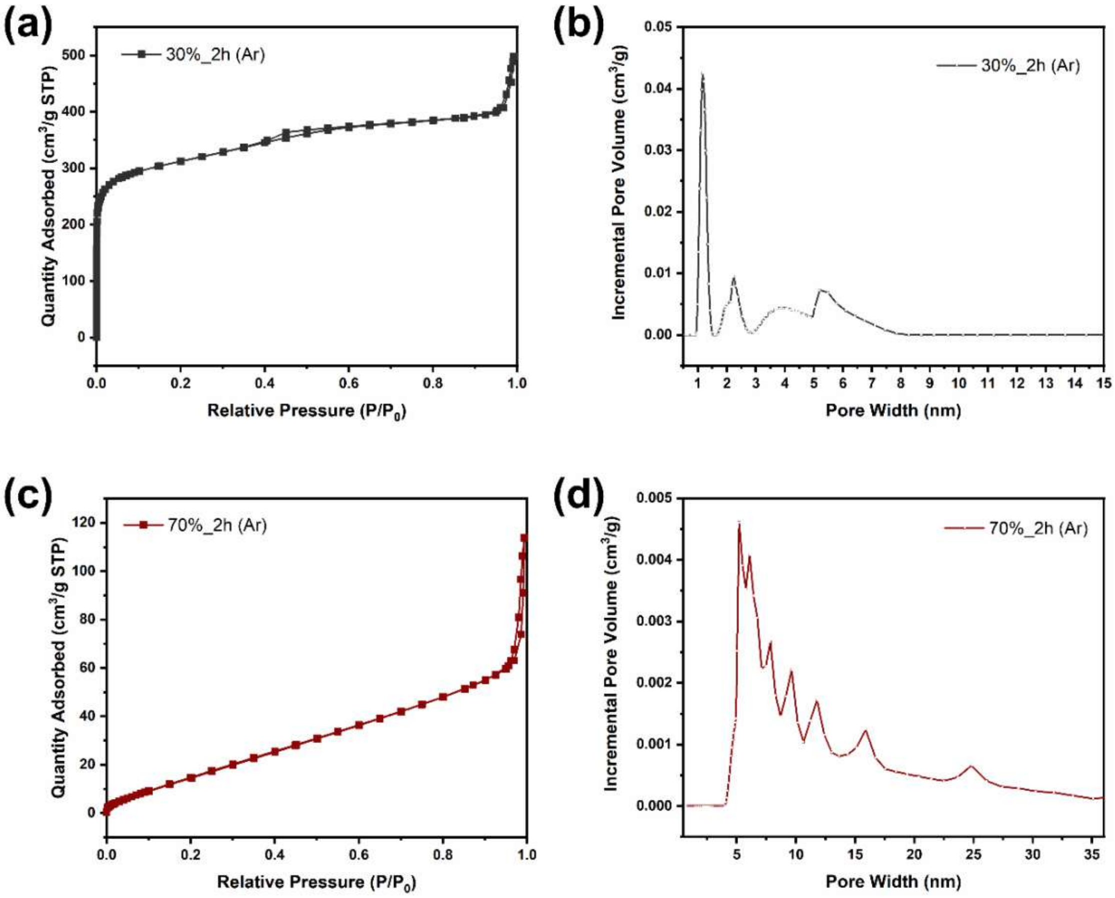

Figure S30. N_2 sorption isotherm (a) and NLDFT porosity distribution (b) of 30%NH_2-ZIF-Ar-2h. N_2 sorption isotherm (c) and NLDFT porosity distribution (d) of 70%NH_2-ZIF-Ar-2h.

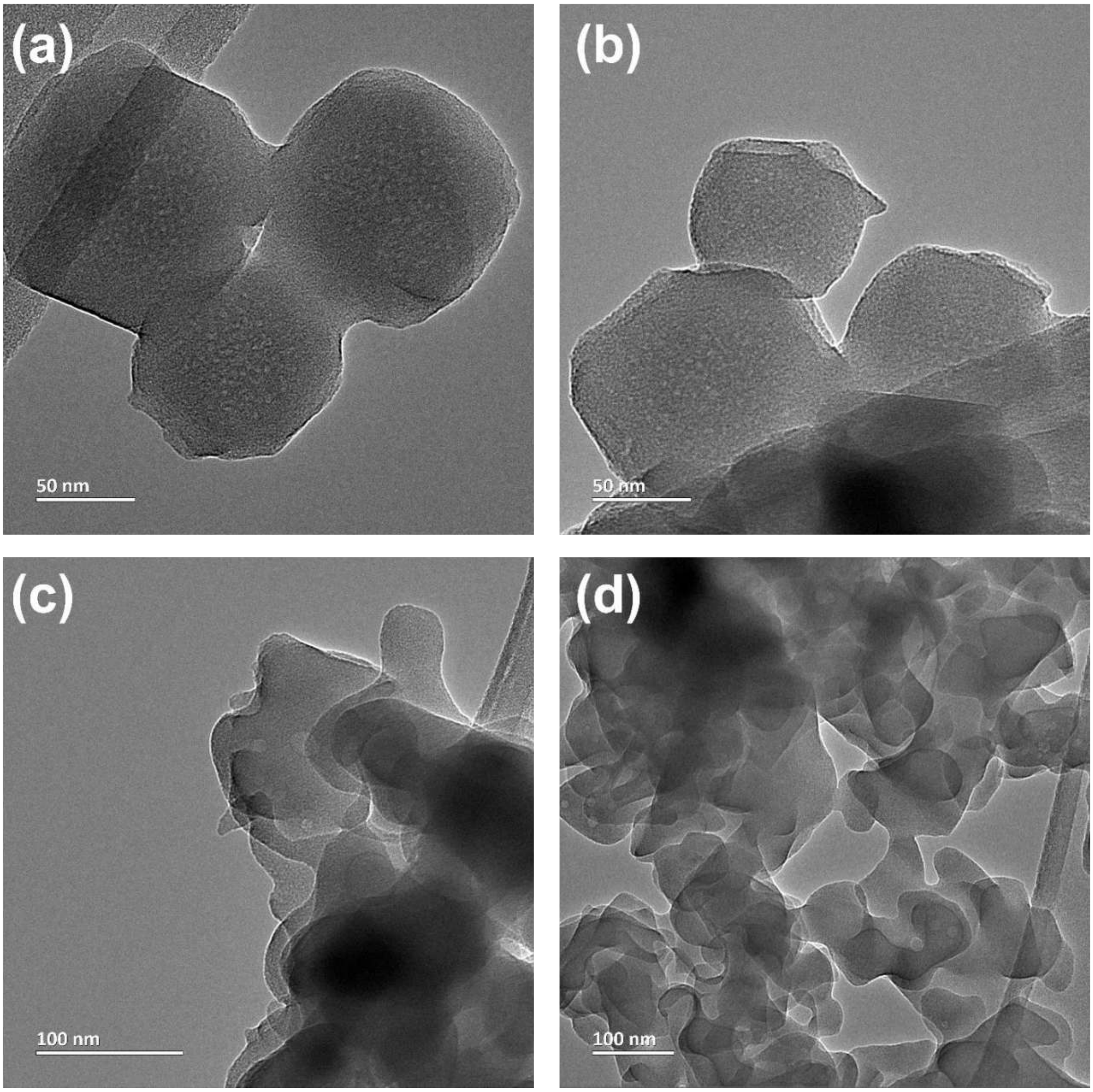

Figure S31. TEM images for single crystals of 30%NH_2-ZIF-Ar-2h (a, b) and 70%NH_2-ZIF-Ar-2h (c, d) after heating treatment in Ar flow.

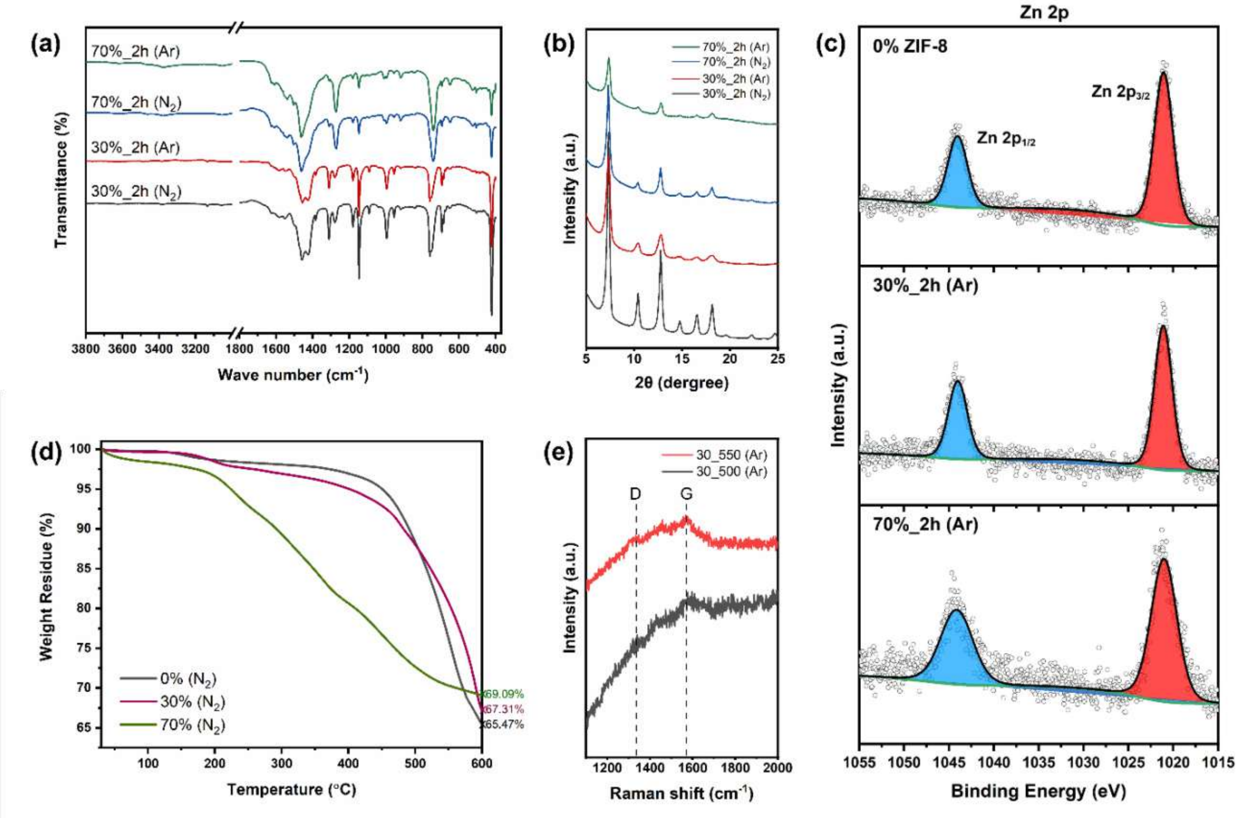

Figure S32. Ex-situ ATR-IR spectra of 30%NH$_2$-ZIF-2h and 70%NH$_2$-ZIF-2h were heated in Ar and N$_2$ atmosphere, respectively (a). XRD patterns of 30%NH$_2$-ZIF-2h and 70%NH$_2$-ZIF-2h in Ar and N$_2$ atmosphere (b). Zn 2p spectrum (c) of XPS for ZIF-8, 30%NH$_2$-ZIF-Ar-2h and 70%NH$_2$-ZIF-Ar-2h. TGA curves of 0%NH$_2$-ZIF (ZIF-8), 30%NH$_2$-ZIF and 70%NH$_2$-ZIF were heated in N$_2$ flow (d). Raman spectra of 30%NH$_2$-ZIF-500℃ and 30%NH$_2$-ZIF-550℃ (e), were heated 2 hours in Ar flow.

S5. DFT simulation models

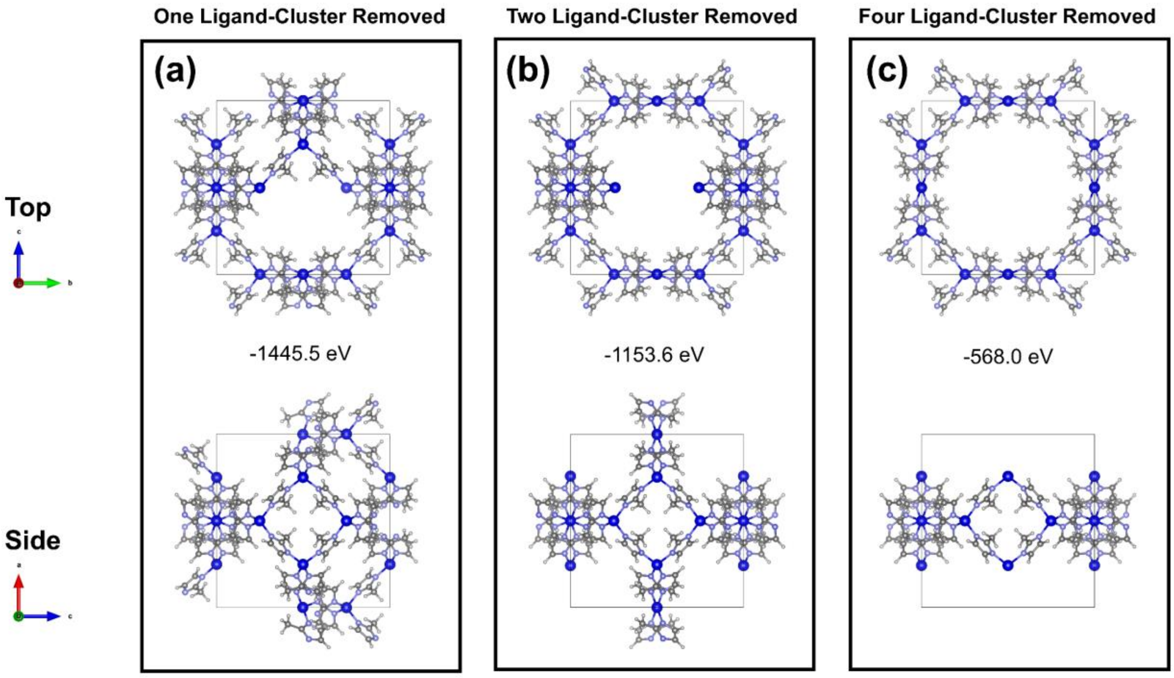

Figure S33. Schematic diagrams (top and side view) of the LR-ZIFs framework with one (a), two (b) and four (c) Zn-N$_4$ clusters and surrounding ligands removed. Original ZIF-8 and ligand-cluster structures are in **Figure S34**. Dark blue for Zn, light blue for N, gray for C and white for H.

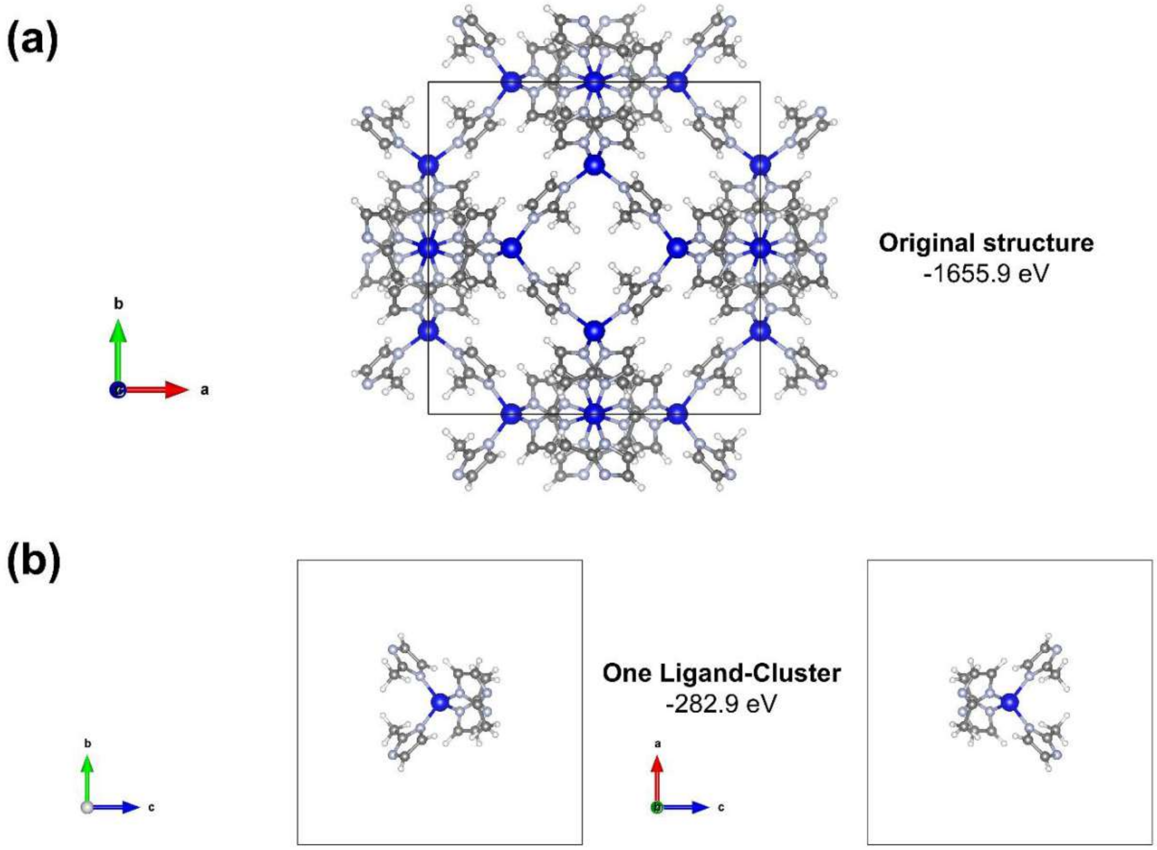

Figure S34. Schematic diagrams of the ZIF-8 original framework (a) and one Zn-$(IM)_4$ ligand-cluster structure (b). Dark blue for Zn, light blue for N, gray for C and white for H.

Table S3. Structural energy of ligand-cluster, ZIF-8 and LR-ZIFs obtained from the DFT calculation.

Number of ligand-clusters removal	**Atomic number: H, C, N, Zn**	**E_o [a] (eV)**	**E_f [b] (eV)**
Original (zero)[c]	120,96,48,12	-1740.1688	-
Remove one	100,80,40,11	-1445.4944	11.7447
Remove two	80,64,32,10	-1153.6422	8.9225
Remove four	40,32,16,8	-567.9773	19.8055
One ligand-cluster	20,16,8,1	-282.9297	-

[a] The initial energy of each system obtained after the DFT calculation.

[b] Formation energy calculated by:

Structural energy with ligand-cluster removed + ligand-cluster energy − structural energy without ligand-cluster removed.

For example, the formation energy of structure with two ligand-clusters removed is: structural energy with two ligand-cluster removed + ligand-cluster energy − structural energy with one ligand-cluster removed.

[c] Original ZIF-8 in the **Figure S34a**.

S6. Enhancing Dyes Adsorption

Evaluation of the adsorption experiment. From kinetic and isotherm curves of MB adsorption (**Figures S35** and **S36)**, it was clearly evident that pure ZIF-8 had essentially little capacity for MB adsorption, and with increase after mixing with the ligand NH_2-bIM. Thankfully, once the ligand was removed, the adsorption capacity of LR-ZIF-8 was considerably enhanced. After fitting all isotherms curves, it was shown that the R^2 values for ML-ZIFs were higher in the Langmuir model than the Freundlich model, indicating their favoring for monolayer adsorption (**Table S5**) [18]. In the kinetic fit, the R^2 values for the PSO model were higher than those for the PFO model, as explained in detail in the main manuscript (**Table S4**).

If the calcination time is 2h, the ranking of the adsorption capacity Q_m is calculated to be 10%NH_2-ZIF-2h > 30%NH_2-ZIF-2h > 50%NH_2-ZIF-2h > 5%NH_2-ZIF-2h > 2%NH_2-ZIF-2h > 70%NH_2-ZIF-2h. Among them, 10%NH_2-ZIF-2h showed the highest capacity (Q_m is 20.835 mg/g) for MB adsorption, 39 times that of pure ZIF-8 (0.531 mg/g) and 5.5 times that of the 10%ML-ZIF (3.874 mg/g), a significant improvement in adsorption capacity. When the mixed-ligand ratio is 10%, the ranking of the different calcination time was 10%NH_2-ZIF-2h > 10%NH_2-ZIF-0.5h > 10%NH_2-ZIF-5h > 10%NH_2-ZIF-20h > 10%NH_2-ZIF-0h. The calcination time beyond 5 hours causes irreversible effects on the NH_2-ZIF's framework, leading to the loss of active sites as a result of hierarchical pores damage/over-oxidation, ultimately led to a dramatic decrease in the 10%NH_2-ZIF-20h (3.931 mg/g). For the same reason, the adsorption capacity of 10%NH_2-ZIF-2h (Ar) was not sufficiently enhanced when heated at higher temperature (in 500°C, **Figure S37c**).

Adsorption of other organic dyes. To further evaluate the water purification of LR-ZIF-8, we conducted experiments with other organic dyes (**Figures S37a** and **S37b**). In the adsorption test for methyl orange, the Q_e of 10%NH_2-ZIF-2h was 19.053 mg/g, again a great increase in adsorption capacity compared to the 4.226 mg/g of 10%NH_2-ZIF-0h, approximately 5 times. Similarly, for Rhodamine B, the Q_e of 10%NH_2-ZIF-2h (23.955 mg/g) was significantly higher than that of 10%NH_2-ZIF-0h (14.584 mg/g).

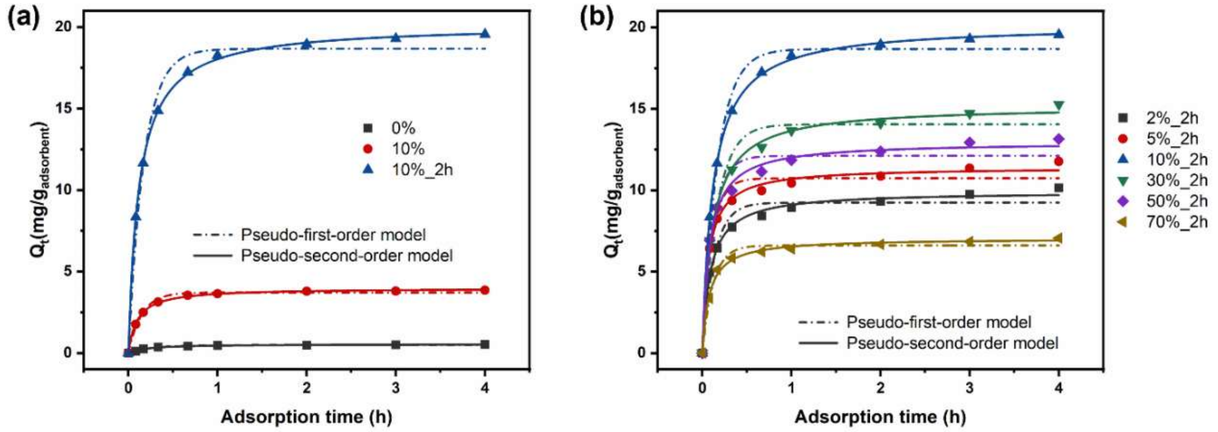

Figure S35. Kinetic curves of Methylene blue for 0%NH_2-ZIF (ZIF-8), 10%NH_2-ZIF and 10%NH_2-ZIF-2h (a), and various ratios of ligands 2-70% removal of R%NH_2-ZIF-2h (b). Kinetic curves are fixed by Pseudo-first-order and Pseudo-second-order models (**Equations S1-S4**).

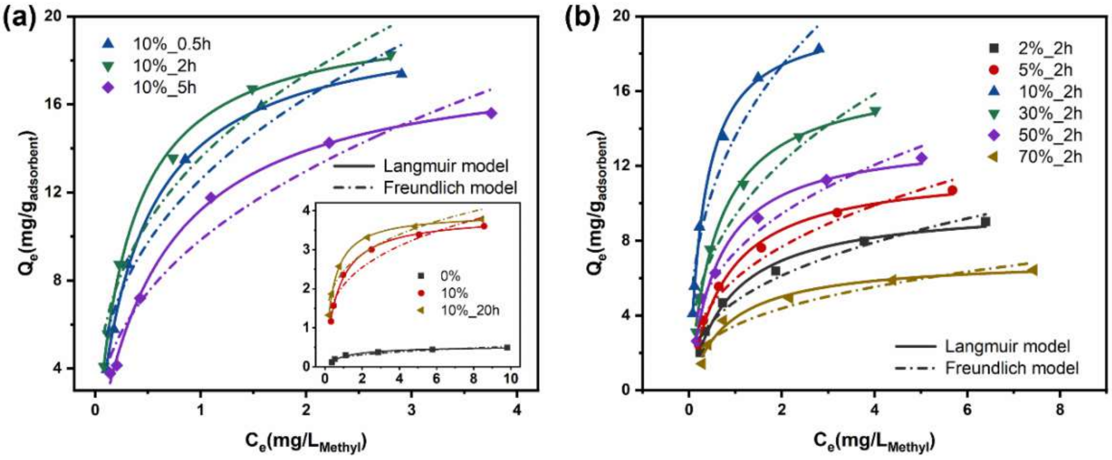

Figure S36. Isotherm curves of MB for 10%NH_2-ZIF-0.5h, 10%NH_2-ZIF-2h and 10%NH_2-ZIF-5h (a). 0%NH_2-ZIF (ZIF-8), 10%NH_2-ZIF-0h and 10%NH_2-ZIF-20h are shown in (a) inset. Various ratios of ligands 2-70% removal of R%NH_2-ZIF-2h (b). Isotherm curves are fixed by Langmuir and Freundlich models (**Equations S5** and **S6**).

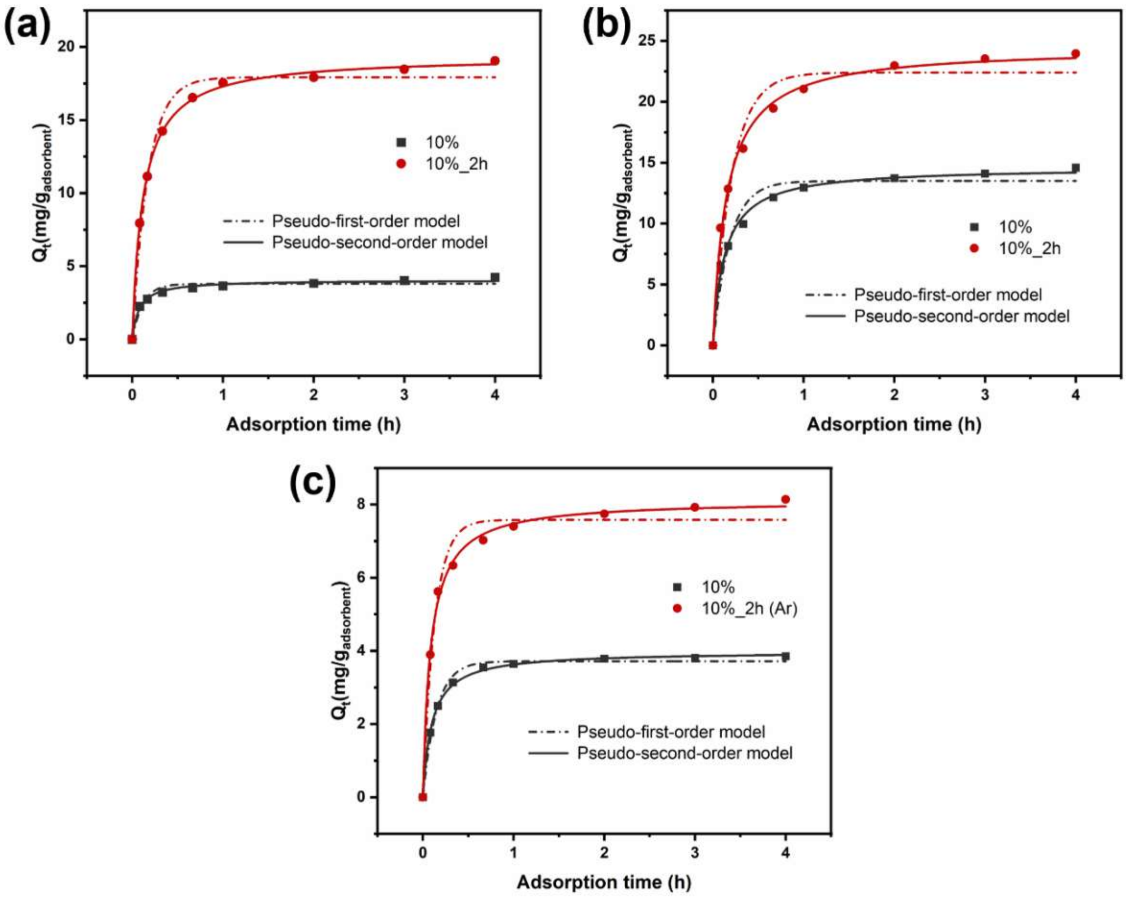

Figure S37. Kinetic curves of methyl orange (a) and rhodamine B (b) for 10%NH_2-ZIF and 10%NH_2-ZIF-2h, the latter being heated 290°C, 2 hours in air atmosphere. Kinetic curves of methylene blue (c) for 10%NH_2-ZIF and 10%NH_2-ZIF-2h (Ar), the latter being heated 500°C, 2 hours in an inert gas of Ar. Kinetic curves are fixed by Pseudo-first-order and Pseudo-second-order models (**Equations S1-S4**).

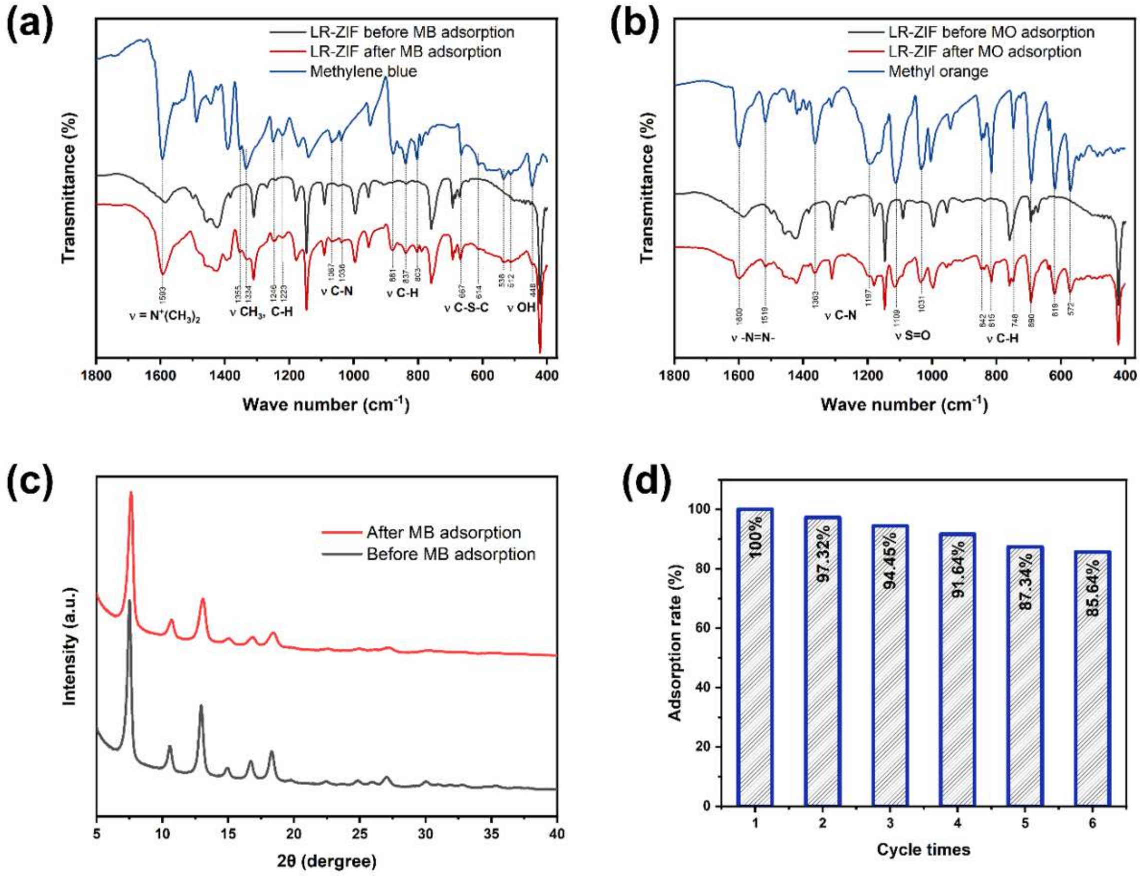

Figure S38. ATR-IR spectra of 10%NH_2-ZIF-2h before and after saturation of methylene blue (a) and methyl orange (b) adsorption. XRD patterns of 10%NH_2-ZIF-2h before and after saturation of methylene blue adsorption (c). Adsorption-desorption cycles with 10%NH_2-ZIF-2h (d), the adsorption of methylene blue reached saturation in each cycle. The slight decrease in adsorption rate after recovery is due to acid washing [19, 20].

Table S4. Kinetics parameters of ZIF-8, ML-ZIF-8 and LR-ZIF-8.

Adsorbents[a]	$Q_{e.exp}$ /mg g^{-1}	**Pseudo-first-order model**			**Pseudo-second-order model**		
		$Q_{e.cal}$ /mg g^{-1}	K_1 /h^{-1}	R^2	$Q_{e.cal}$ /mg g^{-1}	K_2 / g mg^{-1} h^{-1}	R^2
0%NH_2-ZIF (ZIF-8)	0.524	0.495	3.694	0.9867	0.551	8.678	0.9919
2%NH_2-ZIF-2h	10.146	9.238	7.473	0.9614	9.922	1.116	0.9942
5%NH_2-ZIF-2h	11.765	10.731	9.402	0.9643	11.413	1.293	0.9932
10%NH_2-ZIF-0h	3.856	3.716	6.717	0.9901	3.983	2.549	0.9985
10%NH_2-ZIF-2h	19.547	18.665	5.788	0.9831	20.166	0.418	0.9996
30%NH_2-ZIF-2h	15.263	14.046	6.132	0.9639	15.183	0.585	0.9958
50%NH_2-ZIF-2h	13.146	12.111	8.269	0.9551	12.962	0.964	0.9928
70%NH_2-ZIF-2h[a]	7.062	6.609	8.345	0.9837	7.048	1.819	0.9929
10%NH_2-ZIF-2h (Ar)	8.141	7.582	7.727	0.9729	8.124	1.424	0.9965
10%NH_2-ZIF-0h (MO[b])	4.226	3.795	8.536	0.9525	4.055	3.217	0.9897
10%NH_2-ZIF-2h (MO[b])	19.053	17.925	5.724	0.9819	13.385	0.428	0.9989
10%NH_2-ZIF-0h (RhB[c])	14.584	13.495	5.443	0.9541	14.635	0.538	0.9926
10%NH_2-ZIF-2h (RhB[c])	23.955	22.402	4.738	0.9601	24.483	0.271	0.9958

[a] In the air atmosphere range, 2-50% heated at 290°C and 70% heated at 260°C. In the Ar flow, 10%NH_2-ZIF heated to 500°C.

[b] Adsorption Kinetics of Methyl Orange in 20 mg L^{-1}.

[c] Adsorption Kinetics of Rhodamine B in 10 mg L^{-1}.

Table S5. Isotherm parameters of ZIF-8, ML-ZIF-8 and LR-ZIF-8.

Adsorbents[a]	**Langmuir model**			**Freundlich model**		
	$Q_{m.cal}$ /mg g^{-1}	K_L /L mg^{-1}	R^2	n	K_F / (mg g^{-1}) (mg L^{-1})$^{-n}$	R^2
0%NH_2-ZIF (ZIF-8)	0.531	0.965	0.9801	3.043	0.243	0.9158
2%NH_2-ZIF-2h	9.943	1.151	0.9872	2.717	4.753	0.9596
5%NH_2-ZIF-2h	11.905	1.274	0.9898	2.697	5.903	0.9613
10%NH_2-ZIF-0h	3.874	1.451	0.9961	3.546	2.093	0.9066
10%NH_2-ZIF-0.5h	20.673	2.398	0.9986	2.691	12.589	0.9264
10%NH_2-ZIF-2h	20.835	3.159	0.9969	2.828	13.582	0.9411
10%NH_2-ZIF-5h	18.315	1.573	0.9966	2.508	9.843	0.9448
10%NH_2-ZIF-20h	3.931	2.435	0.9993	4.291	2.454	0.8981
30%NH_2-ZIF-2h	17.001	1.691	0.9958	2.634	9.358	0.9466
50%NH_2-ZIF-2h	13.584	1.647	0.9763	2.834	7.391	0.9481
70%NH_2-ZIF-2h[a]	7.043	1.228	0.9781	2.967	3.467	0.9074

[a] In the air atmosphere range, 2-50% heated at 290°C and 70% heated at 260°C. In the Ar flow, 10%NH_2-ZIF heated to 500°C.

S7. Materials Synthesis and Experimental Section

ZIF-8 was synthesized directly by mixing the ligands 2-mIm and zinc nitrate ($Zn(NO_3)_2 \cdot 6H_2O$) at room temperature in methanolic solution, as previously reported [21]. 2 g of 2-methylimidazole was dissolved in 30 ml of HPLC methanol, while 0.87 g of zinc nitrate was dissolved in 20 ml of HPLC methanol. The two solutions were then mixed, sonicated for 10 minutes and continuously stirred for 2 hours to accelerate the growth of ZIF-8 crystals. After being allowed to deposit for 24 hours, the ZIF-8 powder was centrifuged, washed three times with methanol and DI water, and then dried in an oven overnight, resulting in a white ZIF-8 powder.

Mixed-ligand ZIF-8 (ML-ZIF-8 or R%NH_2-ZIF) was synthesized via a solvent-assisted ligand exchange (SALE) method. NH_2-bIm (0.04 g, 0.1 g, 0.2 g, 0.6 g, 1 g and 1.4 g) and 2-mIm (1.96 g, 1.9 g, 1.8 g, 1.4 g, 1 g and 0.6 g) were mixed into 30 ml HPLC methanol at various weight ratios (2%, 5%, 10%, 30%, 50% and 70%). The solution was sonicated for 10 minutes and stirred for 30 minutes to ensure even mixing and dissolution of the ligands. The following synthesis steps were the same as for the pure ZIF-8 synthesis, mixing the methanolic solution of the two ligands with zinc nitrate solution (0.87g $Zn(NO_3)_2 \cdot 6H_2O$; 20 ml HPLC methanol) and stirring for 2 hours. After 24 hours of deposition to allow the crystals formation, the resulting powder was centrifuged and washed three times with methanol and DI water to remove excess ligands. Finally, the obtained NH_2-ZIF powder (R%NH_2-ZIF, where R% indicates the mixing ratio of various NH_2-bIM) was dried overnight, resulting in a white powder.

Ligand-removed ZIF-8 (LR-ZIF-8 or R%NH_2-ZIF-*time*/*temp*), refers to the ZIF-8 samples obtained by thermolysis of ML-ZIF-8 at specific temperatures for specific time periods. The heating process was conducted using either a muffle furnace (LT 5/12 Nabertherm, Germany) in air atmosphere, ramp rate of 10°C/min. Or a tube furnace (HTM Reetz LK-1100, Germany) with argon/nitrogen flow at a ramp rate of 10°C/min. The final temperature was allowed to cool naturally to room temperature. For air atmosphere, the calcination temperature is 290°C for 0-50%NH_2-ZIFs and 260°C for 70%. For argon/nitrogen flow, the calcination temperature was 500°C for 30%NH_2-ZIF and 400°C for 70%NH_2-ZIF. The samples were labeled as R%NH_2-ZIF-*time*/*temp* (or R%-*time*/*temp*), where R% indicates the mixing ratio of various NH_2-bIM, *time* is the calcination time, and *temp* indicates the special calcination temperature.

Mixed-ligand ZIF-67. NH_2-bIM (0 g, 0.2 g, 0.4 g, 0.6 g, 0.8 g and 1 g) and 2-IM (2 g, 1.8 g, 1.6 g, 1.4 g, 1.2 g and 1 g) were mixed into 30 ml HPLC methanol at various weight ratios (0%, 10%, 20%, 30%, 40% and 50%). Using solvent-assisted ligand exchange (SALE), the synthesis was similar to that of ML-ZIF-8, except for the 0.87 g zinc nitrate ($Zn(NO_3)_2\cdot 6H_2O$) was replaced by 0.87 g cobalt nitrate ($Co(NO_3)_2\cdot 6H_2O$). Finally, Purple NH_2-ZIF67 powder (R%NH_2-ZIF67, R% indicates the mixing ratio of various 2-aminobenzimidazole) was obtained.

X-ray Diffraction (XRD). Used PANalytical X'Pert Pro multi-purpose diffractometer (MPD) with Bragg Brentano geometry with Cu anode at 45 kV, 40 mA, equipped with a BBHD Mirror and an X-Celerator multichannel detector. The diffraction patterns were tested at a 2θ angle of 5° and 90°. All measurements were performed with Cu sealed tube Kα and Kß radiation (2:1 ratio) with a wavelength of λ=1.54060 Å at a scan rate of 0.5° min^{-1}. Sample holder is a single crystal silicon on which the sample is immobilized by use of a drop of heptane, and rotated every 4 seconds during the test.

In-situ X-ray Diffraction (In-situ XRD). Same MPD system is used with the addition of the Anton Paar HTK 1200 temperature control system, with heating rate of 5°C/min. The sample was heated with a flow rate of 0.5 mL/min of air, argon and nitrogen.

Attenuated total reflection-Infrared spectroscopy (ATR-IR). Spectra obtained with Perkinelmer Spectrum two FT-IR spectrometer were in the infrared range of 400-4000 cm, with the $LiTaO_3$ (lithium tantalate) MIR detector. Control each data Force Gauge at around 120 with accumulation number of scans is 8 times.

X-ray photoelectron spectroscopy (XPS). Determination of the chemical states of the ALD-synthesized MOF-like material was accomplished by a custom designed XPS, provided by SPECS, using monochromatic AL-Kα (1486,6 eV) radiation and a hemispheric SCIENTA RS4000 photoelectron energy analyzer.

N_2 Physisorption. Measurements were conducted at temperature of 77 K, on a 3Flex instrument by Micromeritics. Before measuring, the samples were vacuum outgassed at 150°C for 3-12 hours. The apparent surface area was calculated by applying the Brunauer-Emmet-Teller (BET) equation, following the recommended procedure for microporous sorbents [22]. The relevant pore size distributions were determined from the adsorption branch of the isotherms using the kernel of nonlocal density functional theory (NLDFT).

Scanning electron microscope (SEM). Images were recorded on a FEI Quanta 250 (Schottky-)FEG-SEM, facilitated by USTEM (university service center for transmission electron microscopy) at TU Wien, equipped with an ETD Secondary electron detector and an EDAX-AMETEK Octane Elite 55 detector for elemental characterization by energy-dispersive X-ray-spectroscopy. The device was operated at a voltage of 10 kV at a working distance of about 5 mm, providing a maximum resolution of roughly 2 nm. Chemical X-ray microanalysis was performed at 20 kV and 10 mm working distance.

Transmission electron microscope (TEM). All HR-TEM measurements displayed in this paper were performed on a Tecnai F20 FEG-TEM, facilitated by USTEM (university service center for transmission electron microscopy) at TU Wien, equipped with a X-FEG, a Gatan Rio16 CCD-camera, Gatan DigiSTEM II with HAADF detector for STEM imaging, an EDAX-AMETEK Apollo XLTW SDD EDX-detector. The operating voltage was kept at 200 kV for all measurements, providing a maximum lattice resolution of approximately 0.14 nm.

Raman spectroscopy. Measurements were carried out using the WITec alpha 300 RSA$^+$, focusing on the range 1000-2800 cm^{-1}. Excitation laser wavelength is 532nm, the laser power is 0.1 mA (very low), the integration time is 1 second and the accumulation number is 10.

UV-Vis absorption spectroscopy and diffuse reflectance spectroscopy (UV-Vis and DRS). Supernatant concentrations of methylene blue after adsorption were obtained at 660-670nm by Jasco V-670. Measurements were carried out using the Jasco V-670 in diffuse reflectance mode with an Ulbricht-sphere. After centrifugation of the methylene blue solution, 1 ml×3 of supernatant was added to a cuvette in the UV-Vis incident light range of 200-800 nm for absorbance measurements and the results were averaged over 3 times for all tests. The concentration of the current MB solution was derived from the peak intensity at 667 nm, MO is 464 nm and RhB is 554 nm. In the powders DRS testing, $MgSO_4$ was used as a baseline, in the range of 200-800 nm. Scan speed is 200 nm/min, data interval is 1 nm for all measurements. All tests were conducted in triplicate, and only the average values are reported here.

Nuclear magnetic resonance spectroscopy (^{1}H NMR). Liquid phase ^{1}H spectra were measured using the Bruker ADVANCE 250 (250.13 MHz) instrument, which is equipped with a 5 mm inverse-broad probe head and z-gradient unit. To serve as an internal reference, Acetic Acid with a

$\delta = 1.96$ ppm was used. Due to the limited solubility of MOFs in typical NMR solvents, the sample weighing 2 mg was digested with 0.5 ml of d_4-acetic acid and then sonicated until it was well dispersed in the acid.

Thermogravimetric analysis (TGA). Measurements were carried out using PerkinElmer 8000 (Waltham, USA) with the sample heated in of Al_2O_3 crucible. The heating rate was 10°C/min, either in air, argon and nitrogen flow, and finally held at 600°C for 1 hour.

Density-functional theory (DFT). All of the calculations were performed by using Vienna ab initio program package (VASP) [23]. The exchange and correlation effects of the electrons were described by using the Perdew-Burke-Ernzerhof (PBE) [24] functional of a generalized gradient approximation (GGA) method [25]. The projector augmented wave (PAW) method was used to describe the electron-ion interaction. Spin polarization considered. The cutoff energy of the plane-wave was set as 400 eV. The (2×2×2) k-point mesh was used for k-space integration in our structure relaxations. Conjugate-gradient algorithm is used to relax the ions into their instantaneous ground state. The structure involved were fully relaxed with the energy and force convergences less than 1×10^{-7} eV and 0.03 eV $Å^{-1}$, respectively.

Adsorption kinetics. Prior to the adsorption experiments, all ZIF adsorbents were dried at 60°C overnight. For the adsorption experiments, 20 mg of adsorbent was added into 50 ml of 10 mg L^{-1} methylene blue solution (20 mg L^{-1} for Methyl orange and 10 mg L^{-1} for Rhodamine B) with deionized (DI) water, and stirred for a suitable period. At regular intervals (ranging from 5 minutes to 4 hours), 1 ml of methylene blue solution was taken out for centrifugation, and the absorbance of the supernatant was measured in the 400-800 nm range. The adsorption capacity of the adsorbent can be calculated by **Equation S1-S2**:

$$Q_t = \frac{(C_i - C_t) \times V}{M} \tag{S1}$$

$$Q_e = \frac{(C_i - C_e) \times V}{M} \tag{S2}$$

where Q_t (mg g^{-1}) is the adsorption capacity for time t. C_i and C_t are the initial and time t concentrations (mg L^{-1}) of MB solution, can be obtained by UV-vis testing the absorbance of the solution. Q_e and C_e is the adsorption capacity and concentrations for MB equilibrium. V, M represent the volume of the MB solution (L) and the weight of the ZIFs (g) respectively.

The resulting adsorption capacity curves for various time periods can be fitted by Pseudo-first-order (PFO) and Pseudo-second-order (PSO) kinetic models [26], as described by the following **Equation S3-S4**:

$$Q_t = Q_e(1 - e^{-K_1 t}) \tag{S3}$$

$$Q_t = \frac{K_2 Q_e^2 t}{1 + K_2 Q_e t} \tag{S4}$$

K_1 (min^{-1}) and K_2 ($\mathrm{g\ mg^{-1}\ min^{-1}}$) are the rate constant for the Pseudo-first-order and Pseudo-second-order model, respectively.

Adsorption isotherms. Prior to the adsorption experiments, all ZIF adsorbents were dried at 60°C overnight. 20 mg of adsorbent was added to the MB solution at various concentrations (1-10 mg $\mathrm{L^{-1}}$). After 2 hours of continuous stirring, the adsorbent was considered to be full saturated (as known by adsorption kinetics). Similarly, C_e and Q_e were calculated from the absorbance data obtained by UV-vis, and the adsorption isotherms were plotted. Langmuir and Freundlich isotherm models [27] were used to fit with the adsorption data at various MB concentrations. Langmuir model represents monolayer molecular adsorption on homogeneous surface and Freundlich model is used for multilayer adsorption on heterogeneous surfaces [18], as described by the following **Equation S4-S5**:

$$Q_e = \frac{Q_{max} K_L C_e}{1 + K_L C_e} \tag{S5}$$

$$Q_e = K_F {C_e}^{1/n} \tag{S6}$$

where Q_{max} ($\mathrm{mg\ g^{-1}}$) is the maximum adsorption capacity, K_L ($\mathrm{L\ mg^{-1}}$) and K_F ($\mathrm{mg\ g^{-1}}$) ($\mathrm{mg\ L^{-1}}$)$^{-n}$ are the Langmuir and Freundlich isotherm constants, respectively, related to the adsorption capacity and adsorbate-adsorbent interactions. n is the adsorption intensity, related to the energy distribution and heterogeneity of the adsorption sites [20].

Adsorption-desorption cycles. After the adsorption experiment, the MB solution was centrifuged to obtain the saturated adsorbed ZIF adsorbent. The adsorbent was then sonicated in HPLC methanol solution for 2 hours, followed by centrifugation and rinsing with 0.1 mol $\mathrm{L^{-1}}$ H_2SO_4 and DI water. This desorption process was repeated three times to obtain adsorbent that could be reused for subsequent adsorption experiments.

S8. References

[1] R. J. Sundberg, R. B. Martin, Chem. Rev. 1974, 74, 471.
[2] K. Eum, K. C. Jayachandrababu, F. Rashidi, K. Zhang, J. Leisen, S. Graham, R. P. Lively, R. R. Chance, D. S. Sholl, C. W. Jones, S. Nair, J. Am. Chem. Soc. 2015, 137, 4191.
[3] L. Feng, S. Yuan, L.-L. Zhang, K. Tan, J.-L. Li, A. Kirchon, L.-M. Liu, P. Zhang, Y. Han, Y. J. Chabal, H.-C. Zhou, J. Am. Chem. Soc. 2018, 140, 2363.
[4] J. B. James, Y. S. Lin, J. Phys. Chem. C 2016, 120, 14015.
[5] J. A. Thompson, J. T. Vaughn, N. A. Brunelli, W. J. Koros, C. W. Jones, S. Nair, Microporous Mesoporous Mater. 2014, 192, 43.
[6] A. Phan, C. J. Doonan, F. J. Uribe-Romo, C. B. Knobler, M. O'Keeffe, O. M. Yaghi, Acc. Chem. Res. 2010, 43, 58.
[7] C. Wu, D. Xie, Y. Mei, Z. Xiu, K. M. Poduska, D. Li, B. Xu, D. Sun, Phys. Chem. Chem. Phys. 2019, 21, 17571.
[8] Y. Zhang, N. Zhang, Y. Liu, Y. Chen, H. Huang, W. Wang, X. Xu, Y. Li, F. Fan, J. Ye, Z. Li, Z. Zou, Nat. Commun. 2022, 13, 2942.
[9] C. Schlumberger, M. Thommes, Adv. Mater. Interfaces 2021, 8, 2002181.
[10] D. Tuncel, A. N. Ökte, Catal. Today 2021, 361, 191.
[11] L. Oliviero, J. Barbier, D. Duprez, Appl. Catal., B 2003, 40, 163.
[12] H. Chen, K. Shen, Q. Mao, J. Chen, Y. Li, ACS Catalysis 2018, 8, 1417.
[13] W. Zhang, X. Jiang, Y. Zhao, A. Carné-Sánchez, V. Malgras, J. Kim, J. H. Kim, S. Wang, J. Liu, J.-S. Jiang, Y. Yamauchi, M. Hu, Chem. Sci. 2017, 8, 3538.
[14] Y. Pan, K. Sun, S. Liu, X. Cao, K. Wu, W.-C. Cheong, Z. Chen, Y. Wang, Y. Li, Y. Liu, D. Wang, Q. Peng, C. Chen, Y. Li, J. Am. Chem. Soc. 2018, 140, 2610.
[15] R. Jiang, T. Liu, R. Wu, C. Guo, Y. Chen, G. Xiang, L. Wang, ACS Appl. Mater. Interfaces 2020, 12, 7270.
[16] J. Tang, R. R. Salunkhe, J. Liu, N. L. Torad, M. Imura, S. Furukawa, Y. Yamauchi, J. Am. Chem. Soc. 2015, 137, 1572.
[17] A. Hu, X. Lu, D. Cai, H. Pan, R. Jing, Q. Xia, D. Zhou, Y. Xia, Molecular Catalysis 2019, 472, 27.
[18] R. Kaur, A. Kaur, A. Umar, W. A. Anderson, S. K. Kansal, Mater. Res. Bull. 2019, 109, 124.
[19] G. Wang, J. Zhang, S. Lin, H. Xiao, Q. Yang, S. Chen, B. Yan, Y. Gu, Cellulose 2020, 27, 2085.
[20] Y. R. Lee, X. H. Do, K. Y. Cho, K. Jeong, K.-Y. Baek, ACS Applied Nano Materials 2020, 3, 9852.
[21] Z. Huang, Q. Zhou, J. Wang, Y. Yu, J. Mater. Sci. Technol. 2022, 112, 68.
[22] F. O. Sánchez-Varretti, G. D. García, A. J. Ramirez-Pastor, F. Romá, J. Chem. Phys. 2009, 130, 194711.
[23] Kresse, Furthmuller, Phys. Rev. B: Condens. Matter 1996, 54, 11169.
[24] J. P. Perdew, A. Ruzsinszky, G. I. Csonka, O. A. Vydrov, G. E. Scuseria, L. A. Constantin, X. L. Zhou, K. Burke, Phys. Rev. Lett. 2008, 100, 4.
[25] J. P. Perdew, K. Burke, M. Ernzerhof, Phys. Rev. Lett. 1996, 77, 3865.
[26] J.-P. Simonin, Chem. Eng. J. 2016, 300, 254.
[27] K. Y. Foo, B. H. Hameed, Chem. Eng. J. 2010, 156, 2.

3.2.2 Article #2

"Engineering of HO–Zn–N_2 Active Sites in Zeolitic Imidazolate Frameworks for Enhanced (Photo)Electrocatalytic Hydrogen Evolution"

*Zheao Huang, Zhouzhou Wang, Qiancheng Zhou, Hannah Rabl, Shaghayegh Naghdi, Ze Yang *, and Dominik Eder **

Angewandte Chemie International Edition, 2024, e202419913

DOI: https://doi.org/10.1002/anie.202419913

As the first author of these articles, I led the entire research process, provided the original idea, conducted most of the testing, and wrote the manuscript. The corresponding Supplement Information can be found on pages 108-135.

Reprinted with permission from *Angewandte Chemie* [117].

GDCh
Research Article
Angewandte Chemie International Edition
www.angewandte.org

How to cite: Angew. Chem. Int. Ed. **2025**, e202419913
doi.org/10.1002/anie.202419913

ZIF Electrocatalysts **Hot Paper**

Engineering of HO–Zn–N_2 Active Sites in Zeolitic Imidazolate Frameworks for Enhanced (Photo)Electrocatalytic Hydrogen Evolution

Zheao Huang, Zhouzhou Wang, Qiancheng Zhou, Hannah Rabl, Shaghayegh Naghdi, Ze Yang, and Dominik Eder**

Abstract: Currently, lack of ways to engineer specific and well-defined active sites in zeolitic imidazolate frameworks (ZIFs) limits our fundamental knowledge with respect to the mechanistic details for (photo)electrocatalytic hydrogen evolution reaction (HER). Here, we introduce the open metal sites into ZIFs through the selective ligand removal (SeLiRe) strategy, comprehensively characterize the altered structural and electronic features, and evaluate their role in HER. In situ electrochemical analysis and X-ray absorption spectroscopy reveal the formation of high-valence HO–Zn–N_2 sites through the binding of Zn–N_2 with electrolyte hydroxide. The optimal OMS-ZIF exhibits a low overpotential of 0.41 V to achieve an ampere-level 1.0 A cm^{-2} with 120-hour stability. Theoretical simulations indicate that these active sites accelerate the water molecules activation kinetics, consequently enhancing the efficiency of the Volmer step. This work demonstrates a versatile strategy to introduce highly active catalytic sites in ZIFs, providing new insights into the electrocatalytic mechanism in alkaline media.

Introduction

Efficient electrochemical water splitting for high-purity hydrogen evolution reaction (HER) is crucial for the utilization and storage of sustainable energy.[1] Currently, alkaline media are commonly used as HER electrolytes, due to their low-cost, industrial feasibility and compatibility with the oxygen evolution reaction (OER).[2] However, compared to acidic or neutral environments, alkaline media present two major challenges for HER catalysts, including: (1) more complex and sluggish kinetics, and (2) difficulty in identifying the main active site and understanding the HER mechanism.[3] Regarding the first challenge, the alkaline HER typically follows the Volmer–Heyrovsky mechanism, where the initial sluggish Volmer step involves the adsorption and dissociation of water molecules ($H_2O+e^-=H^*+OH^-$), hindering the development of efficient HER catalysts.[4] The second challenge arises from the complexity of most studied catalysts, which are prone to structural reconstruction in alkaline media, complicating the atomic-level engineering of active-site structure. Thus, an easily engineered catalytic site with a well-defined, concise and uniform structure, is needed for thorough mechanistic investigation.

Zeolitic imidazolate frameworks (ZIFs) are promising candidates, which are a special sub-class of metal–organic frameworks (MOFs) constructed from metal ions (e.g., Zn, Co) bridged by four imidazolate ligands in a tetrahedral geometry.[5] The periodically arranged nanoscale ZIFs possess rich metal active sites, which not only benefit the catalytic activity but also provide strong operando spectroscopic signals, offering an inherent advantage for both performance regulation and mechanism elucidation.[6] However, most ZIF catalysis only with saturated coordination metal sites, hindering the engineering of accessible active sites for electrocatalytic HER kinetics in alkaline media.[7] In our previous report, we employed a highly selective ligand removal technique (SeLiRe strategy) on mixed-ligand ZIF-8 (ML-ZIFs), constructing a series of uniform open metal sites ZIFs (OMS-ZIFs).[8] The ligand removal process, specifically targeting 2-aminobenzimidazole (NH_2-bIm), was meticulously monitored through a combination of in situ and ex situ techniques, supported by theoretical simulations. A significant advantage of this strategy is the formation of unsaturated Zn–N_2 sites, serving as well-defined atomic-level metal sites, facilitating the unraveling of the complex alkaline HER mechanism. Another is the preservation of the inherent ZIFs framework while creating localized open metal sites, thereby which is advantageous over the MOF-base single-metal atom nitrogen-doped carbon (NC) obtained by the high-temperature annealing strategy.[9]

---

[*] Z. Huang, H. Rabl, Dr. S. Naghdi, Prof. D. Eder
Institute of Materials Chemistry
Technische Universität Wien
1060, Vienna, Austria
E-mail: dominik.eder@tuwien.ac.at

Z. Wang, Q. Zhou, Dr. Z. Yang
Institute of Nanoscience and Nanotechnology, College of Physical Science and Technology
Central China Normal University
430079, Wuhan, China
E-mail: yz@ccnu.edu.cn

Herein, we utilize well-defined OMS-ZIF engineered via the SeLiRe strategy and identify their contribution to the HER mechanism. Through in situ electrochemical Raman spectra and complementary techniques such as synchrotron radiation-based X-ray absorption (XAS), attenuated total reflection-infrared (ATR-IR) and X-ray photoelectron spectroscopy (XPS), we validate that the Zn–N_2 sites preferentially chemisorb electrolyte hydroxide, subsequently forming the HO–Zn–N_2 sites. Density functional theory (DFT) simulations further confirm that the high-valence HO–Zn–N_2 active sites facilitate the water activation kinetics, and thereby promoting the overall HER process.

Results and Discussion

The structural model optimized by density-functional theory (DFT) calculations is depicted in Figures 1a and S1, illustrating the framework structure of 2-methylimidazole (2-mIm) with open Zn sites was constructed by removing two ligands, named by OMS-ZIF. When the two linked 2-aminobenzimidazole (NH_2-bIm) are removed, the Zn coordination number with N partially decreases from 4 to 2, resulting in the OMS-ZIF featuring the localized unsaturated Zn–N_2 sites while maintaining the overall framework integrity (Figure 1b). The simultaneous generation of new electronic states near the Fermi energy level in the density of states (DOS), attributable to changes in the electronic structure of Zn and N, suggesting that OMS-ZIF has a more conductive electronic structure compared to ZIF-8 (Figure 1c). Two-dimensional electron localization function (ELF) analysis indicates that the electron localization at the Zn–N_2 sites in OMS-ZIF is higher compared to ZIF-8 without open metal sites, with an increased electron density around the missing-ligands position (Figure 1d). These calculations predict that the OMS-ZIF catalysis, with the localized well-defined Zn–N_2 sites, possesses an electronic structure beneficial for electrocatalytic HER.

Synchrotron radiation-based X-ray absorption spectroscopy (XAS), which is highly sensitive to both electronic and geometric structures, was adopted to identify the structure evolution of open Zn sites at applied potentials. Figure 2a shows the Zn K-edge X-ray absorption near-edge structure (XANES) spectra of pristine ZIF-8, OMS-ZIF under open-circuit potential (OCP) and −0.5 V applied potential, respectively, along with the data for Zn foil and ZnO as references. Upon −0.5 V potential, the absorption edge of OMS-ZIF shifts slightly to higher energy, approaching the ZnO edge. This shift indicates a tendency for the oxidation state of Zn cations at the open metal sites to increase to a higher valence state during the electrochemical environment.[6a,10]

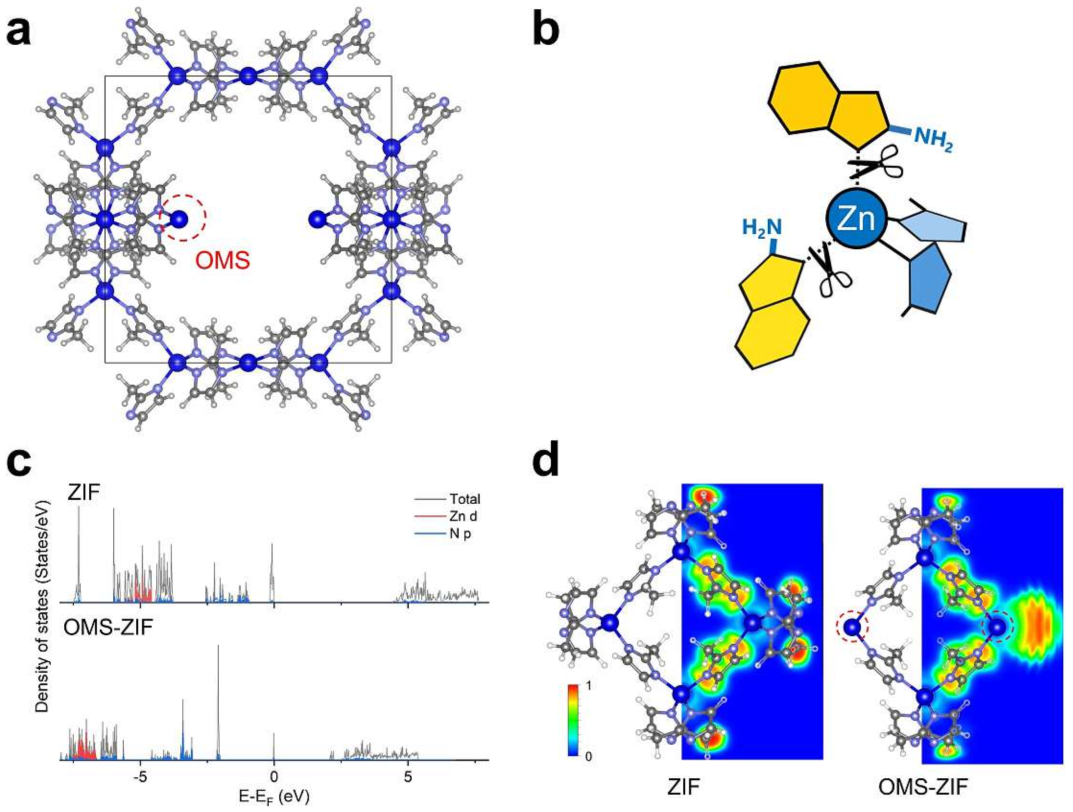

Figure 1. **a**, Optimized model structures of OMS-ZIF with two ligands removed. **b**, Selective ligand removal strategy for NH_2-bIm in ML-ZIF. **c**, **d**, Calculated density of states (**c**) and electron localization function (**d**) of ZIF-8 and OMS-ZIF. Dark blue for Zn, light blue for N, gray for C and white for H.

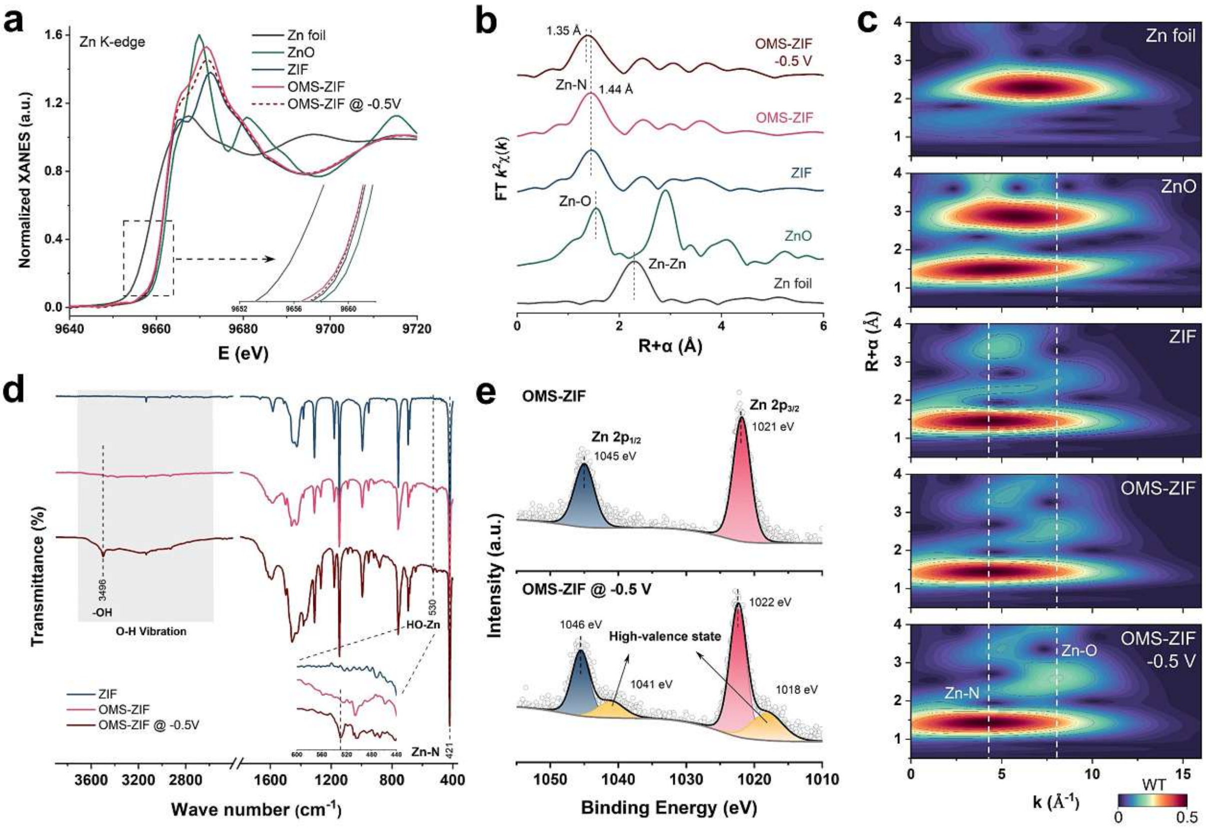

Figure 2. **a**, **b**, Zn K-edge XANES (**a**) and EXAFS Fourier transform (FT) spectra (**b**) of ZIF-8, OMS-ZIF and OMS-ZIF at −0.5 V applied potential, and the data of the reference standards of Zn foil and ZnO. **c**, Comparison of Zn K-edge EXAFS WTs recorded for the reference standards, ZIF-8, OMS-ZIF and OMS-ZIF at −0.5 V applied potential. The intensity maxima in R and K spaces reflecting the coordination number of Zn atoms, WT stands for wavelet transform. **d**, **e**, ATR-IR (**d**) and Zn 2p of XPS (**e**) of OMS-ZIF and OMS-ZIF at −0.5 V applied potential.

As shown in the Fourier-transformed k^2-weighted extended X-ray absorption fine structure (EXAFS) spectra of pristine ZIF-8 and OMS-ZIF in Figure 2b, there is only one main signal observed at 1.44 Å, assigned to the Zn–N coordination. Upon −0.5 V potential, the main signal in OMS-ZIF exhibits an obvious low-R shift from 1.44 Å to 1.35 Å, suggesting a variation in the coordination environment of the Zn site. Meanwhile, the oscillation frequency of the EXAFS $k^2\chi(k)$ function for OMS-ZIF under the applied potential differs from the open-circuit potential (Figure S2). This indicates not only a change in the oxidation state of metal moieties, but also suggests a rearrangement of their localized atomic structure.[3a]

Further analysis of wavelet transform (WT, Figure 2c) indicates that the maximum intensity near 4.8 Å^{-1} for both ZIF-8 and OMS-ZIF can be assigned to the Zn–N coordination. Upon −0.5 V potential, a pronounced intensity increase can be observed at 7.7 Å^{-1} (represented by a dashed line), well matching the location of Zn–O scattering and resembles the ZnO reference. These findings reveal the possibility of incorporated oxygen species as localized coordinators, without disrupting the imidazole-based ZIF structure mainly by Zn–N coordination.

Based on the above analysis, the two Zn–N/Zn–O backscattering pathways considered were quantitatively evaluated through a least-squares EXAFS fitting analysis for the first Zn coordination shell (Figure S3 and Table S1). The fitted structural parameters indicate that the average valence state of the Zn–N in pristine ZIF-8 is about +3.9, closely aligning with the theoretical coordination number of 4 in sodalite-type ZIFs.[11] In contrast, the valence state in OMS-ZIF (OCP) decreases to around +2.6, and its XANES absorption edges closely matches the theoretical spectrum of the Zn–N_2 model,[12] confirming the presence of the localized Zn–N_2 sites formed by the SeLiRe strategy (as depicted in Figure 1a). For OMS-ZIF at −0.5 V, the most reasonable fitting consists of two-fold Zn–N coordination (+2.5) combined with additional Zn–O coordination (+1.0). This indicates that oxygen species from the KOH electrolyte may have been chemisorbed with Zn–N_2 sites, as evidenced by the reduced average bond length in OMS-ZIF.

To better validate the active sites formed by Zn–N_2/ZIF and oxygen species, we further conducted the Attenuated total reflection infrared (ATR-IR) and X-ray photoelectron spectroscopy (XPS) for surface characterization. In the IR spectra shown in Figures 2d and S4, the peak observed at 3496 cm^{-1} in OMS-ZIF at −0.5 V is mainly ascribed to the stretching vibration of the O–H bond. Concurrently, a distinct vibrational peak at 530 cm^{-1} was identified, indicative the presence of HO–Zn bond, formed by the chemisorbed of –OH group onto the Zn site.[13] This peak is notably absent in plain ZIF-8@−0.5 V in the same electrochemical environment, where Zn coordination is fully saturated, underscoring that –OH chemisorption occurs exclusively in post-SeLiRe OMS-ZIF.

The intrinsic Zn–N stretching peak (421 cm^{-1}) of OMS-ZIF at −0.5 V in IR spectra, representing the metal-ligand connectivity, remained intact, highlighting the preservation of the inherent framework structure. This stands in contrast to many reported MOF-base nitrogen-doped carbon materials, which often lose their MOF framework during high-temperature annealing in order to achieve a single-metal atom sites.[9,14] Furthermore, the appearance of the higher-valence state signals (highlighted in yellow, at 1018 and 1041 eV) and the shift of the intrinsic Zn 2p peaks towards higher energy in the XPS fitting, provide additional evidence of chemisorption between oxygen species and unsaturated Zn–N$_2$ sites in OMS-ZIF at −0.5 V potential (Figure 2e).

Advanced in situ electrochemical Raman spectroscopy was employed to further investigate the relationship between the Zn–N$_2$ and OH radicals during alkaline electrocatalysis (Figure 3). The characteristic peak at 285 cm^{-1} corresponds to the Zn–N between the inherent metal and ligands in sodalite-type ZIFs.[15] From −0.1 to −0.5 V, the Zn–N signal in OMS-ZIF shows no significant variation, indicating that the inherent ZIF framework remains unaffected by the applied potential. Meanwhile, new signals at 364 and 379 cm^{-1} appear, corresponding to the HO–Zn bonds formed between open Zn sites and OH^{-}, while the 721 cm^{-1} signal corresponds to free OH radicals.[16] After −0.3 V potential, OMS-ZIF begins to exhibit strong HO–Zn and OH radicals signals, which do not recover as the potential rises from −0.5 V to −0.1 V, indicating an irreversible transition to a higher-valence oxidation state. The resulting active sites, besides two inherent Zn–N coordinations, also include one –OH group chemically bonded to the Zn–N$_2$, forming the high-valence unsaturated HO–Zn–N$_2$ moiety (Figure 5a), consistent with the conclusions drawn from the XAS and IR spectra. Conversely, although ZIF-8 may also be affected by OH radicals in the same electrochemical environment, its already saturated Zn coordination does not show noticeable HO–Zn signals.

Overall, it can be inferred that unsaturated Zn–N$_2$ sites engineered by SeLiRe strategy to chemisorb –OH group driven by the applied potential in alkaline KOH environment, thereby in situ forming the high-valence HO–Zn–N$_2$ sites in the ZIF framework.

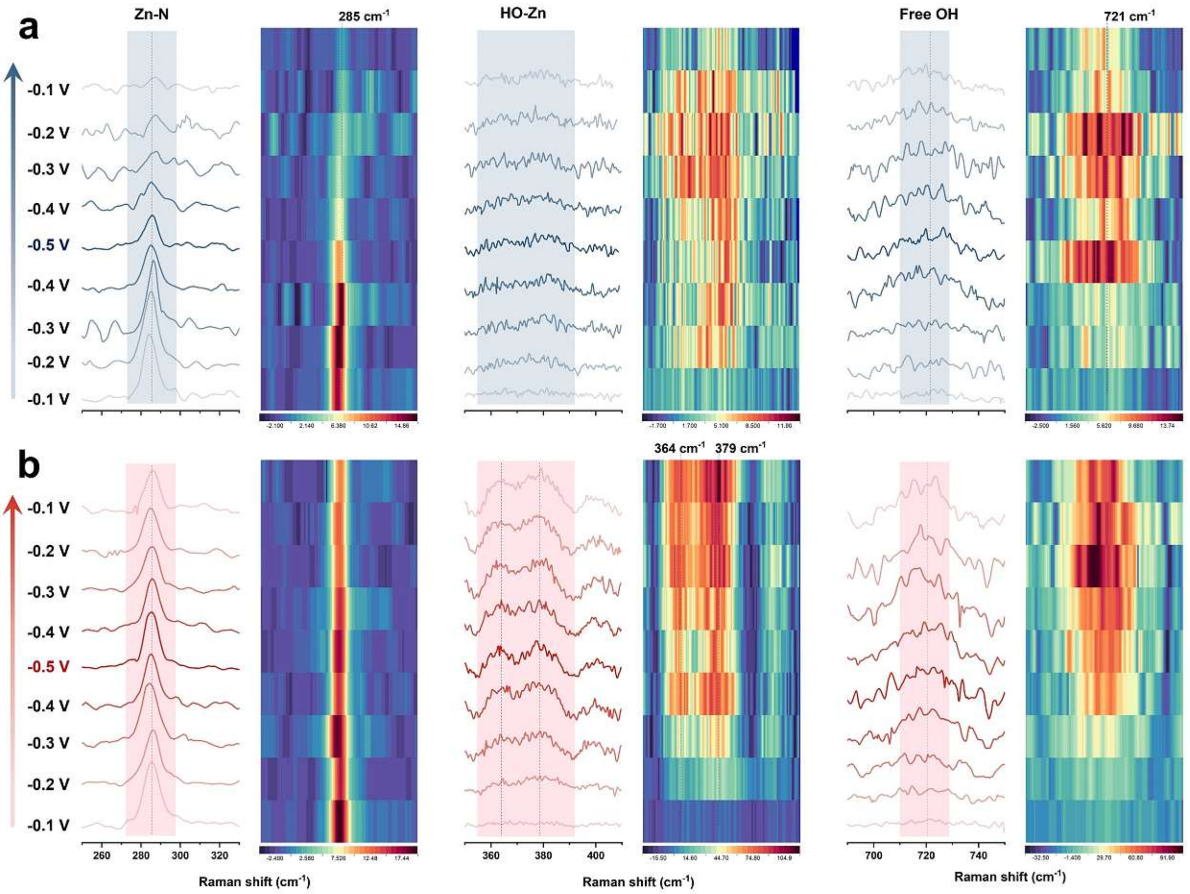

Figure 3. **a**, **b**, In situ electrochemical Raman study of ZIF-8 (**a**) and OMS-ZIF (**b**) at the applied potentials from −0.1 to −0.5 V and −0.5 to −0.1 V.

Generally, the above validated HO–Zn–N_2 sites belonging to high-valence transition-metal oxides species (TMOs) have higher catalytic activity, effectively enhancing the efficiency in the Volmer step during alkaline HER.[3a,17] Therefore, we evaluated the electrocatalytic HER performance using ZIFs sample grown on nickel foam (NF) as working electrodes, with the reversible hydrogen electrode (RHE) serving as the potential reference, and N_2-saturated 1 M KOH as the electrolyte. As shown in Figure 4a, the current densities of NF, ZIF-8, and OMS-ZIF were assessed via linear scanning voltammetry (LSV) under consistent conditions. The OMS-ZIF created through in situ formation of high-valence HO–Zn–N_2 localized sites exhibit higher current densities compared to the parent ZIF-8, achieving 0.01, 0.1 and 1 $A\,cm^{-2}$ at low overpotentials of 0.07, 0.19 and 0.41 V, respectively (Figure 4b), consistent with the predictions from DFT simulations. This is substantially lower than the overpotentials required for pristine ZIF-8 (0.31 V bei 10 $mA\,cm^{-2}$) and other OMS-ZIFs with variation NH_2-bIm removal ratios (Figure S5, as details in Supplementary Note 1). Furthermore, the OMS-ZIF requires an overpotential of only 0.67 V to achieve higher ampere-level current density of 4 $A\,cm^{-2}$ (Figure S6a).

In the evaluation of the Tafel slope (Figure 4c), the OMS-ZIF demonstrates the lowest slope of 45.71 $mV\,dec^{-1}$ compared to ZIF-8 (170.92 $mV\,dec^{-1}$), indicating superior kinetic characteristics for HER catalysis.[4a] Since the electrochemically active surface area (ECSA) is directly proportional to the electrochemical double-layer capacitance (C_{dl}), it was estimated based on the non-Faradaic region of the cyclic voltammetry (CV) curves at different scan rates (20 to 100 $mV\,s^{-1}$; see Figure S7). As shown in Figure 4d, OMS-ZIF exhibits a higher ECSA ($C_{dl} = 12.24\ mF\,cm^{-2}$) compared to ZIF-8 ($C_{dl} = 1.83\ mF\,cm^{-2}$). The ECSA-normalized LSV curves for OMS-ZIF still demonstrate a lower overpotential compared to ZIF-8 (Figure S6b). This indicates that, aside

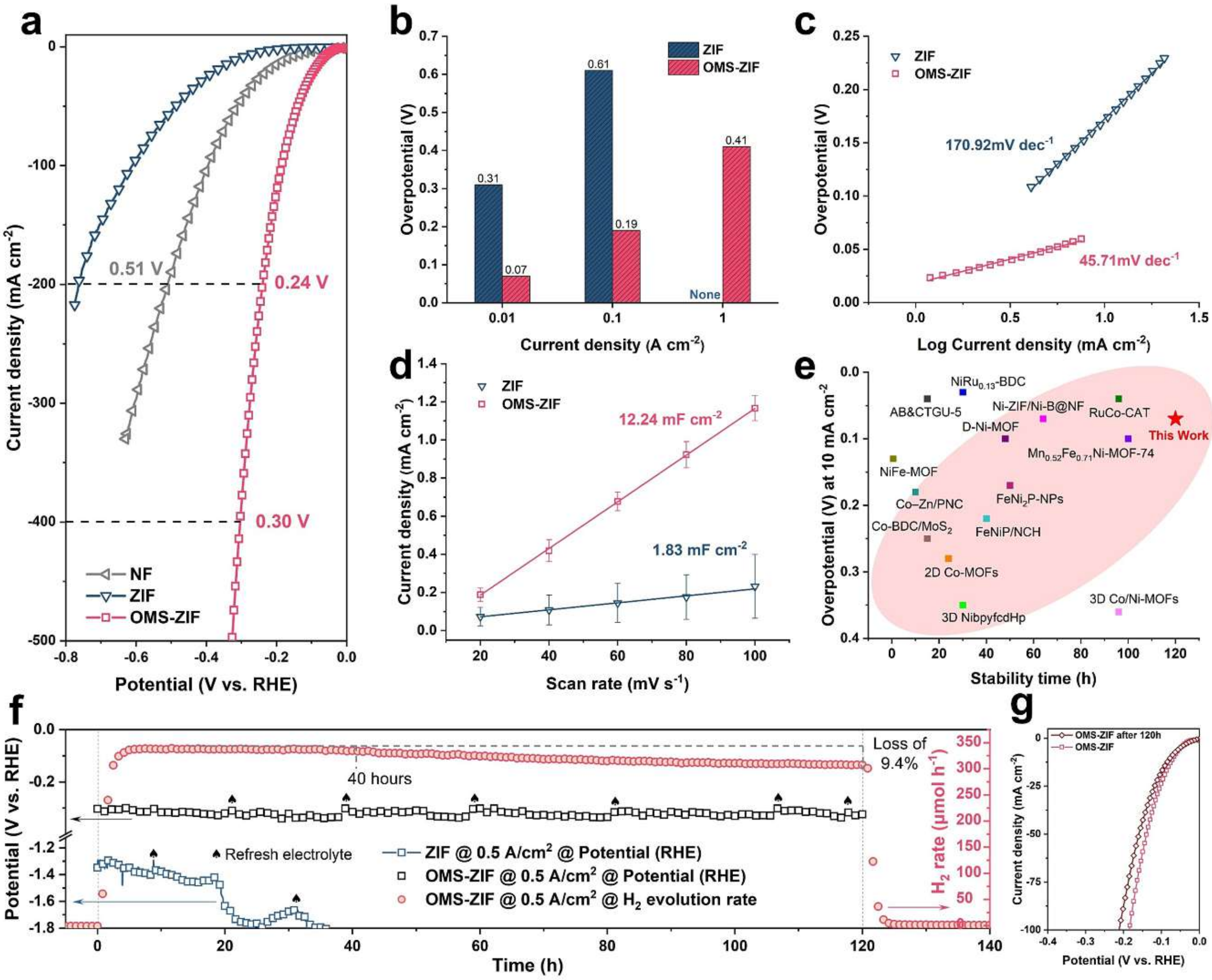

Figure 4. **a**, LSV curves toward HER of nickel foam, ZIF-8 and OMS-ZIF. **b**, Overpotentials at 0.01, 0.1 and 1 $A\,cm^{-2}$ of ZIF-8 and OMS-ZIF. **c**, **d**, Tafel slopes (**c**) and capacitive currents (**d**) of ZIF-8 and OMS-ZIF. Capacitive currents data are from Figure S6, error bars correspond to the standard deviation of the three C_{dl} measurements. **e**, Diagram comparing of overpotential and stability of OMS-ZIF with other reported MOF-base catalysts, more details in Table S2. **f**, Potentiometric curve and H_2 evolution rate of ZIF-8 and OMS-ZIF for 120 hours. **g**, LSV curves of OMS-ZIF before and after the 120-hour potentiometric test.

from the effect of the number of active sites, the HO–Zn–N_2 site possesses higher intrinsic activity. Additionally, owing to the partial removal of organic ligands, electrochemical impedance spectroscopy (EIS; see Figure S8) and electrical conductivity test reveal that OMS-ZIF has lower resistance, with a higher conductivity ($18.9 \pm 1.2\ \mu S\,m^{-1}$) compared to ZIF-8 ($11.4 \pm 0.7\ \mu S\,m^{-1}$). This increase in electrical conductivity further contributes to the enhancement in HER performance.

Electrocatalytic performance stability of samples was evaluated using a 120-hour potentiometric test (Figure 4f). We integrated an in situ H_2 gas flow detection system into the cell during the potentiometric test, allowing real-time monitoring of changes in potential and H_2 evolution rate. Sample OMS-ZIF exhibits a stable potential for a long period of 120 hours at $0.5\ A\,cm^{-2}$ with a negligible loss in H_2 evolution rate (9.4 %). In contrast, the HER performance of pristine ZIF-8 decreased rapidly. Comparing the LSV curves before and after 120-hour measurement, OMS-ZIF shows only slight degradation, indicating its high electrochemical stability (Figure 4g).

After the 120-hour potentiometric test, the OMS-ZIF retains the Bragg peaks characteristic of sodalite-type ZIF in XRD patten, with no obvious decrease in crystallinity (Figure S9a). Similarly, in XPS analysis, the signal of high oxidation state of Zn atom in the HO–Zn–N_2 sites was preserved (Figure S9b). During the previous applied potential tests, the Zn–N intensity in the IR and Raman signals of OMS-ZIF remains relatively unchanged, whereas it decreased dramatically to nearly disappear for ZIF-8 (Figures 3 and S4). This implies that OMS-ZIF maintains its inherent framework structure and high-valence HO–Zn–N_2 sites during long-term reactions at a certain potential.

In conclusion, the SeLiRe strategy can serve as a universal approach for engineering open metal sites and enhancing the HER performance in ZIFs. Sample OMS-ZIF with high-valence HO–Zn–N_2 active sites demonstrates the great electrocatalytic activity and stability, against previous reported MOF-base HER electrocatalysts (Figure 4e and Table S2).

In situ electrochemical UV/Vis absorption spectroscopy and photoluminescence (PL) spectroscopy were utilized to investigate the photoelectronic properties during the 5-hour amperometry. Pristine ZIF-8 exhibits an inherent ultraviolet absorption peak at 218 nm (Figure S10a). OMS-ZIF, on the other hand, exhibits the absorption peak in the visible light range, indicating its potential for visible-light-driven catalysis (Figure S10b). As the reaction progresses under −0.3 V amperometry, the absorption peak of ZIF-8 decreases rapidly, while OMS-ZIF exhibits only negligible changes. In situ electrochemical PL analysis further confirms the electrochemical stability of OMS-ZIF. The intrinsic PL peak of OMS-ZIF at 433 nm shows no significant shifts or weakening for up to 5 hours (Figure S11). This stability underscores the robustness of the OMS-ZIF structure and its suitability for extended electrochemical operations.

Based on the visible-light absorption capability observed in OMS-ZIF, which contrasts with the solely UV-light absorption of pristine ZIF-8 and ML-ZIFs, the visible-light photoelectrocatalysis offers a promising approach to enhancing real-world application involving HER. Moreover, the imposition of an applied potential serves as an effective strategy to prevent the recombination of photogenerated electron-hole (e^-/h) pairs.[18] Therefore, we investigated the visible-light HER performance of OMS-ZIF on fluorine-doped tin oxide (FTO) glass.

As shown in Figure S12, the current density and H_2 evolution rate of OMS-ZIF under visible light was evaluated using amperometry at −0.3 V applied potential. Visible light illumination led to a rapid increase in both current density and H_2 evolution rate, reaching about 1.5 times higher levels. Even after continuous operation for 10 hours, the HER performance of OMS-ZIF remains stable. In contrast, ML-ZIF (the precursor of OMS-ZIF) shows no activity enhancement under visible light, as it only absorbs ultraviolet light (Figure S13). This indicates that the SeLiRe strategy can extend the light absorption range of OMS-ZIF to the visible-light region, thereby imparting them with specific photoelectrocatalytic properties.

The aforementioned analysis provides clear evidence that the formation of unsaturated Zn–N_2 sites in OMS-ZIF catalysts is linked to an increase in valence state via chemisorption of –OH group under alkaline electrocatalysis, without compromising the intrinsic framework structure of sodalite-type ZIFs (Figures 5a and S14). Compared to the saturated Zn–N_4 in the ZIF-8 and ML-ZIF, the engineering of highly reactive TMOs HO–Zn–N_2 active sites in OMS-ZIF is the main reason for the enhancement of alkaline HER performance by an order of magnitude.

To elucidate the reaction mechanism, we conducted theoretical investigations of HO–Zn–N_2 active sites based on DFT calculations, complementing the results of (photo)electrocatalytic experiments. In the alkaline HER

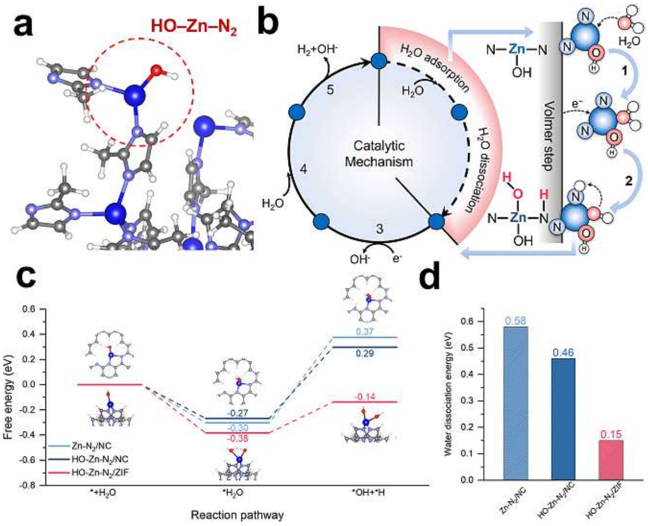

Figure 5. **a**, Optimized HO–Zn–N_2 active sites in OMS-ZIF model. **b**, Electrocatalytic HER mechanism of OMS-ZIF in alkaline aqueous solution. **c**, **d**, Calculated free energy (**c**) and water dissociation energy (**d**) of Zn–N_2/NC, HO–Zn–N_2/NC and HO–Zn–N_2/ZIF on the alkaline HER mechanism. Dark blue for Zn, light blue for N, red for O, gray for C and white for H.

mechanism, the unsaturated HO–Zn–N_2 serve as adsorption sites for H_2O molecules (step 1). This is followed by their dissociation into OH* and H* in step 2 (Figure 5b). In subsequent steps, OH* detaches from the Zn site, while H* remains on the ligand N reacts with a proton from other H_2O molecules to generate H_2. Since the sluggish Volmer step currently limits the HER efficiency of the current catalysts,[3a,4a] our focus is on the kinetics of H_2O molecule adsorption and dissociation in the first two steps. Figure 5c illustrates the Gibbs free energies for the OMS-ZIF model with HO–Zn–N_2 as the real active sites, using a nitrogen-doped carbon (NC) with single-atom Zn sites for comparison (Figures S15–17). The HO–Zn–N_2/ZIF model has a Zn–N bond length of 1.928 Å, and a Zn–O bond length of 2.058 Å, which are close aligned with the XAS experimental results (Table S1, Zn–N is 1.88 ± 0.01 Å and Zn–O is 2.02 ± 0.01 Å). This corroborates the structural accuracy of the model. In Step 1, the free energy change of H_2O adsorption on HO–Zn–N_2/ZIF is −0.38 eV, more negative than that of Zn–N_2/NC (−0.30 eV) and HO–Zn–N_2/NC (−0.27 eV), indicating a more favorable H_2O adsorption. The energy barrier for H_2O dissociation (Step 2) on HO–Zn–N_2/ZIF is 0.24 eV, is also significantly lower than the 0.67 eV and 0.56 eV required for Zn–N_2/NC and HO–Zn–N_2/NC, respectively. Similarly, when comparing the H_2O dissociation energy alone, the 0.15 eV for HO–Zn–N_2/ZIF is also lower than the 0.58 eV and 0.46 eV for Zn–N_2/NC and HO–Zn–N_2/NC (Figure 5d). These findings collectively indicate that, the OMS-ZIF model with the HO–Zn–N_2 sites theoretically facilitates the H_2O dissociation into OH* and H*, more readily compared to traditional single-atom NC materials. Notably, the saturated Zn sites in ZIF-8 require a significant formation energy to remove or exchange ligands (8.92 eV for two ligands), which is nearly impossible to achieve during the HER process.[8] From these theoretical calculations, it can be concluded that the unsaturated HO–Zn–N_2 sites theoretically accelerate the activation kinetics of H_2O molecules, thereby enhancing the efficiency of the Volmer step and the overall HER performance of OMS-ZIF.

Conclusions

Highly selective ligand removal (SeLiRe) strategy has evolved as a promising route to introduce open metal sites (OMS) as real active sites into ZIFs without altering the inherent framework structure. By altering the Zn coordination number from saturated Zn–N_4 to unsaturated Zn–N_2, we engineered the open zinc sites using the SeLiRe strategy. Then structural and electronic features of the OMS-ZIF were analyzed through a range of state-of-the-art in situ and ex situ techniques along with theoretical calculations. Under actual process conditions (alkaline electrolytes and applied potential), these open Zn–N_2 sites chemisorb hydroxyl groups from the KOH electrolyte, forming high-valence HO–Zn–N_2 as real active sites for (photo)electrocatalytic HER.

The introduction of the HO–Zn–N_2 sites has considerably lowered the overpotential for HER from 0.31 V (ZIF-8) to 0.07 V (10 mA cm^{-2}), thus increasing the overall electrocatalytic efficiency. These active sites also decreased the band gap and hence rendered the OMS-ZIF visible light active, in contrast to the UV-limited ZIF-8.

DFT simulations further revealed that the high-valence HO–Zn–N_2 sites theoretically favor the adsorption and dissociation steps of the H_2O molecules, and enhancing overall HER performance. This study demonstrates a versatile SeLiRe strategy for introducing highly active catalytic sites in ZIFs and MOFs, also verifies that altering the electronic structure potentially enhances catalytic activity and renders the materials visible light active.

Acknowledgements

Z.H. was financially supported by China Scholarship Council (Nos. 202106770017). This research was funded by the Austrian Science Fund (FWF, 10.55776/I5413, Cluster of Excellence MECS 10.55776/COE5, and doctoral college TU-DX 10.55776/DOC142) and the National Key Research and Development Program of China (2022YFB3803600). The authors gratefully acknowledge the services provided by the analytical instrumentation center (AIC), X-ray Center (XRC) at TU Wien.

Conflict of Interest

The authors declare no conflict of interest.

Data Availability Statement

The data that support the findings of this study are available from the corresponding author upon reasonable request.

Keywords: zeolitic imidazole frameworks · electrocatalysis · hydrogen · single atom sites · selective ligand removal

---

[1] H. Jin, C. Guo, X. Liu, J. Liu, A. Vasileff, Y. Jiao, Y. Zheng, S.-Z. Qiao, *Chem. Rev.* **2018**, *118*, 6337–6408.

[2] R. Subbaraman, D. Tripkovic, K.-C. Chang, D. Strmcnik, A. P. Paulikas, P. Hirunsit, M. Chan, J. Greeley, V. Stamenkovic, N. M. Markovic, *Nat. Mater.* **2012**, *11*, 550–557.

[3] a) L. Cao, Q. Luo, W. Liu, Y. Lin, X. Liu, Y. Cao, W. Zhang, Y. Wu, J. Yang, T. Yao, S. Wei, *Nature Catalysis* **2019**, *2*, 134–141; b) R. Subbaraman, D. Tripkovic, D. Strmcnik, K.-C. Chang, M. Uchimura, A. P. Paulikas, V. Stamenkovic, N. M. Markovic, *Science* **2011**, *334*, 1256–1260.

[4] a) J. Zhang, T. Wang, P. Liu, Z. Liao, S. Liu, X. Zhuang, M. Chen, E. Zschech, X. Feng, *Nat. Commun.* **2017**, *8*, 15437; b) Y. Zheng, Y. Jiao, Y. Zhu, L. H. Li, Y. Han, Y. Chen, M. Jaroniec, S.-Z. Qiao, *J. Am. Chem. Soc.* **2016**, *138*, 16174–16181.

[5] Z. Huang, Z. Wang, H. Rabl, S. Naghdi, Q. Zhou, S. Schwarz, D. H. Apaydin, Y. Yu, D. Eder, *Nat. Commun.* **2024**, *15*, 9393.

[6] a) S. Zhao, C. Tan, C.-T. He, P. An, F. Xie, S. Jiang, Y. Zhu, K.-H. Wu, B. Zhang, H. Li, J. Zhang, Y. Chen, S. Liu, J. Dong, Z. Tang, *Nat. Energy* **2020**, *5*, 881–890; b) I. Liberman, W. He, R. Shimoni, R. Ifraemov, I. Hod, *Chem. Sci.* **2020**, *11*, 180–185.
[7] a) F. Cheng, X. Peng, L. Hu, B. Yang, Z. Li, C.-L. Dong, J.-L. Chen, L.-C. Hsu, L. Lei, Q. Zheng, M. Qiu, L. Dai, Y. Hou, *Nat. Commun.* **2022**, *13*, 6486; b) S. Zhao, Y. Wang, J. Dong, C.-T. He, H. Yin, P. An, K. Zhao, X. Zhang, C. Gao, L. Zhang, J. Lv, J. Wang, J. Zhang, A. M. Khattak, N. A. Khan, Z. Wei, J. Zhang, S. Liu, H. Zhao, Z. Tang, *Nat. Energy* **2016**, *1*, 16184.
[8] Z. Huang, J. Rath, Q. Zhou, A. Cherevan, S. Naghdi, D. Eder, *Small* **2024**, *20*, 2307981.
[9] C. Chen, J. Li, X. Tan, Y. Zhang, Y. Li, C. He, Z. Xu, C. Zhang, C. Chen, *EES Catalysis* **2024**, *2*, 71–93.
[10] J. Jiang, F. Sun, S. Zhou, W. Hu, H. Zhang, J. Dong, Z. Jiang, J. Zhao, J. Li, W. Yan, M. Wang, *Nat. Commun.* **2018**, *9*, 2885.
[11] L. Tong, S. Huang, Y. Shen, S. Liu, X. Ma, F. Zhu, G. Chen, G. Ouyang, *Nat. Commun.* **2022**, *13*, 951.
[12] F. Li, Y. Bu, G.-F. Han, H.-J. Noh, S.-J. Kim, I. Ahmad, Y. Lu, P. Zhang, H. Y. Jeong, Z. Fu, Q. Zhong, J.-B. Baek, *Nat. Commun.* **2019**, *10*, 2623.
[13] J. Zheng, R. Zhang, X. Wang, P. Yu, *Res. Chem. Intermed.* **2018**, *44*, 6637–6648.
[14] a) Y. Xiong, J. Dong, Z.-Q. Huang, P. Xin, W. Chen, Y. Wang, Z. Li, Z. Jin, W. Xing, Z. Zhuang, J. Ye, X. Wei, R. Cao, L. Gu, S. Sun, L. Zhuang, X. Chen, H. Yang, C. Chen, Q. Peng, C.-R. Chang, D. Wang, Y. Li, *Nat. Nanotechnol.* **2020**, *15*, 390–397; b) X. Zhao, R. Fang, F. Wang, X. Kong, Y. Li, *Nat. Commun.* **2022**, *13*, 7873.
[15] M. Bergaoui, M. Khalfaoui, A. Awadallah-F, S. Al-Muhtaseb, *J. Nat. Gas Sci. Eng.* **2021**, *96*, 104289.
[16] a) A. Li, J. Yu, J. Lin, M. Chen, X. Wang, L. Guo, *J. Phys. Chem. Lett.* **2020**, *11*, 1859–1866; b) H. Qiu, X. Du, J. Zhao, Y. Wang, J. Ju, Z. Chen, Z. Hu, D. Yan, X. Zhou, G. Cui, *Nat. Commun.* **2019**, *10*, 5374.
[17] X. Zheng, B. Zhang, P. De Luna, Y. Liang, R. Comin, O. Voznyy, L. Han, F. P. García de Arquer, M. Liu, C. T. Dinh, T. Regier, J. J. Dynes, S. He, H. L. Xin, H. Peng, D. Prendergast, X. Du, E. H. Sargent, *Nat. Chem.* **2018**, *10*, 149–154.
[18] S. Ye, Y. Chen, X. Yao, J. Zhang, *Chemosphere* **2021**, *273*, 128503.

Manuscript received: October 15, 2024
Accepted manuscript online: December 17, 2024
Version of record online: ■■, ■■

Research Article

ZIF Electrocatalysts

Z. Huang, Z. Wang, Q. Zhou, H. Rabl,
S. Naghdi, Z. Yang,*
D. Eder* **e202419913**

Engineering of HO–Zn–N_2 Active Sites in Zeolitic Imidazolate Frameworks for Enhanced (Photo)Electrocatalytic Hydrogen Evolution

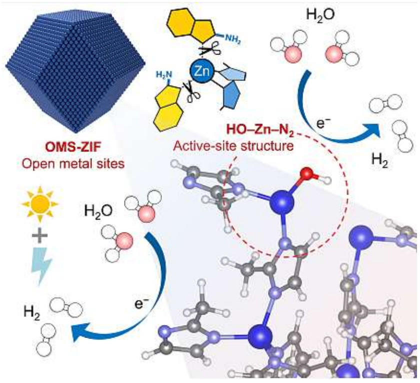

A selective ligand removal strategy was developed to engineer active catalytic sites of unsaturated HO–Zn–N_2 in zeolitic imidazolate frameworks, which significantly accelerate the hydrogen evolution reaction by reducing the overpotential water adsorption from 0.31 V to 0.07 V at 10 mA cm^{-2}.

Angewandte Chemie
Eine Zeitschrift der Gesellschaft Deutscher Chemiker

Supporting Information

Engineering of HO–Zn–N$_2$ Active Sites in Zeolitic Imidazolate Frameworks for Enhanced (Photo)Electrocatalytic Hydrogen Evolution

Z. Huang, Z. Wang, Q. Zhou, H. Rabl, S. Naghdi, Z. Yang, D. Eder**

Supporting Information

Engineering of HO–Zn–N_2 Active Sites in Zeolitic Imidazolate Frameworks for Enhanced (Photo)Electrocatalytic Hydrogen Evolution

Zheao Huang [a], *Zhouzhou Wang* [b], *Qiancheng Zhou* [b], *Hannah Rabl* [a], *Shaghayegh Naghdi* [a],
Ze Yang [*,b] *and Dominik Eder* [*, a]

[a] Institute of Materials Chemistry, Technische Universität Wien, 1060, Vienna, Austria
[b] Institute of Nanoscience and Nanotechnology, College of Physical Science and Technology, Central China Normal University, 430079, Wuhan, China

* Corresponding author: dominik.eder@tuwien.ac.at and yz@ccnu.edu.cn

Chemicals. Zinc nitrate hexahydrate ($Zn(NO_3)_2 \cdot 6H_2O$, 98%, ACROS), 2-methylimidazole (2-mIm, $C_4H_6N_2$, 99%, Sigma-Aldrich), 2-aminobenzimidazole (NH_2-bIm, $C_7H_7N_3$, 97%, Sigma-Aldrich), Methanol (MeOH, 99.9%, HiPerSolv CHROMANORM, VWR), Postassium hydroxide (KOH, 85%%, Sigma-Aldrich), Nafion™ perfluorinated resin solution (nafion, 5 wt.%, Sigma-Aldrich).

Synthesis of Open metal sites ZIF-8 (OMS-ZIF). Sample OMS-ZIF obtained by thermolysis of ML-ZIF (Mixed-ligand ZIF-8) at specific temperatures for specific time periods. For synthesis details on the precursor ML-ZIF and ZIF-8, please refer to our previous report [1]. The heating process was conducted using a muffle furnace (LT 5/12 Nabertherm, Germany) in air atmosphere, the calcination temperature and time is 290°C and 30 minutes, ramp rate of 10°C/min. The final temperature was allowed to cool naturally to room temperature.

ZIF@Nickel Foam electrode. The electrode was prepared by synthesizing ZIF crystals uniformly grown on a nickel foam electrode using microwave reaction. The process involves soaking nickel foam in a zinc nitrate solution (0.87g $Zn(NO_3)_2 \cdot 6H_2O$; 20 ml HPLC methanol) and then using a microwave synthesis reactor (Monowave 300, Anton Paar) to uniformly load zinc ions onto the nickel foam by heating at 150°C for 60 minutes. Subsequently, the treated nickel foam electrode is immersed in the ligand solution (2g 2-methylimidazole; 20 ml HPLC methanol) and subjected to microwave synthesis (to accelerate crystal growth) by heating at 150°C for 30 minutes. The resulting ZIF@NF electrode is then dried overnight in a vacuum oven at 60°C. For OMS-ZIF@NF electrodes, the ligand solution is replaced with a specific mixture of 2-aminobenzimidazole and 2-methylimidazole. After vacuum drying, the obtained NF electrodes are annealed in a muffle furnace (LT 5/12 Nabertherm, Germany) at 290°C, with heating time of 30 minutes.

ZIF@FTO glass electrode. The electrode was prepared by uniformly drop-case ZIF powder onto the fluorine-doped tin oxide (FTO) glass surface, as previously reported [2]. 1 mg of the ZIF samples is mixed with 950 μl of HPLC methanol and 50 μl of nafion solution, and the mixture is sonicated for 30 minutes. Subsequently, the mixed solution is drop-cased onto the surface of the FTO glass (1 cm × 3 cm). Finally, the ZIF@FTO electrode is placed in a vacuum oven and dried overnight at 60°C. For the preparation of OMS-ZIF@FTO electrodes, the ML-ZIF solution (1 mg ML-ZIF; 950 μl of HPLC methanol; 50 μl of nafion) is first drop-cast onto the surface of FTO glass. After vacuum drying, the obtained FTO electrodes are annealed in a muffle furnace (LT 5/12 Nabertherm, Germany) at 290°C, with a heating time of 30 minutes.

X-ray Diffraction (XRD). Used PANalytical X'Pert Pro multi-purpose diffractometer (MPD) with Bragg Brentano geometry with Cu anode at 45 kV, 40 mA, equipped with a BBHD Mirror and an X-Celerator multichannel detector. The diffraction patterns were recorded at a 2θ angle of 5° and 90°. All measurements were performed with Cu sealed tube Kα and Kß radiation (2:1 ratio) with a wavelength of λ=1.54060 Å at a scan rate of 0.5° min^{-1}. A sample holder is a single crystal silicon on which the sample is immobilized by use of a drop of heptane, and rotated every 4 seconds during the test.

Attenuated total reflection-infrared spectroscopy (ATR-IR). Spectra obtained with Perkin Elmer Spectrum two FT-IR spectrometer were in the infrared range of 400-4000 cm^{-1}, with the $LiTaO_3$ (lithium tantalate) MIR detector. Control each data Force Gauge at around 120 with accumulation number of scans is 8 times.

X-ray photoelectron spectroscopy (XPS). All XPS measurements were executed using a custom-built SPECS XPS spectrometer equipped with a monochromatized Al-Kα X-ray source (μFocus 350) and a hemispherical WAL-150 analyzer (acceptance angle: 60°). The In-foil was fixed to the sample holder using double sided carbon tape. For spectral acquisition, pass energies of 100 eV and 30 eV, along with energy resolutions of 1 eV and 100 meV, were employed for survey and detailed spectra, respectively. An excitation energy of 1486.6 eV, beam energy and a spot size of 70 W to 400 μm at an angle of 51° to the sample surface normal were used. The base pressure reached a value of 5x10^{-10} mbar, and the pressure throughout the measurement was 5x10^{-9} mbar.

X-ray absorption near-edge structure spectroscopy (XANES). The metal (Zn) K-edge XAS data were collected at beamlines 1W1B and 1W2B in the Beijing Synchrotron Radiation Facility (BSRF, operated at 2.5 GeV with a maximum current of 250 mA). The obtained XAFS data was processed in Athena (version 0.9.26) [3] for background, pre-edge line and post-edge line calibrations. Then Fourier transformed fitting was carried out in Artemis (version 0.9.26) [3]. The k^2 weighting, k-range of 3 – ~11 Å^{-1} and R range of 1-3 Å were used for the fitting of Zn-foil; The k^2 weighting, k-range of 3 – ~10 Å^{-1} and R range of 1-2 Å were used for the fitting of Samples. For Wavelet Transform analysis, the $\chi(k)$ exported from Athena was imported into the Hama Fortran code. The parameters were listed as follow: R range, 0-4 Å; k range, 0-16 Å^{-1}; k weight; and Morlet function with κ=10, σ=1 was used as the mother wavelet to provide the overall distribution.

In-situ electrochemical Raman spectroscopy. Measurements were collected on HORIBA LabRAM Spectrometer with a 532 nm laser. In-situ measurement was conducted within a three-electrode system, with the working electrode securely positioned in a specialized Raman electrolytic cell.

In-situ electrochemical UV-Vis absorption spectroscopy (UV-Vis). Absorbance of each ZIF@FTO glass were obtained at 350-700nm by Jasco V-670. Measurements were carried out using the Jasco V-670 in diffuse reflectance mode with an Ulbricht-sphere. In-situ measurement was conducted within a three-electrode system, with the working electrode securely positioned in a colorimetric cell serving as the electrolytic cell.

In-situ electrochemical Photoluminescence spectroscopy. Measurements were carried out with a PicoQuant FluoTime 300 spectrophotometer. The excitation source was a xenon arc lamp (power = 300 W), coupled with a double-grating monochromator. The detection system comprised of a PMA Hybrid 07 detector along with a high-resolution double monochromator. Samples were excited directly at a wavelength of 425 nm with ZIF@FTO glass. In-situ measurement was conducted within a three-electrode system, with the working electrode securely positioned in a colorimetric cell serving as the electrolytic cell.

(Photo)electrochemical measurements. All electrochemical tests were conducted in a three-electrode system. 1 M KOH solution (Potassium hydroxide) was chosen as the electrolyte, with Ag/AgCl/3M KCl serving as the reference electrode and Pt as the counter electrode. The working electrode consisted of ZIF@FTO or ZIF@NF, the ZIF@FTO is utilized for all in-situ measurements. The conversion of the potential vs. Ag/AgCl/3M KCl to the reversible hydrogen electrode (RHE) follows:

$$E\ (RHE) = E\ (Ag/AgCl) + E_0\ (Ag/AgCl) + 0.059pH$$

In-situ H_2 flow detection system employed an argon gas to continuously purge the cell reactor at a flow rate of 30 mL min^{-1}, delivering H_2 to the X-stream analyzer (Emerson Process Management). The H_2 concentrations (ppm) measured in the stream is converted to the HER rate (μmol h^{-1}) by the ideal gas equation.

Electrical resistance of ZIF-8@NF and OMS-ZIF@NF were measured using a two-probe measurement method. The conversion equation for electrical conductivity (σ) and resistance (R) is

$\sigma = l/RA$, where l is the thickness of the ZIFs (~1 μm by microscope), and A is the NF area (1 cm × 3 cm).

Photoelectrocatalytic experiments were performed using visible light (400-700 nm, 2.36 W) from SUPERLITE SUV-DC-E (Lumatec) as a light source.

Density functional theory (DFT) calculations. All of the calculations were performed by using Vienna ab initio program package (VASP) [4]. The exchange and correlation effects of the electrons were described by using the Perdew-Burke-Ernzerhof (PBE) [5] functional of a generalized gradient approximation (GGA) method [6]. The projector augmented wave (PAW) method was used to describe the electron-ion interaction. Spin polarization considered. The cutoff energy of the plane-wave was set as 500 eV. The (1×1×1) k-point mesh was used for k-space integration in structure relaxation of MOF structures with different number of ligands, the (4×4×4) k-point mesh was used and for DOS calculation of them. Conjugate-gradient algorithm is used to relax the ions into their instantaneous ground state. The structures involved were fully relaxed with the energy and force convergences less than 1×10^{-6} eV and 0.03 eV Å^{-1}, respectively. For the calculation of water adsorption on Zn–NC, the (4×4×1) k-point mesh was used for k-space integration, a $Zn–N_2$ coordination structure similar to that in Zn-MOF was used to ensure the reliability of the results, as shown in **Figures S14-17**.

Supplementary Note 1. Electrocatalytic HER performance of other OMS-ZIF.

The OMS-ZIF mentioned in the main text was obtained using 30%ML-ZIF as a precursor through the SeLiRe strategy. In our previous studies [1], we also investigated other R%OMS-ZIF samples with varying distributions of open metal sites and porosity, constructed based on 10%, 50%, and 70%ML-ZIF. Here, R% represents the mass ratio of NH_2-bIm to NH_2-bIm + 2-mIm.

Electrocatalytic HER tests were conducted on both 10%, 50% and 70%OMS-ZIFs; it is noteworthy that their current densities under same conditions are much lower than that of 30%OMS-ZIF, but still higher than pristine ZIF-8 (**Figure S8a**). Specifically, 10%, 50% and 70%OMS-ZIFs achieve 0.1 A cm^{-2} at overpotentials of 0.49 V, 0.34 V and 0.29 V, respectively (**Figure S8b**). As well, their Tafel slopes are significantly higher than that of 30%OMS-ZIF, with 10% at 127.43 mV dec^{-1}, 50% at 124.52 mV dec^{-1}, and 70% at 111.05 mV dec^{-1} (**Figure S8c**).

In summary, the electrocatalytic HER activity of all OMS-ZIF samples ranks as follows: 30% > 70% > 50% > 10%. The main reasons for this differentiation are the varying contents of localized Zn−N_2 sites and their porosity. As concluded from the XAS results, the 30%OMS-ZIF possesses the optimal Zn−N_2 active sites, which leads to stronger chemisorb of –OH groups in the electrochemical environment, ultimately forming more high-valence HO−Zn−N_2 active sites that are beneficial for the HER process.

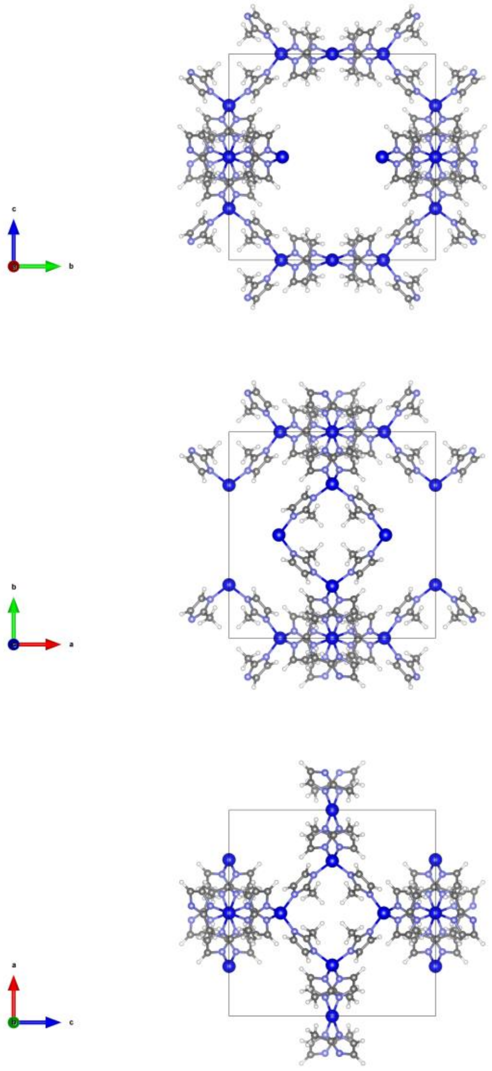

Figure S1. Models structure of OMS-ZIF optimized from DFT simulation. Dark blue for Zn, light blue for N, gray for C and white for H.

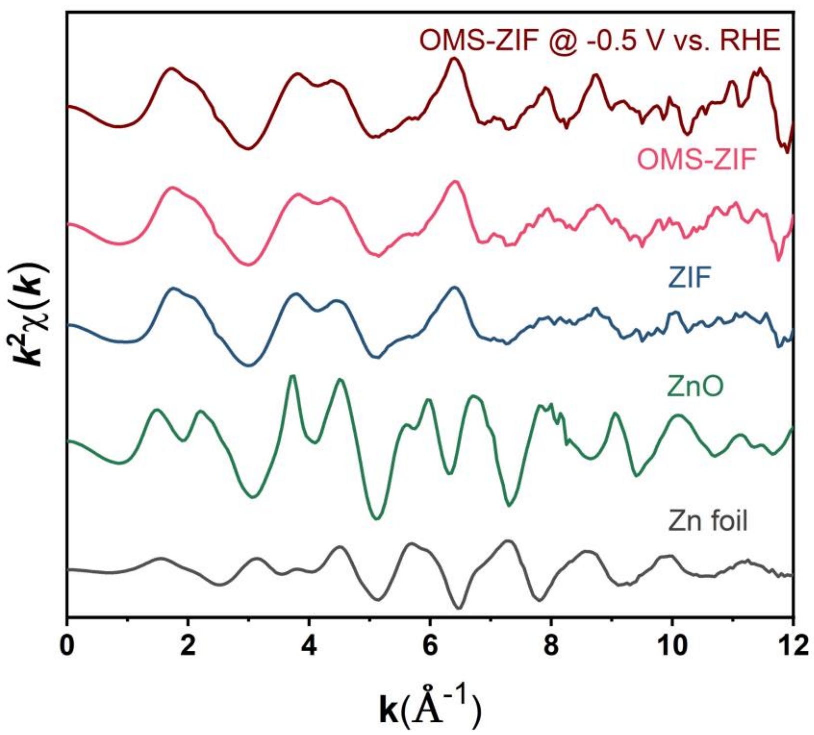

Figure S2. $K^2\chi(k)$ oscillations of Zn K-edge EXAFS analysis for Zn foil, ZnO, ZIF-8, OMS-ZIF and OMS-ZIF at −0.5 V applied potential.

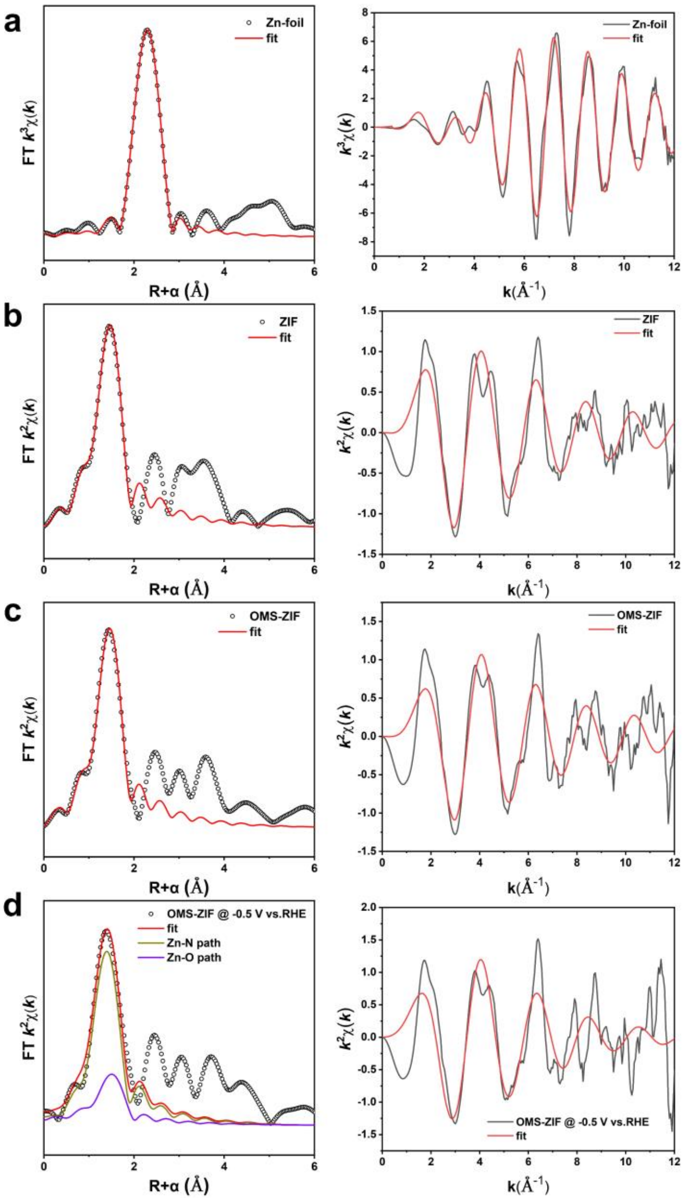

Figure S3. Fitting of Zn K-edge EXAFS spectra and Fourier-transformed magnitudes for Zn foil (**a**), ZIF-8 (**b**), OMS-ZIF (**c**) and OMS-ZIF at −0.5 V applied potential (**d**).

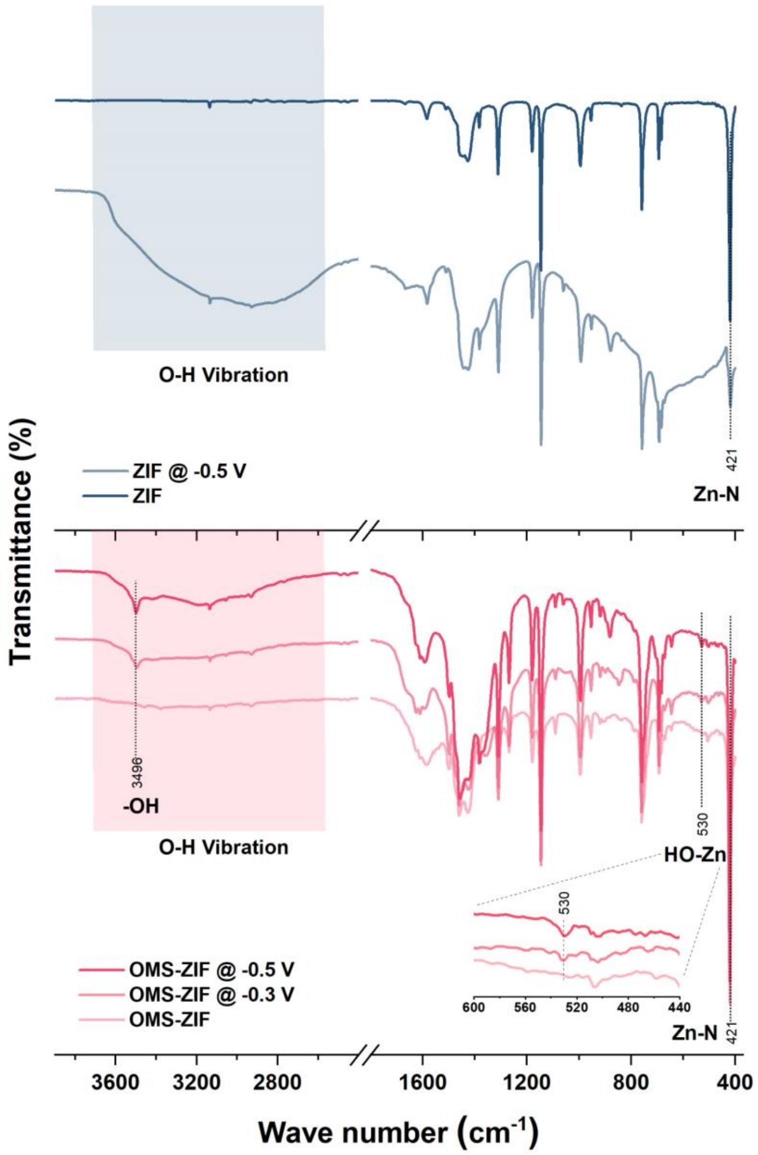

Figure S4. ATR-IR spectra of ZIF-8 and OMS-ZIF at the open-circuit potential and applied potentials of −0.3 V and −0.5 V.

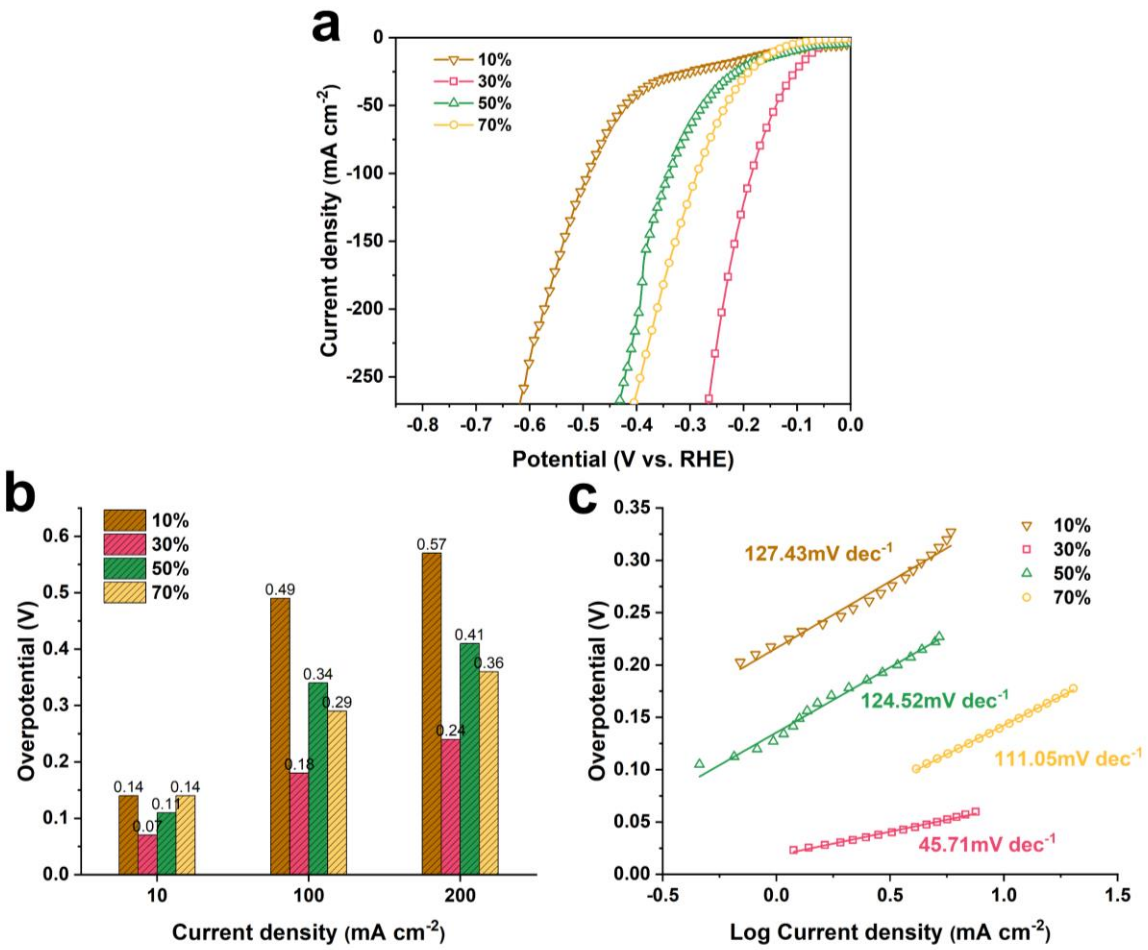

Figure S5. a, LSV curves toward HER of 10%, 30%, 50% and 70%OMS-ZIF. **b**, **c**, Overpotentials at 100 and 200 mA cm^{-2} (**b**) and Tafel slopes (**c**) of 10%, 30%, 50% and 70%OMS-ZIF. Here, the 30%OMS-ZIF corresponds to the OMS-ZIF in all the above mentioned as well as in the main text, more detail in **Supplementary Note 1**.

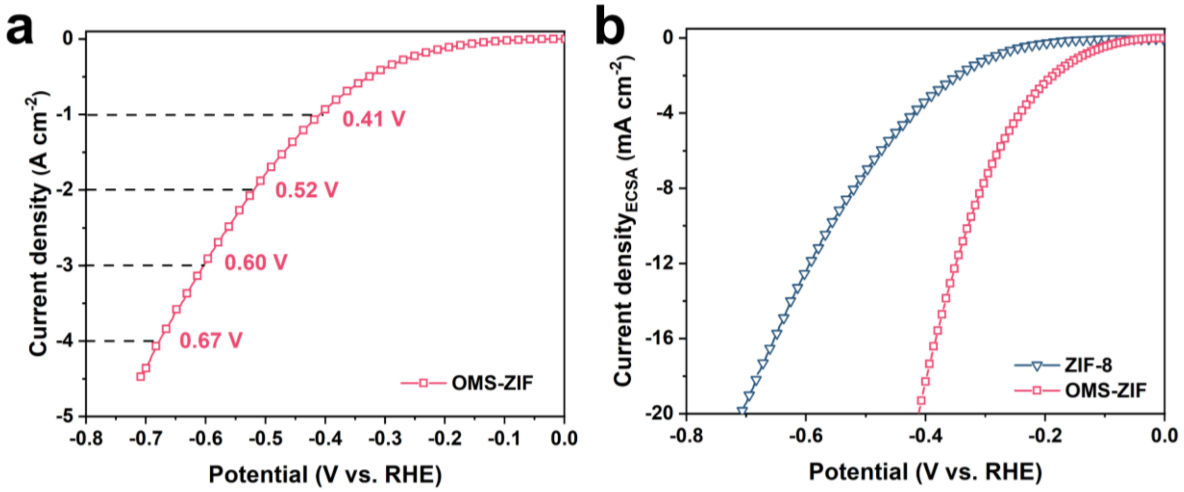

Figure S6. LSV curve of OMS-ZIF at ampere-level current density (**a**). ECSA-normalized LSV curves of ZIF-8 and OMS-ZIF (**b**).

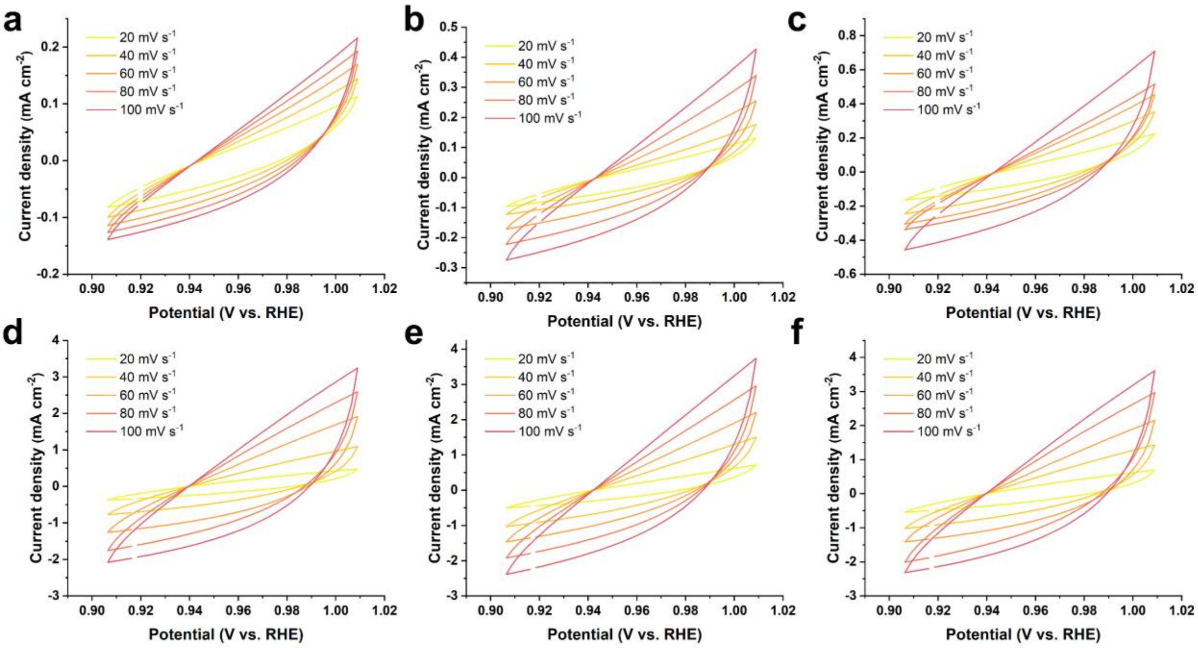

Figure S7. Cyclic voltammetry curves of ZIF-8 (**a-c**) and OMS-ZIF (**d-f**) at different scan rates in 1.0 M KOH, each sample measured three times. ECSA is directly proportional to its electrochemical double-layer capacitance (C_{dl}) according to the following equation:

$$ECSA = \frac{C_{dl}}{C_s}$$

where C_s is the specific capacitance of the sample, 1 M KOH is usually taken with C_s assumed to be 0.04 mF cm^{-2} [7]. where C_{dl} is the electrochemical double-layer capacitance of the sample, estimated according to the above CV curves of the non-Faraday region [8].

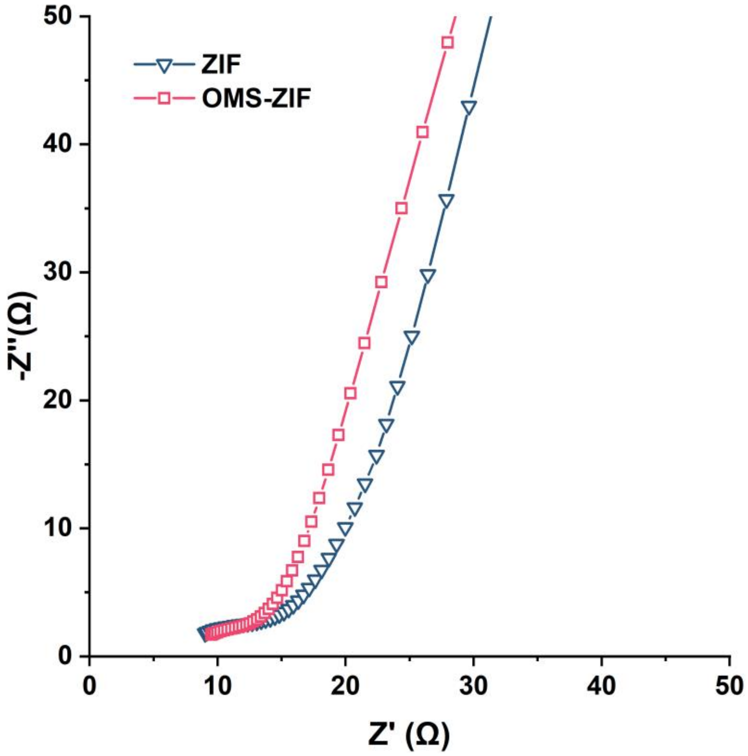

Figure S8. EIS Nyquist plots of ZIF-8 and OMS-ZIF.

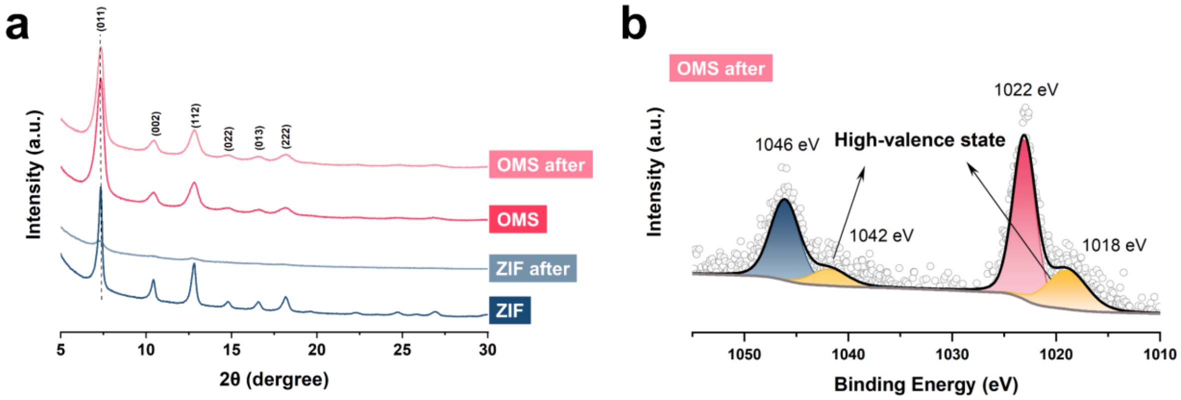

Figure S9. XRD patterns of ZIF-8 and OMS-ZIF before and after the 120-hour potentiometric test (**a**). XPS of OMS-ZIF after the 120-hour potentiometric test (**b**).

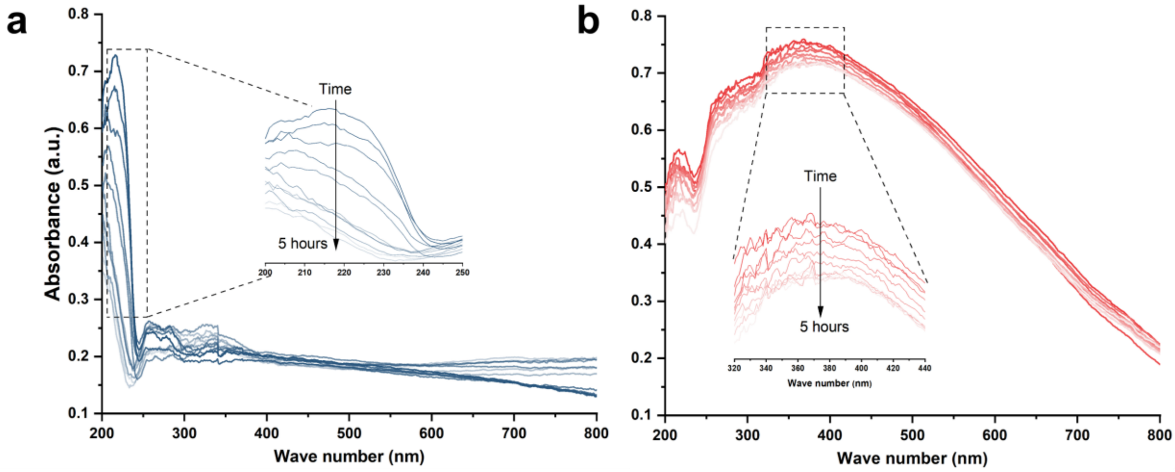

Figure S10. In-situ electrochemical UV-Vis absorption spectroscopy of ZIF-8 (**a**) and OMS-ZIF (**b**) at –0.3 V applied potential for 5 hours.

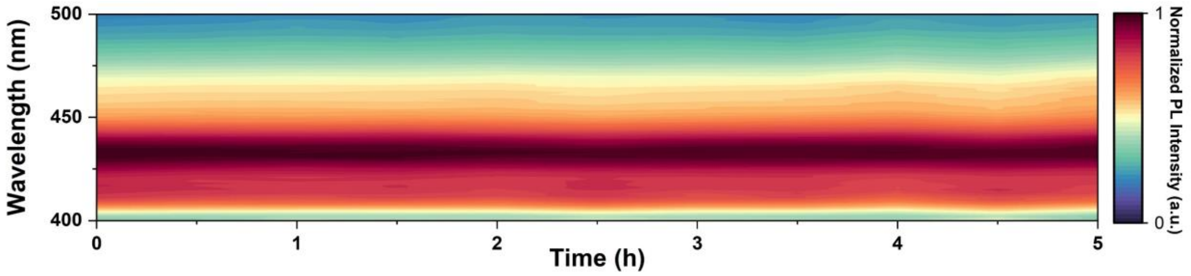

Figure S11. In-situ electrochemical Photoluminescence spectroscopy of OMS-ZIF at –0.3 V applied potential for 5 hours.

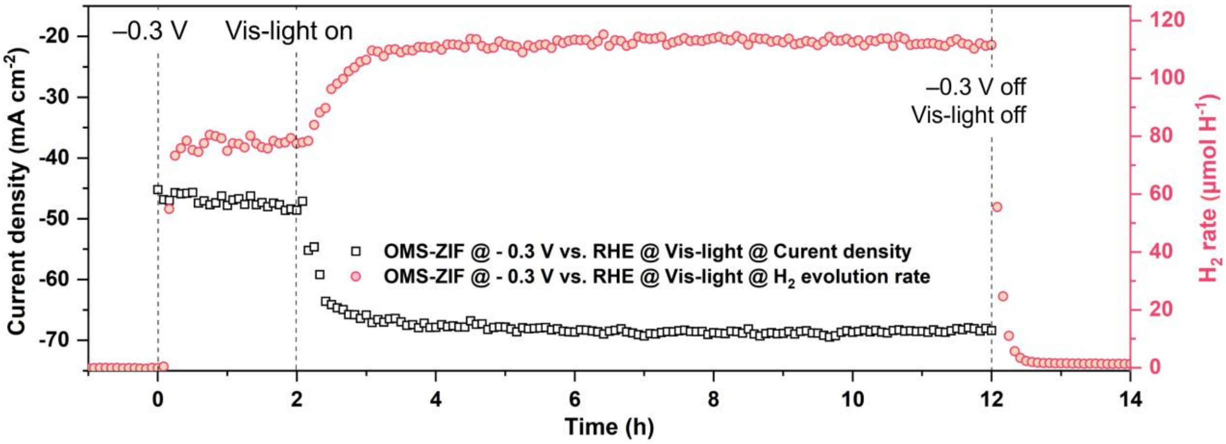

Figure S12. Chronoamperometric curve and H_2 evolution rate of OMS-ZIF for 12 hours at –0.3 V under visible light.

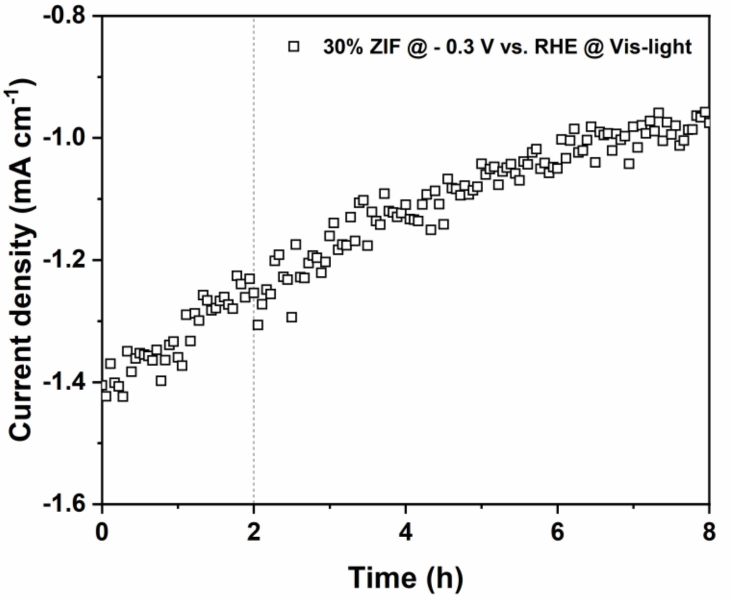

Figure S13. Chronoamperometric curve of 30%ML-ZIF at –0.3 V under visible light.

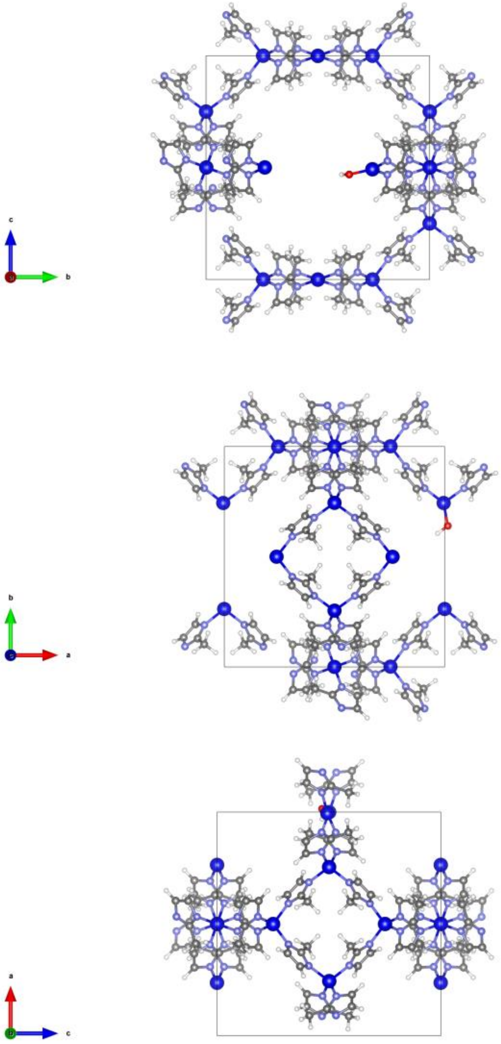

Figure S14. HO–Zn–N_2/ZIF structure optimized from DFT simulation. Dark blue for Zn, light blue for N, red for O, gray for C and white for H.

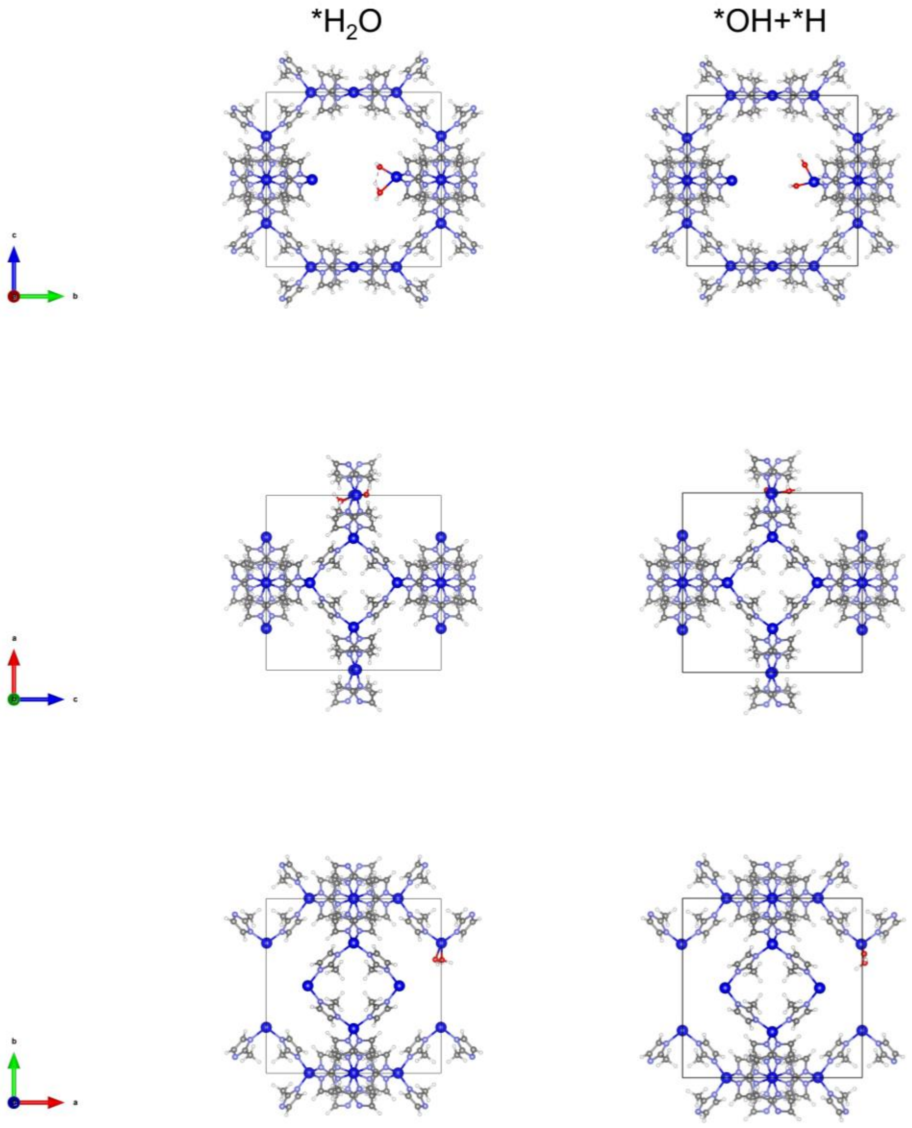

Figure S15. Reaction steps for H_2O adsorption/dissociation of HO–Zn–N_2/ZIF. Dark blue for Zn, light blue for N, red for O, gray for C and white for H.

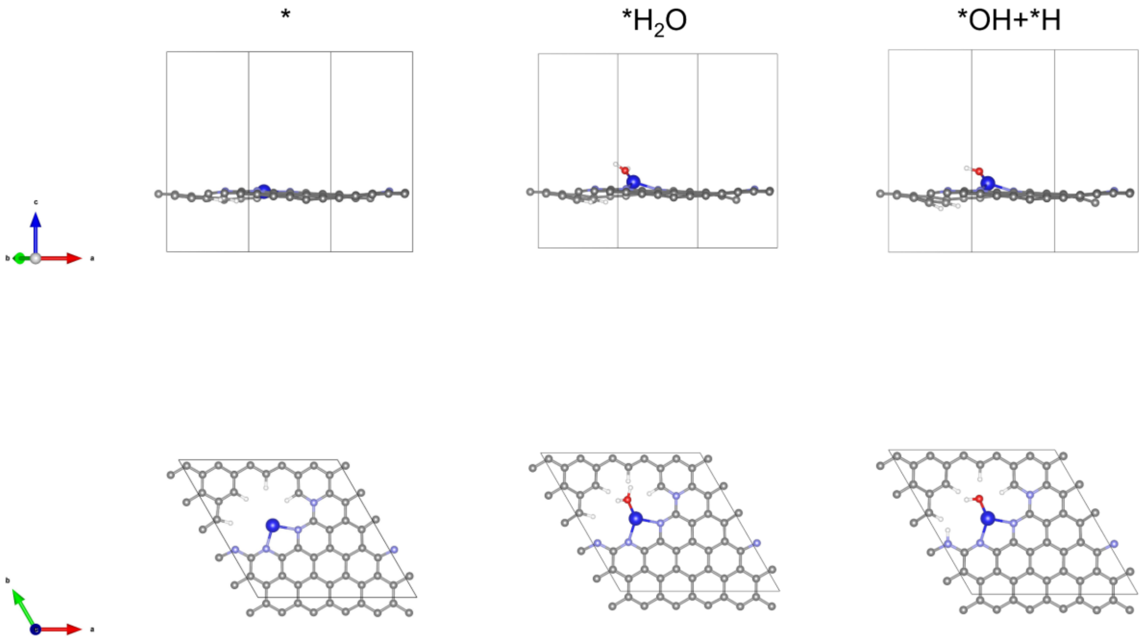
* $*H_2O$ $*OH+*H$

Figure S16. Reaction steps for H_2O adsorption/dissociation of Zn–N_2/NC. Dark blue for Zn, light blue for N, red for O, gray for C and white for H.

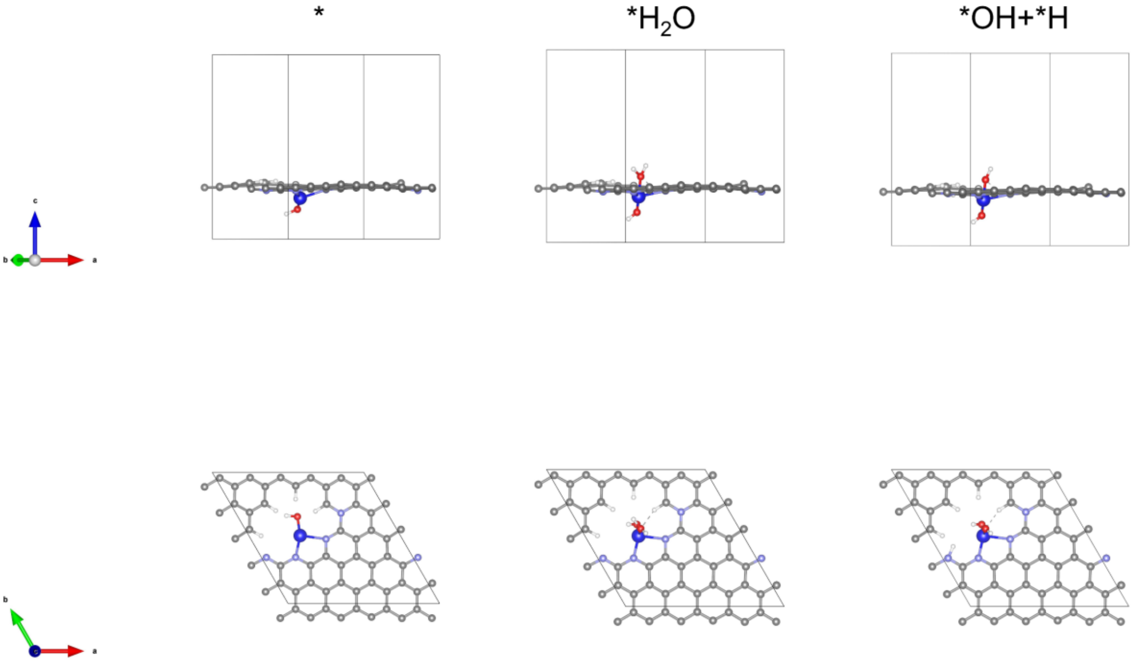

Figure S17. Reaction steps for H_2O adsorption/dissociation of HO–Zn–N_2/NC. Dark blue for Zn, light blue for N, red for O, gray for C and white for H.

Table S1. EXAFS fitting parameters at the Zn K-edge for various samples (S_0^2=0.8 from Zn-foil).

Samples	shell	CN[a]	R (Å)[b]	σ^2 (Å^2)[c]	ΔE_0 (eV)[d]	R factor[e]
Zn-foil	Zn−Zn1	6	2.64±0.01	0.0094	2.1±0.9	0.0013
	Zn−Zn2	6	2.76±0.01	0.0189		
ZIF-8	Zn−N	3.9±0.3	1.95±0.01	0.0037	-0.4±2.1	0.0080
OMS-ZIF	Zn−N	2.6±0.2	1.92±0.01	0.0031	-0.2±2.6	0.0139
OMS-ZIF @ −0.5 V	Zn−N	2.5±0.3	1.88±0.01	0.0046	-2.3±1.0	0.0163
	Zn−O	1.0±0.4	2.02±0.01	0.0043		

[a] CN: coordination numbers.

[b] R: bond distance.

[c] σ^2: Debye-Waller factors.

[d] ΔE_0: the inner potential correction.

[e] R factor: goodness of fit. Error bounds that characterize the structural parameters obtained by EXAFS spectroscopy were estimated as CN±20%; R±1%; σ^2±20%.

Table S2. Comparison of electrocatalytic HER performances of OMS-ZIF with other reported MOF-base catalysts.

Catalysts	**Electrolyte**	**Overpotential (V)^a**	**Tafel slope (mV/dec)**	**Stability (hour)**	**Ref.**
OMS-ZIF	**1 M KOH**	**0.07**	**45.71**	**120**	**This work**
$NiRu_{0.13}$-BDC	1 M KOH	0.03	32	30	[9]
AB&CTGU-5	0.5 M H_2SO_4	0.04	45	96	[10]
RuCo-CAT	1 M KOH	0.04	32	15	[11]
Ni-ZIF/Ni-B@NF	1 M KOH	0.07	101	64	[12]
D-Ni-MOF	1 M KOH	0.10	51	48	[13]
$Mn_{0.52}Fe_{0.71}$Ni-MOF-74	1 M KOH	0.10	104	100	[14]
NiFe-MOF	0.1 M KOH	0.13	-	0.56	[15]
$FeNi_2P$-NPs	1 M KOH	0.17	66	50	[16]
Co–Zn/PNC	1 M KOH	0.18	100	10	[17]
FeNiP/NCH	1 M KOH	0.22	125	40	[18]
Co-BDC/MoS_2	1 M KOH	0.25	86	15	[19]
2D Co-MOFs	0.5 M H_2SO_4	0.28	86	24	[20]
3D NibpyfcdHp	0.5 M H_2SO_4	0.35	60	30	[21]
3D Co/Ni-MOFs	0.5 M H_2SO_4	0.36	107	96	[22]

[a] All samples were overpotentialed at a current density of 10 mA cm^{-2}.

References

[1] Z. Huang, J. Rath, Q. Zhou, A. Cherevan, S. Naghdi, D. Eder, *Small* **2023**, *n/a*, 2307981.

[2] Z. Huang, Z. Wang, H. Rabl, S. Naghdi, Q. Zhou, S. Schwarz, D. H. Apaydin, Y. Yu, D. Eder, *Nat. Commun.* **2024**, *15*, 9393.

[3] H. Funke, A. C. Scheinost, M. Chukalina, *Physical Review B* **2005**, *71*, 094110.

[4] Kresse, Furthmuller, *Phys. Rev. B: Condens. Matter* **1996**, *54*, 11169-11186.

[5] J. P. Perdew, A. Ruzsinszky, G. I. Csonka, O. A. Vydrov, G. E. Scuseria, L. A. Constantin, X. L. Zhou, K. Burke, *Phys. Rev. Lett.* **2008**, *100*, 4.

[6] J. P. Perdew, K. Burke, M. Ernzerhof, *Phys. Rev. Lett.* **1996**, *77*, 3865-3868.

[7] F. Cheng, X. Peng, L. Hu, B. Yang, Z. Li, C.-L. Dong, J.-L. Chen, L.-C. Hsu, L. Lei, Q. Zheng, M. Qiu, L. Dai, Y. Hou, *Nat. Commun.* **2022**, *13*, 6486.

[8] T. T. N. Tran, T.-K. Truong, J. Yu, L. Peng, X. Liu, L. H. T. Nguyen, S. Park, Y. Kawazoe, T. B. Phan, N. H. T. Tran, N. H. Vu, N. Q. Tran, *ACS Appl. Mater. Interfaces* **2024**.

[9] Y. Sun, Z. Xue, Q. Liu, Y. Jia, Y. Li, K. Liu, Y. Lin, M. Liu, G. Li, C.-Y. Su, *Nat. Commun.* **2021**, *12*, 1369.

[10] Y.-P. Wu, W. Zhou, J. Zhao, W.-W. Dong, Y.-Q. Lan, D.-S. Li, C. Sun, X. Bu, *Angew. Chem. Int. Ed.* **2017**, *56*, 13001-13005.

[11] Y. He, F. Yan, X. Zhang, C. Zhu, Y. Zhao, B. Geng, S. Chou, Y. Xie, Y. Chen, *Advanced Energy Materials* **2023**, *13*, 2204177.

[12] H. Xu, B. Fei, G. Cai, Y. Ha, J. Liu, H. Jia, J. Zhang, M. Liu, R. Wu, *Advanced Energy Materials* **2020**, *10*, 1902714.

[13] J. Zhou, Y. Dou, X.-Q. Wu, A. Zhou, L. Shu, J.-R. Li, *Small* **2020**, *16*, 1906564.

[14] W. Zhou, Z. Xue, Q. Liu, Y. Li, J. Hu, G. Li, *ChemSusChem* **2020**, *13*, 5647-5653.

[15] J. Duan, S. Chen, C. Zhao, *Nat. Commun.* **2017**, *8*, 15341.

[16] S. Li, J. Wang, X. Lv, S. Zheng, J. Wang, Z. Li, *Catalysis Science & Technology* **2023**, *13*, 1512-1517.

[17] W. Peng, G. Zheng, Y. Wang, S. Cao, Z. Ji, Y. Huan, M. Zou, X. Yan, *Int. J. Hydrogen Energy* **2019**, *44*, 19782-19791.

[18] Y.-S. Wei, M. Zhang, M. Kitta, Z. Liu, S. Horike, Q. Xu, *J. Am. Chem. Soc.* **2019**, *141*, 7906-7916.

[19] D. Zhu, J. Liu, Y. Zhao, Y. Zheng, S.-Z. Qiao, *Small* **2019**, *15*, 1805511.

[20] Y.-S. Li, J.-W. Yi, J.-H. Wei, Y.-P. Wu, B. Li, S. Liu, C. Jiang, H.-G. Yu, D.-S. Li, *J. Solid State Chem.* **2020**, *281*, 121052.

[21] V. Khrizanforova, R. Shekurov, V. Miluykov, M. Khrizanforov, V. Bon, S. Kaskel, A. Gubaidullin, O. Sinyashin, Y. Budnikova, *Dalton Transactions* **2020**, *49*, 2794-2802.

[22] X. Wang, J.-Y. Luo, J.-W. Tian, D.-D. Huang, Y.-P. Wu, S. Li, D.-S. Li, *Inorg. Chem. Commun.* **2018**, *98*, 141-144.

3.2.3 Article #3

"Ligand Engineering Enhances (Photo)Electrocatalytic Activity and Stability of Zeolitic Imidazolate Frameworks via In-situ Surface Reconstruction"

*Zheao Huang, Zhouzhou Wang, Hannah Rabl, Shaghayegh Naghdi, Qiancheng Zhou, Sabine Schwarz, Dogukan Hazar Apaydin, Ying Yu *, and Dominik Eder **

Nature Communications, **2024**, *15* (1), 939.

DOI: https://doi.org/10.1038/s41467-024-53385-0

As the first author of these articles, I led the entire research process, provided the original idea, conducted most of the testing, and wrote the manuscript. The corresponding Supplement Information can be found on pages 151-222.

Reprinted with permission from *Nature Communications* [118].

nature communications

Article

https://doi.org/10.1038/s41467-024-53385-0

Ligand engineering enhances (photo) electrocatalytic activity and stability of zeolitic imidazolate frameworks via in-situ surface reconstruction

Received: 21 June 2024

Accepted: 10 October 2024

Zheao Huang[1], **Zhouzhou Wang**[2], **Hannah Rabl**[1], **Shaghayegh Naghdi**[1], **Qiancheng Zhou**[2], **Sabine Schwarz**[3], **Dogukan Hazar Apaydin**[1], **Ying Yu**[2] & **Dominik Eder**[1]

The current limitations in utilizing metal-organic frameworks for (photo) electrochemical applications stem from their diminished electrochemical stability. In our study, we illustrate a method to bolster the activity and stability of (photo)electrocatalytically active metal-organic frameworks through ligand engineering. We synthesize four distinct mixed-ligand versions of zeolitic imidazolate framework-67, and conduct a comprehensive investigation into the structural evolution and self-reconstruction during electrocatalytic oxygen evolution reactions. In contrast to the conventional single-ligand ZIF, where the framework undergoes a complete transformation into CoOOH via a stepwise oxidation, the ligand-engineered zeolitic imidazolate frameworks manage to preserve the fundamental framework structure by in-situ forming a protective cobalt (oxy)hydroxide layer on the surface. This surface reconstruction facilitates both conductivity and catalytic activity by one order of magnitude and considerably enhances the (photo)electrochemical stability. This work highlights the vital role of ligand engineering for designing advanced and stable metal-organic frameworks for photo- and electrocatalysis.

Metal-organic frameworks (MOFs) are intricate structures comprised of secondary building units (SBUs) or clusters formed by the coordination of metal nodes with organic ligands, the synthesis and applications of which have been thoroughly investigated within the materials field[1,2]. A surge in research efforts has explored the direct applications of MOFs in electrochemical applications, where the metal nodes often serve as active catalytic sites for electrocatalysis, especially in Co-MOFs[3,4], Ni-MOFs[5–7], and mixed-metal MOFs[8,9]. Despite these advancements, the stability and conductivity of MOF materials in electrochemical environments and their feasibility as direct electrocatalysts remain contentious due to the relatively weaker coordinating bonds between metal nodes and ligands, in contrast to the robust ionic bonds found in traditional inorganic materials[10,11].

For instance, the direct electrocatalysis of pristine zeolitic imidazolate framework-67 (ZIF-67) leads to the complete reconstruction (CR) of its organic framework over time and, eventually to phase transition to $Co(OH)_2$ and CoOOH in alkaline environments (KOH)[12]. Despite the higher catalytic activity of oxygenated cobalt species, the self-reconstruction is typically unavoidable, making it impossible to consider ZIF-67 as an electrocatalyst directly[13,14]. Tang et al. found a two-step dynamic structural reconstruction in NiCo-MOF-74 during the oxygen evolution reaction (OER) process, from the MOF structure

---

[1]Institute of Materials Chemistry, Technische Universität Wien, 1060 Vienna, Austria. [2]Institute of Nanoscience and Nanotechnology, College of Physical Science and Technology, Central China Normal University, 430079 Wuhan, China. [3]Service Center for Electron Microscopy (USTEM), Technische Universität Wien, 1040 Vienna, Austria. e-mail: yuying01@ccnu.edu.cn; dominik.eder@tuwien.ac.at

to $NiCo(OH)_2$ and then further to NiCoOOH at higher potentials[15]. This nature is prevalent when MOFs are used as OER anodes in alkaline electrolytes, where they undergo the irreversible electro-oxidation process[16,17]. Ultimately, MOFs are constructed into metal-based oxyhydroxides as the real catalytic species, rather than the original metal node. The fundamental nature of the CR process of MOFs during electrochemical treatment is the ligand substitution process, which disrupts the framework stabilization and primitive metal nodes of MOFs. Therefore, we contend that in addition to enhancing electrocatalytic activity, improving the electrochemical stability and mitigating the CR process of MOFs is particularly crucial in (photo) electrochemical applications.

Designing stable MOF electrocatalysts through ligand engineering has gained increasing attention[18,19]. For instance, Dang et al. introduced multiple ligands in MOFs, constructing a multivariate MOF-5 structure with unique properties of CO_2-selective adsorption[20]. ZIF-62, which incorporates two different ligands, exhibits suitable thermal stability and undergoes melting before thermal decomposition, making it widely employed in quenching to form distinct MOF glasses[21–23]. Others, Wang et al. and Wu et al., prepared a series of the MOFs or MOF composites as stable and efficient photocatalysts through ligand engineering[24,25]. We thus envision the development of a stable electrocatalyst by employing ligand engineering on ZIFs to balance the electrochemical stability and activity.

According to the hard-soft acid-base (HSAB) principle, two strategies can be envisioned to construct stable MOFs based on the coordination bond strength: (a) hard acid/hard base; (b) soft acid/soft base[25,26]. Unfortunately, commonly used low-valent metals (Zn^{2+} and Co^{2+}) in ZIFs belong to soft acids, and it is difficult to design ZIFs with suitable crystallinity using corresponding soft bases (such as pyrazolate ligand)[27]. Considering the literature report claiming to enhance the electrical conductivity of MOFs by tuning the stacked aromatic carbon rings[28], and combining with our previous studies on mixed-ligand ZIFs[29], we here select four secondary ligands featuring aromatic carbon ring and amino group. These ligands were mixed with the original ligand by microwave synthesis reactor, thereby constructing ligand-engineered ZIFs (LE-ZIFs) aimed at achieving a balance between electrochemical activity and stability. Previous studies have easily confused the electrochemical "performance" stability and electrochemical stability, and the main reason for this ambiguity lies in the absence of in-situ electrochemical characterization[10,30,31]. Here we combine the continuous cyclic voltammetry (CV), in-situ UV–Vis absorption spectroscopy, in-situ Raman spectroscopy and in-situ photoluminescence (PL) spectroscopy to elucidate the reconstruction phenomena of as-prepared ZIFs during (photo)electrocatalytic reaction. Ex-situ characterizations and density functional theory (DFT) calculations provide compelling evidence for the robust electrochemical stability and OER activity of AE-ZIF (refer to Fig. 1a, mixed 2-

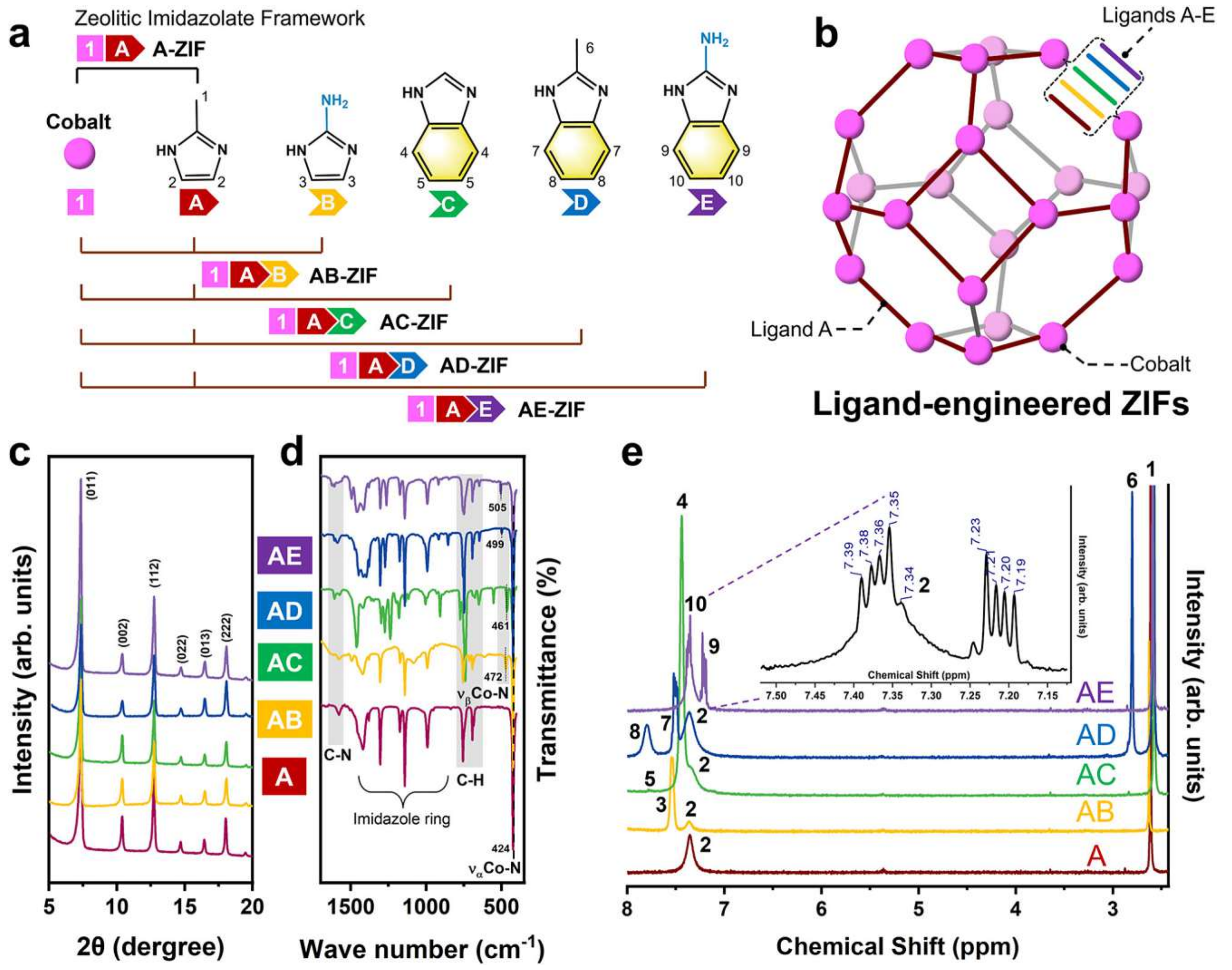

Fig. 1 | Structural characterization of Ligand-engineered ZIFs. a, b Schematic diagram of the various ligands A-E mixed in LE-ZIFs (**a**) and unit cell of each LE-ZIFs (**b**). **c**–**e** XRD patterns (**c**), ATR-IR (**d**) and ^{1}H NMR spectroscopy (**e**) of A-ZIF, AB-ZIF, AC-ZIF, AD-ZIF and AE-ZIF, more details in Figs. S1, S3 and S21–S25. All samples were digested using d^4-acetic acid and then tested by ^{1}H NMR. The numbers in Fig. 1e are for H at the corresponding positions on the ligand in Fig. 1a.

aminobenzimidazole). This study opens up a feasible pathway to enhance OER activity and stability by modulating the organic ligands in the stabilized LE-ZIFs synthesis.

Results

Structural characterization of Ligand-engineered ZIFs

Single-ligand ZIF-67 (A-ZIF) is formed by the tetrahedral coordination of cobalt ions with the ligand 2-methylimidazole (2-mIm, termed as A) which creates a sodalite (SOD) structure. For the ligand-engineered ZIFs (LE-ZIFs), we introduced four secondary ligands: 1H-Imidazol-2-amine (NH_2-mIm, B), Benzimidazole (bIm, C), 2-methylbenzimidazole (2-bIm, D), and 2-aminobenzimidazole (NH_2-bIm, E). Each ligand was mixed with the original ligand A using a microwave process to construct the ZIF structures (Fig. 1a, b). The X-ray powder diffraction (XRD) pattern and attenuated total reflection infra-red (ATR-IR) spectrum of A-ZIF match well with the previous literature reports[32,33]. The XRD patterns of the LE-ZIFs also exhibit a close resemblance to those of A-ZIF, indicating that the intrinsic structure is well-preserved and exhibits high crystallinity (Figs. 1c and S1). The absence of secondary or impurity phases implies that the ligand substitution occurred solely within the framework. Note that the embedding of ligand B results in structural distortion in AB-ZIF, which impacts the “optimal” particle growth, e.g., an increase in particle size (as observed in scanning electron microscopy, SEM, in Fig. S2).

ATR-IR spectra reveal the incorporation of secondary ligands within the LE-ZIFs framework. All as-prepared ZIFs show the characteristic band about 435 cm^{-1}, which corresponds to the Co-N_α coordination with ligand A. New bands between 472 and 505 cm^{-1} correspond to Co-N_β vibrations with the respective secondary ligands (Figs. 1d and S3). The simultaneous presence of these two metal-ligand vibrational modes confirms the successful incorporation of both ligands in the LE-ZIFs framework.

N_2 physisorption at 77 K reveals that A-ZIF exhibits a high specific surface area (1867.9 $m^2\,g^{-1}$) and a 1.2 nm microporous structure (0.655 $cm^3\,g^{-1}$ in Table S1). In comparison, the introduction of a secondary ligand has reduced the respective specific surface areas (717.8–1092.9 $m^2\,g^{-1}$) and pore volumes (0.365-0.489 $cm^3\,g^{-1}$), while preserving the microporous structure around 1.2 nm (Figs. S4 and S5).

^1H nuclear magnetic resonance (^1H NMR) spectrum of A-ZIF contains the expected features (peaks 1 and 2) corresponding to the methyl group and imidazole. In addition, the spectra of LE-ZIFs (Fig. 1e) exhibit new features (peaks 3–10) that correspond to the respective secondary ligands B-E. Quantitative analysis of the ligand composition by ^1H NMR reveals that the actual ratios are as follows: ligand B at 51.2 ± 1.6 mol%, ligand C at 41.4 ± 0.4 mol%, ligand D at 39.0 ± 0.7 mol%, and ligand E at 36.9 ± 1.2 mol%. Their respective contents are in good agreement with the nominal values (as detailed in Table S3), providing further validation of the precision in ligand incorporation into the LE-ZIFs.

Electrocatalytic studies

For all electrocatalytic studies, as shown in Fig. S6a, the as-prepared ZIFs were drop-cast onto fluorine-doped tin oxide (FTO) glass and used as working electrodes in an aqueous 1 M KOH solution, with the potential referenced to the reversible hydrogen electrode (RHE). At a high potential (0.85–1.55 V), the CV plot of A-ZIF changes with increasing cycle numbers and two distinct redox peaks appear denoted as $R_{SL\text{-}A}1$ and $R_{SL\text{-}A}2$ (Fig. 2a). The $R_{SL\text{-}A}1$ represents the electro-oxidation process from Co^{2+} to Co^{3+} transition, while $R_{SL\text{-}A}2$ indicates the Co^{3+} to Co^{4+} transition[34]. The presence of these signals indicates the beginning of self-reconstruction, which intensifies with increasing CV cycles[12]. After 50 cycles, the current density of A-ZIF reaches a maximum and then starts to decrease, indicating a partial degradation of the framework, accompanied by the formation of oxygenated Co species. This trend is somewhat delayed at medium potentials (0.85–1.30 V). At low potentials (0.85–1.05 V), A-ZIF shows typical capacitive behaviour, with the current mainly originating from the adsorption and release of hydroxide ions within the double-layer capacitor (Fig. S6b–e). Other LE samples exhibit distinctly differences CV plots; for instance, AB and AE only show signs of the Co^{2+} to Co^{3+} transition, while the oxidation of Co^{3+} to Co^{4+} seems to be suppressed, which is closely related to their mixed secondary ligands (Fig. S7).

The quantitative analysis of the anodic peaks in the CV plots is summarized in Figs. 2b and S8. Concerning the anodic peak (region 1), the charges of $R_{LE\text{-}AE}1$ reaches the highest value (0.047 mC) after 80 cycles, followed by $R_{LE\text{-}AC}1$ and $R_{LE\text{-}AD}1$, while $R_{SL\text{-}A}1$ remains the lowest. This anodic charge corresponds to the number of electron-accessible Co^{2+} sites[12]. Additionally, the anodic peak positions generally shift towards the higher potentials, indicating the transformation of Co^{2+} species into more stable states. The final stabilization of $R_{LE\text{-}AE}1$ at a maximum of 1.329 V suggests that AE-ZIF requires a higher potential to be electro-oxidation compared to the other ZIF samples. When using electrochemical double-layer capacitance (C_{dl}) to reflect the electrochemical active surface area (ECSA, in Fig. S9), it is evident that after 100 CV cycles, the reduction in ECSA for AE-ZIF (8%) is less pronounced compared to the significantly decrease observed for A-ZIF (48%). This also indicates that AE-ZIF exhibits stronger resistance properties to continuous electro-oxidation.

The variation trend of O_2 evolution rates and reaction parameters during CV test is illustrated in Fig. 2c. Oxygen flow data are provided in real-time by an in-situ oxygen flow detection configuration connected to the electrolytic cell. For A-ZIF, the overpotential and Tafel slope reach the minimum at 50 cycles and then increase, exhibiting an inverted volcano-shaped curve. This implies that the optimal OER activity of A-ZIF occurs at 50 cycles, and an additional CV cycle leads to excessive structural reconstruction and degradation, thus decreasing the performance. In contrast, AE-ZIF stabilizes its overpotential and Tafel slope after 80 cycles, exhibiting higher electrocatalytic activity and O_2 evolution rate. Compared to other LE samples in Figs. S11 and S14, it can be inferred that AE-ZIF has the highest OER activity and electrical conductivity, as discussed in Supplementary Section S2.

According to the multistep potentiometry, samples A and AE exhibit relative potential fluctuations at certain current densities due to the reconstruction effects (Figs. 2d and S12a). Further combined with CV analysis, applying potentials of 1.05, 1.35 and 1.65 V to detect their time-dependent amperometry is reasonable (Fig. 2e and Fig. S12b, c). Evidently, the current density rapidly increases within the initial 2 h of OER, indicating rapid reconstruction of the ZIFs electrode, consistent with the CV analysis results. Subsequently, the current density and O_2 evolution rate of A-ZIF decrease continuously starting after 2.5 h, indicating ongoing reconstruction, ultimately losing 35.4% O_2 evolution rate after 12 h at 1.65 V. In contrast, the structural reconstruction in AE-ZIF ceased after 2 h and maintained a more stable current under constant potential or intermittent bias, exhibiting a current density and O_2 evolution rate that were an order of magnitude higher than those of A-ZIF (Fig. 2e and Fig. S13d).

Hence, combined with the collective insights from current density, O_2 evolution rate, conductivity, electrochemical impedance of other LE samples (Figs. S7–15, refer to Supplementary Section S2), the performance and structural reconstruction under electrocatalysis in as-prepared ZIFs are confirmed. The conclusion drawn is that AE-ZIF outperforms A-ZIF and other LE-ZIFs in both OER activity and electrochemical stability, with the process of self-reconstruction being effectively suppressed.

Structural evolution and reconstruction during electrocatalytic reaction

Figure 3a shows the disappearance of Bragg peaks belonging to sodalite-type ZIF-67 in the XRD pattern of A-ZIF within the CV cycles in

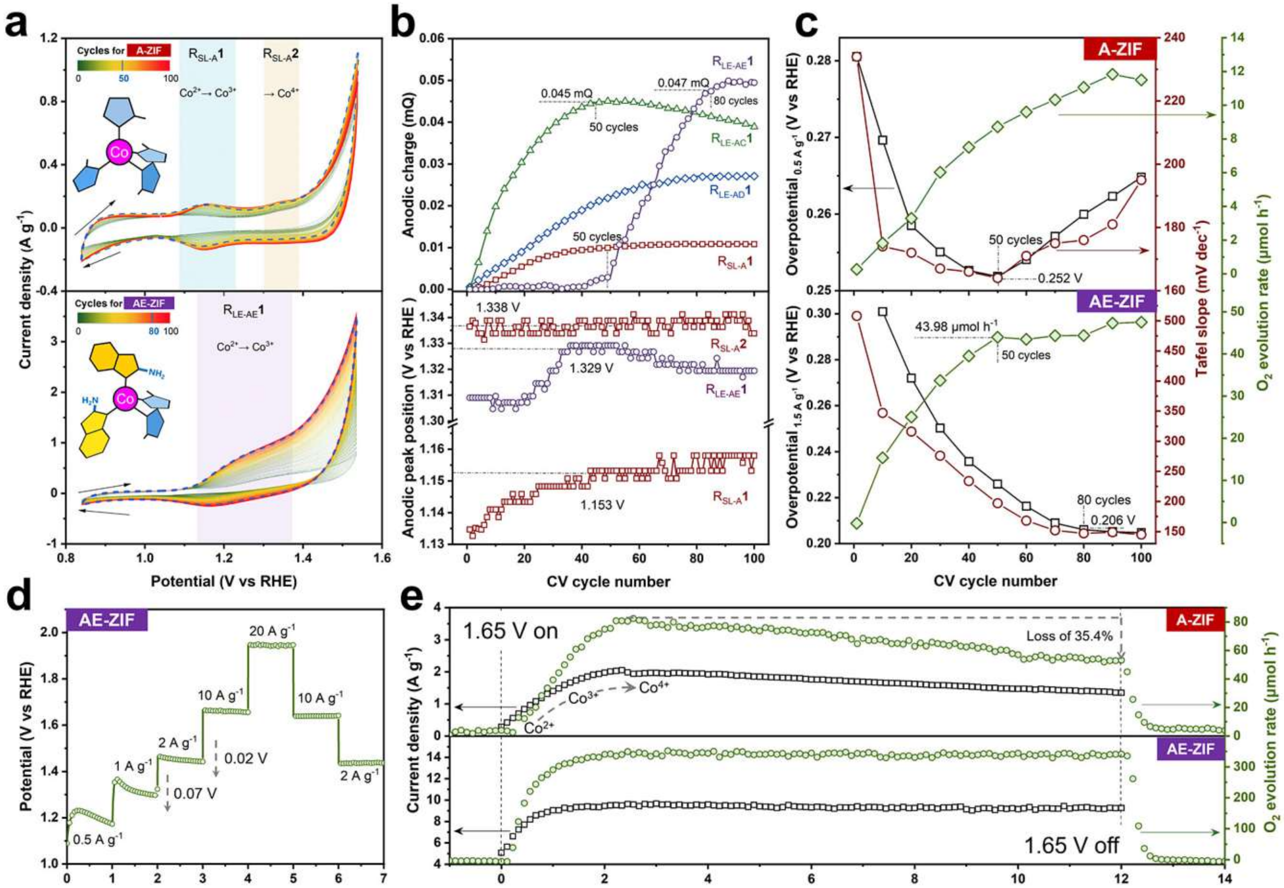

Fig. 2 | Cyclic voltammetry, potentiometry and amperometry of ZIFs. **a** Continuous cyclic voltammograms at high potential window between 0.85 to 1.55 V of A-ZIF and AE-ZIF. Dashed line is the current density maximum, the scan rate is 10 mV s^{-1}. **b** Anodic charge and peak position plots with CV cycles of A-ZIF and LE-ZIFs. **c** Overpotential (current density is 0.5 A g^{-1} for A-ZIF and 1.5 A g^{-1} for AE-ZIF), Tafel slope and O_2 reaction rate plots with CV cycles of A-ZIF and AE-ZIF. The calculation data for the Tafel slope are from Fig. S10. **d** Multistep potentiometric plot of AE-ZIF at different current densities. **e** Amperometric and O_2 evolution rate plots of A-ZIF and AE-ZIF at certain potentials of 1.65 V. All data were not calibrated with the iR correction, and the measurements were performed only once due continuous running.

the high potential window. At 50 CV cycles, additional peaks at 19.1° and 38.0° appeared that correspond to the (001) and (101) planes of $Co(OH)_2$[35]. Beyond 100 cycles, the $Co(OH)_2$ peaks disappeared while new diffractions arose at 19.9° and 39.1°, corresponding to the (003) and (101) planes of CoOOH, respectively[35,36]. These changes are mitigated to some extent upon limiting the scanning range of the CV to lower and medium potential windows.

In contrast, the well-defined XRD pattern of AE-ZIF was clearly preserved up to about 100 CV cycles, even in the high potential window, indicating superior stability under all used electrocatalytic conditions. On the other hand, AB-ZIF exhibited the lowest stability, characterized by complete amorphization (Fig. 3b). Samples AC and AD were relatively stable, retaining the Bragg peaks of ZIF under a high potential window. Note that AC-ZIF displays additional CoOOH peaks after 100 CV cycles, indicating a higher degree of electro-oxidation compared to AD and AE.

The structural changes were investigated in more detail by ^1H NMR. The spectra (Figs. S21–25) reveal that the ligand 2-mIm in A-ZIF disappeared almost completely upon cycling, indicating substitution of the original ligand. Conversely, AD and AE showed only a minor loss of secondary ligands of about 3–6 mol% (Table S3), the overall framework structure was largely preserved throughout the electrochemical cycling. This is also evident in the ATR-IR spectra taken after the reconstruction process, which still shows the stretching vibrations from Co-N and 2-mIm ligands in AE-ZIF even after 100 CV cycles, while they disappeared in A-ZIF after 50 cycles (Fig. S26).

Figure 3c, d summarize the results from X-ray photoelectron spectroscopy (XPS) analysis of the as-prepared ZIFs before and after electrocatalysis. The Co $2p_{3/2}$ spectra of A-ZIF show two peaks before the reaction, corresponding to Co^{2+} coordinated to N on the ligand (782.09 eV, red) and satellite peak (787.79 eV, blue)[37,38]. After 100 CV cycles in the medium or high potential ranges, a new distinct peak appeared at 779.14 eV (green) typically ascribed to Co^{3+} generated from Co^{2+} oxidation [39–41]. For comparison, no significant evolution of Co^{3+} was observed in A-ZIF in the low potential window. Note that electrochemical CV cycling induced a gradual decrease in the N/Co atomic ratio of A-ZIF from 3.9 – 2.4 at low potential and to zero in medium and high potential windows (Table S2). This supports the aforementioned framework degradation of A-ZIF which starts with Co-N cleavage at certain potentials. Concurrently, the N/O atomic ratio also decreases from 0.5 to zero, which is explained by the substitution of the 2-mIm ligand by hydroxide radicals (-OH) during the complete reconstruction (CR) process. This is further supported by the vanishing N *1s* signals corresponding to C-N (400.15 eV, blue) and Co-N (398.85 eV, red), respectively.

In contrast, samples AC, AD and AE show no apparent formation of Co^{3+}, even in the high potential window. Moreover, both signals in the N *1s* region remained unaltered (Figs. 3d, S19 and S20). Notably, the N/Co atomic ratio in AE-ZIF still decreased slightly from 4.5 to 3.6 at high potential window (with low and medium potentials being negligible). This suggests that the AE-ZIF electrode may undergo only partial substitution processes, i.e. such as occurring in the surface

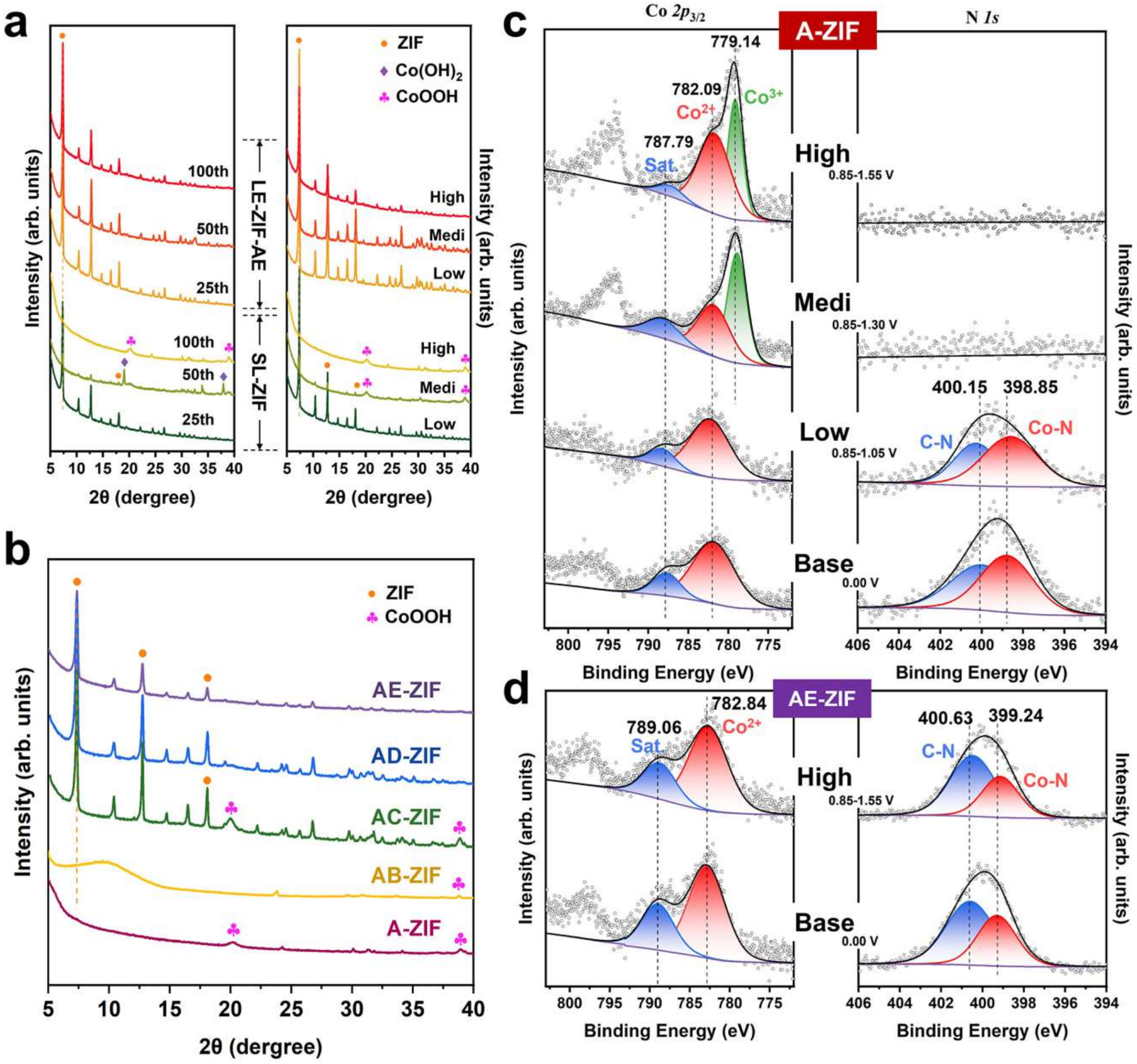

Fig. 3 | Structure evolution of ZIFs after electrocatalysis. **a** XRD patterns of A-ZIF and AE-ZIF with different CV cycles (25, 50 and 100) at 0.85–1.55 V, with 100 CV cycles at different potential windows (Low: 0.85–1.05 V, Medi: 0.85–1.30 V, High: 0.85–1.55 V). **b**, XRD patterns of A-ZIF, AB-ZIF, AC-ZIF, AD-ZIF and AE-ZIF with 100 CV cycles at 0.85–1.55 V. **c**, **d** Co $2p_{3/2}$ and N *1 s* of XPS spectra for A-ZIF (**c**) and AE-ZIF (**d**) with 100 CV cycles at different potential window (Low: 0.85–1.05 V, Medi: 0.85–1.30 V, High: 0.85–1.55 V), for whole sample scan see Fig. S17.

reconstruction (SR) process rather than the no-reconstruction (NR) process. The absence of new signals in the Co $2p_{3/2}$ spectra may be attributed to the incomplete detection caused by the low content of oxygenated Co species in AE-ZIF after the SR process. As predicted, the disappearance of XPS signals in AB-ZIF indicates the degradation of framework structure (Fig. S18), as discussed in Supplementary Section S3.

Transmission electron microscopy (TEM) and energy-dispersive spectrum (EDS) provide more insights into the structural reconstruction and elemental composition of each ZIF particles after 12 h amperometry. In accordance with predictions from XRD and XPS analysis, A-ZIF fails to maintain the dodecahedral morphology and crystal structure post-reaction, as illustrated in Figs. S27 and S28. The morphology ultimately transforms into nanosheets with lattice fringes characteristic of Co(OH)$_2$ and CoOOH, as confirmed by the bright spotting in the selected-area electron diffraction (SAED) pattern[42,43]. The XRD pattern of post-reaction also confirms the presence of high-valence cobalt oxides (Fig. S16). Elemental mapping through EDS reveals a homogeneous distribution of Co and O elements within the nanosheets as the dominant elements (Fig. S28d), confirming the conversion into (oxy)hydroxide during amperometry.

In contrast, the TEM images of AE-ZIF pre- and post-reaction clearly showcase the particles retain their typical dodecahedral morphology. Importantly, after amperometry, the edges of the AE-ZIF particle are no longer sharp, and the presence of a distinct thin layer suggests the formation of a core-shell structure (Fig. 4a–e). Elemental mapping reveals a noticeable decrease in N and C and a significant increase in Co and O concentration in the shell region, contrasting the homogeneous distribution of each element observed pre-reaction (Fig. 4c and f). The bright spots in the corresponding selected-area fast Fourier transform (FFT) patterns and lattice fringes further confirm the crystalline characters of the outer layer as cobalt (oxy)hydroxide (Figs. 4e and S30). These results suggest that in-situ reconstruction occurs exclusively on the outermost surface of AE-ZIF, eventually

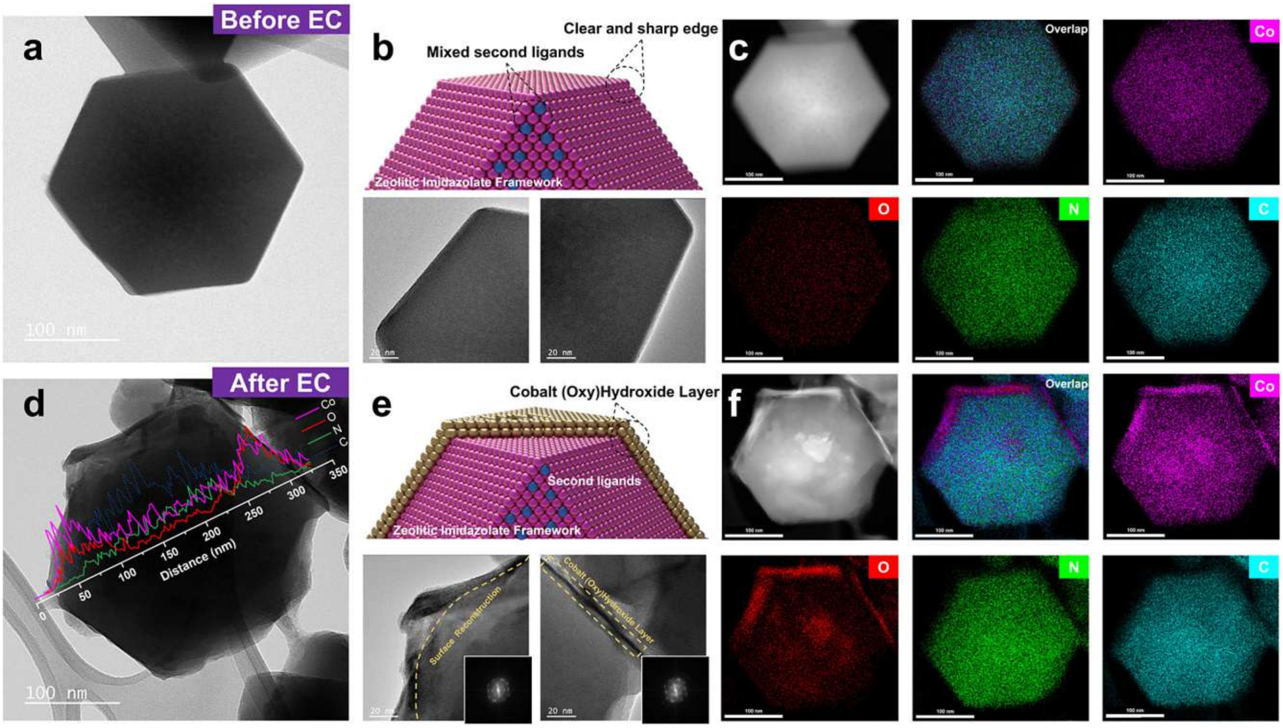

Fig. 4 | Morphology evolution of AE-ZIF after electrocatalysis. a, **d** TEM images of single-particle AE-ZIF before (**a**) and after 12 h amperometry (**d**). **b**, **e** Schematic diagrams and enlarged TEM images of AE-ZIF edge before (**b**) and after 12 h amperometry (**e**), the lower corresponding FFT patterns. **c**, **f** Elemental mapping of single-particle AE-ZIF before (**c**) and after (**f**) 12 h amperometry showing the Co, O, N and C distribution.

yielding a thin stable (oxy)hydroxide layer without affecting the core structure. Morphological and elemental composition of other AC and AD after the amperometry also reveals similar core-shell structures through TEM and EDS analysis (Figs. S27–33, refer to Supplementary Section S4).

The combined results clearly indicate that the in-situ formation of a cobalt (oxy)hydroxide layer on the particle surface effectively suppresses the self-reconstruction process, contributing to the outstanding electrochemical stability and OER activity in AE-ZIF.

In-situ electrochemical spectroscopy analysis

In-situ electrochemical UV–Vis absorption and Raman spectroscopy was used to gain a clearer understanding of the underlying electro-oxidation process. Similar to the electrocatalytic studies mentioned above, a three-electrode configuration was employed for all electrochemical cells, with ZIFs drop-casted onto the working electrode using the same approach (Figs. 5a and S34). The working electrode remains an FTO glass to allow penetration of UV–Vis and fluorescence light, enabling the reception of structural signals by the spectra receiver.

Figure 5b compares the UV–Vis absorption trends of A and AE during 100 CV cycles, while the other LE samples are shown in Fig. S35a–c. Sample A-ZIF exhibits a distinctive broad signal in the 500–650 nm range, which can be fitted to 539, 567 and 589 nm as spin-orbital coupling triplet peaks, representing the transition of tetrahedral Co species from $^4A_2(F)$ to $^4T_1(P)$[32]. With increasing CV cycles, the intensity of the triplet peaks in A-ZIF rapidly decreases at high potential window, completely disappearing after 40 cycles. This indicates the degradation of the Co-$(mIm)_4$ tetrahedral structure, which is mitigated in the low and medium potential windows (Fig. S35d, e). The broad signal associated with tetrahedral Co species in AE-ZIF remains nearly unchanged, indicating higher electrochemical stability, consistent with the conclusions drawn from our previous electrocatalytic and ex-situ characterization analyses.

In-situ electrochemical Raman spectroscopy provides further sensitivity to unveil the reconstruction of as-prepared ZIFs during electrochemical treatments. The characteristic peaks at 126 – 313 cm^{-1} and 425 cm^{-1} are typically assigned to the vibrational modes of the stretching vibrations of ligand 2-mIm and Co-N bonds within sodalite-type ZIF-67 (Fig. 5c)[44–46]. As the applied potential gradually increases, the intensity of ligand signals in A-ZIF decreases and eventually disappears at 1.40 V. Commencing from 1.20 V, new peaks appear at 498, 535, 586 and 632 cm^{-1}, which can be assigned to the vibration modes of $Co(OH)_2$ and CoOOH, respectively[47–49]. Furthermore, the peak at 801 cm^{-1} can be attributed to surface-adsorbed *O-OH species by O-O stretch[50]. Subsequent to 1.55 V, the peak intensity of $Co(OH)_2$ nearly disappears, while the CoOOH peak remains unaltered, corresponding to electro-oxidation process $Co^{2+} \rightarrow Co^{3+} \rightarrow Co^{4+}$ within A-ZIF derived from previous experiments.

In contrast, AE-ZIF shows only weak peaks of $Co(OH)_2$ (498 cm^{-1}) and CoOOH (617 cm^{-1}) after 1.35 V and, importantly, no discernible changes of the inherent ligand signals. Note that the CoOOH peak in AE-ZIF is comparatively weak and broad, indicating its confinement to the surface of the particles, which also accounts for the undetectability of Co^{3+} signal in XPS analysis. The appearance of (oxy)hydroxide signals is thus related to the in-situ formation of a protective thin layer on the AE-ZIF surface during the SR process, in line with the CV and TEM results (Figs. 2 and 4). The decrease in peak intensity after 1.60 V is attributed to the O_2 evolution of gas bubbles on the FTO electrode surface, affecting the signal reception of the Raman laser. Similarly, continuous CV tests show the CR in A-ZIF starting at 20 cycles, whereas SR in AE-ZIF is postponed, indicating mixed-ligand AE-ZIF has superior stability (Fig. 5d). For other LE samples, the ligand signals are also well-preserved in the AC and AD, whereas in AB-ZIF, they rapidly disappear as the reaction progresses (Figs. S36 and S37, refer to Supplementary Section S5).

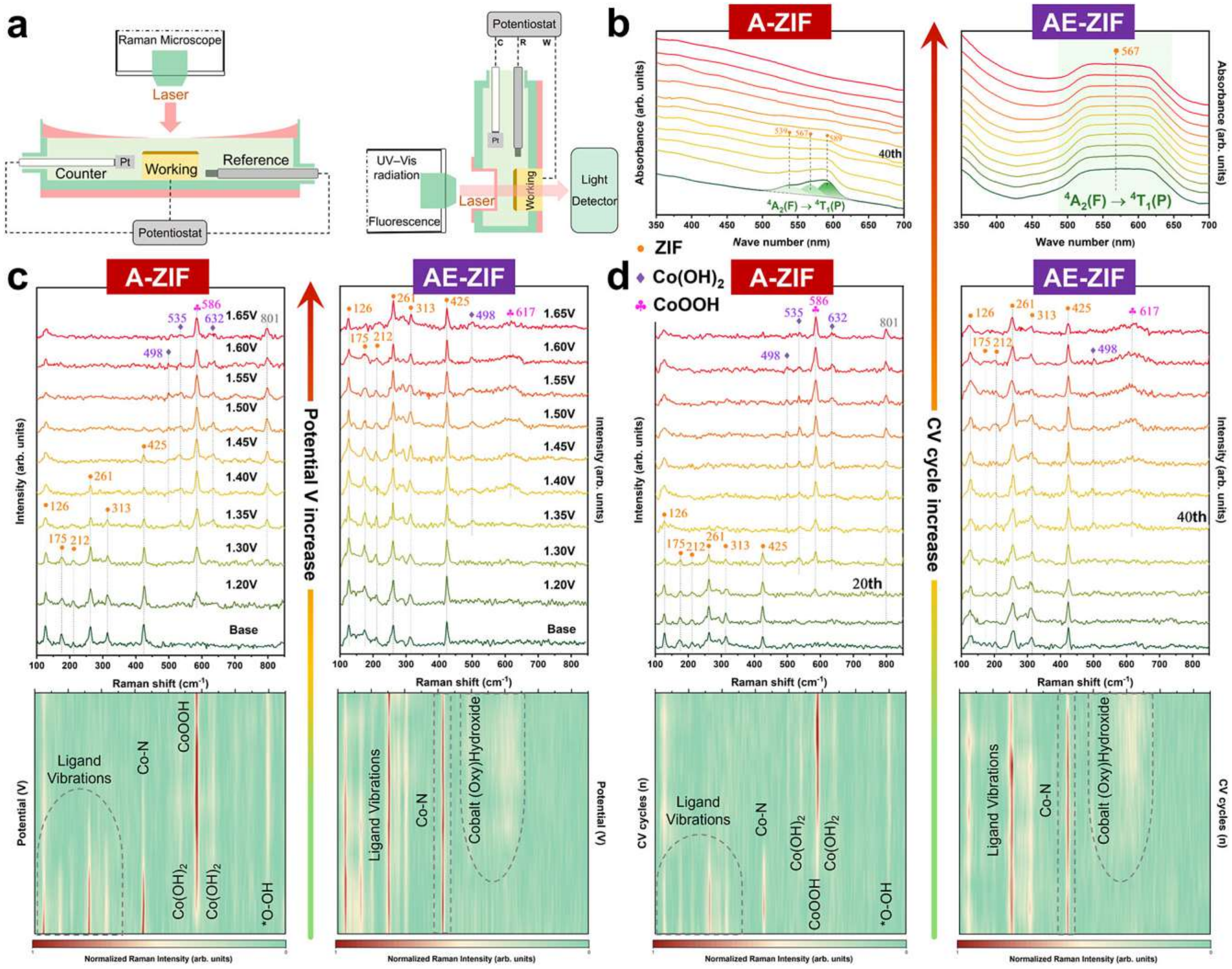

Fig. 5 | Structural reconstruction of as-prepared ZIFs by in-situ spectro-electrochemical analysis. a Cell schematic diagram in the three-electrode configuration of in-situ electrochemical Raman and UV–vis absorption spectroscopy. **b** In-situ electrochemical UV–Vis absorption spectroscopy of A-ZIF and AE-ZIF with 100 CV cycles at 0.85–1.55 V. **c** In-situ electrochemical Raman spectroscopy and 2D contour plots of A-ZIF and AE-ZIF at various applied potentials from 1.20 – 1.65 V. **d** In-situ electrochemical Raman spectroscopy and 2D contour plots of A-ZIF and AE-ZIF with 100 CV cycles at 0.85–1.55 V.

Comprehensive analysis of photoelectrocatalytic activity, photoluminescence, and band gaps

In the field of light-absorbing materials, Co-based ZIFs have garnered attention for their inherent capability to absorb visible light. Integrating electro- with photocatalysis, referred to as photoelectrocatalysis, presents a promising avenue for augmenting the OER activity of ZIFs. Moreover, the imposition of an applied potential serves as an effective strategy to prevent the recombination of photogenerated electron-hole (e^-/h) pairs[51]. As anticipated, samples A and AE demonstrate visible light photoelectrocatalytic capabilities; however, their current density and O_2 evolution rate have markedly different variation trends due to the reconstruction effect (Fig. 6).

Figure 6a illustrates the outcomes of in-situ electrochemical photoluminescence (PL) analysis. The inherent PL peak of A-ZIF are clearly blue-shifted from 566 to 482 nm after 40 CV cycles, showcasing the phase transition by the CR process, consequently altering its fluorescence properties[52]. Similarly, the band gaps obtained through UV–vis absorption spectroscopy and Mott–Schottky plots[53] exhibit a consistent trend, increasing from 1.75 eV at the beginning to 2.75 eV after 40 CV cycles accompanied by a significant gap widening (Fig. 6b and Fig. S38). Current density and O_2 evolution rate both increase upon visible light exposure at the early stages, but decrease after only 2 h, eventually (after 6 h) approaching values similar to those obtained under dark conditions (Fig. 6c). This phenomenon is clearly linked to the CR process in A-ZIF during electrocatalysis, which leads to a loss of the inherent visible light absorption capability along with an increase in band gap.

In contrast, current density and O_2 evolution rate of AE-ZIF remain highly stable upon illumination throughout 12 h amperometry, which underlines that the impact of light exposure on the structural and catalytic stability is negligible (Fig. 6c). Notably, within the initial hour of amperometry, the AE-ZIF even shows a rapid rise in efficiency during in-situ formation of cobalt (oxy)hydroxide layer through the SR process. Subsequently, the efficiency stabilizes before it eventually experiences a comparatively small decrease of only 7.4% after 12 h. Note that under illumination, AE-ZIF yields a stable current density of 16.3 A g^{-1} and an O_2 evolution rate of 570.8 μmol h^{-1}, which is twice that observed under dark conditions (Fig. 2e). The stable performance of AE-ZIF in contrast to A-ZIF can further be linked to the band gap and PL intensity, which experience only a small decrease from 1.35 to 1.21 eV, as only surface reconstruction occurrs (Fig. 6d, e and Fig. S39). Samples AC and AD exhibit visible-light catalytic activity, whereas the AB-ZIF has none, primarily attributed to an excessively wide band gap (Figs. S38–45, refer to Supplementary Section S6).

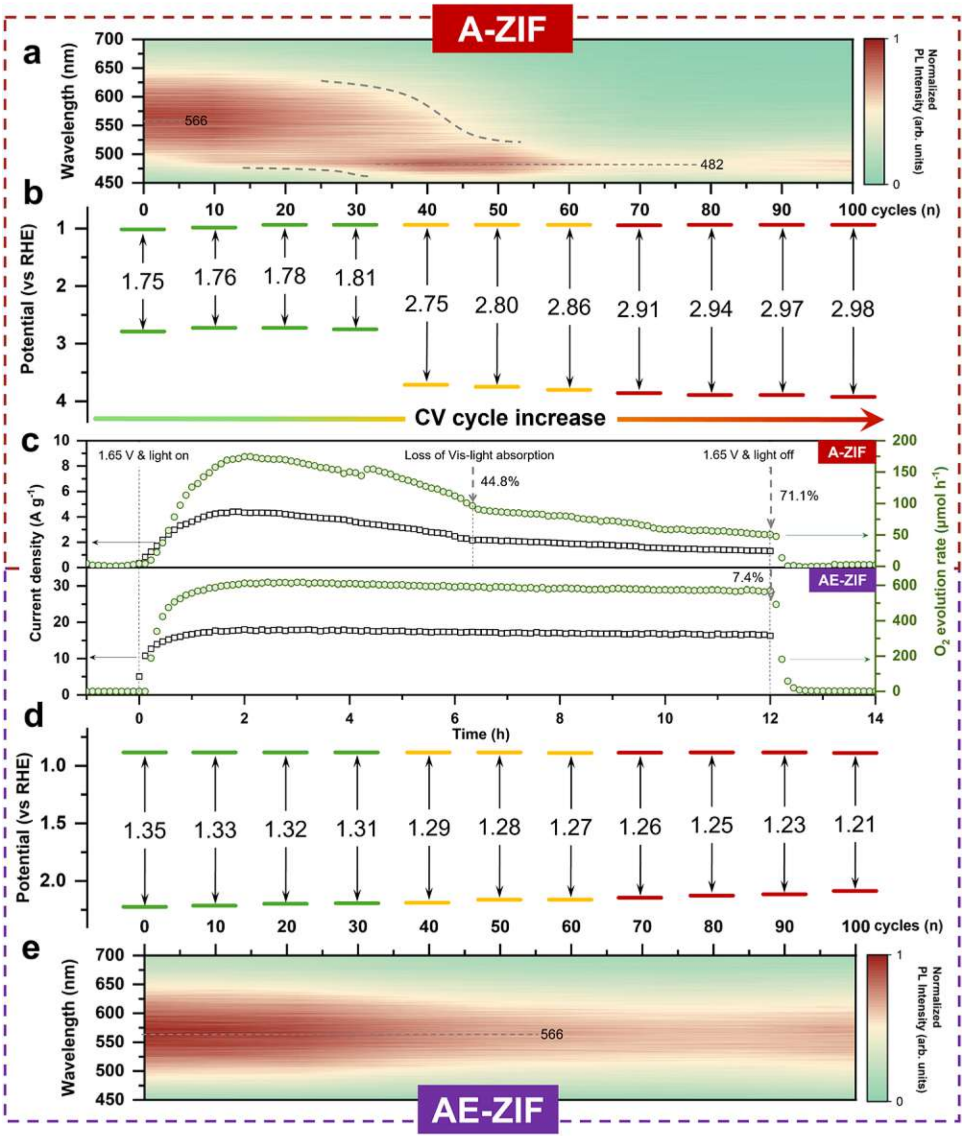

Fig. 6 | **Photoelectrocatalytic OER activity, PL intensity and band gaps. a**, **b** In-situ electrochemical Photoluminescence spectroscopy (**a**) and band potential diagram (**b**) of A-ZIF with 100 CV cycles at 0.85–1.55 V. **c** Amperometric plots and O_2 evolution rates of A-ZIF and AE-ZIF at certain potentials of 1.65 V and visible light. **d**, **e** Band potential diagram (**d**) and in-situ electrochemical PL spectroscopy (**e**) of AE-ZIF with 100 CV cycles at 0.85–1.55 V.

DFT simulation and Mechanistic Study of Ligand-engineered ZIFs as (photo)electrocatalysts

In the preceding analysis, samples A and AB undergo the CR process, leading to the formation of additional phases, i.e. (oxy)hydroxide nanosheets in A-ZIF and an amorphous phase in AB-ZIF. This is accompanied by a considerable change in surface area, band gap, morphology and OER activity. Conversely, samples AC, AD and AE undergo the SR process within the initial 2 h reaction, forming a cobalt (oxy)hydroxide layer on the outermost shell without compromising the internal framework structure. This surface limitation preserves their electrochemical stability during 12 h amperometry, as well as their optoelectronic properties and band gap. Among these samples, AE-ZIF demonstrated the highest OER performance and stability.

To elucidate the fundamental reasons for the activity-stability differences among various LE-ZIFs in electrocatalysis, density functional theory (DFT) calculations were performed using optimized models with about 30% mixed-ligands (Fig. 7a). The density of states (DOS) for LE-ZIF models in Fig. 7b reveal that the upper spins of AC, AD and AE are closer to the Fermi level compared to A and AB, indicating their electron structures likely are more conductive, which aligns well with the experimental results. This can be attributed to the π-π stacking aromatic carbon rings from the secondary ligands (C, D and E) in the crystal as conductive pathway, enhancing the electrical conductivity[28,54]. Furthermore, the energy difference (ΔE) between ε_d (Co band center) and ε_p (N band center) of AE-ZIF is the lowest at 1.33 eV, followed by AD-ZIF at 1.45 eV, while AB-ZIF exhibits the highest at 4.56 eV (Fig. S51 and Table S4). According to previous studies[55,56], this suggests that the Co-N in AE-ZIF has the strongest orbital hybridization and greatest covalency, facilitating electron transfer between Co and N atoms. Similarly, the additional electron adsorption of the -NH_2 group in ligand E also contributes favourably to electrocatalytic reaction, and thereby improving the overall OER performance[57,58].

Further DFT calculations were performed by connecting ligands A and E into the CoOOH model. The charge density difference diagram in Fig. 7c shows that ligand E exhibits a more concentrated electron density at the Co-N-O interface compared to original ligand A. Moreover, the Gibbs free energy was also calculated for each elementary step for OER, using the adsorbate evolution mechanism (AEM). Upon

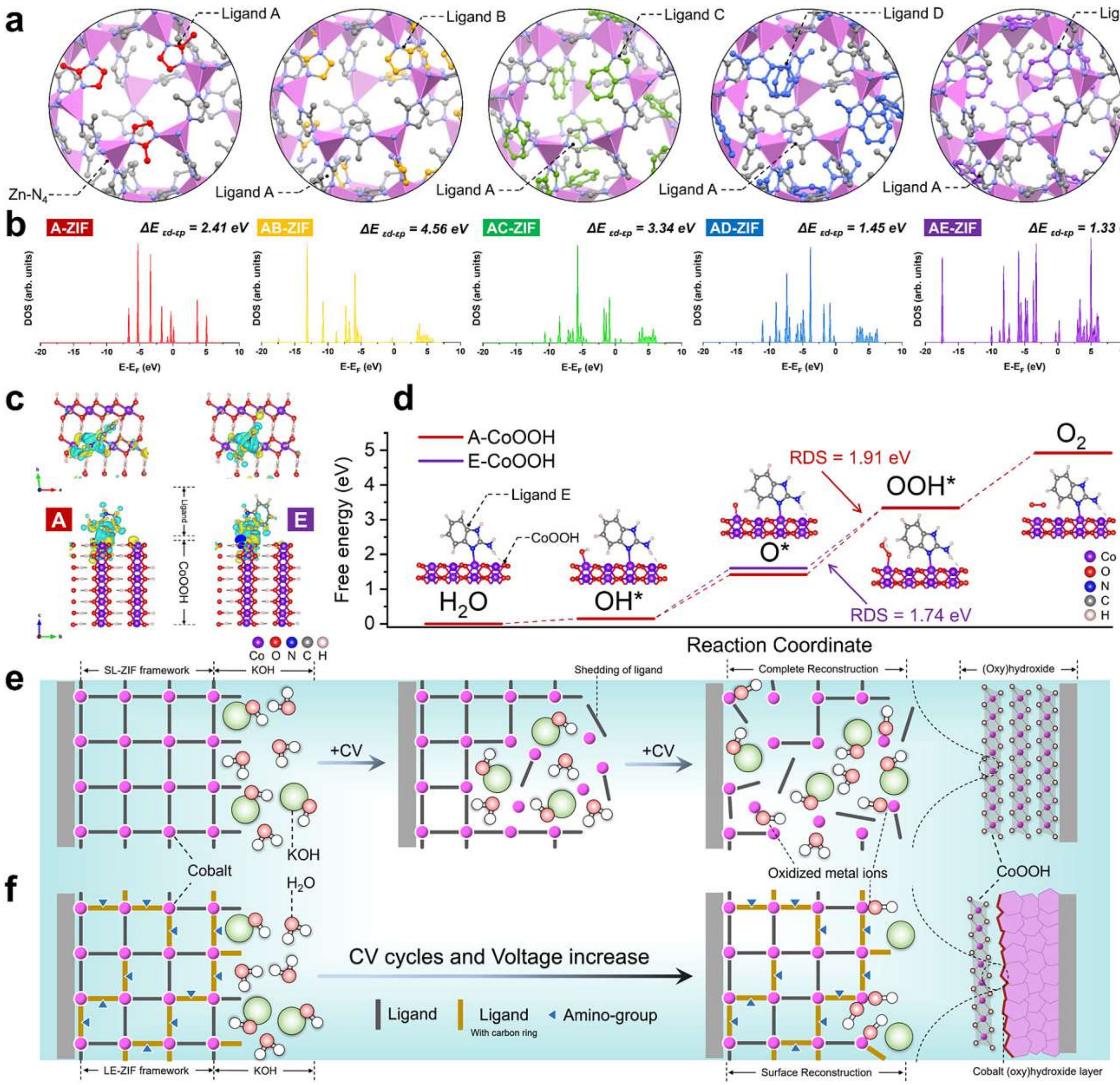

Fig. 7 | DFT simulations and mechanisms diagram of as-prepared ZIFs reconstruction. **a**, **b** Optimized model structures (**a**) and calculated total DOS (**b**) of A-ZIF, AB-ZIF, AC-ZIF, AD-ZIF and AE-ZIF. **c** Charge density difference of the CoOOH incorporating ligands A and E models. **d** Free energies diagram of the CoOOH incorporating ligands A and E models. More details of the structure models and the free energy calculation steps are provided in Figs. S46–54, Supplementary Data 1, and Supplementary Data 2. **e**, **f** Schematic diagram of the complete reconstruction mechanism (**e**) and surface reconstruction mechanism (**f**) in (photo)electrocatalytic reaction.

incorporating ligand E, the energy barrier for the rate-determining step (RDS, O* oxidized to OOH*) of CoOOH model decreases from 2.02 eV to 1.74 eV, lower than ligand A at 1.91 eV (Fig. 7d and Fig. S54). This implies there is likely a synergistic interaction between the ligand E and CoOOH at the reconstructed interface. In summary, the ligand E mixed in AE-ZIF probably play a vital role enhancing OER activity, featuring both additional -NH_2 groups and π-π stacking aromatic carbon rings, which provide superior electronic absorption and transfer capabilities compared to ligands B, C and D.

Figure 7e shows a schematic representation of the CR mechanism as occurring in A and AB. Upon weakening of the ligand coordination, the Co species either leach into the solution or directly react with OH^- ions from the alkaline electrolyte to form (oxy)hydroxide compounds. This phase transition process is associated with changes in morphology and surface chemistry that result in a complete loss of porosity as well as a decrease in the number of available active sites and, consequently, activity towards electrocatalytic OER. Moreover, this conversion leads to an increase in band gap and, thus, a loss of ability to absorb visible light.

On the other hand, the SR mechanism inherent to AC, AD and AE is depicted in Fig. 7f. Here, the framework structure is largely preserved due to the stronger ligand-metal coordination due to the added secondary ligand, as represented by lower potential energies. Therefore, the phase transformation to CoOOH is confined to a thin layer on the particles surface (Fig. 4e). After 2 h, the activity tends to stabilize, indicating the establishment of a stable protective core-shell structure, with the inner layer as the core retaining the inherent framework structure. Outer (oxy)hydroxide layer enables to maintain the electrode durability during electrocatalysis in alkaline environment, enhancing conductivity and promoting electron transport under large current density[49,59].

Discussion

In summary, we have constructed a series of mixed-ligand ZIF catalysts through ligand engineering to investigate the (photo)electrocatalytic OER mechanisms in alkaline environments. Among these catalysts, AE-ZIF engineered with ligand 2-aminobenzimidazole, showcased electrocatalytic activity that was an order of magnitude higher than the single-ligand A-ZIF, with an 8-fold increase in current density and a 7-fold increase in O_2 evolution rate. Similarly, the same behaviour was observed in photoelectrocatalysis, with performance of AE-ZIF under visible light about doubling compared to dark conditions.

Incorporating the secondary ligand, particularly in AE-ZIF, significantly enhances the structural robustness in (photo)electrocatalytic cases, maintaining electrochemical stability for at least 12 h compared to the degradation observed in single-ligand A-ZIF after only 2 h. Advanced electrochemical techniques, including in-situ UV–vis absorption, Raman and Photoluminescence spectroscopy, reveal a complete mechanism induced by the addition of a secondary ligand.

Samples A-ZIF and AB-ZIF undergo complete reconstruction leading to the formation of additional phases, i.e. (oxy)hydroxide nanosheets and an amorphous phase, resulting in significant loss of porosity, electrical conductivity and visible light absorption capabilities. In contrast, mixing a secondary ligand with π-π stacking aromatic carbon rings, i.e AC-ZIF, AD-ZIF and AE-ZIF, largely preserved the inherent framework structure and porosity, forming a thin stable (oxy)hydroxide layer on the particle surface. This outer layer effectively protected and passivated the ZIF framework, by creating a more stable core-shell structure.

Theoretical calculations further underscored the synergistic effect between the secondary ligand and the (oxy)hydroxide layer, which likely accelerates electron transfer and reduce Gibbs free energy, ultimately enhancing overall OER activity. Additionally, the unique functional groups (aromatic carbon ring and amino group) in the secondary ligands can improve the electronic conductivity and strengthened the Co-N covalency. This mixed-ligand engineering has achieved notable enhancements and offers a feasible pathway for designing more active and stable ZIFs, extending applications beyond electro- and photoelectrocatalysis.

Methods

Chemicals

Cobalt nitrate hexahydrate ($Co(NO_3)_2·6H_2O$, 99%, STREM), 2-methylimidazole (2-mIm, $C_4H_6N_2$, 99%, Sigma-Aldrich), 1H-Imidazol-2-amine (NH_2-mIm, $C_3H_5N_3$, 97%, BLD pharm), Benzimidazole (bIm, $C_7H_6N_2$, 98%, Sigma-Aldrich), 2-methylbenzimidazole (2-bIm, $C_8H_8N_2$, 98%, abcr GmbH), 2-aminobenzimidazole (NH_2-bIm, $C_7H_7N_3$, 97%, Sigma-Aldrich), Methanol (MeOH, 99.9%, HiPerSolv CHROMANORM, VWR), Postassium hydroxide (KOH, 85%, Sigma-Aldrich), Nafion™ perfluorinated resin solution (nafion, 5 wt.%, Sigma-Aldrich), d_4-acetic acid for NMR (CD_3CO_2D, 99.4%, Thermo scientific).

A-ZIF

2 g of 2-mIm was dissolved in 10 ml of HPLC methanol, while 0.87 g of $Co(NO_3)_2·6H_2O$ was dissolved in 10 ml of HPLC methanol. The two solutions were then mixed in microwave synthesis reactor (Monowave 300, Anton Paar), at 150 °C for 2 h to accelerate the growth of A-ZIF crystals. After being allowed to deposit for 24 h, the powder was centrifuged, washed three times with methanol and DI water, and then vacuum dried in an oven overnight, resulting in a purple A-ZIF powder.

AB-ZIF

1 g of NH_2-mIm and 1 g of 2-mIm were mixed into 10 ml of HPLC-grade methanol. The solution was placed into a microwave synthesis reactor (Monowave 300, Anton Paar) and heated to 100 °C for 30 min to ensure even mixing and dissolution of the ligands. Meanwhile, 0.87 g of $Co(NO_3)_2·6H_2O$ was dissolved in 10 ml of HPLC-grade methanol, sonicated for 10 min, and stirred for 30 min. The two solutions were then combined and heated in the microwave synthesis reactor at 150 °C for 2 h to accelerate the growth of ZIF crystals. After 24 h of deposition, the resulting powder was centrifuged and washed three times with methanol and deionized water. Finally, AB-ZIF was obtained by vacuum drying overnight.

AC-ZIF

1 g of bIm and 1 g of 2-mIm were mixed into 10 ml of HPLC-grade methanol. The solution was placed into a microwave synthesis reactor (Monowave 300, Anton Paar) and heated to 100 °C for 30 min to ensure even mixing and dissolution of the ligands. Meanwhile, 0.87 g of $Co(NO_3)_2·6H_2O$ was dissolved in 10 ml of HPLC-grade methanol, sonicated for 10 min, and stirred for 30 min. The two solutions were then combined and heated in the microwave synthesis reactor at 150 °C for 2 h to accelerate the growth of ZIF crystals. After 24 h of deposition, the resulting powder was centrifuged and washed three times with methanol and deionized water. Finally, AC-ZIF was obtained by vacuum drying overnight.

AD-ZIF

1 g of 2-bIm and 1 g of 2-mIm were mixed into 10 ml of HPLC-grade methanol. The solution was placed into a microwave synthesis reactor (Monowave 300, Anton Paar) and heated to 100 °C for 30 min to ensure even mixing and dissolution of the ligands. Meanwhile, 0.87 g of $Co(NO_3)_2·6H_2O$ was dissolved in 10 ml of HPLC-grade methanol, sonicated for 10 min, and stirred for 30 min. The two solutions were then combined and heated in the microwave synthesis reactor at 150 °C for 2 h to accelerate the growth of ZIF crystals. After 24 h of deposition, the resulting powder was centrifuged and washed three times with methanol and deionized water. Finally, AD-ZIF was obtained by vacuum drying overnight.

AE-ZIF

1 g of NH_2-bIm and 1 g of 2-mIm were mixed into 10 ml of HPLC-grade methanol. The solution was placed into a microwave synthesis reactor (Monowave 300, Anton Paar) and heated to 100 °C for 30 min to ensure even mixing and dissolution of the ligands. Meanwhile, 0.87 g of $Co(NO_3)_2·6H_2O$ was dissolved in 10 ml of HPLC-grade methanol, sonicated for 10 min, and stirred for 30 min. The two solutions were then combined and heated in the microwave synthesis reactor at 150 °C for 2 h to accelerate the growth of ZIF crystals. After 24 h of deposition, the resulting powder was centrifuged and washed three times with methanol and deionized water. Finally, AE-ZIF was obtained by vacuum drying overnight.

ZIF@FTO glass electrode

The ZIF powders are prepared by drop-casting onto the fluorine-doped tin oxide (FTO) glass surface. To prepare the mixture, 3 mg of the ZIF samples are combined with 280 μl of HPLC methanol and 20 μl of nafion solution, and the mixture is sonicated for 30 min. Subsequently, the mixed solution is dropped onto the surface of the three FTO glass (1 cm × cm). This entire process is repeated to obtain three ZIF@FTO electrodes. Finally, the ZIF@FTO electrodes are placed in a vacuum oven and dried overnight. The same procedure is applied to prepare electrodes for each ZIF@FTO sample.

Material characterizations

X-ray diffraction (XRD) were carried out using a PANalytical X'Pert Pro multi-purpose diffractometer (MPD) with Bragg Brentano geometry, equipped with a Cu anode at 45 kV and 40 mA, a BBHD Mirror, and an X-Celerator multichannel detector[60]. X-ray photoelectron spectroscopy were carried out using a custom-built SPECS XPS spectrometer, featuring a monochromatized Al-Kα X-ray source (μFocus 350) and a hemispherical WAL-150 analyzer (acceptance angle: 60°)[61]. The high-resolution transmission electron microscopy (TEM) images presented in this paper were acquired on a Tecnai F20 FEG-TEM at USTEM (university service center for transmission electron microscopy) at TU Wien, equipped with an X-FEG, a Gatan Rio16 CCD-camera, a Gatan DigiSTEM II with HAADF detector for STEM imaging, and an EDAX-AMETEK Apollo XLTW SDD EDX-detector. Liquid phase Nuclear magnetic resonance spectroscopy (NMR) was conducted using a Bruker ADVANCE 250 (250.13 MHz) instrument, equipped with a 5 mm inverse-broad probe head and z-gradient unit[29].

In-situ electrochemical Raman spectroscopy was performed with a HORIBA LabRAM spectrometer with a 532 nm laser, in-situ electrochemical UV–Vis absorption spectroscopy was obtained at 350–700 nm by Jasco V-670, and in-situ electrochemical Photoluminescence spectroscopy was carried out with a PicoQuant FluoTime 300 spectrophotometer[60]. All in-situ measurement were conducted within a three-electrode configuration, with the working electrode securely positioned in a specialized electrolytic cell. For more characterization details as described in the Supplementary Section S8.

(Photo)electrochemical measurements

Potentiostats (Autolab AUT85726 and CHI 760E) are used to perform all electrochemical experiments in a three-electrode configuration. Electrocatalytic cell used in the experiments was a 231 mL sourced from PerfectLight, Ltd. A saturated Ag/AgCl serving as the reference electrode, and a Pt electrode serves as the counter electrode; both are sourced from Gaoss Union, Ltd. 1 M KOH solution is used as the electrolyte (pH13.721 ± 0.01), prepared by dissolving an appropriate amount of potassium hydroxide in deionized water, then saturated it with nitrogen gas and stored it at room temperature. The working electrode consists of ZIF@FTO glass, including all in-situ electrochemical measurements. The potential is converted to the reversible hydrogen electrode (RHE) using the Nernst equation: $E_{RHE} = E_{Ag/Ag/Cl} + 0.21 + 0.059 \times \mathrm{pH}$. Cyclic voltammetry (CV) cycles are tested at a scan rate of 10 mV s^{-1}. Three potential windows are selected: a low potential window of 0.85–1.05 V, a medium potential window of 0.85–1.30 V, and a high potential window of 0.85–1.55 V (vs. RHE). Electrochemical impedance spectroscopy (EIS) is measured with a frequency range from 10^5 – 0.1 Hz. All data are not calibrated with the iR correction.

Conversion formula for the current density unit of each samples from A g^{-1} to mA cm^{-2} is: 3.33 A g^{-1} = 10 mA cm^{-2}. Using this formula, the overpotential for AE-ZIF at 10 mA cm^{-2} is 0.3 V, while A-ZIF only reaches 2 mA cm^{-2} at the same potential.

In-situ O_2 flow detection configuration was employed an argon gas to continuously purge the cell reactor (same cell as electrocatalysis) at a flow rate of 30 mL min^{-1}, delivering O_2 to the X-stream analyzer (Emerson Process Management). The O_2 concentrations (ppm) measured in the stream is converted to the O_2 evolution rate (μmol h^{-1}) by the ideal gas equation.

Photoelectrocatalytic experiments were performed using visible light (400–700 nm, 2.36 W) from SUPERLITE SUV-DC-E (Lumatec) as a visible light source.

Electrochemical surface area (ECSA) is directly proportional to its electrochemical double-layer capacitance according to the following equation: $\mathrm{ECSA} = C_{dl}/C_s$, where C_s is the specific capacitance of the sample, 1 M KOH is usually taken with C_s assumed to be 0.04 mF cm^{-2} [62]. C_{dl} is the electrochemical double-layer capacitance of the sample, estimated according to the above CV curves of the non-Faraday region[63].

Electrical resistance of each ZIF@FTO samples were estimated using a two-probe measurement method with the probes positioned primarily on the FTO glass. The conversion equation for electrical conductivity (σ) and resistance (R) is $\sigma = l/RA$, where l is the thickness of the ZIFs, and A is the area covered by the ZIFs[64].

Reference electrode preparation and calibration, first the silver wire was ground using 240-grit SiC sandpaper, then rinsed with deionized water, and dipped into a 1 M HCl solution. The electrochemical deposition of AgCl was then conducted with the following setup: CV test with a scan from 0.7 to 0.2 V (vs. Ag/AgCl/3 M KCl) for 10 cycles, followed by amperometry at 0.3 V for 2 min, and another test at 0.7 V for 15 min.

Calculation of band gap, LUMO, and HUMO

Band gap was calculated with the equation proposed by Tauc/Davis and Mott et al.:

$$(\alpha h\upsilon)^{1/n} = A(h\upsilon - E_g)$$

Where α is absorbance index, h is Planck's constant, υ is the frequency, A is a constant, E_g is the semiconductor band gap, and n is related to the related to band gap type ($n = 1/2$ for direct band gap and $n = 2$ for indirect band gap)[32].

Flat band potential was calculated with the following equation:

$$\frac{1}{C_{sc}^2} = 2\left(\frac{\triangle\Phi_{\mathrm{sc}} - RT/F}{q\varepsilon\varepsilon_0 N}\right)$$

Where C_{sc} is the charge capacitance, $\Delta\Phi_{\mathrm{sc}}$ is the absolute value of difference between the electrode potential and the flat band potential, ε is the relative dielectric constant, ε_O is the vacuum dielectric constant, N is the donor (for n-type semiconductor) or acceptor (for p-type semiconductor) density[32]. The flat band potential, determined as the point where the tangent of the Mott–Schottky plot intersects the horizontal axis, is about equal to the position of the lowest unoccupied molecular orbital (LUMO) potential for ZIFs, which behave similarly to n-type semiconductors[65]. Highest occupied molecular orbital (HOMO) potential can be then calculated based on the known LUMO potential and their band gap.

Density functional theory (DFT) calculations

All calculations were conducted using Vienna ab initio program package (VASP)[66]. Electron exchange and correlation effects were described using the Perdew-Burke-Ernzerhof (PBE) functional[67], which is part of the generalized gradient approximation (GGA) method[68]. The projector augmented wave (PAW) approach was employed to describe the interaction between electrons and ions, with spin polarization taken into account. A plane-wave cutoff energy of 500 eV was applied. A (3 × 3 × 1) k-point mesh was used for k-space integration in ligand binding to cobalt hydroxide structure relaxations. For the structure relaxation of MOF structures with different ligands, a (1 × 1 × 1) k-point mesh was used, while a (4 × 4 × 4) k-point mesh was applied for DOS calculation. The conjugate-gradient algorithm was used to relax the ions into their instantaneous ground state. All structures were fully relaxed with energy and force convergences of $<1 \times 10^{-6}$ eV and 0.03 eV $Å^{-1}$, respectively.

For the calculation of OER free energy diagram, a vacuum layer of 20 Å was set to mitigate the influence of crystal periodicity. The widely accepted method to model the OER process involves a four-electron reaction pathway:

$$H_2O + {*} \rightarrow OH^* + H^+ + e^-$$

$$OH^* \rightarrow O^* + H^+ + e^-$$

$$H_2O + O^* \rightarrow OOH^* + H^+ + e^-$$

$$OOH^* \rightarrow {*} + O_2 + H^+ + e^-$$

where * represents an active site on the bare catalyst surface, while OH*, O*, and OOH* denote different intermediates[69].

For each elementary step, the Gibbs free energy ΔG_i (i = 1, 2, 3, 4) can be calculated as:

$$\Delta G_i = \Delta E + \Delta \mathrm{ZPE} - \mathrm{T}\Delta \mathrm{S}$$

where ΔE is the total energy difference between the reactant and product molecules in the four steps, ΔZPE is the change in zero-point energy, and $T\Delta S$ is the contribution of entropy[70].

Data availability

All data supporting the findings of this study are available within the article and its Supplementary Information file, as well as available from the corresponding author upon reasonable request. Source data are provided with this paper.

References

1. Chen, L. & Xu, Q. Metal-organic framework composites for catalysis. *Matter* **1**, 57–89 (2019).
2. Yang, D. & Gates, B. C. Catalysis by metal organic frameworks: perspective and suggestions for future research. *ACS Catal.* **9**, 1779–1798 (2019).
3. Sun, D. et al. One-step electrodeposition of silver nanostructures on 2D/3D metal–organic framework ZIF-67: comparison and application in electrochemical detection of hydrogen peroxide. *ACS Appl. Mater. Interfaces* **12**, 41960–41968 (2020).
4. Ghoshal, S. et al. ZIF 67 based highly active electrocatalysts as oxygen electrodes in water electrolyzer. *ACS Appl. Energy Mater.* **2**, 5568–5576 (2019).
5. Duan, J., Chen, S. & Zhao, C. Ultrathin metal-organic framework array for efficient electrocatalytic water splitting. *Nat. Commun.* **8**, 15341 (2017).
6. Chongdar, S., Mondal, U., Chakraborty, T., Banerjee, P. & Bhaumik, A. A Ni-MOF as fluorescent/electrochemical dual probe for ultrasensitive detection of picric acid from aqueous media. *ACS Appl. Mater. Interfaces* **15**, 14575–14586 (2023).
7. Shrestha, N. K. et al. Cerium guided site-selective crystal disorder engineering of MIL-88B(Ni) frameworks for electrocatalysis offering high-performance water oxidation. *Mater. Today Phys.* **38**, 101252 (2023).
8. Hu, C., Xu, J., Lu, Z., Cao, C. & Wang, Y. Core-shell structured ZIF-7@ZIF-67 with high electrochemical performance for all-solid-state asymmetric supercapacitor. *Int J. Hydrog. Energy* **46**, 32149–32160 (2021).
9. Dong, P. et al. Regulation of electron delocalization between flower-like (Co, Ni)-MOF array and WO3/W photoanode for effective photoelectrochemical water splitting. *Appl. Catal. B: Environ. Energy* **350**, 123925 (2024).
10. Zheng, W. & Lee, L. Y. S. Metal–organic frameworks for electrocatalysis: catalyst or precatalyst? *ACS Energy Lett.* **6**, 2838–2843 (2021).
11. Tayyab, M. et al. A new breakthrough in photocatalytic hydrogen evolution by amorphous and chalcogenide enriched cocatalysts. *Chem. Eng. J.* **455**, 140601 (2023).
12. Zheng, W., Liu, M. & Lee, L. Y. S. Electrochemical instability of metal–organic frameworks: in situ spectroelectrochemical investigation of the real active sites. *ACS Catal.* **10**, 81–92 (2020).
13. Li, X., Niu, Z., Jiang, J. & Ai, L. Cobalt nanoparticles embedded in porous N-rich carbon as an efficient bifunctional electrocatalyst for water splitting. *J. Mater. Chem. A* **4**, 3204–3209 (2016).
14. Pan, Y. et al. Core–shell ZIF-8@ZIF-67-derived CoP nanoparticle-embedded N-doped carbon nanotube hollow polyhedron for efficient overall water splitting. *J. Am. Chem. Soc.* **140**, 2610–2618 (2018).
15. Zhao, S. et al. Structural transformation of highly active metal–organic framework electrocatalysts during the oxygen evolution reaction. *Nat. Energy* **5**, 881–890 (2020).
16. Zhong, H. et al. Fundamental understanding of structural reconstruction behaviors in oxygen evolution reaction electrocatalysts. *Adv. Energy Mater.* **13**, 2301391 (2023).
17. Zhang, L. et al. Self-reconstructed metal-organic framework heterojunction for switchable oxygen evolution reaction. *Angew. Chem. Int Ed.* **61**, e202214794 (2022).
18. Feng, L., Wang, K.-Y., Willman, J. & Zhou, H.-C. Hierarchy in metal–organic frameworks. *ACS Cent. Sci.* **6**, 359–367 (2020).
19. Luo, Y., Ahmad, M., Schug, A. & Tsotsalas, M. Rising up: hierarchical metal–organic frameworks in experiments and simulations. *Adv. Mater.* **31**, 1901744 (2019).
20. Deng, H. et al. Multiple functional groups of varying ratios in metal-organic frameworks. *Science* **327**, 846–850 (2010).
21. Frentzel-Beyme, L., Kloß, M., Kolodzeiski, P., Pallach, R. & Henke, S. Meltable mixed-linker zeolitic imidazolate frameworks and their microporous glasses: from melting point engineering to selective hydrocarbon sorption. *J. Am. Chem. Soc.* **141**, 12362–12371 (2019).
22. Gao, C. et al. Metal-organic framework glass anode with an exceptional cycling-induced capacity enhancement for lithium-ion batteries. *Adv. Mater.* **34**, 2110048 (2022).
23. Ma, N. & Horike, S. Metal–organic network-forming glasses. *Chem. Rev.* **122**, 4163–4203 (2022).
24. Wang, S. et al. Linker engineering of sandwich-structured metal–organic framework composites for optimized photocatalytic H2 production. *Adv. Mater.* **35**, 2302512 (2023).
25. Wu, K. et al. Linker engineering for reactive oxygen species generation efficiency in ultra-stable nickel-based metal–organic frameworks. *J. Am. Chem. Soc.* **145**, 18931–18938 (2023).
26. He, T., Kong, X.-J. & Li, J.-R. Chemically stable metal–organic frameworks: rational construction and application expansion. *Acc. Chem. Res.* **54**, 3083–3094 (2021).
27. Yuan, S. et al. Stable metal–organic frameworks: design, synthesis, and applications. *Adv. Mater.* **30**, 1704303 (2018).
28. Chen, C.-L. et al. Conductive lanthanide metal–organic frameworks with exceptionally high stability. *J. Am. Chem. Soc.* **145**, 16983–16987 (2023).
29. Huang, Z. et al. Hierarchically micro- and mesoporous zeolitic imidazolate frameworks through selective ligand removal. *Small* **20**, 2307981 (2024).
30. Kim, H. S., Kang, M. S. & Yoo, W. C. Boost-up electrochemical performance of MOFs via confined synthesis within nanoporous carbon matrices for supercapacitor and oxygen reduction reaction applications. *J. Mater. Chem. A* **7**, 5561–5574 (2019).
31. Cao, Y., Li, P., Wu, T., Liu, M. & Zhang, Y. Electrocatalysis of N2 to NH3 by HKUST-1 with high NH3 yield. *Chem. – Asian J.* **15**, 1272–1276 (2020).
32. Huang, Z. et al. Stable core–shell ZIF-8@ZIF-67 MOFs photocatalyst for highly efficient degradation of organic pollutant and hydrogen evolution. *J. Mater. Res.* **36**, 602–614 (2021).
33. Saliba, D., Ammar, M., Rammal, M., Al-Ghoul, M. & Hmadeh, M. Crystal growth of ZIF-8, ZIF-67, and their mixed-metal derivatives. *J. Am. Chem. Soc.* **140**, 1812–1823 (2018).
34. Mefford, J. T., Akbashev, A. R., Zhang, L. & Chueh, W. C. Electrochemical reactivity of faceted β-Co(OH)2 single crystal platelet particles in alkaline electrolytes. *J. Phys. Chem. C.* **123**, 18783–18794 (2019).
35. Liu, Y.-C., Koza, J. A. & Switzer, J. A. Conversion of electrodeposited Co(OH)2 to CoOOH and Co3O4, and comparison of their catalytic activity for the oxygen evolution reaction. *Electrochim. Acta* **140**, 359–365 (2014).

36. Chang, Z., Li, H., Tang, H., Yuan, X. Z. & Wang, H. Synthesis of γ-CoOOH and its effects on the positive electrodes of nickel batteries. *Int J. Hydrog. Energy* **34**, 2435–2439 (2009).
37. Xue, Z. et al. Missing-linker metal-organic frameworks for oxygen evolution reaction. *Nat. Commun.* **10**, 5048 (2019).
38. Chen, H. et al. Preparation of reduced graphite oxide loaded with cobalt(II) and nitrogen co-doped carbon polyhedrons from a metal-organic framework (type ZIF-67), and its application to electrochemical determination of metronidazole. *Microchimica. Acta* **186**, 623 (2019).
39. Yang, J., Liu, H., Martens, W. N. & Frost, R. L. Synthesis and characterization of cobalt hydroxide, cobalt oxyhydroxide, and cobalt oxide nanodiscs. *J. Phys. Chem. C.* **114**, 111–119 (2010).
40. Zhu, R. et al. Quasi-ZIF-67 for boosted oxygen evolution reaction catalytic activity via a low temperature calcination. *ACS Appl. Mater. Interfaces* **12**, 25037–25041 (2020).
41. Xue, S. et al. In situ constructing Co/Co-Ox/Co-Nx diverse active sites on hollow porous carbon spheres derived from Co-MOF for efficient bifunctional electrocatalysis in rechargeable Zn-air. *Mater. Today Phys.* **37**, 101209 (2023).
42. Zuo, F. et al. Electrochemical interfacial catalysis in Co-based battery electrodes involving spin-polarized electron transfer. *Proc. Natl Acad. Sci. USA* **120**, e2314362120 (2023).
43. Gao, Z. et al. Electrochemical oxidation induced in-situ transformation of lamellar cobalt nitrate-hydroxide to oxygen vacancy-rich porous Ce Doped-CoOOH nanosheet for efficient oxygen evolution reaction. *Mater. Today Sustain.* **24**, 100601 (2023).
44. Öztürk, Z., Filez, M. & Weckhuysen, B. M. Decoding nucleation and growth of zeolitic imidazolate framework thin films with atomic force microscopy and vibrational spectroscopy. *Chem. Eur. J.* **23**, 10915–10924 (2017).
45. Sun, H. et al. Metal–organic frameworks as surface enhanced raman scattering substrates with high tailorability. *J. Am. Chem. Soc.* **141**, 870–878 (2019).
46. Kumari, G., Jayaramulu, K., Maji, T. K. & Narayana, C. Temperature induced structural transformations and gas adsorption in the zeolitic imidazolate framework ZIF-8: a raman study. *J. Phys. Chem. A* **117**, 11006–11012 (2013).
47. Jia, J. et al. Role of cobalt phthalocyanine on the formation of high-valent cobalt species revealed by in situ raman spectroscopy. *J. Mater. Chem. A* **11**, 8141–8149 (2023).
48. Guo, W. et al. Ge-doped cobalt oxide for electrocatalytic and photocatalytic water splitting. *ACS Catal.* **12**, 12000–12013 (2022).
49. Huang, C. et al. Functional bimetal Co-modification for boosting large-current-density seawater electrolysis by inhibiting adsorption of chloride ions. *Adv. Energy Mater.* **13**, 2301475 (2023).
50. Budiyanto, E., Salamon, S., Wang, Y., Wende, H. & Tüysüz, H. Phase segregation in cobalt iron oxide nanowires toward enhanced oxygen evolution reaction activity. *JACS Au* **2**, 697–710 (2022).
51. Li, X. et al. Boosting photoelectrocatalytic oxygen evolution activity of BiVO4 photoanodes via caffeic acid bridged to NiFeOOH. *Appl. Catal. B: Environ. Energy* **353**, 124096 (2024).
52. Lin, H. et al. Epitaxial growth of lead-free double perovskite shell for CsPbX3/Cs2SnX6 (X = Cl, Br, and I) core/shell perovskite nanocrystals with enhanced photoelectric properties and stability. *Adv. Funct. Mater.* **n/a**, 2309480 (2023).
53. Chen, M. et al. Metalloporphyrin based MOF-545 coupled with solid solution ZnxCd1-xS for efficient photocatalytic hydrogen production. *J. Colloid Interf. Sci.* **653**, 380–389 (2024).
54. Ma, X. et al. Structure–activity relationships in Ni- carboxylate-type metal–organic frameworks' metamorphosis for the oxygen evolution reaction. *ACS Catal.* **13**, 7587–7596 (2023).
55. Li, S. et al. Coordination environment tuning of nickel sites by oxyanions to optimize methanol electro-oxidation activity. *Nat. Commun.* **13**, 2916 (2022).
56. Zhou, Y. et al. Enlarged Co-O covalency in octahedral sites leading to highly efficient spinel oxides for oxygen evolution reaction. *Adv. Mater.* **30**, 1802912 (2018).
57. Jia, Z., Dai, X., Liu, B., Li, Y. & Bo, C. Poly(sodium 4-styrenesulfonate) brushes-functionalized UiO-66-NH2 metal-organic framework for high and selective adsorption of dyes. *Colloids Surf., A* **639**, 128312 (2022).
58. Xiang, L. et al. Amino-functionalized ZIF-7 nanocrystals: improved intrinsic separation ability and interfacial compatibility in mixed-matrix membranes for CO2/CH4 separation. *Adv. Mater.* **29**, 1606999 (2017).
59. Niu, S. et al. Mitigating the reconstruction of metal sulfides for ultrastable oxygen evolution at high current density. *CCS Chem.* **0**, 1–12 (2023).
60. Naghdi, S. et al. Selective ligand removal to improve accessibility of active sites in hierarchical MOFs for heterogeneous photocatalysis. *Nat. Commun.* **13**, 282 (2022).
61. Rabl, H. et al. Microwave-assisted synthesis of metal-organic chalcogenolate assemblies as electrocatalysts for syngas production. *Commun. Chem.* **6**, 43 (2023).
62. Cheng, F. et al. Accelerated water activation and stabilized metal-organic framework via constructing triangular active-regions for ampere-level current density hydrogen production. *Nat. Commun.* **13**, 6486 (2022).
63. Tran T. T. N. et al. Dopant-induced charge redistribution on the 3D sponge-like hierarchical structure of quaternary metal phosphides nanosheet arrays derived from metal–organic frameworks for natural seawater Splitting. *ACS Appl. Mater. Inter.* **16**, 2270–2282 (2024).
64. Chang, T.-E. et al. Iridium-functionalized metal-organic framework nanocrystals interconnected by carbon nanotubes competent for electrocatalytic water oxidation. *ChemCatChem* **14**, e202200199 (2022).
65. Huang, Z., Zhao, S. & Yu, Y. Experimental method to explore the adaptation degree of type-II and all-solid-state Z-scheme heterojunction structures in the same degradation system. *Chin. J. Catal.* **41**, 1522–1534 (2020).
66. Kresse, G. & Furthmüller, J. Efficient iterative schemes for ab initio total-energy calculations using a plane-wave basis set. *Phys. Rev. B Condens Matter.* **54**, 11169–11186 (1996).
67. Perdew, J. P. et al. Restoring the density-gradient expansion for exchange in solids and surfaces. *Phys. Rev. Lett.* **100**, 4 (2008).
68. Perdew, J. P., Burke, K. & Ernzerhof, M. Generalized gradient approximation made simple. *Phys. Rev. Lett.* **77**, 3865–3868 (1996).
69. Huang, C. et al. The rapid self-reconstruction of Fe-modified Ni hydroxysulfide for efficient and stable large-current-density water/seawater oxidation. *Energy Environ. Sci.* **15**, 4647–4658 (2022).
70. Xue, Z., Zhang, X., Qin, J. & Liu, R. Revealing Ni-based layered double hydroxides as high-efficiency electrocatalysts for the oxygen evolution reaction: a DFT study. *J. Mater. Chem. A* **7**, 23091–23097 (2019).

Acknowledgements

Z.H. was financially supported by China Scholarship Council (Nos. 202106770017). This research was supported by Austrian Science Fund (FWF: I5413-N, Cluster of Excellence MECS: 10.55776/COE5, and doctoral college TU-DX: 10.55776/DOC142) and Natural Science Foundation of China (Nos. U20A20246 and 52472205). The authors gratefully acknowledge the services provided by the analytical instrumentation center (AIC) at TU Wien, X-ray Center (XRC) at TU Wien, University Service for Transmission Electron Microscopy at TU Wien (USTEM).

Author contributions

Z.H. contributed most of the experiments and analysis and wrote the initial manuscript. Z.W. contributed in-situ electrochemical Raman

Die approbierte gedruckte Originalversion dieser Dissertation ist an der TU Wien Bibliothek verfügbar.
The approved original version of this doctoral thesis is available in print at TU Wien Bibliothek.
TU WIEN Bibliothek Your knowledge hub

analysis, reviewing & editing the manuscript. H.R. contributed XPS measurement and analysis, reviewing & editing the manuscript. S.N. contributed N_2 physisorption and ^{1}H NMR measurement, reviewing & editing the manuscript. Q.Z. contributed DFT simulations. S.S. contributed TEM measurement. D.H.A. contributed reviewing & editing the manuscript. Y.Y. contributed experimental equipment, reviewing & editing the manuscript. D.E. contributed the project concept, funding and experimental equipment and reviewing & editing the manuscript. All authors discussed the results and commented on the manuscript.

Competing interests

The authors declare no competing interests.

Additional information

Supplementary information The online version contains supplementary material available at https://doi.org/10.1038/s41467-024-53385-0.

Correspondence and requests for materials should be addressed to Ying Yu or Dominik Eder.

Peer review information *Nature Communications* thanks Yong Ding, Yung-Jung Hsu and the other anonymous reviewer(s) for their contribution to the peer review of this work. A peer review file is available.

Reprints and permissions information is available at http://www.nature.com/reprints

Publisher's note Springer Nature remains neutral with regard to jurisdictional claims in published maps and institutional affiliations.

Open Access This article is licensed under a Creative Commons Attribution 4.0 International License, which permits use, sharing, adaptation, distribution and reproduction in any medium or format, as long as you give appropriate credit to the original author(s) and the source, provide a link to the Creative Commons licence, and indicate if changes were made. The images or other third party material in this article are included in the article's Creative Commons licence, unless indicated otherwise in a credit line to the material. If material is not included in the article's Creative Commons licence and your intended use is not permitted by statutory regulation or exceeds the permitted use, you will need to obtain permission directly from the copyright holder. To view a copy of this licence, visit http://creativecommons.org/licenses/by/4.0/.

© The Author(s) 2024

Supporting Information

Ligand Engineering Enhances (Photo)Electrocatalytic Activity and Stability of Zeolitic Imidazolate Frameworks via In-situ Surface Reconstruction

Zheao Huang [1], Zhouzhou Wang [2], Hannah Rabl [1], Shaghayegh Naghdi [1], Qiancheng Zhou [2], Sabine Schwarz [3], Dogukan Hazar Apaydin [1], Ying Yu [,2] and Dominik Eder [*,1]*

[1] Institute of Materials Chemistry, Technische Universität Wien, 1060, Vienna, Austria
[2] Institute of Nanoscience and Nanotechnology, College of Physical Science and Technology, Central China Normal University, 430079, Wuhan, China
[3] Service Center for Electron Microscopy (USTEM), Technische Universität Wien, 1040, Vienna, Austria

* Corresponding authors: dominik.eder@tuwien.ac.at and yuying01@ccnu.edu.cn

Content

S1. Structural characterization of LE-ZIFs

The XRD patterns of LE-ZIFs, incorporating various secondary ligands, exhibit well-maintained crystallinity with Bragg peaks corresponding to A-ZIF (ZIF-67 in Fig. S1a). The introduction of secondary ligands occurred in a one-to-one weight ratio during the synthesis process, i.e., the stations have a 50 wt.%. However, due to competitive coordination among ligands, the actual content of the secondary ligand deviates from the nominal values, as detailed in the ^{1}H NMR analysis (Table S3). A comparison of the XRD patterns of as-prepared ZIFs reveals that the impact of different ligands on the positions of the (011)/(112) peaks is not significant in LE-ZIFs compared to the single-ligand ZIF-67 (Fig. S1b). The SEM images of as-prepared ZIFs exhibit typical ZIF-67 morphology, characterized by dodecahedral particles (Fig. S2). With the exception of a size increase in AB-ZIF, the particle sizes of other LE samples closely resemble those of A-ZIF, around 350 nm.

In the ATR-IR spectra of as-prepared ZIFs, distinct from A-ZIF, the incorporation of secondary ligands results in the appearance of new bands in the range of 472 to 505 cm^{-1} (Fig. S3). These bands are located at 472 cm^{-1} (B), 461 cm^{-1} (C), 499 cm^{-1} (D), and 505 cm^{-1} (E), respectively, closely resembling the Co-N$_\alpha$ band (435 cm^{-1}) of the original ligand (A). Based on the conclusions drawn from previous reports on mixed-ligand ZIFs [1, 2, 3], these new bands are attributed to the bonding of the secondary ligands with metal ions, referred to herein as Co-N$_\beta$. The emergence of the Co-N$_\beta$ bands signify the achievement of ligand substitution process through the successful integration of the secondary ligands into the ZIF-67 framework. Influence by the secondary ligands, the LE-ZIFs exhibit notable differences in the imidazole ring stretching region (700 to 1500 cm^{-1}) compared to A-ZIF.

Through N_2 physisorption at 77 K, as-prepared ZIFs exhibit type-I isotherms, characteristic of typical microporous materials (Fig. S4). Utilizing nonlocal density functional theory (NLDFT), we observed that the distinct peak centered at 1.2 nm, representative of intrinsic micropores, is largely preserved independent of the initial ligand mixing. Interestingly, samples AC and AD exhibit additional pores in the range from 2 to 20 nm (Fig. S5), possibly influenced by incorporation of secondary ligands, a phenomenon commonly observed in previous literature [3, 4]. However, their micropore volume still predominates in total pore distribution. Compared to A-ZIF (2291.3 m^2 g^{-1}), other LE-ZIFs exhibit varying degrees of decrease in Brunauer-Emmett-Teller (BET) specific surface area due to the disorder and bond stretching caused by the secondary ligands [5, 6]. Specifically, AB-ZIF has a surface area of 1092.9 m^2 g^{-1}, AC-ZIF has 717.8 m^2 g^{-1}, AD-ZIF has 860.6 m^2 g^{-1}, and AE-ZIF has 807.7 m^2 g^{-1} (Table S1).

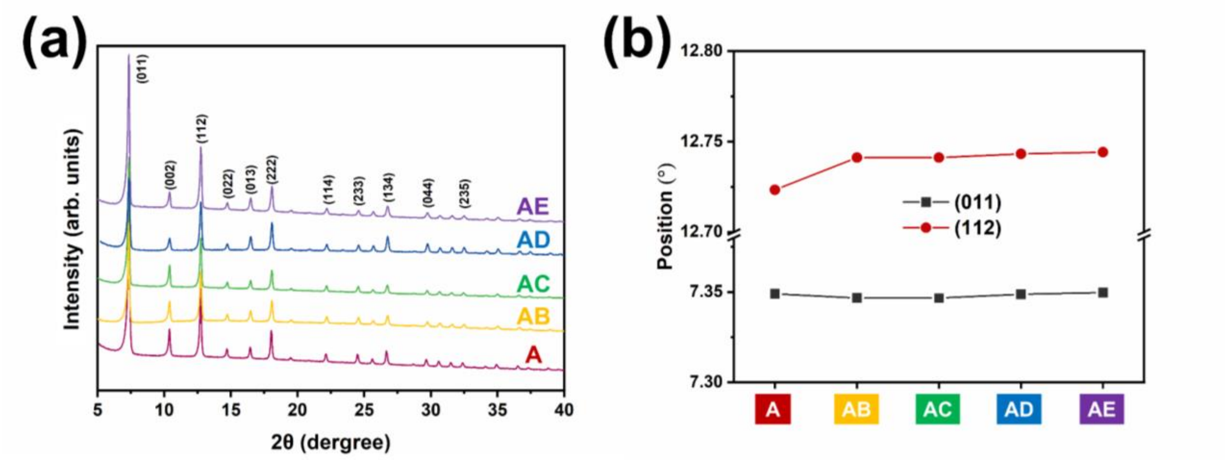

Fig. S1. **a**, XRD patterns of A-ZIF, AB-ZIF, AC-ZIF, AD-ZIF and AE-ZIF. **b**, Evolution plots of (011)/(112) peak position in A-ZIF, AB-ZIF, AC-ZIF, AD-ZIF and AE-ZIF.

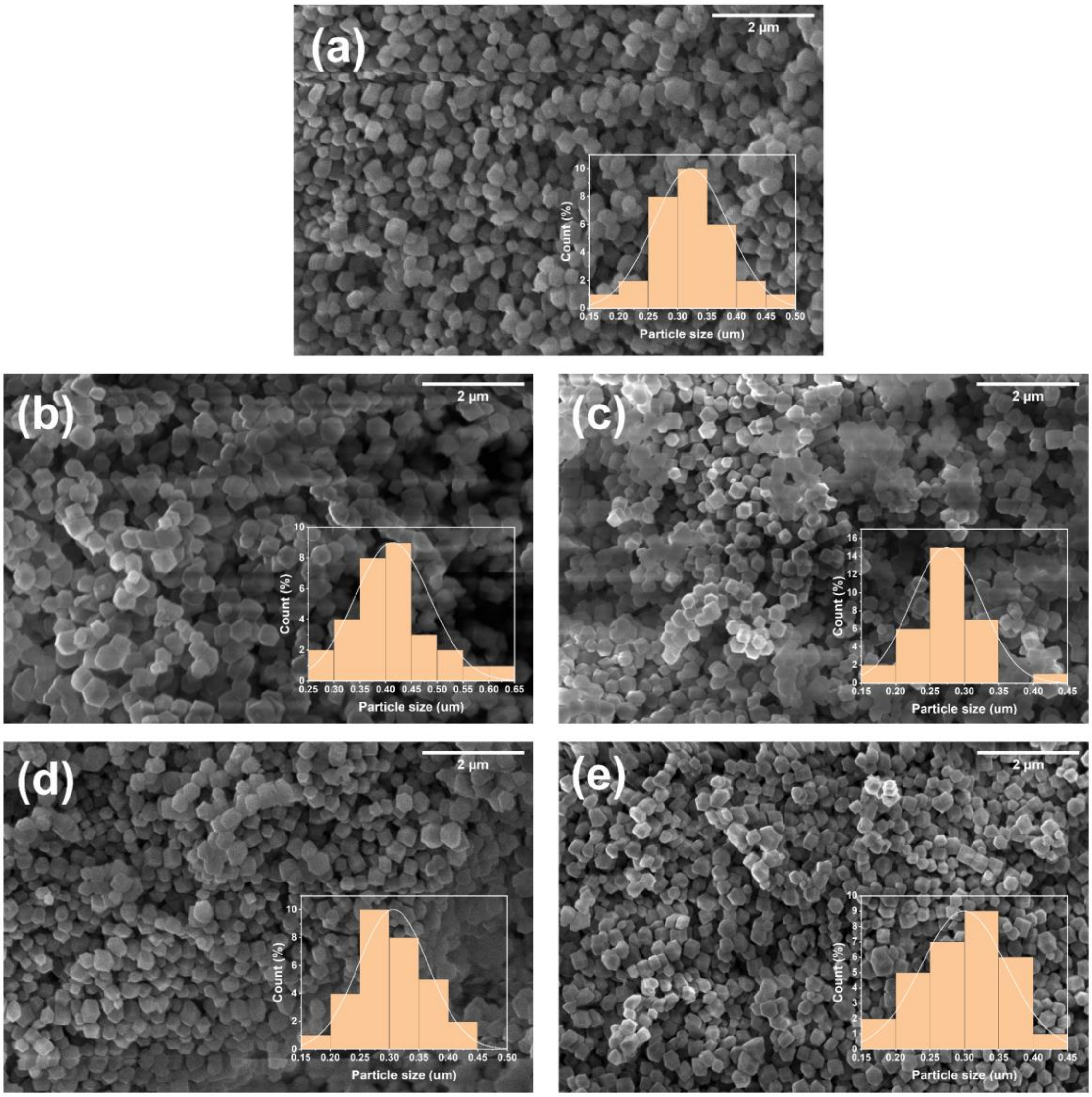

Fig. S2. SEM images of A-ZIF (**a**), AB-ZIF (**b**), AC-ZIF (**c**), AD-ZIF (**d**) and AE-ZIF (**e**). An ImageJ program was used to select 30 particles for particle size statistics from each sample.

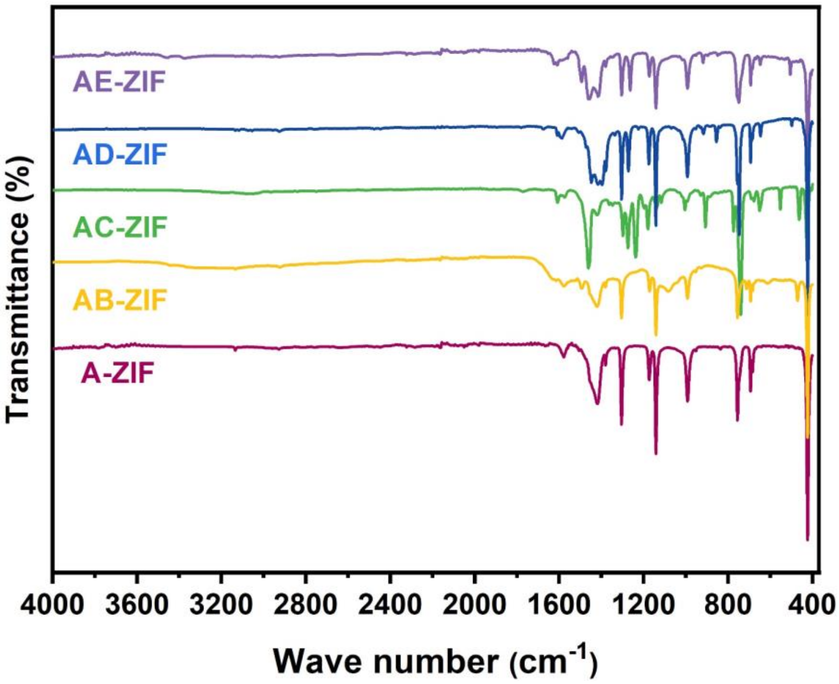

Fig. S3. ATR-IR spectra of A-ZIF, AB-ZIF, AC-ZIF, AD-ZIF and AE-ZIF.

Table S1. Specific surface area and porosity parameters of as-prepared ZIFs.

Samples	**Specific surface area**[a] **($m^2\ g^{-1}$)**	**Total Pore Volume ($cm^3\ g^{-1}$)**	**Micropore Volume**[b] **($cm^3\ g^{-1}$)**	**Total Area in Pores ($m^2\ g^{-1}$)**
A-ZIF	1867.9	0.655	0.647	1977.7
AB-ZIF	1092.9	0.489	0.424	1571.2
AC-ZIF	717.8	0.456	0.213	902.5
AD-ZIF	860.6	0.482	0.292	1214.8
AE-ZIF	891.3	0.365	0.320	1236.0

[a] Brunauer-Emmett-Teller specific surface area.

[b] Cumulative adsorption volume of micropores from 0 to 2 nm in diameter in diameter according to International Union of Pure and Applied Chemistry (IUPAC) [7].

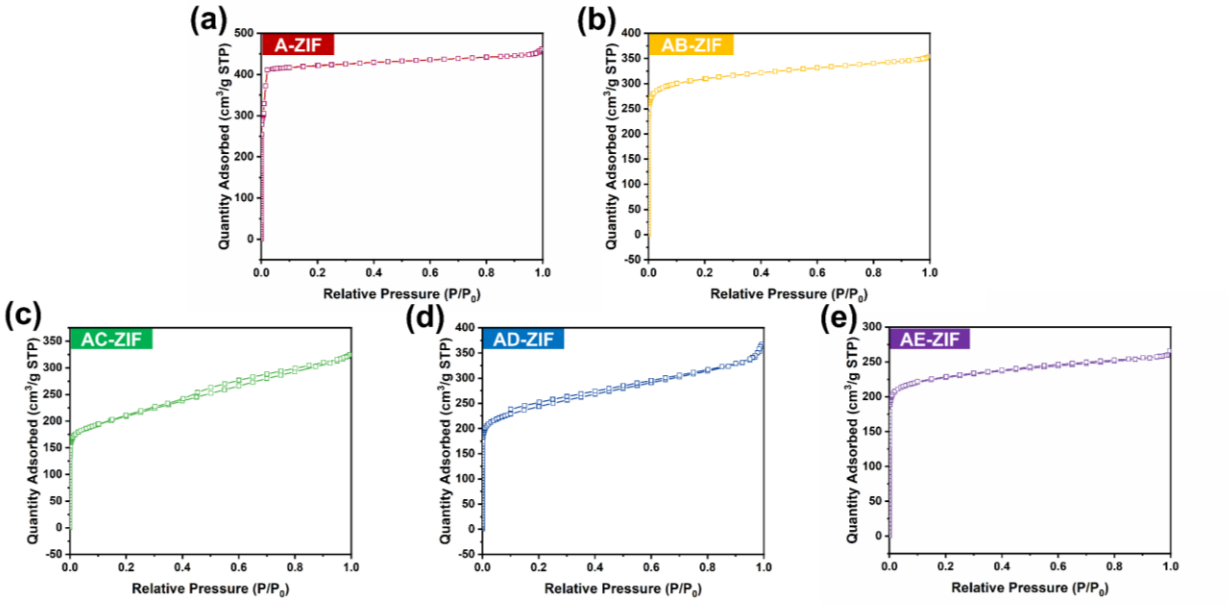

Fig. S4. N_2 sorption isotherm of A-ZIF (**a**), AB-ZIF (**b**), AC-ZIF (**c**), AD-ZIF (**d**) and AE-ZIF (**e**).

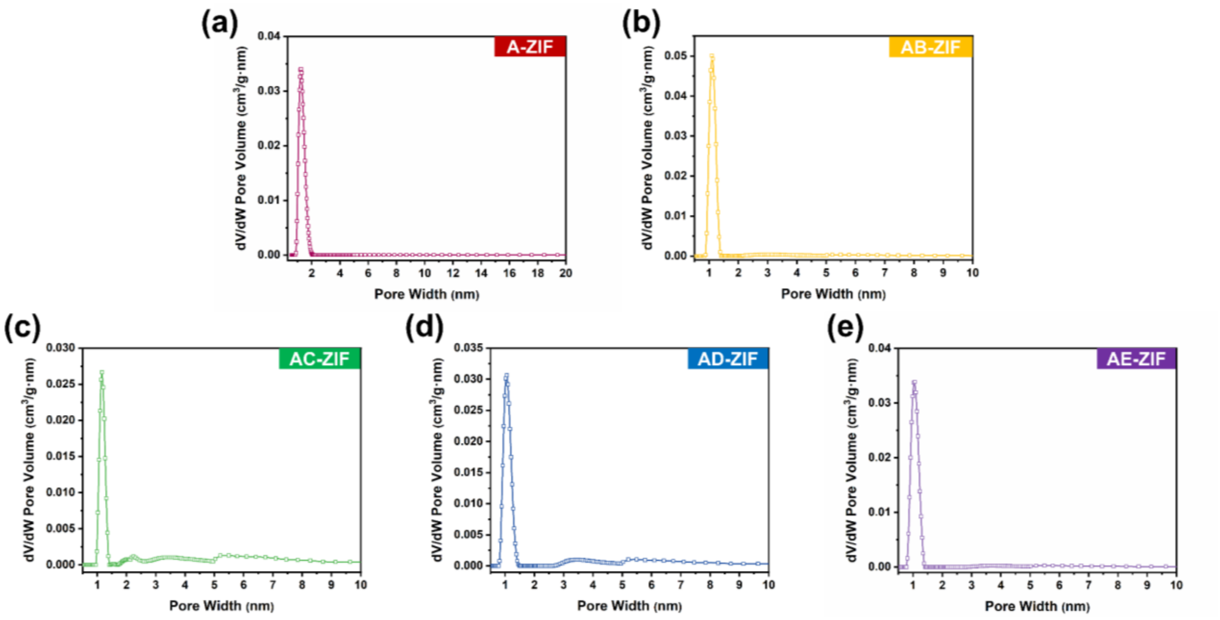

Fig. S5. NLDFT porosity distributions of A-ZIF (**a**), AB-ZIF (**b**), AC-ZIF (**c**), AD-ZIF (**d**) and AE-ZIF (**e**).

S2. Electrocatalytic studies

The following potentials are all referenced to the reversible hydrogen electrode (RHE). As shown in Fig. S7a, AB-ZIF exhibits a continuous decrease from the beginning of the CV cycles until stabilizing at 20 cycles. Similarly, the charge of $R_{LE\text{-}AB}1$ rapidly decreases within the first 10 CV cycles, suggesting that the framework structure of AB-ZIF had been completely degraded (Fig. S8b). The CR process of AB-ZIF at low CV cycles leads to a rapid increase in the overpotential and Tafel slope of unstable AB-ZIF within the first 20 cycles (Fig. S11a), indicating a quickly response of its electrocatalytic rate to potential changes [8]. All these findings collectively indicate the poor stability of AB-ZIF in electrocatalytic reaction.

After 60 CV cycles, the current density of AC-ZIF slightly decreases, and its overpotential exhibits an inverted volcano-shaped curve, decreasing initially and then increasing (Figs. S7b and S11b). In contrast, the current density, overpotential, and Tafel slope of AD-ZIF show no significant changes after 80 CV cycles, remaining relatively stable (Figs. S7c and S11c). These observations indicate that AC-ZIF is more strongly influenced by the electro-oxidation process compared to AD-ZIF during electrocatalysis.

Since electrochemically active surface area (ECSA) is directly proportional to the electrochemical double-layer capacitance (C_{dl}), which was estimated based on the non-Faradaic region of the cyclic voltammetry (CV) curves at different scan rates (20 to 100 mV s^{-1}; see Fig. S9a-e). As shown in Figs. S9c and S9f, before the electrocatalytic activation, A-ZIF and AE-ZIF exhibited similar ECSA values of 64.25 cm^{-2} and 78.00 cm^{-2}, respectively. However, after 100 cycles, the ECSA of A-ZIF decreased significantly to 33.25 cm^{-2} due to its own complete reconstruction, representing a reduction of about 48%. In contrast, AE-ZIF, which experienced only surface reconstruction, maintained a high ECSA value of 71.50 cm^{-2}, showing a minor decrease of 8%. These conclusions are consistent with our TEM analysis of the two samples. The degradation of the surface area of the AE-ZIF particles caused by the 5 nm thick cobalt (oxy)hydroxide layer (Fig. 4) corresponds exactly to a decrease of 8% ECSA, while the decrease of 48% ECSA for A-ZIF corresponding to the transformation of particles into nanosheets.

In a 12-hour amperometry at 1.65V, sample AB exhibits severe current fluctuations (Fig. S13a). Its current density significantly decreases within the initial 2 hours, while the O_2 evolution rate initially increases before declining and final loss of 79.8%, consistent with the conclusions in the CV analysis. AC-ZIF loses 21.4% of the O_2 evolution rate after 12 hours, indicating poorer stability than AD and AE (Fig. S13b). The current density trend of AD-ZIF is similar to AE-ZIF, rapidly increasing in the initial 2 hours and then stabilizing (Fig. S13c). This indicates that their electrodes only undergo rapid reconstruction in the initial 2 hours, and have higher stability in electrochemical performance compared to other ZIF samples. However, both AC and AD do not perform as well as AE-ZIF, exhibiting only about one- eighth of the performance in terms of current density and O_2 evolution rate.

Under intermittent biased conditions, after stopping and restarting the application of 1.65 V, the current density and O_2 evolution rate of AE-ZIF quickly returned to their original levels and remained stable (Fig. S13d). Unlike the initial three hours, AE-ZIF did not exhibit a gradual increase in current density due to surface reconstruction again, indicating that AE-ZIF formed a stable cobalt (oxy)hydroxide layer within the first two hours. This layer effectively inhibited further electro-oxidation process, achieving in a structurally stable state.

The electrical conductivity of each ZIF@FTO glass was evaluated using the two-probe method, where the initial conductivity of AC, AD and AE surpass that of A and AB. This improvement can be attributed to the incorporation of π-π stacking aromatic carbon rings in the secondary ligands (C, bIm; D, 2-bIm; E, NH_2-bIm), which function as additional conductive pathway, effectively facilitating electron transfer [9]. With the increase in the number of CV cycles at high potential window, the electrical conductivity for each ZIF@FTO exhibit discernible changes and closely mirroring with the trends in current density, indicating a strong correlation between OER activity and conductivity (Fig. S14). Apart from AB-ZIF, other ZIFs show varying degrees of conductivity increase, typically attributed to the formation of high-valence Co species and ligand shedding. Sample AE-ZIF@FTO exhibits the highest electrical conductivity among other LE samples, reaching approximately −1.0 (log S/cm) after CV cycles. On the other hand, the trends in electrochemical impedance spectroscopy (EIS) are less pronounced in the CV cycles, as illustrated in Fig. S15.

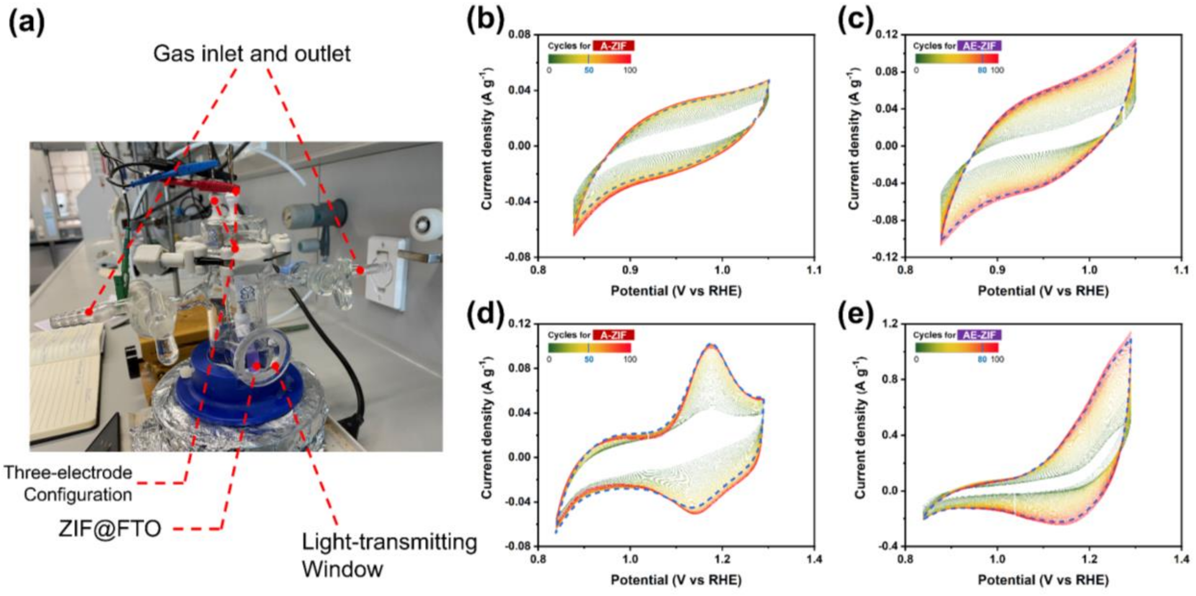

Fig. S6. a, Experimental setup for a standard three-electrode configuration used in electrocatalytic measurements. **b**, **c**, Continuous cyclic voltammograms at low potential window between 0.85 to 1.05 V of A-ZIF (**b**) and AE-ZIF (**c**). **d**, **e**, At medium potential window between 0.85 to 1.30 V of A-ZIF (**d**) and AE-ZIF (**e**).

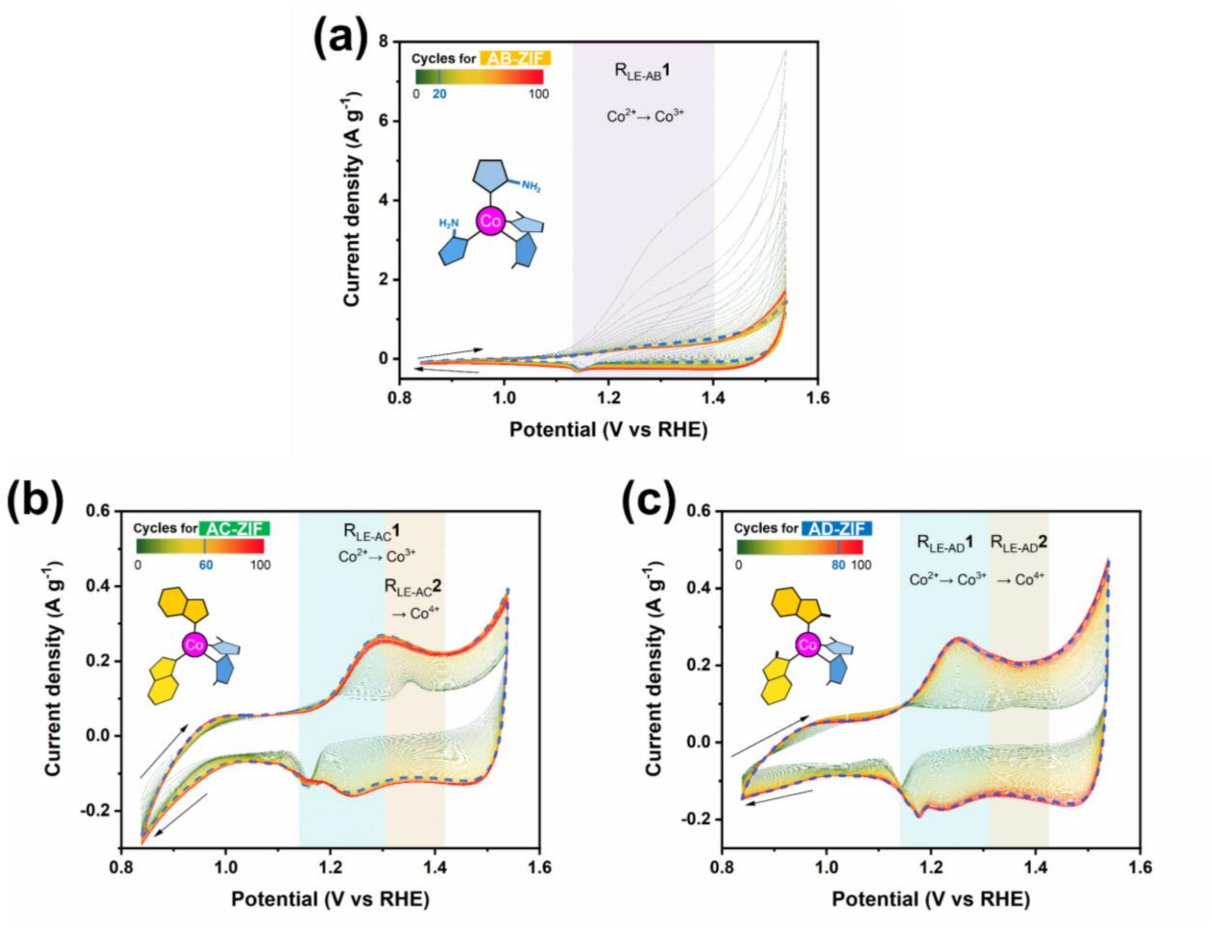

Fig. S7. Continuous cyclic voltammograms at higher potential window between 0.85 to 1.55 V of AB-ZIF (**a**), AC-ZIF (**b**) and AD-ZIF (**c**). Dashed line is the current density maximum, the scan rate is 10 mV s^{-1}.

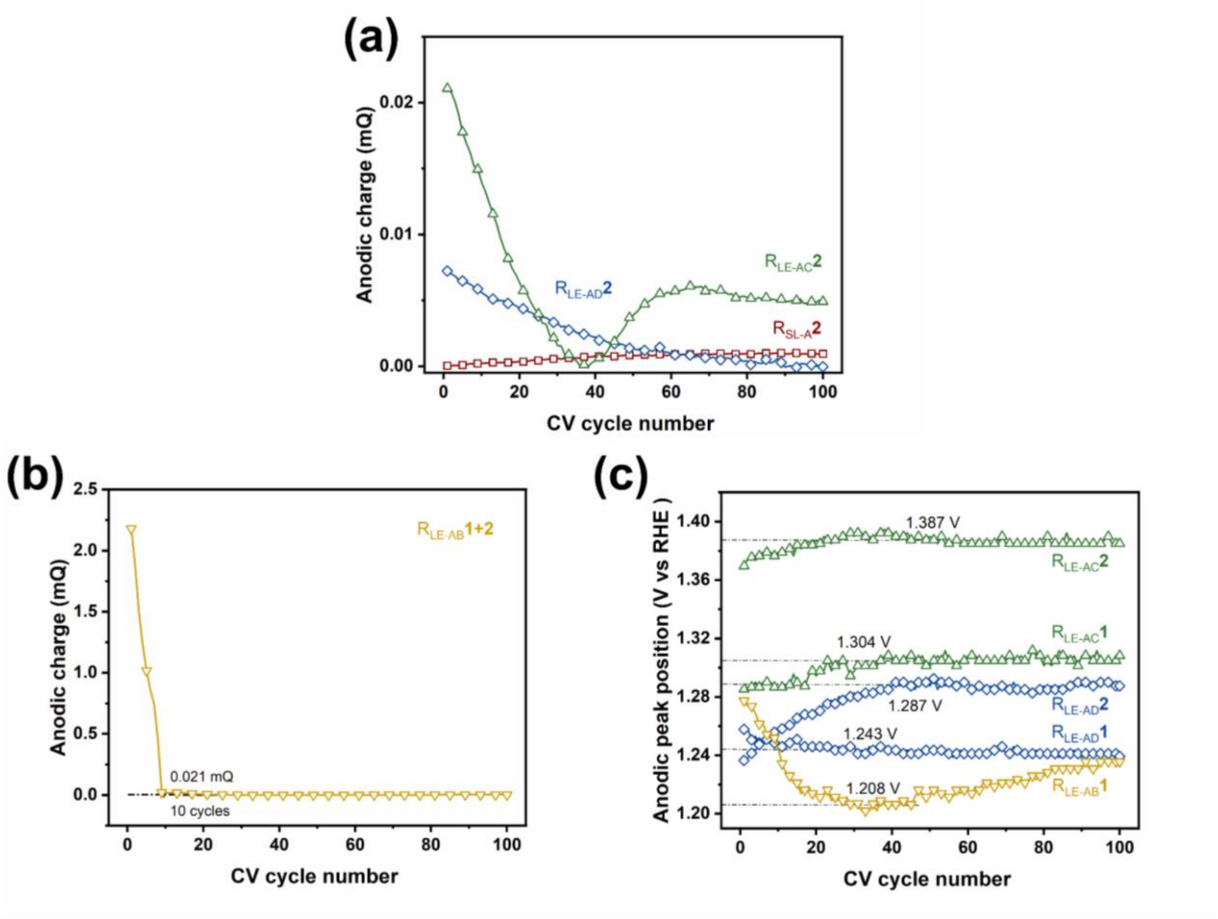

Fig. S8. **a**, **b**, Anodic charge plots with CV cycles of A-ZIF, AC-ZIF, AD-ZIF (**a**) and AB-ZIF (**b**). **c**, Peak position plots with CV cycles of AB-ZIF, AC-ZIF and AD-ZIF.

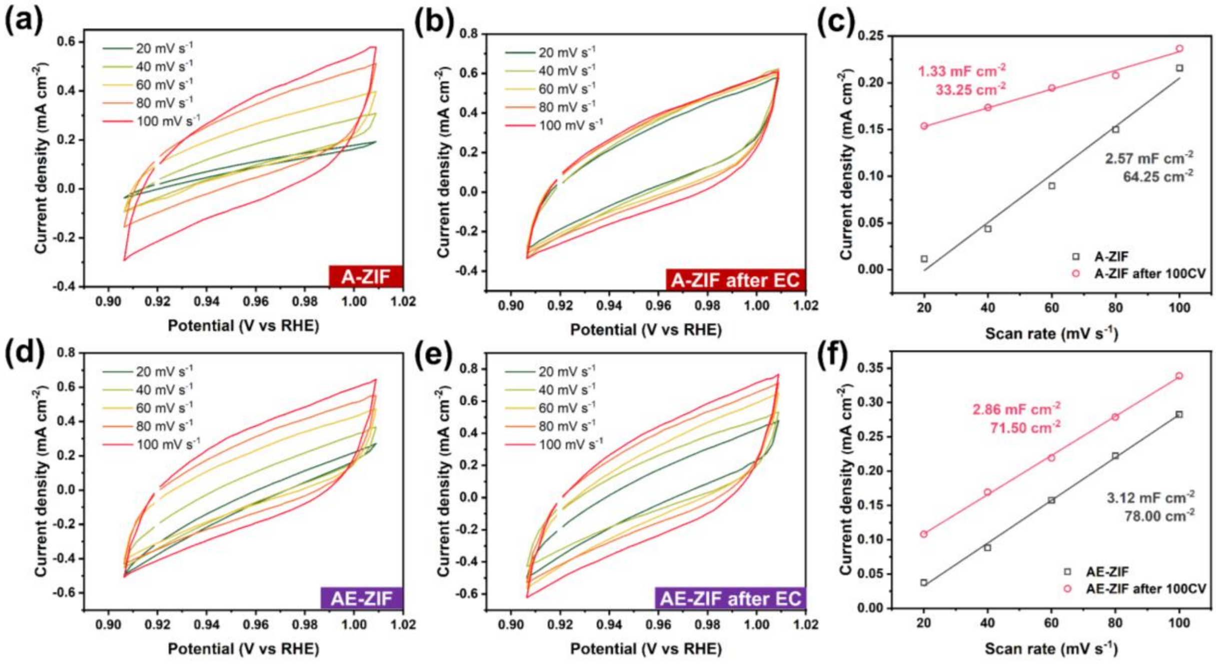

Fig. S9. **a**, **b**, **d**, **e**, Cyclic voltammetry curves of A-ZIF (**a**), A-ZIF after 100 CV (**b**), AE-ZIF (**d**) and AE-ZIF after 100 CV (**e**) at different scan rates in 1.0 M KOH. **c**, **f**, Capacitive currents of A-ZIF (**c**) and AE-ZIF (**f**).

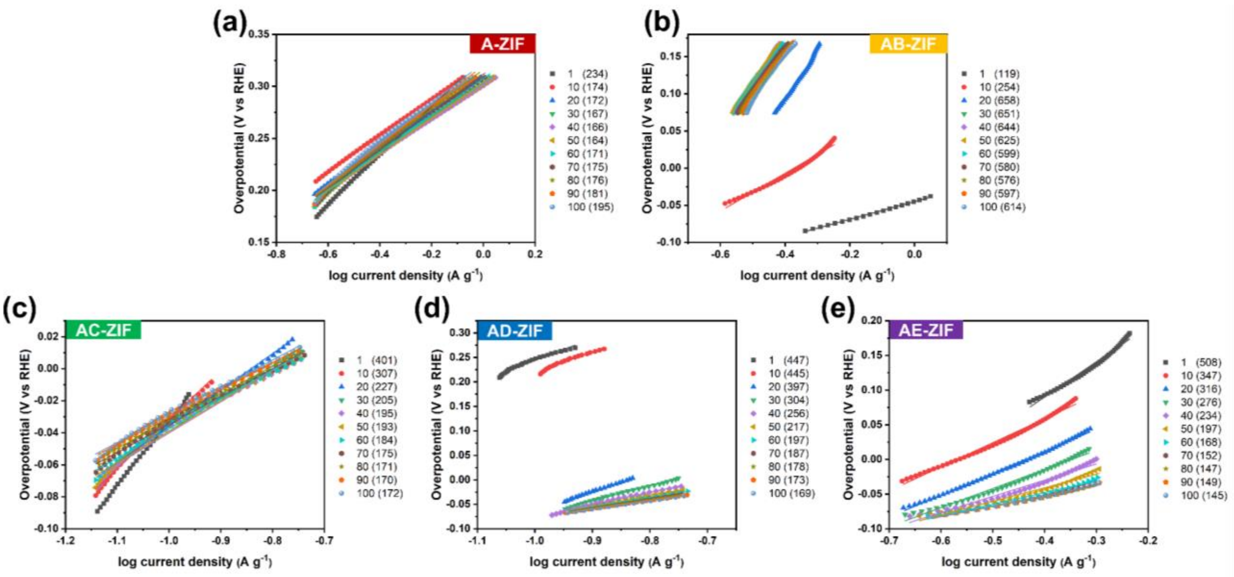

Fig. S10. Tafel plots of OER activity of A-ZIF (**a**), AB-ZIF (**b**), AC-ZIF (**c**), AD-ZIF (**d**) and AE-ZIF (**e**) between 0.85-1.55 V for different CV cycles (0, 10, 20, 30, 40, 50, 60, 70, 80, 90 and 100). Labeled as CV cycle number before parentheses, Tafel plots in parentheses (mV dec^{-1}).

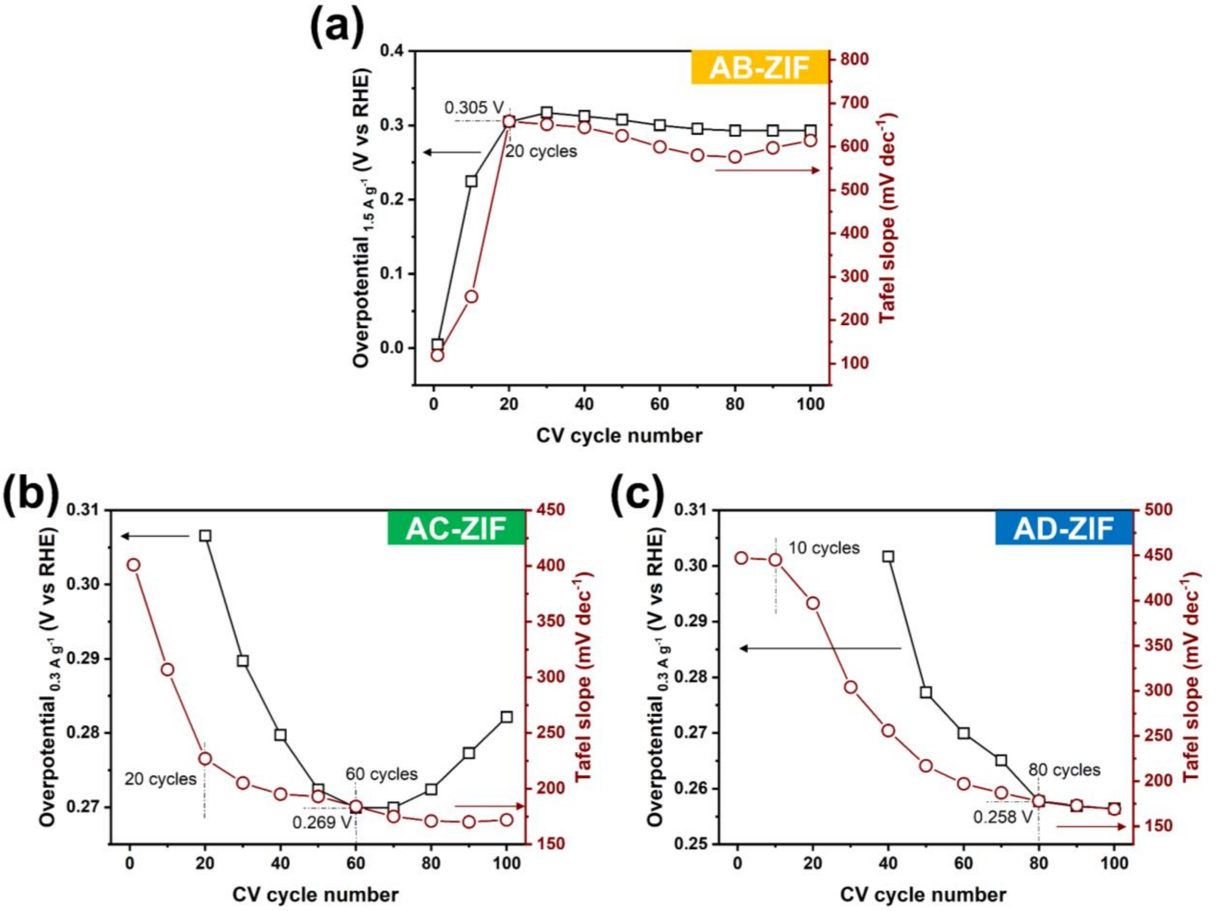

Fig. S11. Overpotential (current density is 1.5 A g^{-1} for AB-ZIF, 0.3 A g^{-1} for AC-ZIF and AD-ZIF) and Tafel slope plots with CV cycles of AB-ZIF (**a**), AC-ZIF (**b**) and AD-ZIF (**c**). The data for the Tafel slope for each CV are from Fig. S7, and calculations are from Fig. S10.

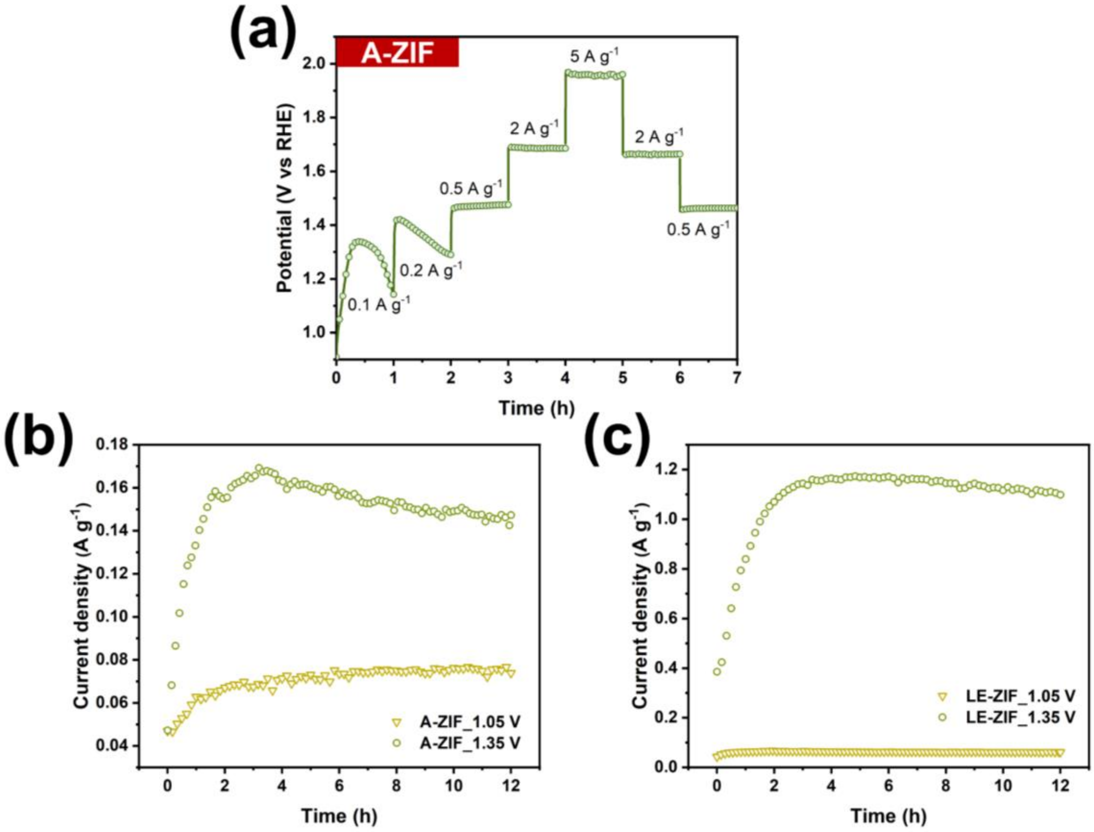

Fig. S12. **a**, Multistep potentiometric plot of A-ZIF at different current densities. **b**, **c**, Amperometric plots of A-ZIF (**b**) and AE-ZIF (**c**) at certain potentials of 1.05 and 1.35 V.

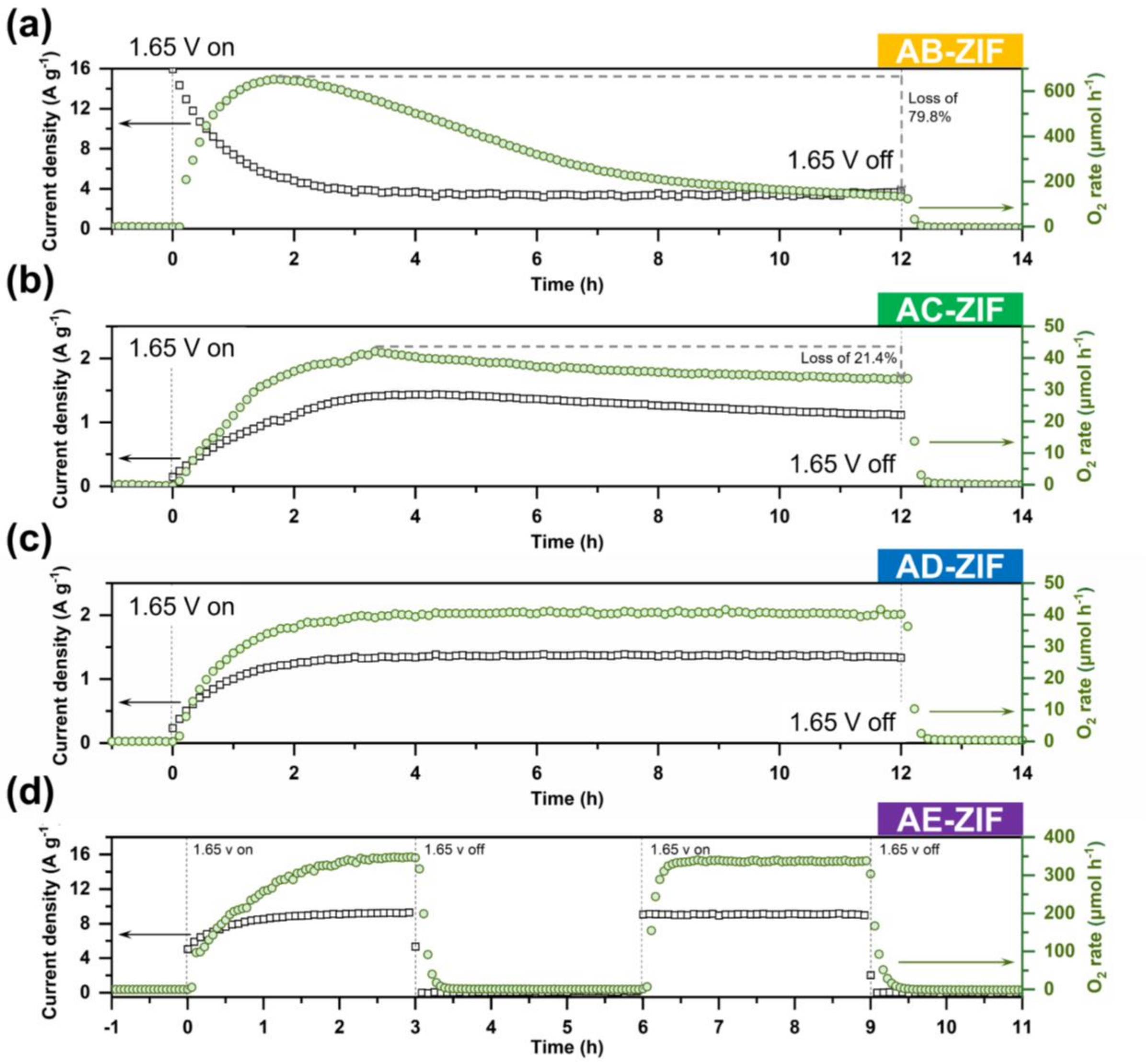

Fig. S13. a, **b**, **c**, Amperometric and O_2 evolution rate plots of AB-ZIF (**a**), AC-ZIF (**b**) and AD-ZIF (**c**) at certain potentials of 1.65 V. **d,** Amperometric and O_2 evolution rate plots of AE-ZIF under intermittent biased condition.

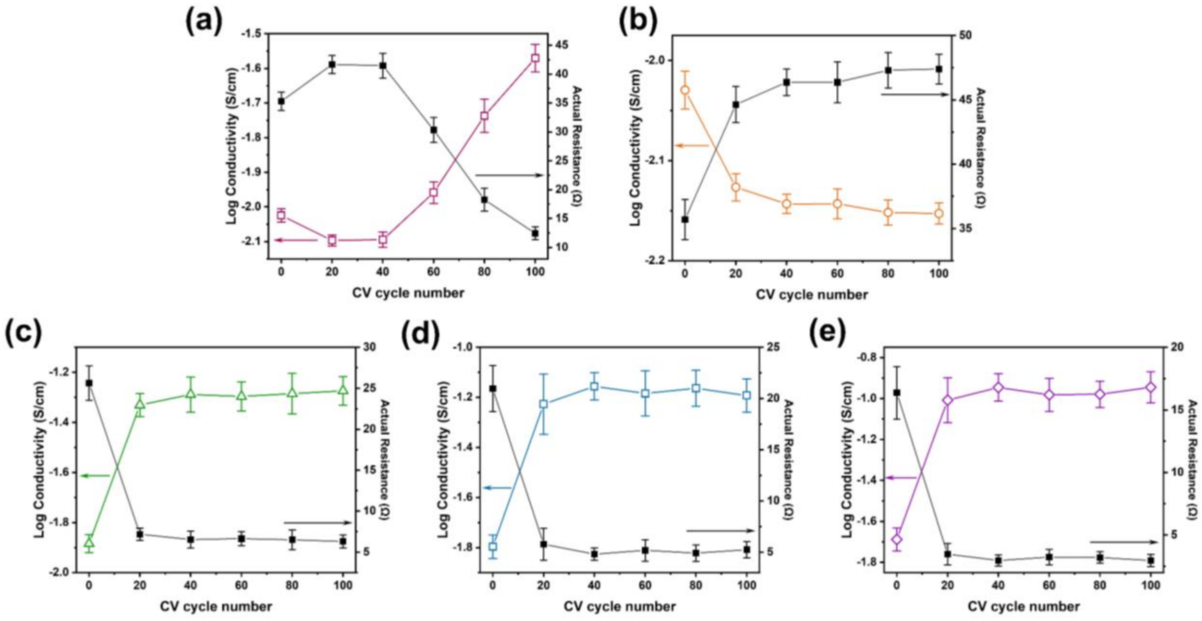

Fig. S14. Actual resistance value and electrical conductivity (log scale) of A-ZIF (**a**), AB-ZIF (**b**), AC-ZIF (**c**), AD-ZIF (**d**) and AE-ZIF (**e**) on FTO glass between 0.85-1.55 V with different CV cycles (0, 10, 20, 30, 40, 50, 60, 70, 80, 90 and 100).

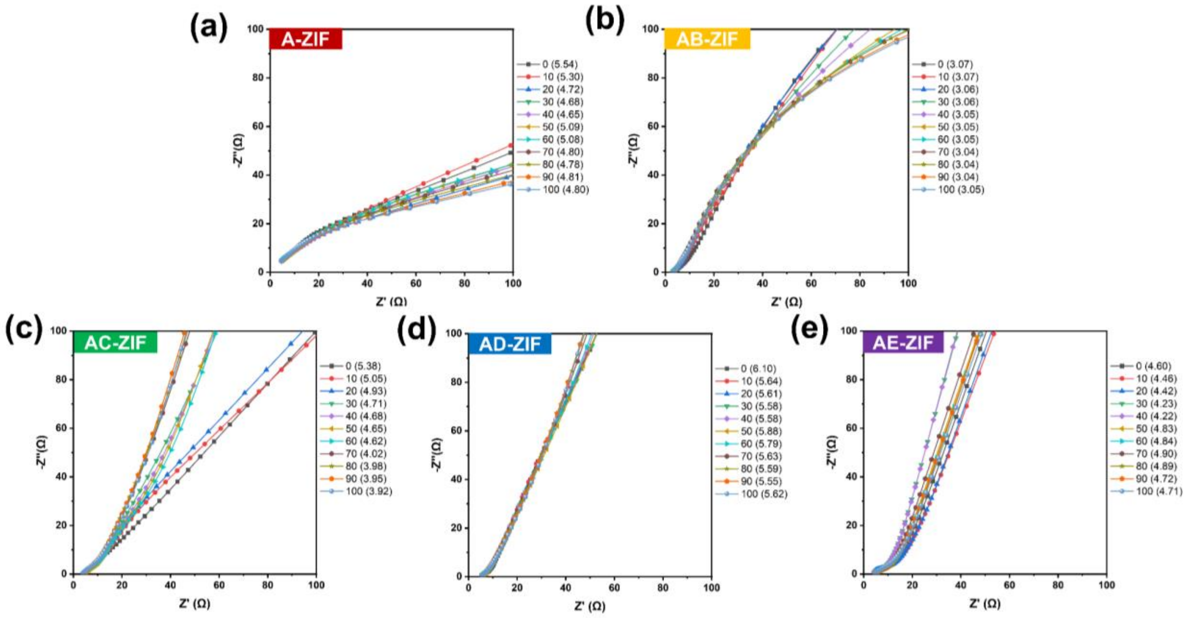

Fig. S15. Electrochemical impedance spectroscopy of A-ZIF (**a**), AB-ZIF (**b**), AC-ZIF (**c**), AD-ZIF (**d**) and AE-ZIF (**e**) on FTO glass between 0.85-1.55 V with different CV cycles (0, 10, 20, 30, 40, 50, 60, 70, 80, 90 and 100). Labeled as CV cycle number before parentheses, resistance value (R_Ω) at high frequency in parentheses.

S3. Structure evolution after electrocatalytic reaction

After 12-hour amperometry, except for an additional peak of $Co(OH)_2$ which appeared at 19.1°, the XRD patterns of AD and AE remain unchanged compared to before electrocatalysis (Fig. S16). This observation suggests that even under extended exposure to high potentials (1.65 V), AD and AE can preserve the inherent crystallinity of ZIF-67 well. The relatively low intensity of the additional $Co(OH)_2$ peak can be attributed to a cobalt (oxy)hydroxide layer constructed by surface reconstruction (Fig. 4). For other ZIF samples, the XRD patterns of A, AC and AB were consistent with the results after their respective CV tests.

In XPS analysis of AC and AD, no discernible signal indicative of Co^{3+} formation through electro-oxidation was detected during the high potential CV cycles. Moreover, two signals corresponding to Co-N (red) and C-N (blue) were retained in the N *1s* spectra [10], as depicted in Figs. S19 and S20. The N/Co ratio in AC and AD has still decreased slightly, from 6.63 and 5.51 (base) to 4.93 and 3.45 (high potential in Table S2). Conversely, the complete absence of the Co *2p* and N *1s* signals observed in AB-ZIF after electrocatalysis suggests the degradation of the framework structure (Fig. S18). This degradation is further evidenced by a significant decrease in the N/Co ratio, dropping from 3.83 (base) to 1.26 (high) under high potential window.

Quantitative analysis of ^1H NMR spectra before and after 100 CV cycles revealed the absence of the ligand NH_2-mIm in AB-ZIF, consistent with the results from XRD and XPS. The actual ratio of ligand bIm in AC-ZIF, increases from 41.4 mol% to 60.2 mol% (Table S3), indicating the detachment of the original ligands and the electro-oxidation of some Co species to higher valences.

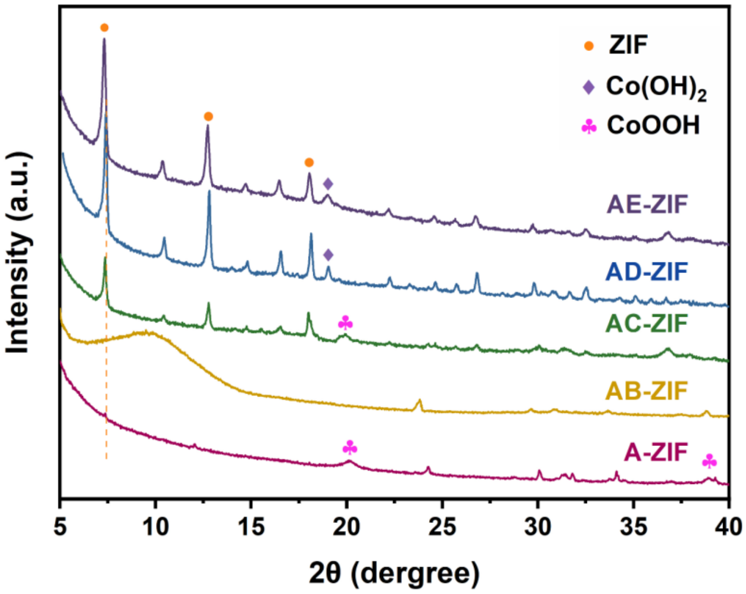

Fig. S16. XRD patterns of A-ZIF, AB-ZIF, AC-ZIF, AD-ZIF and AE-ZIF after 12-hour amperometry.

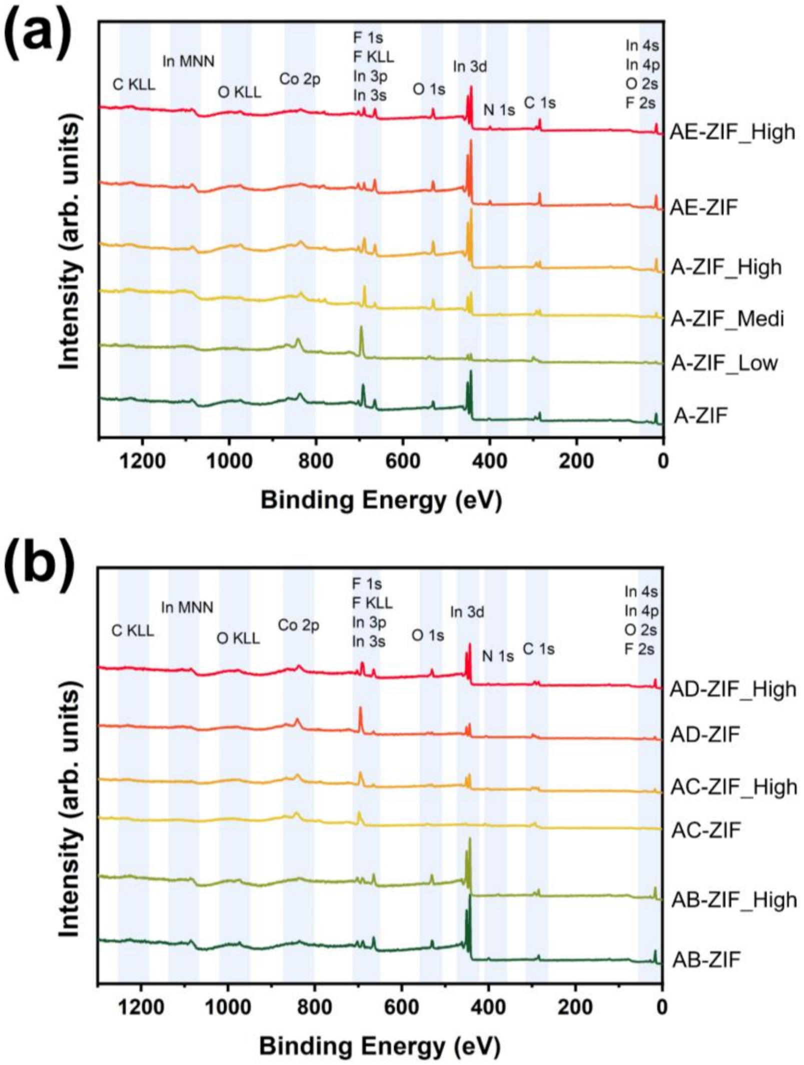

Fig. S17. XPS survey spectra of A-ZIF, AE-ZIF (**a**) and AB-ZIF, AC-ZIF, AD-ZIF (**b**) with 100 CV cycles at different potential window (Low: 0.85-1.05 V, Medi: 0.85-1.30 V, High: 0.85-1.55 V). Elemental Fluorine was obtained from the Nafion solution in the synthetic electrode.

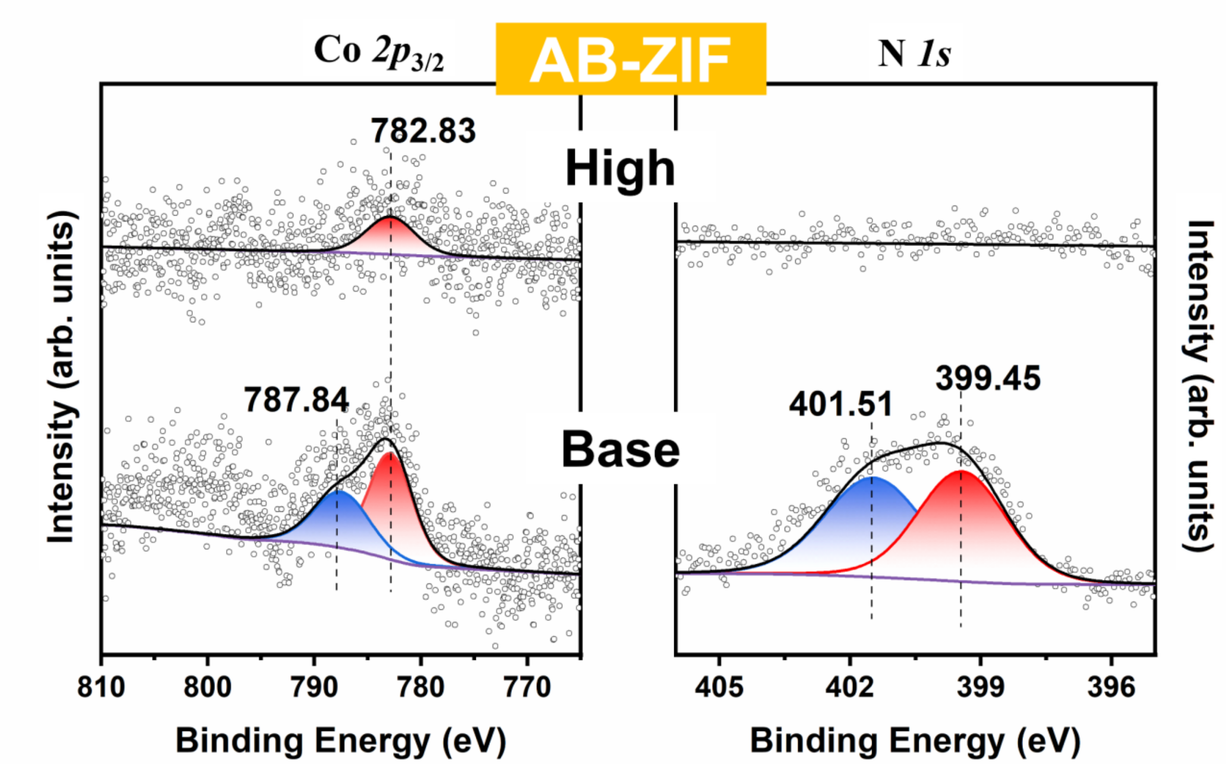

Fig. S18. Co *2p*$_{3/2}$ and N *1s* of XPS spectra of AB-ZIF with 100 CV cycles at high potential window (0.85-1.55 V).

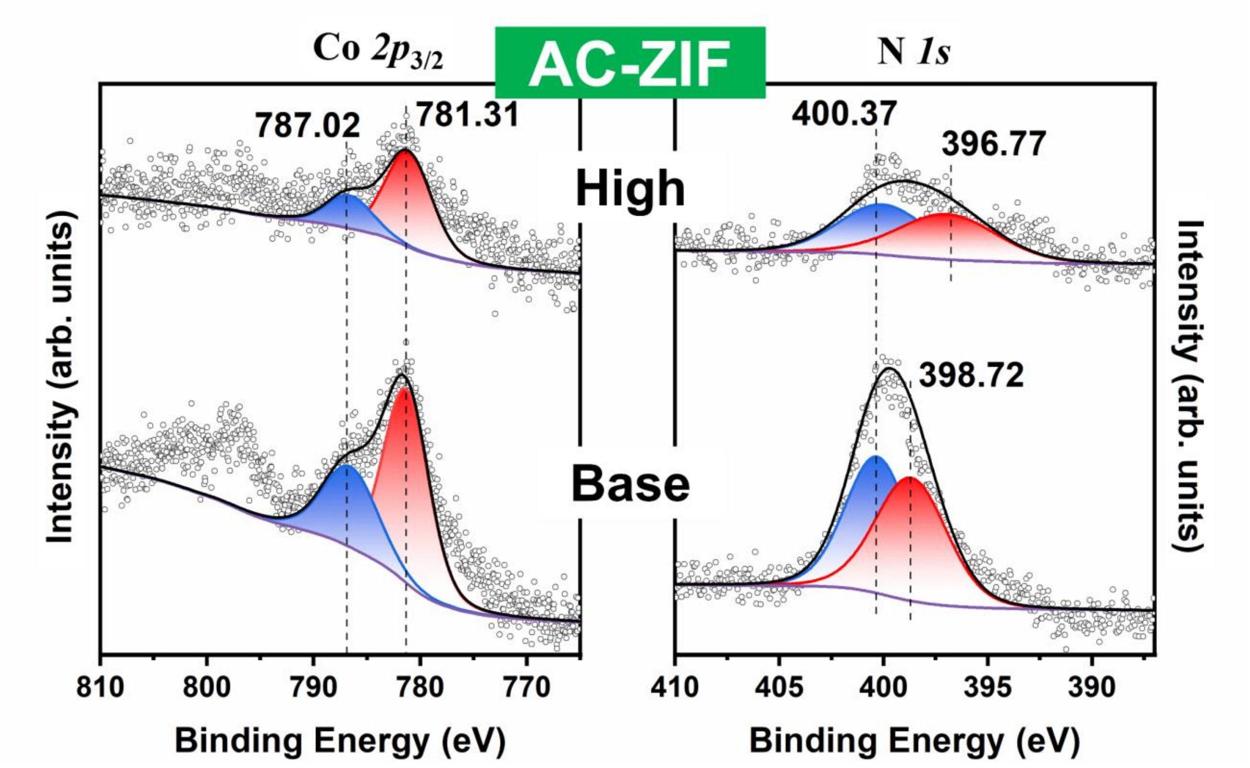

Fig. S19. Co *2p*3/2 and N *1s* of XPS spectra of AC-ZIF with 100 CV cycles at high potential window (0.85-1.55 V).

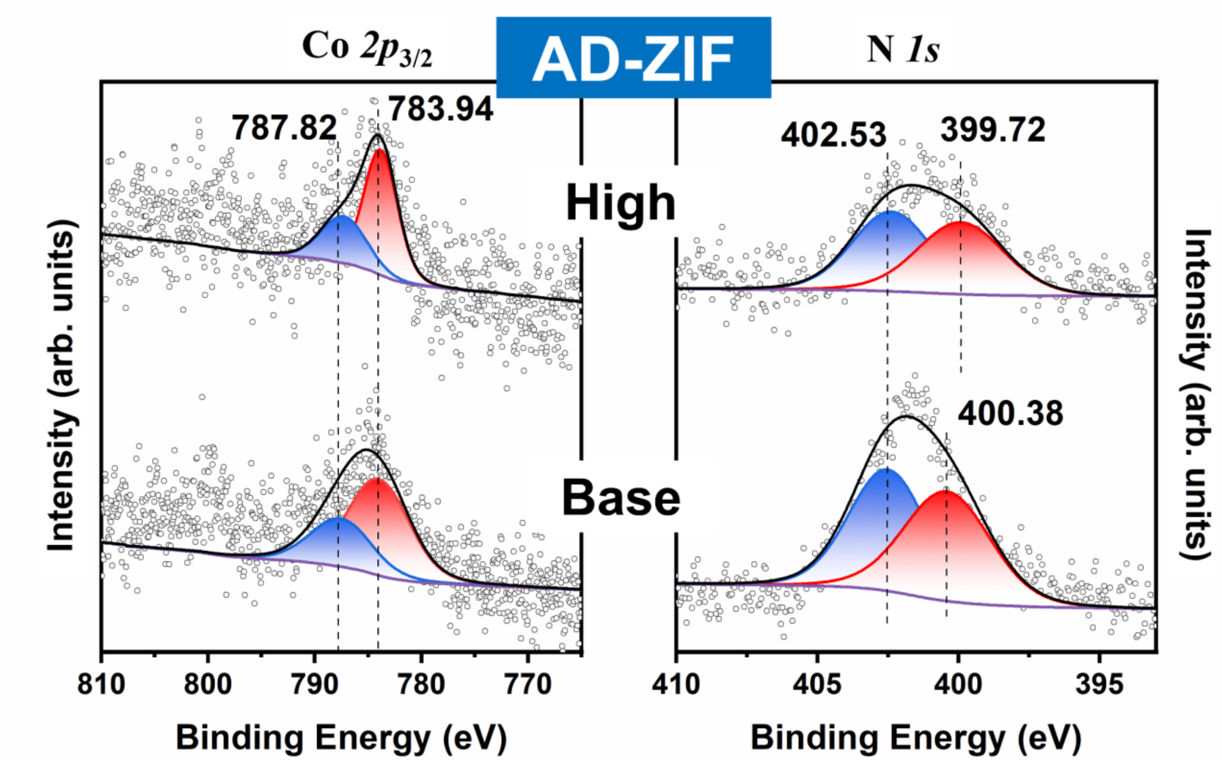

Fig. S20. Co *2p*3/2 and N *1s* of XPS spectra of AD-ZIF with 100 CV cycles at high potential window (0.85-1.55 V).

Table S2. Cobalt, nitrogen and oxygen atomic ratios by XPS spectra.

Sample[a]	Co 2p[b] (At.%)	N 1s (At.%)	O 1s (At.%)	N/Co	N/O
A-ZIF_Base	2.0	7.8	14.7	3.9	0.5
A-ZIF_Low	2.8	6.5	14.6	2.4	0.4
A-ZIF_Medi	3.3	0.0	27.6	0.0	0.0
A-ZIF_High	2.3	0.0	29.8	0.0	0.0
AB-ZIF_Base	2.8	10.9	26.2	3.8	0.4
AB-ZIF_High	0.6	0.7	28.2	1.3	0.0
AC-ZIF_Base	1.2	7.6	13.6	6.6	0.6
AC-ZIF_High	1.4	7.1	14.3	4.9	0.5
AD-ZIF_Base	1.4	7.8	16.2	5.5	0.5
AD-ZIF_High	1.6	5.5	23.0	3.5	0.2
AE-ZIF_Base	2.6	11.6	22.4	4.5	0.5
AE-ZIF_High	2.6	9.4	19.1	3.6	0.5

[a] Base means the sample before electrocatalysis. Low, medium, and high correspond to samples with 100 CV cycles at different potential window (Low: 0.85-1.05 V, Medi: 0.85-1.30 V, High: 0.85-1.55 V).

[b] All atomic ratios were determined by XPS spectroscopy in Fig. S17.

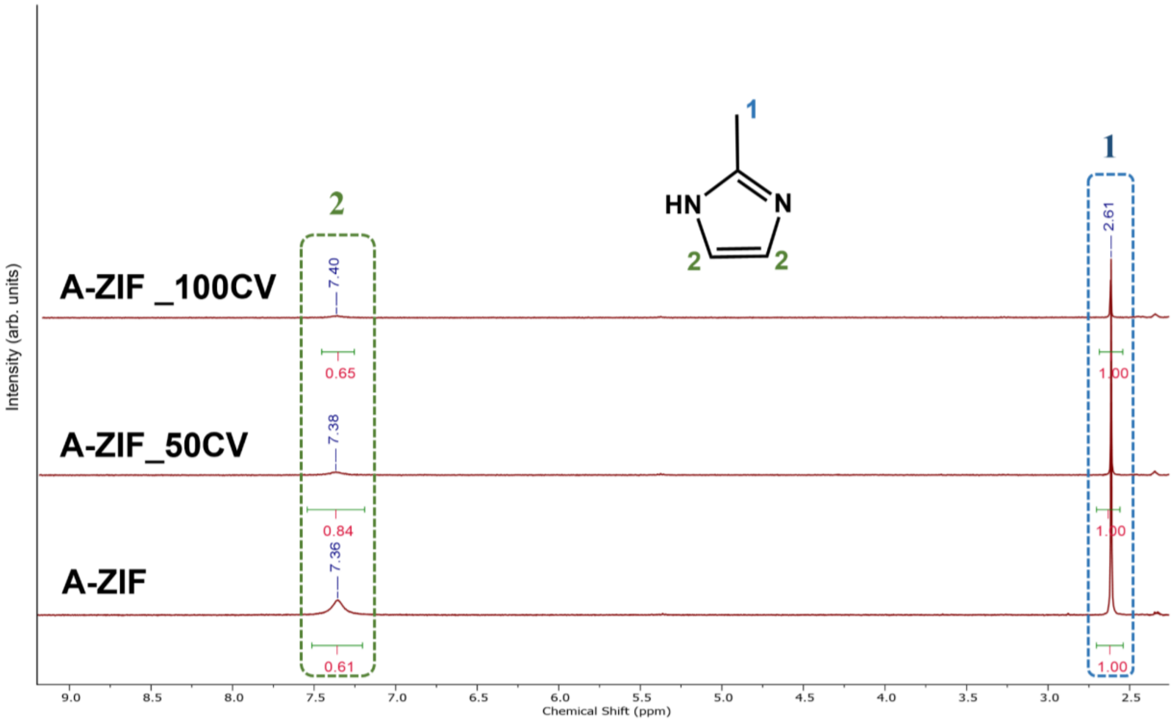

Fig. S21. ^{1}H NMR of A-ZIF, A-ZIF after 50 CV and A-ZIF after 100 CV cycles at high potential window (0.85-1.55 V).

A-ZIF: *^{1}H NMR (250 MHz, Acetic Acid-d_4) δ 7.36 (s, 1H), 2.61 (s, 1H).* A-ZIF after 50 CV: *^{1}H NMR (250 MHz, Acetic Acid-d_4) δ 7.38 (s, 1H), 2.63 (s, 1H).* A-ZIF after 100 CV: *^{1}H NMR (250 MHz, Acetic Acid-d_4) δ 7.40 (s, 1H), 2.65 (s, 1H).*

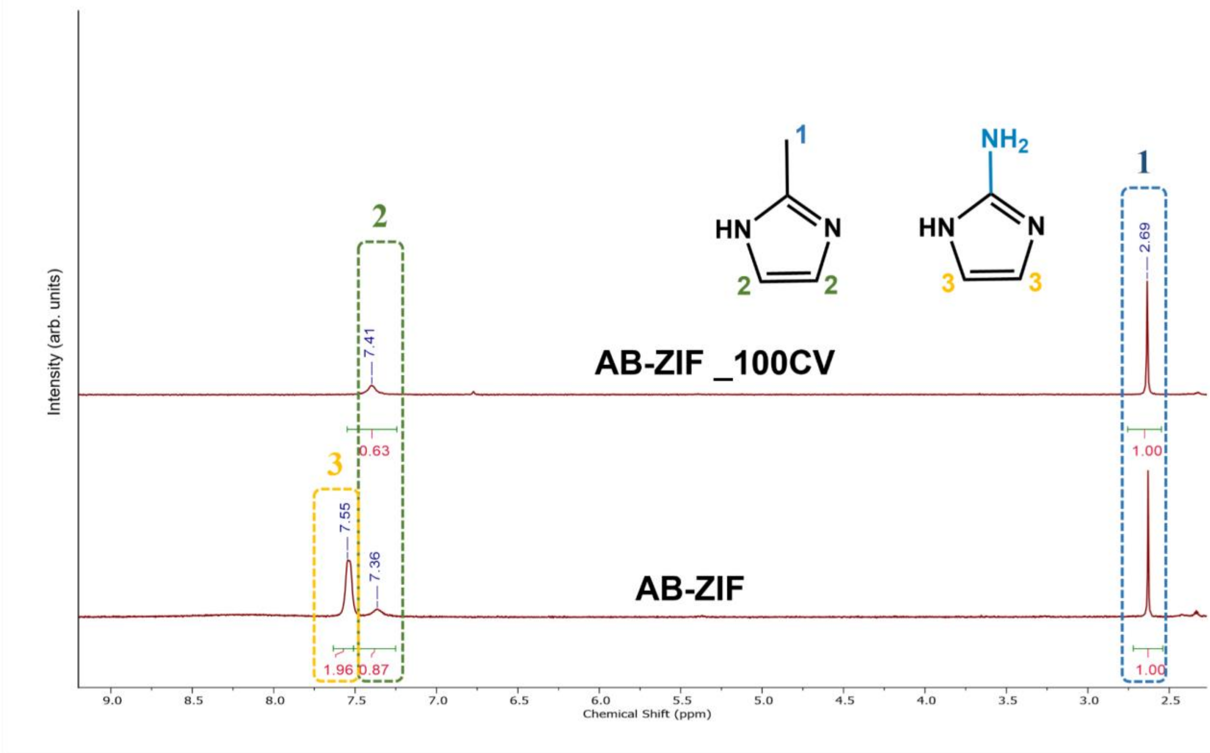

Fig. S22. ^{1}H NMR of AB-ZIF and AB-ZIF after 100 CV cycles at high potential window (0.85-1.55 V).

AB-ZIF: *^{1}H NMR (250 MHz, Acetic Acid-d_4) δ 7.55 (s, 2H), 7.36 (s, 1H), 2.63 (s, 1H).* AB-ZIF after 100 CV: *^{1}H NMR (250 MHz, Acetic Acid-d_4) δ 7.41 (s, 1H), 2.69 (s, 1H).*

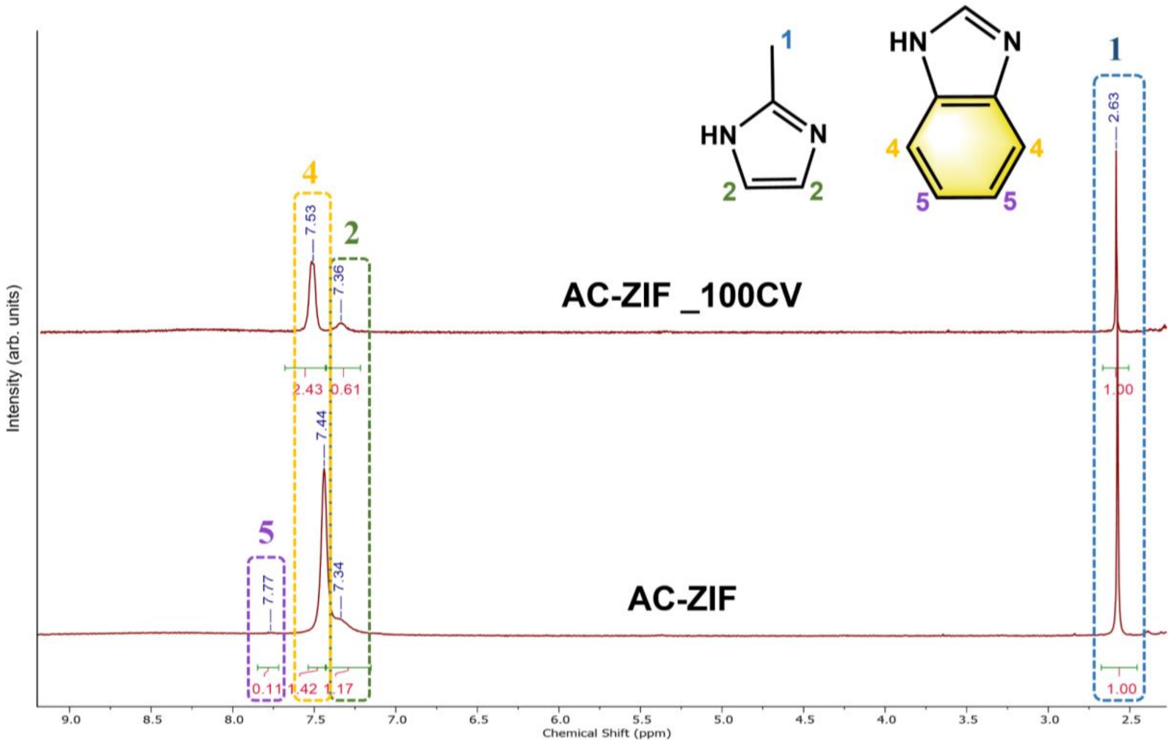

Fig. S23. ^{1}H NMR of AC-ZIF and AC-ZIF after 100 CV cycles at high potential window (0.85-1.55 V).

AC-ZIF: *^{1}H NMR (250 MHz, Acetic Acid-d_4) δ 7.44 (s, 1H), 7.34 (s, 1H), 2.58 (s, 1H)*. AC-ZIF after 100 CV: *^{1}H NMR (250 MHz, Acetic Acid-d_4) δ 7.53 (s, 2H), 7.36 (s, 1H), 2.63 (s, 1H).*

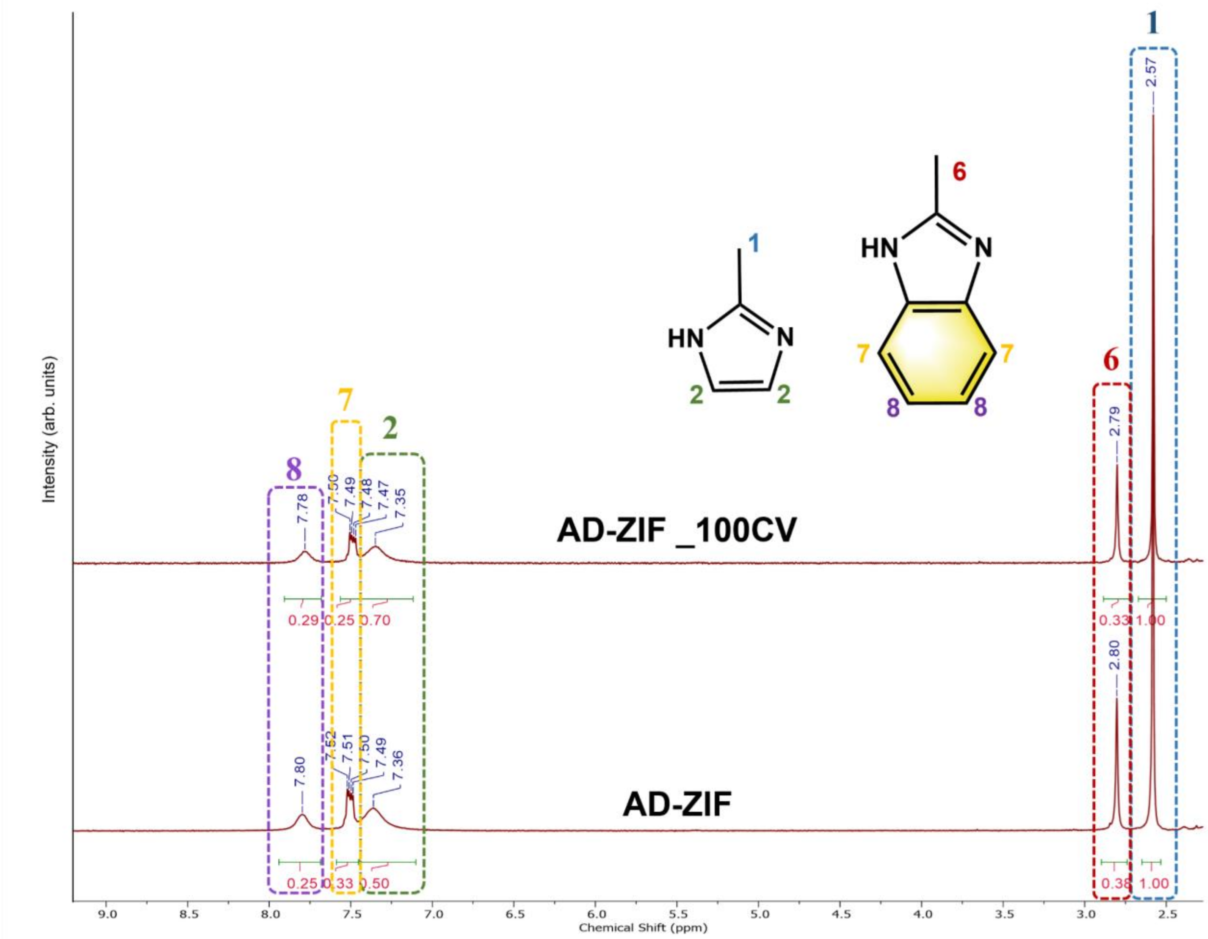

Fig. S24. ^{1}H NMR of AD-ZIF and AD-ZIF after 100 CV cycles at high potential window (0.85-1.55 V).

AD-ZIF: *^1H NMR (250 MHz, Acetic Acid-d_4) δ 7.80 (s, 0H), 7.50 (dd, J = 6.1, 2.9 Hz, 0H), 7.36 (s, 1H), 2.80 (s, 0H), 2.58 (s, 1H).* AC-ZIF after 100 CV: *^1H NMR (250 MHz, Acetic Acid-d_4) δ 7.78 (s, 0H), 7.49 (dd, J = 6.1, 2.9 Hz, 0H), 7.35 (s, 1H), 2.79 (s, 0H), 2.57 (s, 1H).*

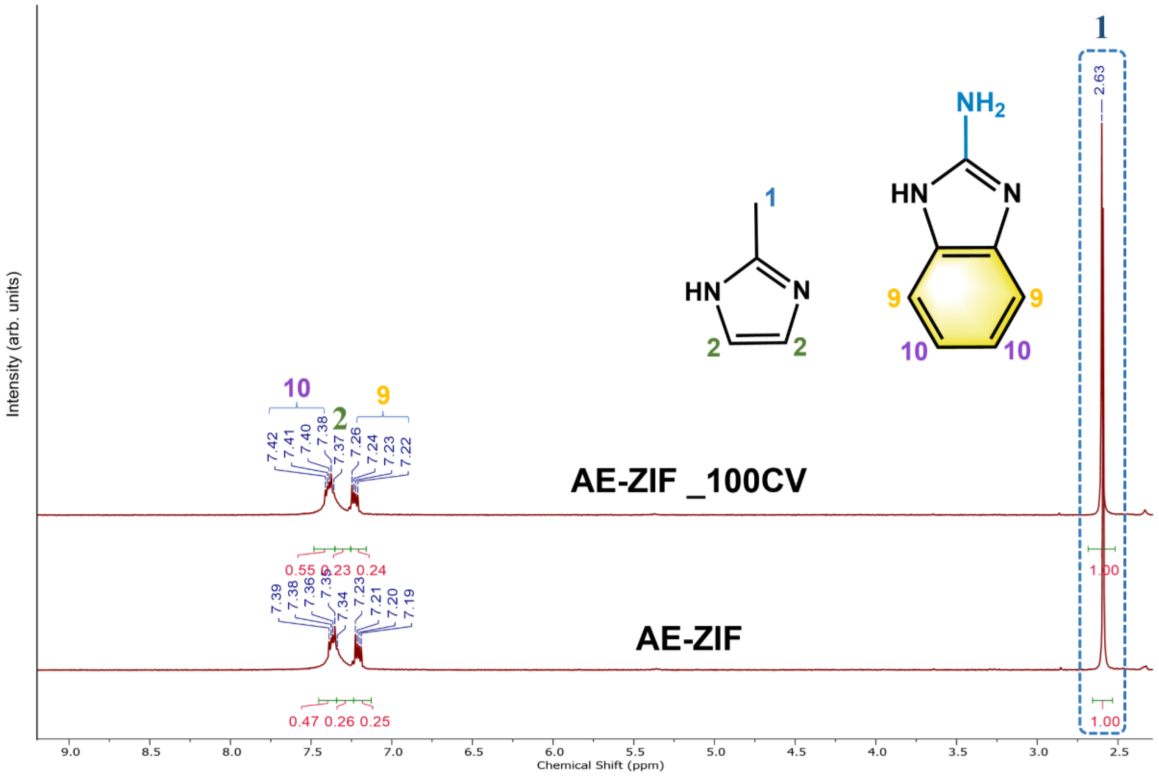

Fig. S25. ^{1}H NMR of AE-ZIF and AE-ZIF after 100 CV cycles at high potential window (0.85-1.55 V).

AE-ZIF: *^{1}H NMR (250 MHz, Acetic Acid-d_4) δ 7.37 (dd, J = 5.9, 3.2 Hz, 0H), 7.34 (s, 0H), 7.21 (dd, J = 5.9, 3.2 Hz, 0H), 2.59 (s, 1H).* AE-ZIF after 100 CV: *^{1}H NMR (250 MHz, Acetic Acid-d_4) δ 7.40 (dd, J = 5.9, 3.2 Hz, 0H), 7.37 (s, 0H), 7.24 (dd, J = 5.9, 3.2 Hz, 0H), 2.63 (s, 1H).*

Table S3. Calculation of the ligand ratio in LE-ZIFs by ^{1}H NMR.

Samples	**AB-ZIF**	**AC-ZIF**	**AD-ZIF**	**AE-ZIF**
Synthetic mass of ligand B-E/A (g/g)	1/1	1/1	1/1	1/1
Synthetic ratio of ligand B-E (mol%)	49.6	41.0	38.3	38.1
Actual ratio of ligand B-E (mol%)	51.2	41.4	39.0	36.9
Actual ratio of ligand B-E after 100 CV (mol%)	-	60.2	33.9	39.1

All ^{1}H NMR data were quantified from Figs. S21-25.

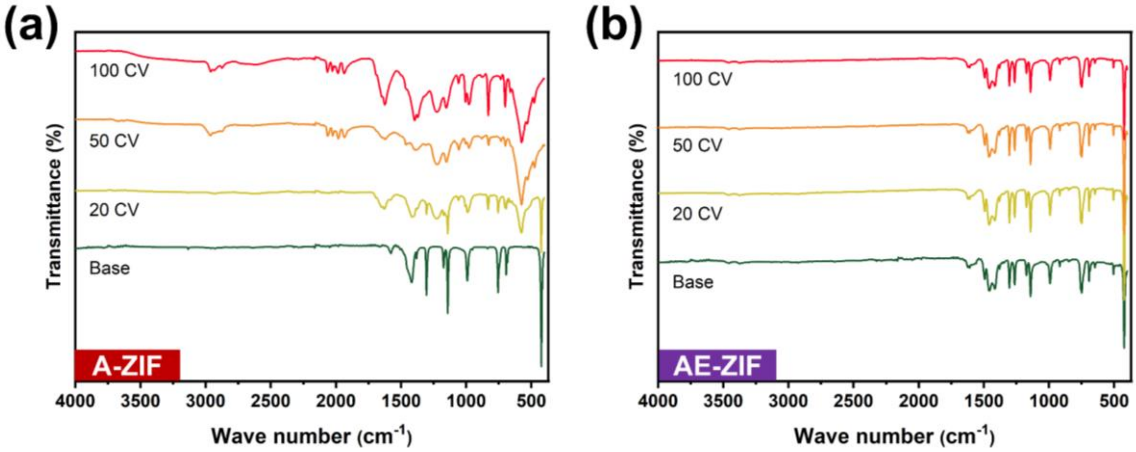

Fig. S26. ATR-IR spectra of A-ZIF (**a**) and AE-ZIF (**b**) between 0.85-1.55 V with different CV cycles (0, 20, 50 and 100).

S4. Evolution of morphology and elemental distribution after electrocatalytic reaction

Both A and AE exhibit distinct dodecahedral crystal grains with clear and sharp edges before electrocatalytic reaction, indicating their well-defined morphology (Figs. 4 and S27). Elemental mapping via EDS reveals the uniform distribution of elements within ZIF particles, indicating the homogeneous distribution of the secondary ligand without aggregation together, contrasting markedly with the structured evolution post electrocatalysis.

After 12-hour amperometry, enlargement of the AE-ZIF particle edge in Fig. S30 reveals the lattice fringes of 0.23, 0.24 and 0.27 nm within surface layer, corresponding well with the (012) plane of CoOOH and (101) and (100) planes of $Co(OH)_2$, as indicated by bright rings in the SAED pattern [11, 12]. Other LE samples, AC and AD exhibit the in-situ formation of a cobalt (oxy)hydroxide layer similar to AE-ZIF on their surfaces (Figs. S32 and S33). The apparent aggregation of Co and O elements on the particle surfaces in the EDS mapping further confirms the presence of the outer layer structure. Interestingly, although AB-ZIF transitions to an amorphous during electrocatalysis according to XRD pattern, some agglomerates of $Co(OH)_2$ and CoOOH nanoparticles are still observed in TEM images. The distribution of Co and O elements in EDS mapping, lattice fringes, and bright spots in the corresponding selected area FFT patterns further confirm the crystalline characteristics of these agglomerated particles (Fig. S31).

The atomic ratio of oxygen elements increases significantly to 49.21% and 23.23% after 12-hour amperometry for A and AB, contrasting with the nearly negligible oxygen content before the reaction (Figs. S28e and S31f). This further supports the complete reconstruction of A and AB, transitioning into high-valence cobalt (oxy)hydroxides. In contrast, the atomic ratio of oxygen elements in AC, AD and AE remains clearly controlled within the range of 1 to 3.12%, indicating incomplete reconstruction with only slight electro-oxidation occurring on the particle surface.

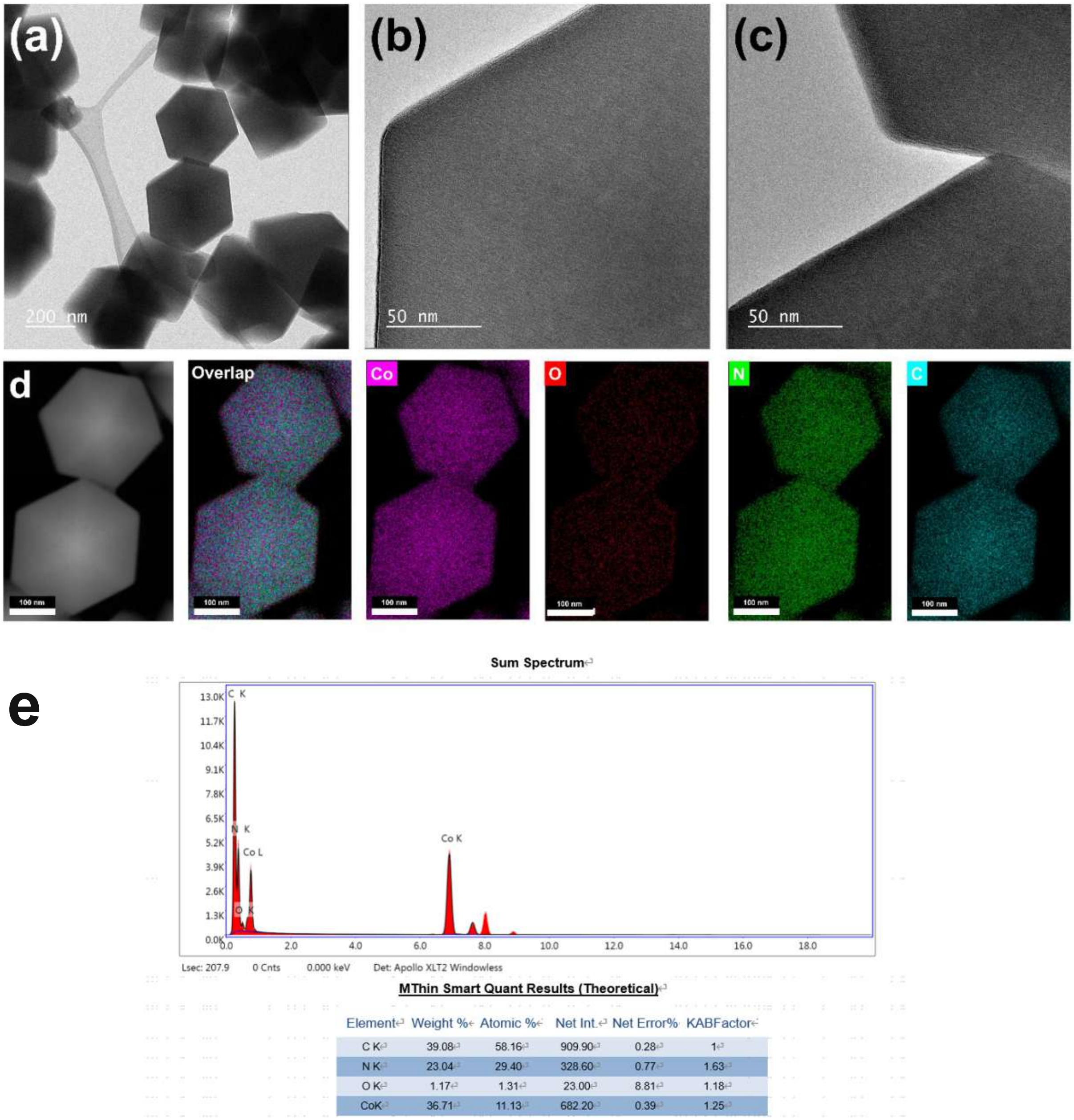

MThin Smart Quant Results (Theoretical)

Element	Weight %	Atomic %	Net Int.	Net Error%	KABFactor
C K	39.08	58.16	909.90	0.28	1
N K	23.04	29.40	328.60	0.77	1.63
O K	1.17	1.31	23.00	8.81	1.18
CoK	36.71	11.13	682.20	0.39	1.25

Fig. S27. a, TEM image of A-ZIF. **b**, **c**, Enlarged TEM images of A-ZIF. **d**, Elemental mapping of A-ZIF showing the Co, O, N and C distribution. **e**, EDS quantitative elemental analysis of A-ZIF.

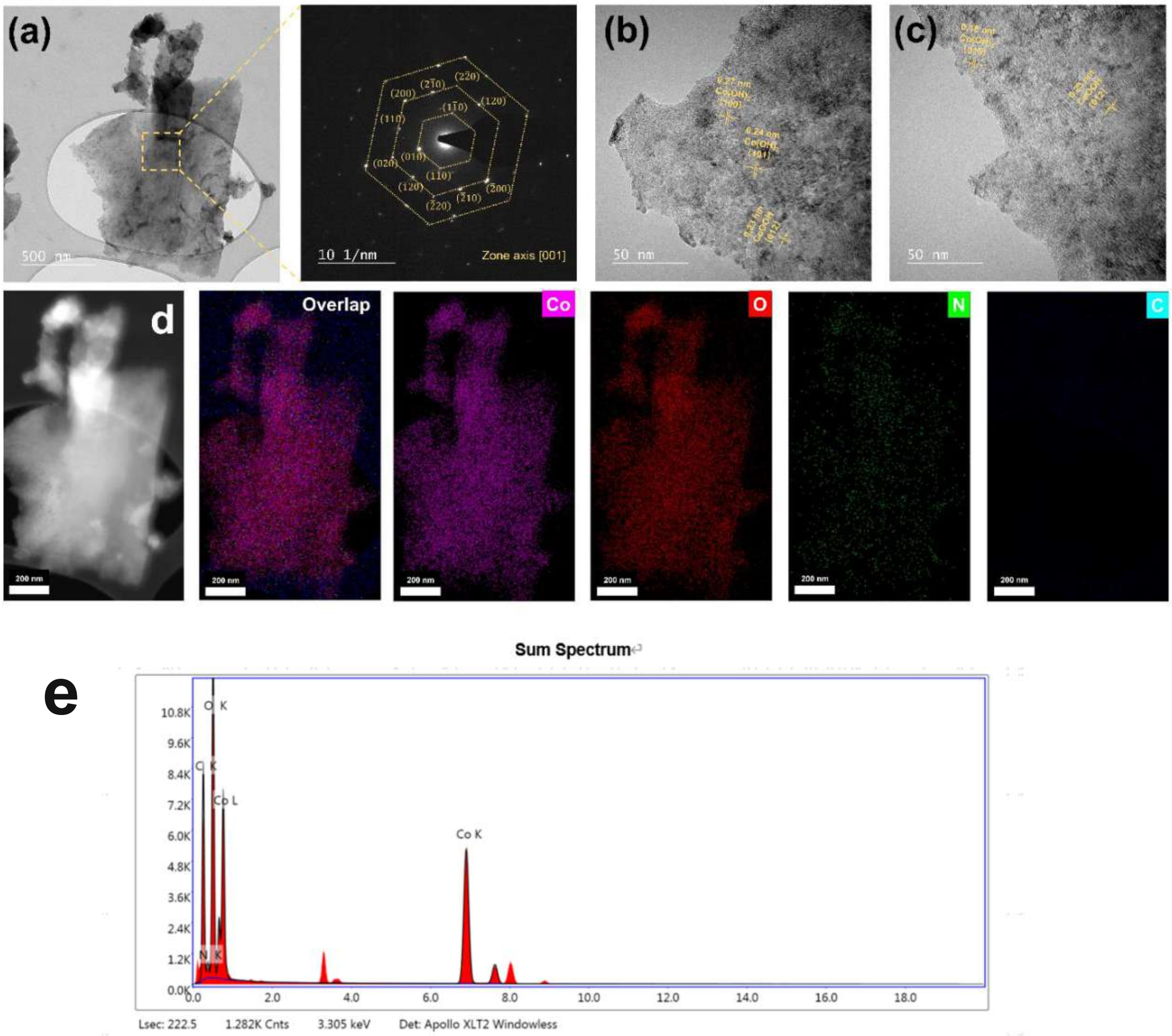

MThin Smart Quant Results (Theoretical)

Element	Weight %	Atomic %	Net Int.	Net Error%	KABFactor
C K	19.57	33.57	446.40	0.42	0.84
N K	2.19	3.23	30.70	3.37	1.38
O K	38.21	49.21	735.90	0.33	1
CoK	40.03	13.99	729.00	0.33	1.06

Fig. S28. **a**, TEM image of A-ZIF after 12-hour amperometry, with the corresponding SAED pattern. **b**, **c**, Enlarged TEM images of A-ZIF after 12-hour amperometry. **d**, Elemental mapping of A-ZIF after 12-hour amperometry showing the Co, O, N and C distribution. **e**, EDS quantitative elemental analysis of A-ZIF after 12-hour amperometry.

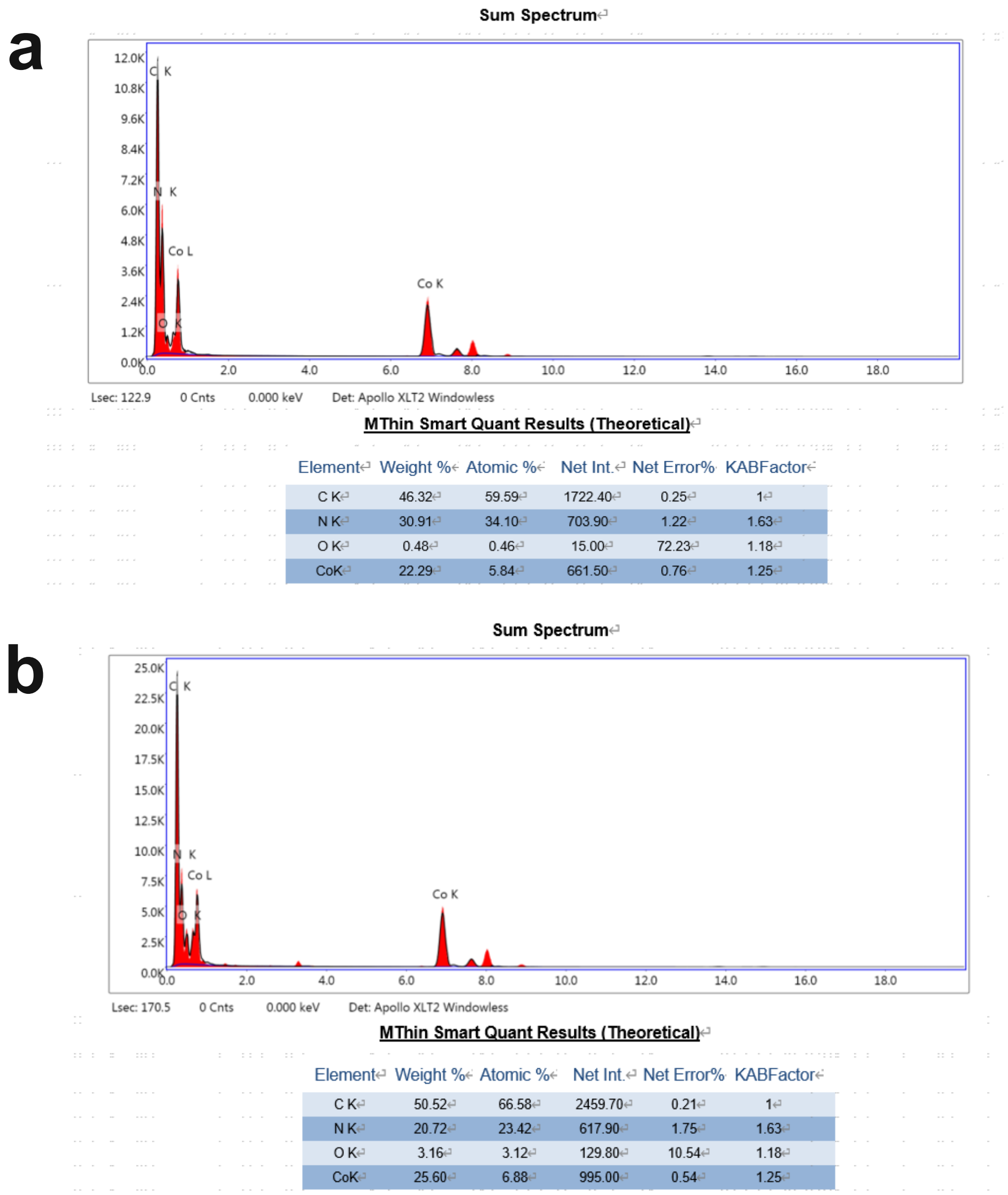

MThin Smart Quant Results (Theoretical)

Element	Weight %	Atomic %	Net Int.	Net Error%	KABFactor
C K	46.32	59.59	1722.40	0.25	1
N K	30.91	34.10	703.90	1.22	1.63
O K	0.48	0.46	15.00	72.23	1.18
CoK	22.29	5.84	661.50	0.76	1.25

MThin Smart Quant Results (Theoretical)

Element	Weight %	Atomic %	Net Int.	Net Error%	KABFactor
C K	50.52	66.58	2459.70	0.21	1
N K	20.72	23.42	617.90	1.75	1.63
O K	3.16	3.12	129.80	10.54	1.18
CoK	25.60	6.88	995.00	0.54	1.25

Fig. S29. EDS quantitative elemental analysis of AE-ZIF before (**a**) and after 12-hour amperometry (**b**).

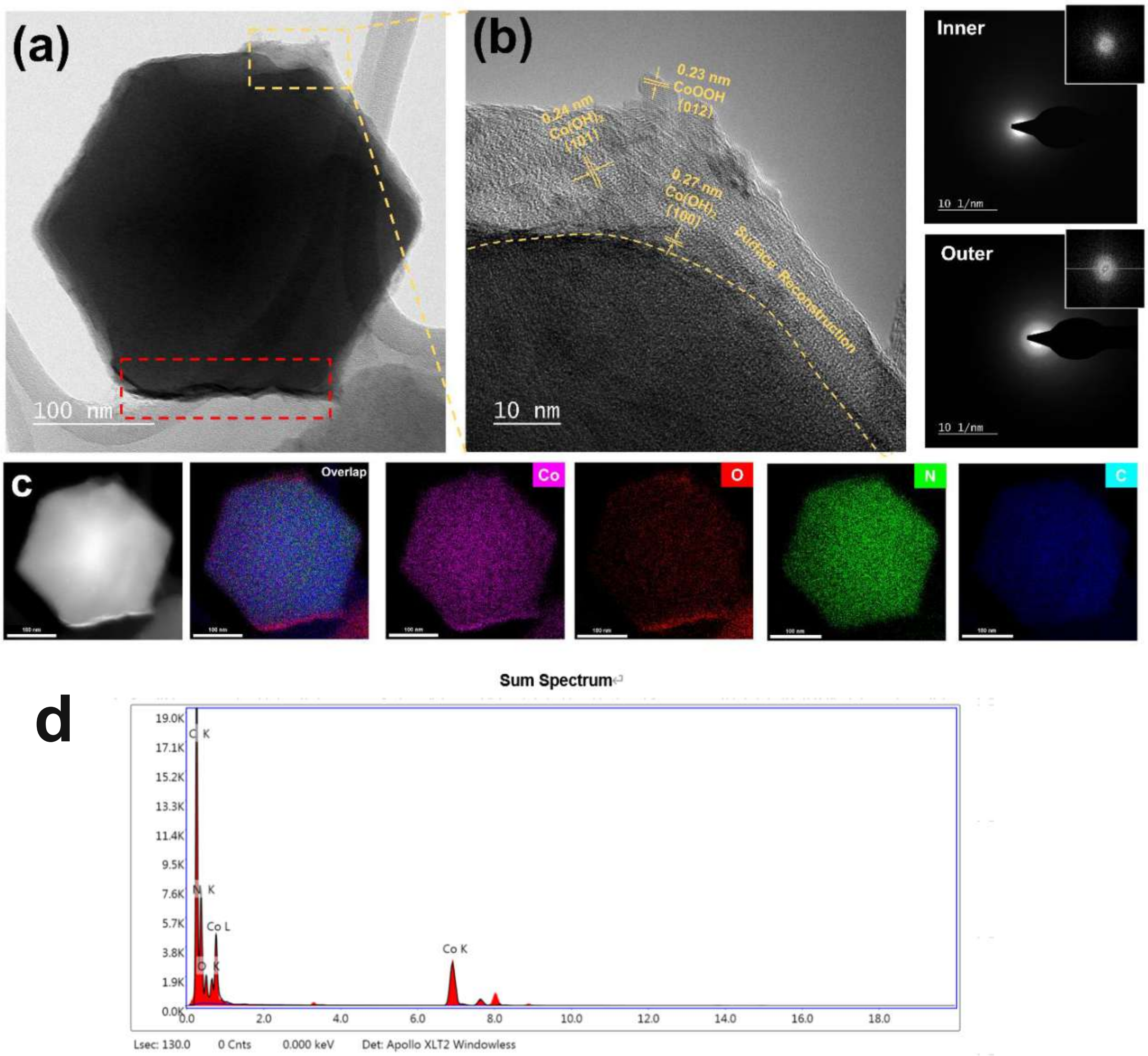

MThin Smart Quant Results (Theoretical)

Element	Weight %	Atomic %	Net Int.	Net Error%	KABFactor
C K	51.74	65.61	2436.20	0.32	1
N K	24.59	26.74	709.20	1.62	1.63
O K	2.21	2.11	88.00	15.99	1.18
CoK	21.46	5.55	806.60	0.71	1.25

Fig. S30. a, TEM image of single-particle AE-ZIF after 12-hour amperometry. **b**, Enlarged TEM image of AE-ZIF edge after 12-hour amperometry, the corresponding SAED pattern. **c**, Elemental mapping of single-particle AE-ZIF after 12-hour amperometry showing the Co, O, N and C distribution. **d**, EDS quantitative elemental analysis of AE-ZIF after 12-hour amperometry.

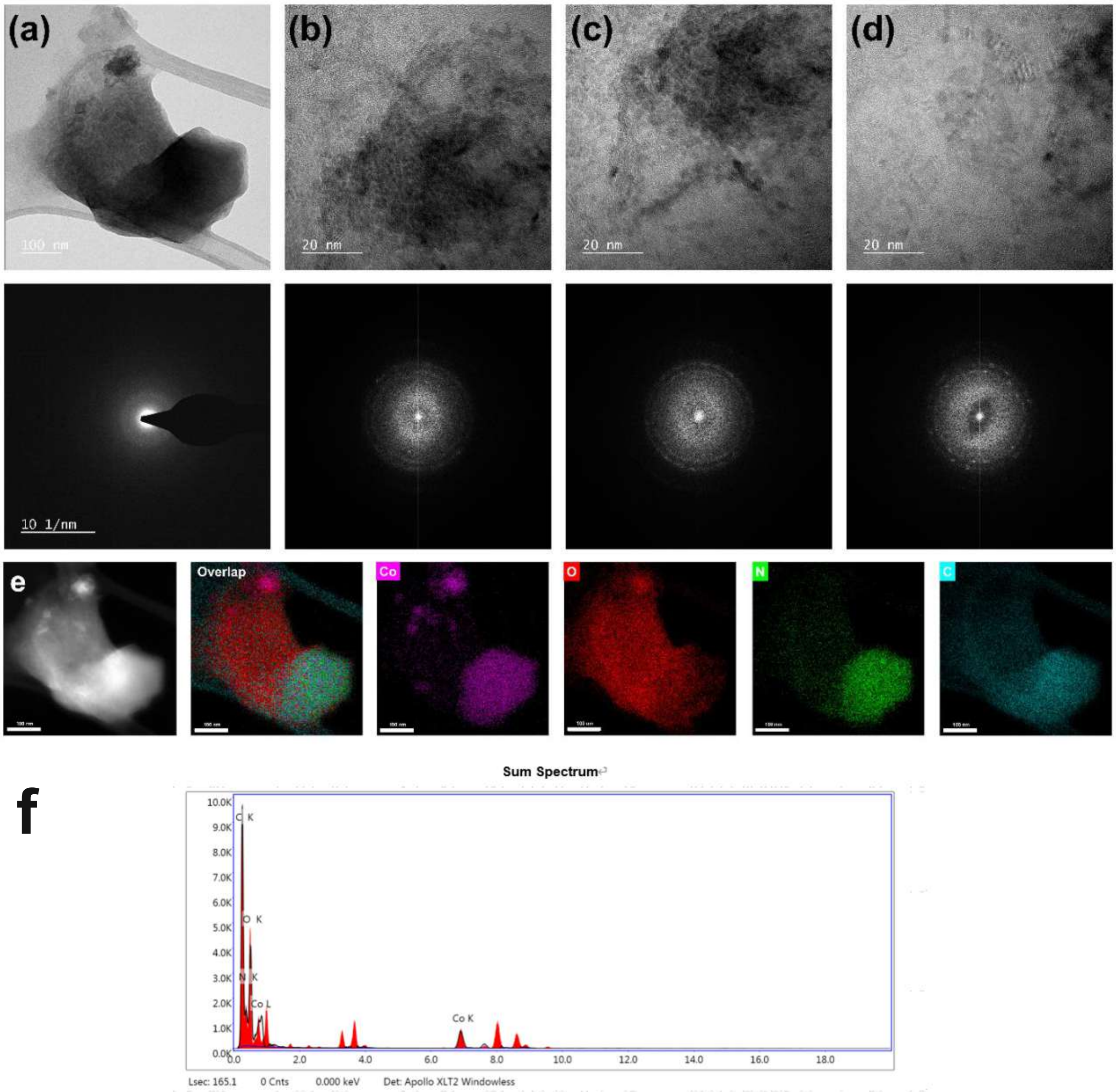

MThin Smart Quant Results (Theoretical)

Element	Weight %	Atomic %	Net Int.	Net Error%	KABFactor
C K	54.02	64.36	1050.20	0.42	1
N K	9.70	9.91	115.50	3.76	1.63
O K	25.97	23.23	426.30	1.57	1.18
CoK	10.31	2.50	159.90	1.22	1.25

Fig. S31. **a**, TEM image of AB-ZIF after 12-hour amperometry, with the corresponding SAED and FFT patterns. **b**, **c**, **d**, Enlarged TEM images of AB-ZIF after 12-hour amperometry. **e**, Elemental mapping of AB-ZIF after 12-hour amperometry showing the Co, O, N and C distribution. **f**, EDS quantitative elemental analysis of AB-ZIF after 12-hour amperometry.

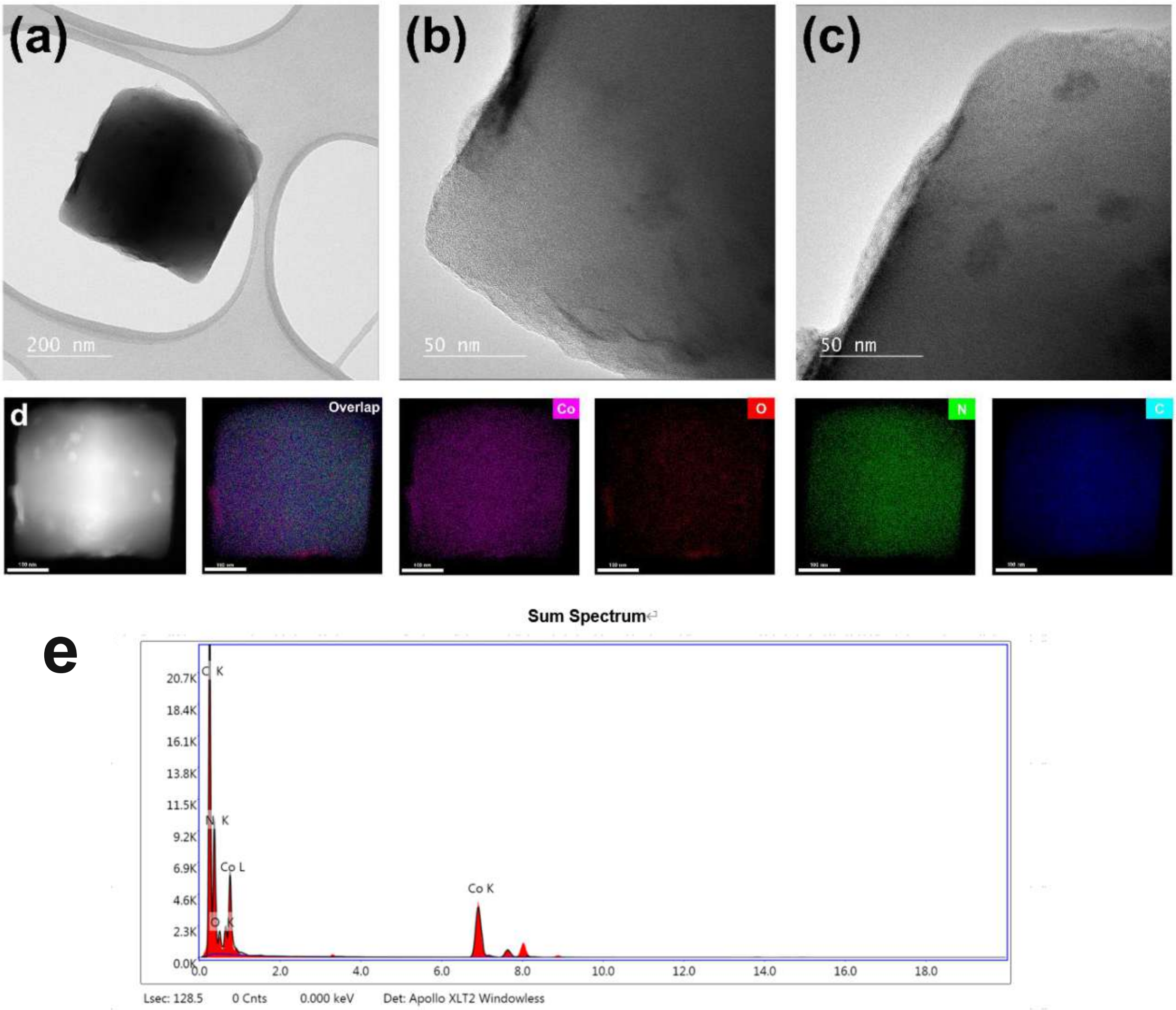

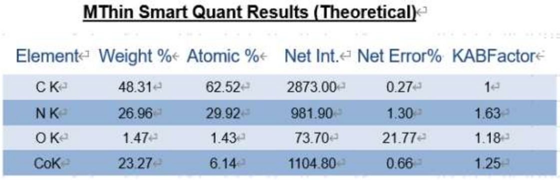

MThin Smart Quant Results (Theoretical)

Element	Weight %	Atomic %	Net Int.	Net Error%	KABFactor
C K	48.31	62.52	2873.00	0.27	1
N K	26.96	29.92	981.90	1.30	1.63
O K	1.47	1.43	73.70	21.77	1.18
CoK	23.27	6.14	1104.80	0.66	1.25

Fig. S32. **a**, TEM image of AC-ZIF after 12-hour amperometry. **b**, **c**, Enlarged TEM images of AC-ZIF after 12-hour amperometry. **d**, Elemental mapping of AC-ZIF after 12-hour amperometry showing the Co, O, N and C distribution. **e**, EDS quantitative elemental analysis of AC-ZIF after 12-hour amperometry.

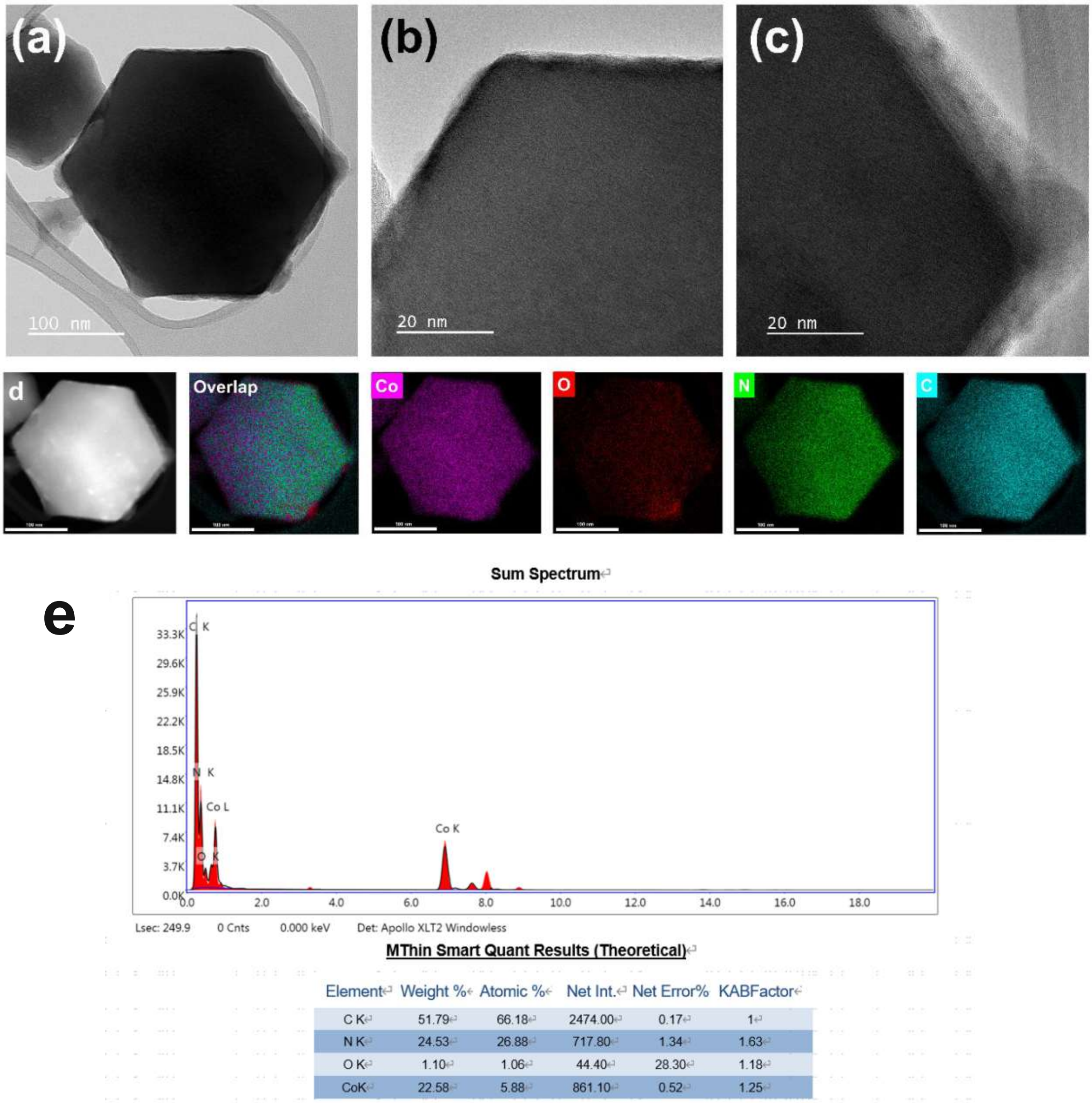

MThin Smart Quant Results (Theoretical)

Element	Weight %	Atomic %	Net Int.	Net Error%	KABFactor
C K	51.79	66.18	2474.00	0.17	1
N K	24.53	26.88	717.80	1.34	1.63
O K	1.10	1.06	44.40	28.30	1.18
CoK	22.58	5.88	861.10	0.52	1.25

Fig. S33. **a**, TEM image of AD-ZIF after 12-hour amperometry. **b**, **c**, Enlarged TEM images of AD-ZIF after 12-hour amperometry. **d**, Elemental mapping of AD-ZIF after 12-hour amperometry showing the Co, O, N and C distribution. **e**, EDS quantitative elemental analysis of AD-ZIF after 12-hour amperometry.

S5. In-situ UV–Vis absorption and Raman spectroscopy during electrocatalytic reactions

During the in-situ electrochemical UV–Vis absorption measurements, AC, AD and AE also exhibit the broad feature, associated to the same transition of tetrahedral Co species. Sample AB-ZIF only shows absorption signals at 328 and 354 nm, corresponding to ligand 2-mIm and NH_2-mIm, respectively (Fig. S35a). The broad signals associated with tetrahedral Co species in AC and AD noticeably weaken after 50 and 60 CV cycles, in addition to AC-ZIF displaying a CoOOH signal at 369 nm (Figs. S35b and S35c) [13]. The most unstable one is AB-ZIF, where the ligand signals disappear after 10 CV cycles, indicating that the intrinsic framework had been degraded.

For the other LE-ZIFs analyzed by in-situ electrochemical Raman spectroscopy, the secondary ligands bIm and 2-bIm are attributed to characteristic peaks at 701, 775 and 685 cm^{-1} in AC and AD (Figs. S36 and S37) [14, 15]. Under high applied potential or after higher CV cycles, the preservation of ligand peaks in AD-ZIF is notably better than in AC-ZIF. Additionally, there are slightly signals in the range of 498 to 617 cm^{-1} indicating the presence of high-valence cobalt species. Combined with the AE-like core-shell structure observed in TEM images (Figs. S32 and S33), this implies that they undergo the SR process, continuous generation of cobalt (oxy)hydroxide layer while preserving the inherent framework structure as the core. In the case of AB-ZIF, the characteristic peaks rapidly weaken and disappear after 1.30 V or 20 CV cycles, with signals of probably CoOOH appearing only after 80 cycles. Subsequently, no distinct features were observed in the Raman spectra, indicating rapid structural degradation to form the amorphous structures.

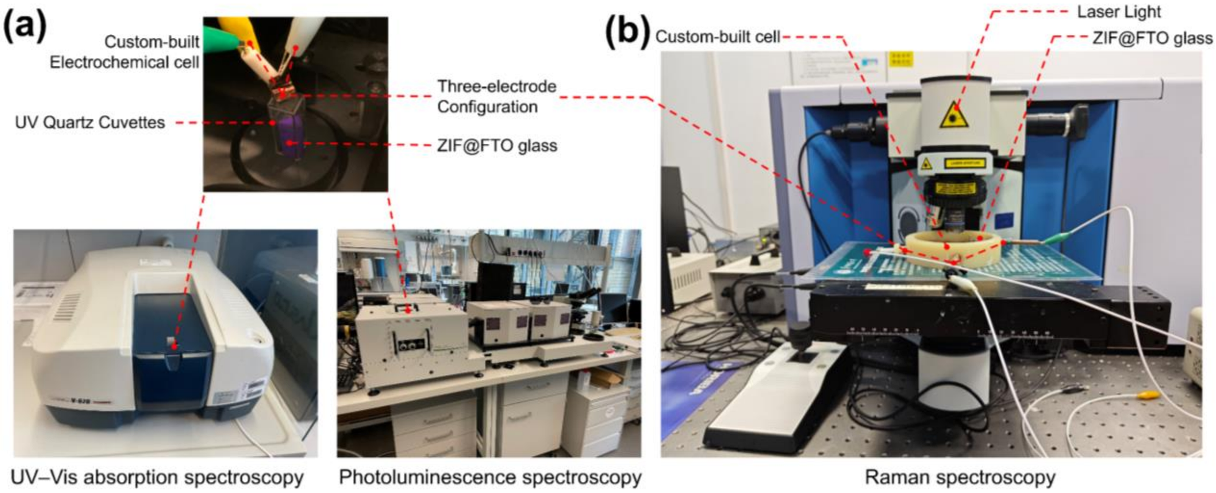

Fig. S34. Experimental setup for In-situ electrochemical UV–Vis absorption/Photoluminescence (**a**) and Raman (**b**) measurements.

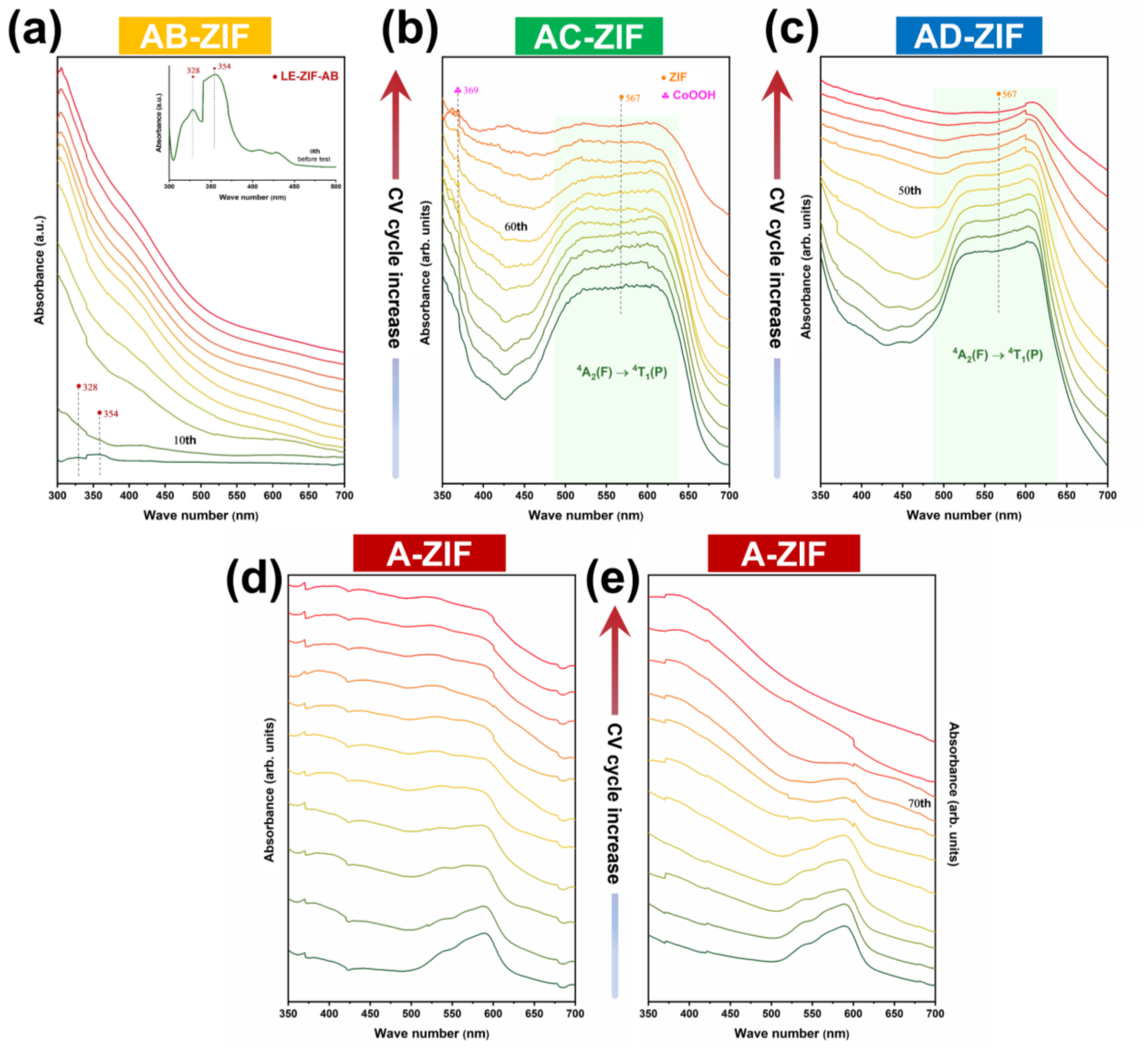

Fig. S35. a, b, c, In-situ electrochemical UV–Vis absorption spectroscopy of AB-ZIF (**a**), AC-ZIF (**b**) and AD-ZIF (**c**) with 100 CV cycles at high potential window from 0.85-1.55 V. **d, e**, In-situ electrochemical UV–Vis absorption spectroscopy of A-ZIF with 100 CV cycles at low potential window from 0.85-1.05 V (**d**) and medium potential window from 0.85-1.30 V (**e**).

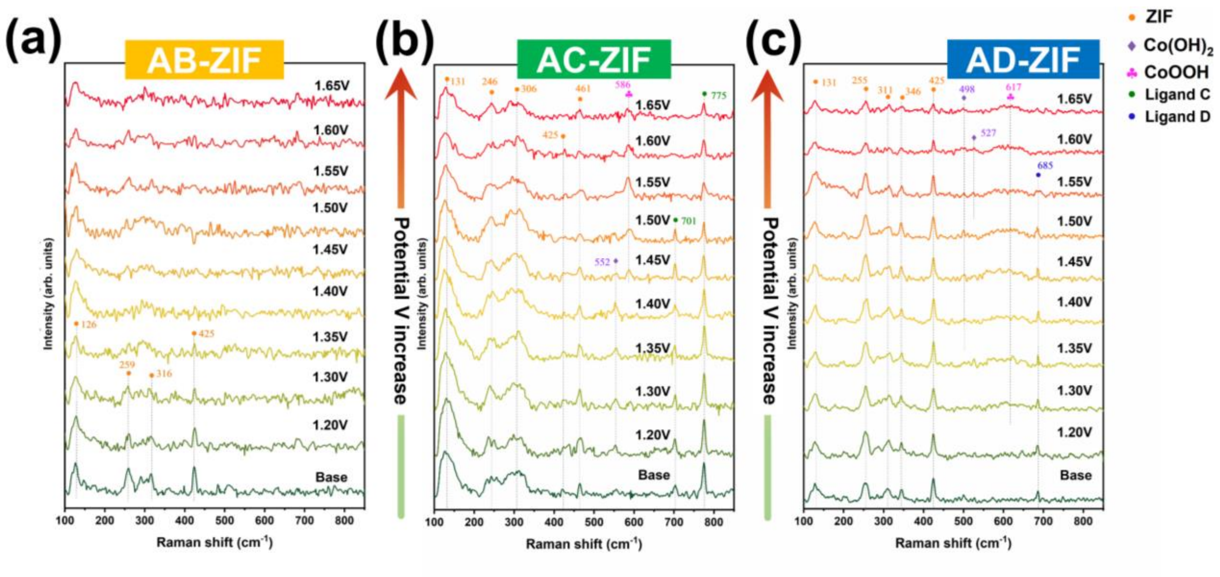

Fig. S36. In-situ electrochemical Raman spectroscopy of AB-ZIF (**a**), AC-ZIF (**b**) and AD-ZIF (**c**) from at various applied potentials 1.20 to 1.65 V.

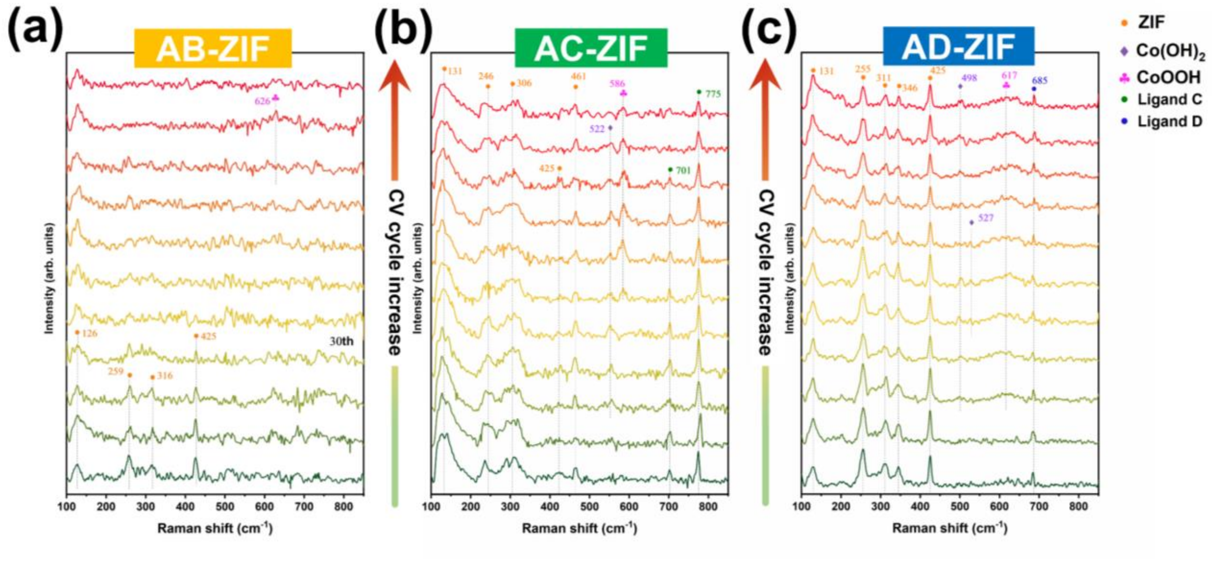

Fig. S37. In-situ electrochemical Raman spectroscopy of AB-ZIF (**a**), AC-ZIF (**b**) and AD-ZIF (**c**) with 100 CV cycles at high potential window from 0.85-1.55 V, the scan rate is 10 mV s^{-1}.

S6. Photoelectrocatalysis and band gaps calculation

Samples AC and AD exhibit similar trends in band gap and PL peak intensity to AE-ZIF, which decrease with an increasing number of CV cycles (Figs. S43 and S45). Specifically, the band gap of AC-ZIF decreases from 1.41 to 1.07 eV, while that of AD-ZIF from 1.43 to 0.91 eV. The decrease in band gap aligns with the varying degrees of self-reconstruction and structural evolution during photoelectrocatalysis. The slight decrease in PL peak intensity of AC and AD can be attributed to the in-situ formation of the cobalt (oxy)hydroxide layer during CV test. Samples AC and AD exhibit relatively low current density and O_2 evolution rate under visible light, with reductions of 23.6% and 23.2% after 12 hours, indicating their inferior activity and stability under photoelectrocatalysis compared to AE-ZIF. Compared to A-ZIF, they still maintain visible light catalytic performance under amperometry for 12 hours, with about 1.5 or 2-fold enhancement compared to the dark condition.

Conversely, AB-ZIF shows poor photoelectrochemical stability, with the PL peak disappearing after 10 CV cycles, indicating a phase transition. Furthermore, AB-ZIF has a band gap exceeding 2 eV and lacks visible light absorption ability, resulting in a negligible enhancement of OER efficiency in the visible light (Fig. S41).

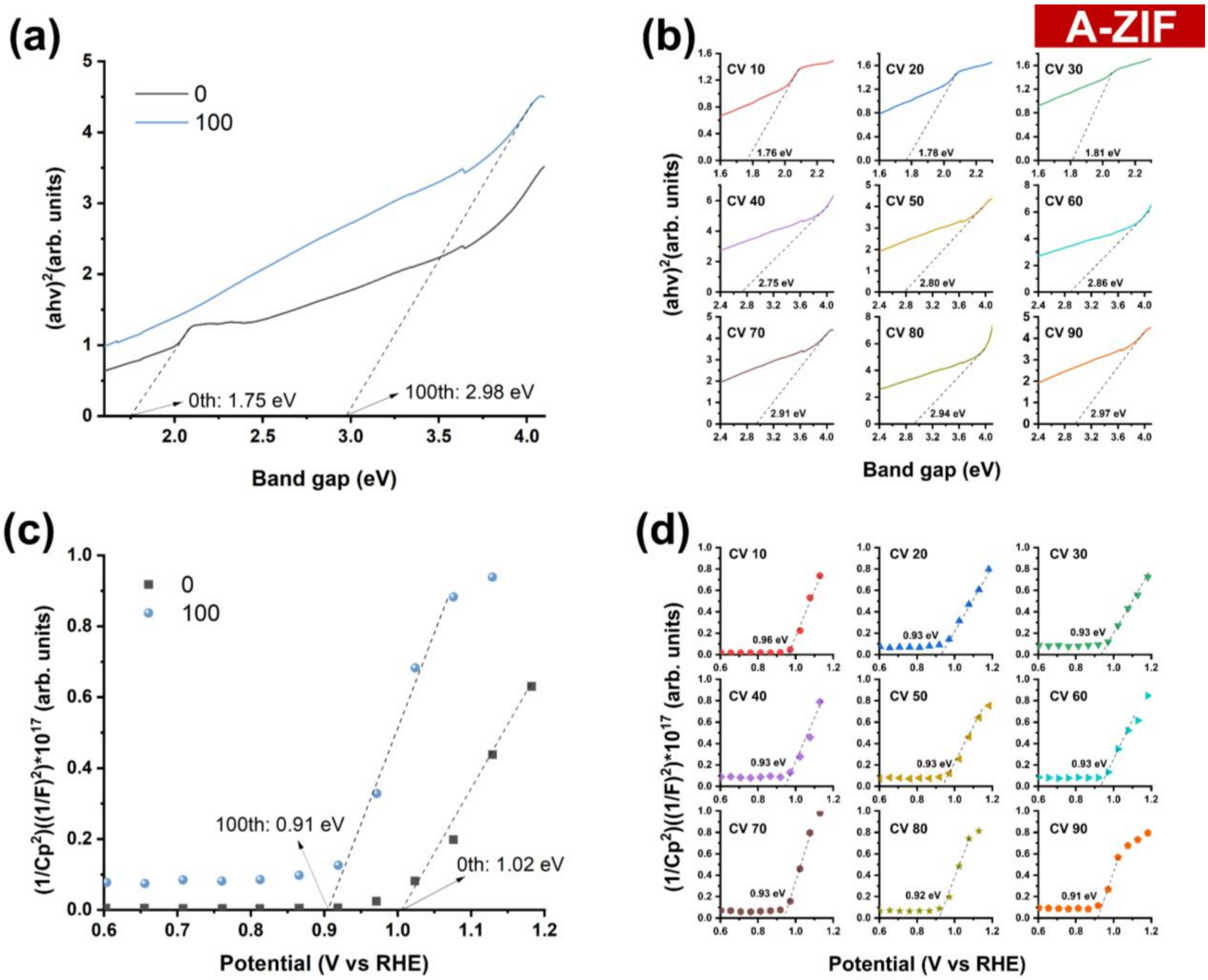

Fig. S38. **a**, **b**, Band gap of A-ZIF calculated from in-situ UV–Vis absorption spectra from 0 to 100 CV cycles at 0.85-1.55 V. **c**, **d**, Flat band potentials of A-ZIF calculated from Mott-Schottky plots from 0 to 100 CV cycles at 0.85-1.55 V.

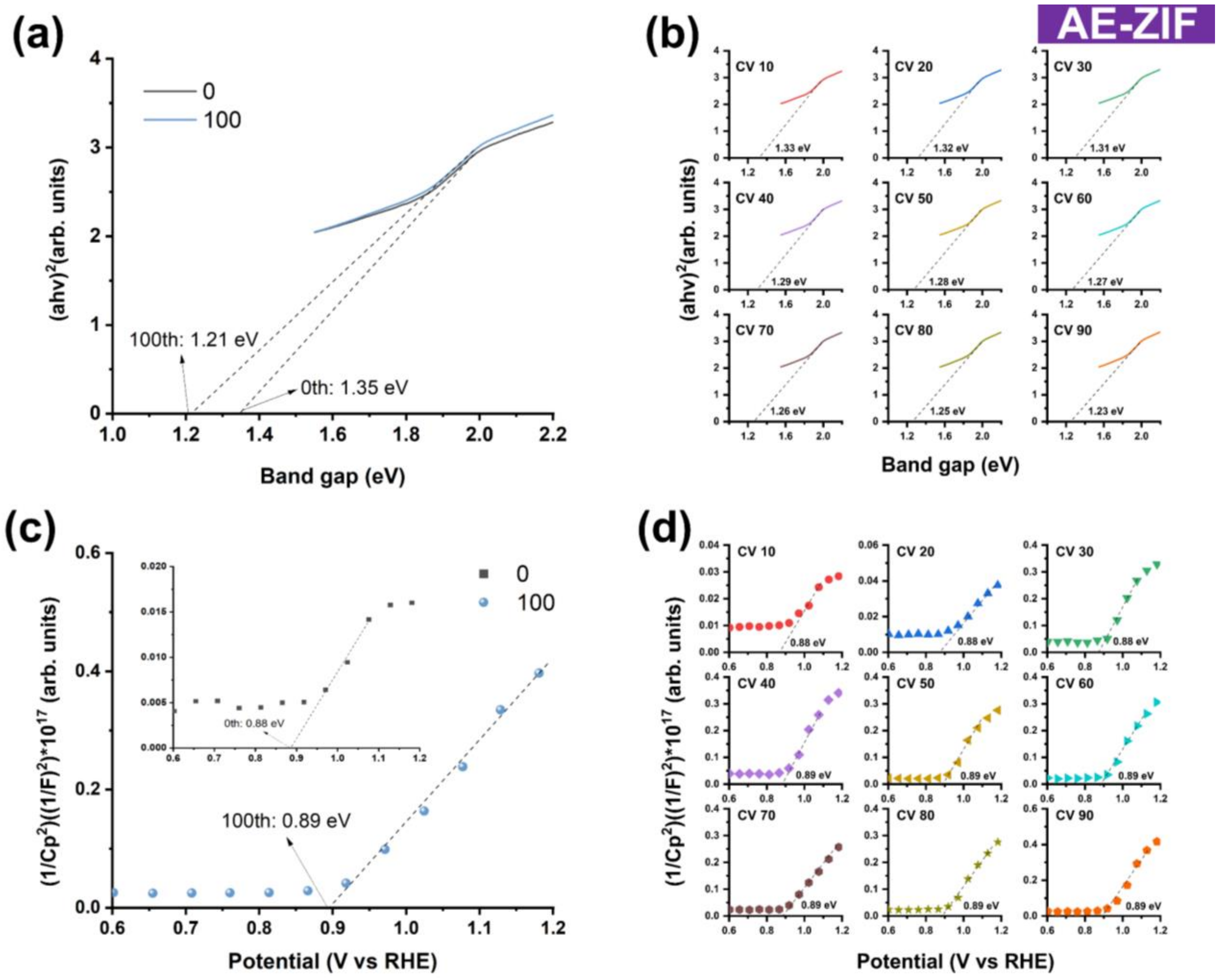

Fig. S39. **a**, **b**, Band gap of AE-ZIF calculated from in-situ UV–Vis absorption spectra from 0 to 100 CV cycles at 0.85-1.55 V. **c**, **d**, Flat band potentials of AE-ZIF calculated from Mott-Schottky plots from 0 to 100 CV cycles at 0.85-1.55 V.

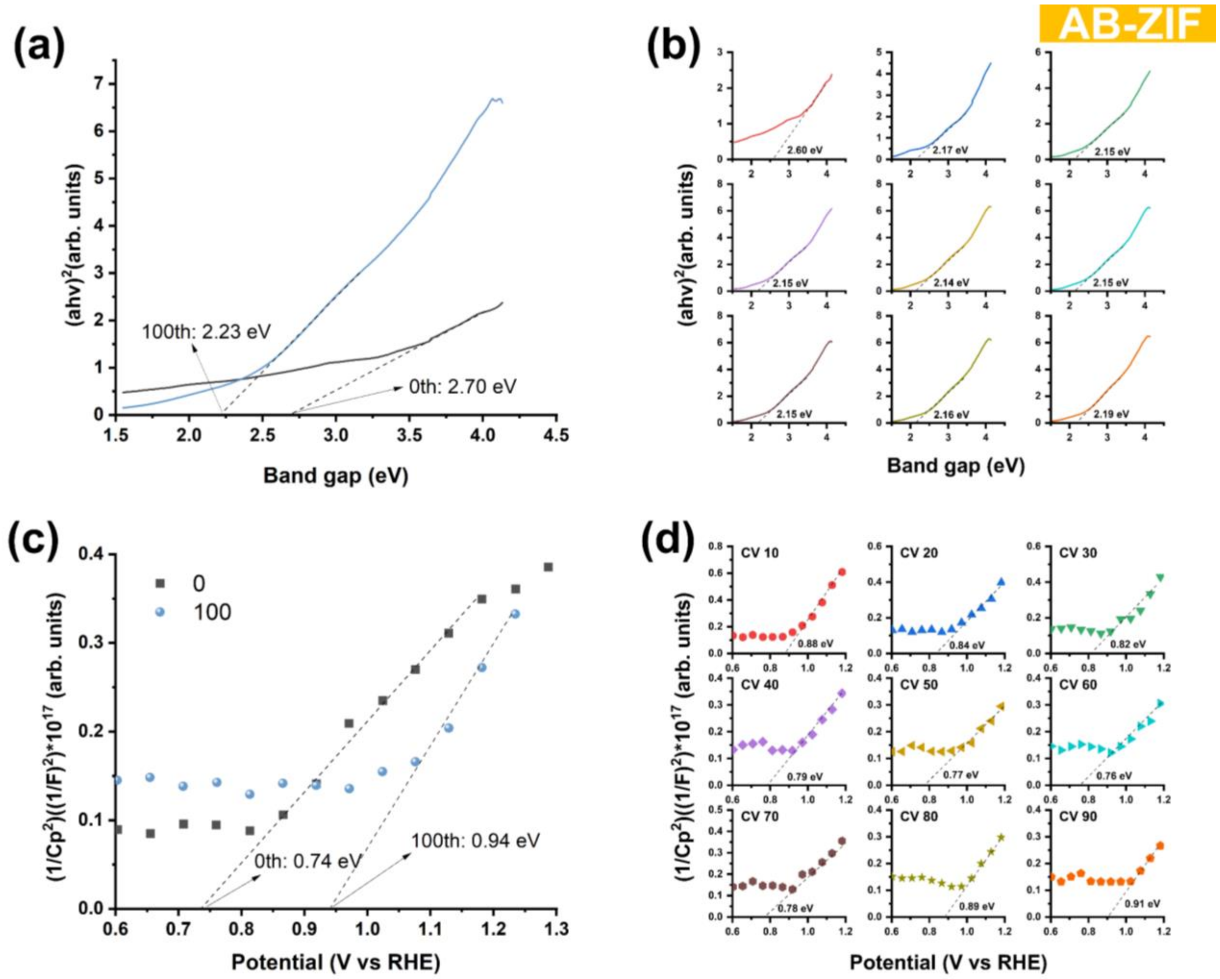

Fig. S40. **a**, **b**, Band gap of AB-ZIF calculated from in-situ UV–Vis absorption spectra from 0 to 100 CV cycles at 0.85-1.55 V. **c**, **d**, Flat band potentials of AB-ZIF calculated from Mott-Schottky plots from 0 to 100 CV cycles at 0.85-1.55 V.

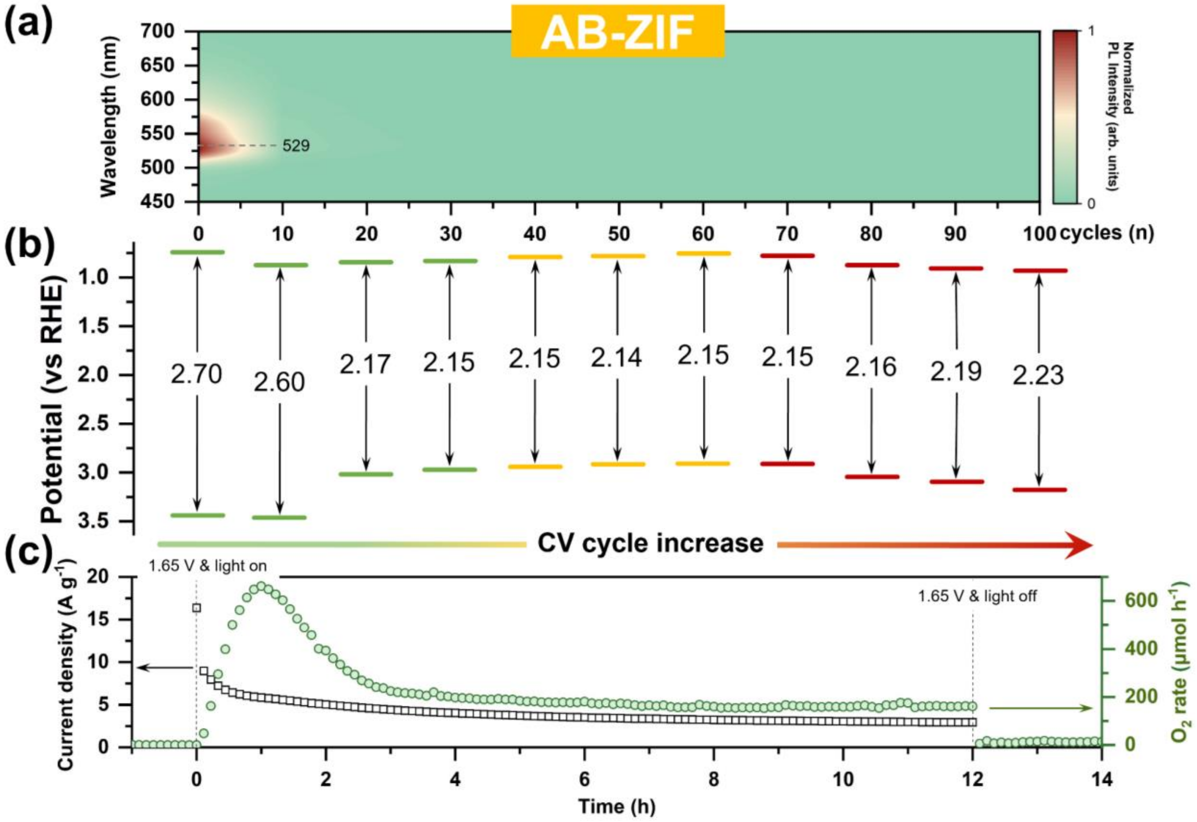

Fig. S41. a, **b**, In-situ electrochemical Photoluminescence (PL) spectroscopy (**a**) and band potential diagram (**b**) of AB-ZIF with 100 CV cycles at 0.85-1.55 V. **c**, Amperometric plots and O_2 evolution rates of AB-ZIF at certain potentials of 1.65 V and visible light.

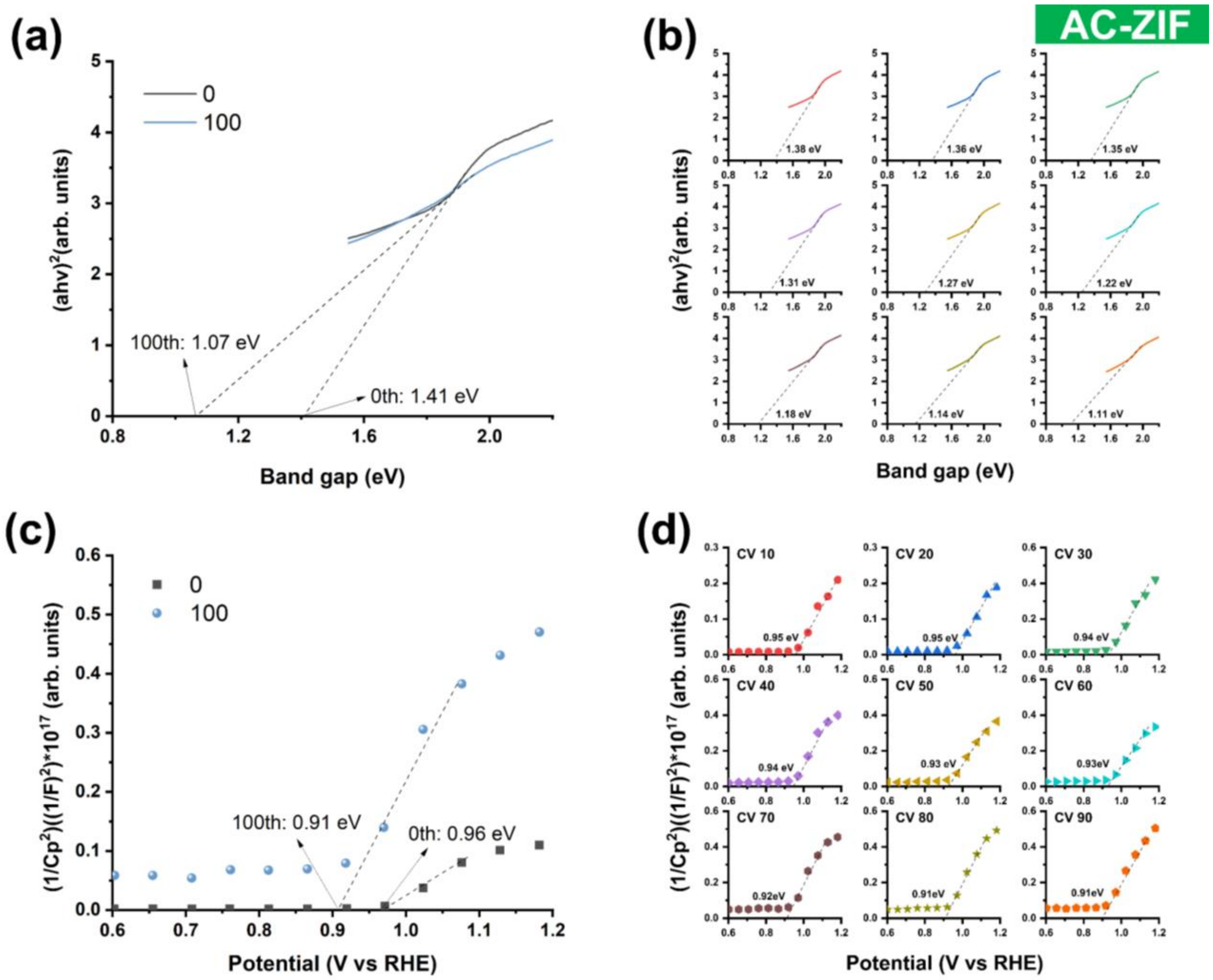

Fig. S42. a, **b**, Band gap of AC-ZIF calculated from in-situ UV–Vis absorption spectra from 0 to 100 CV cycles at 0.85-1.55 V. **c**, **d**, Flat band potentials of AC-ZIF calculated from Mott-Schottky plots from 0 to 100 CV cycles at 0.85-1.55 V.

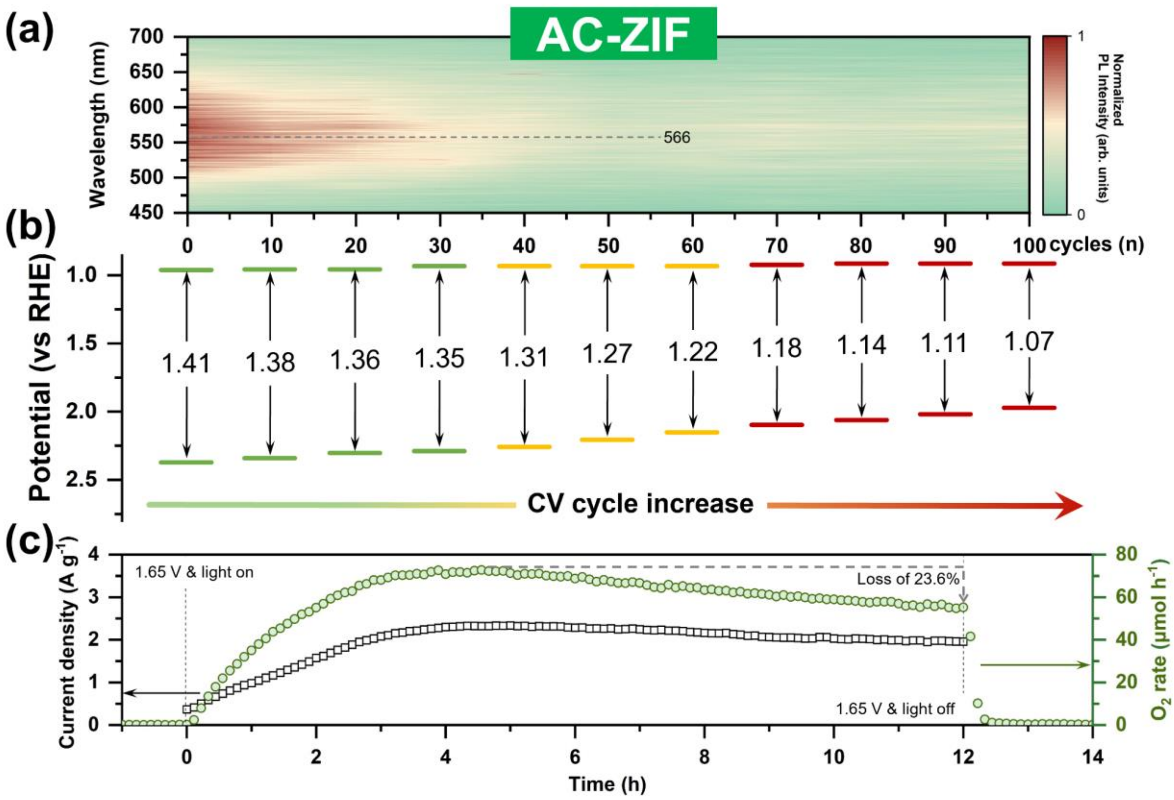

Fig. S43. a, **b**, In-situ electrochemical Photoluminescence (PL) spectroscopy (**a**) and band potential diagram (**b**) of AC-ZIF with 100 CV cycles at 0.85-1.55 V. **c**, Amperometric plots and O_2 evolution rates of AC-ZIF at certain potentials of 1.65 V and visible light.

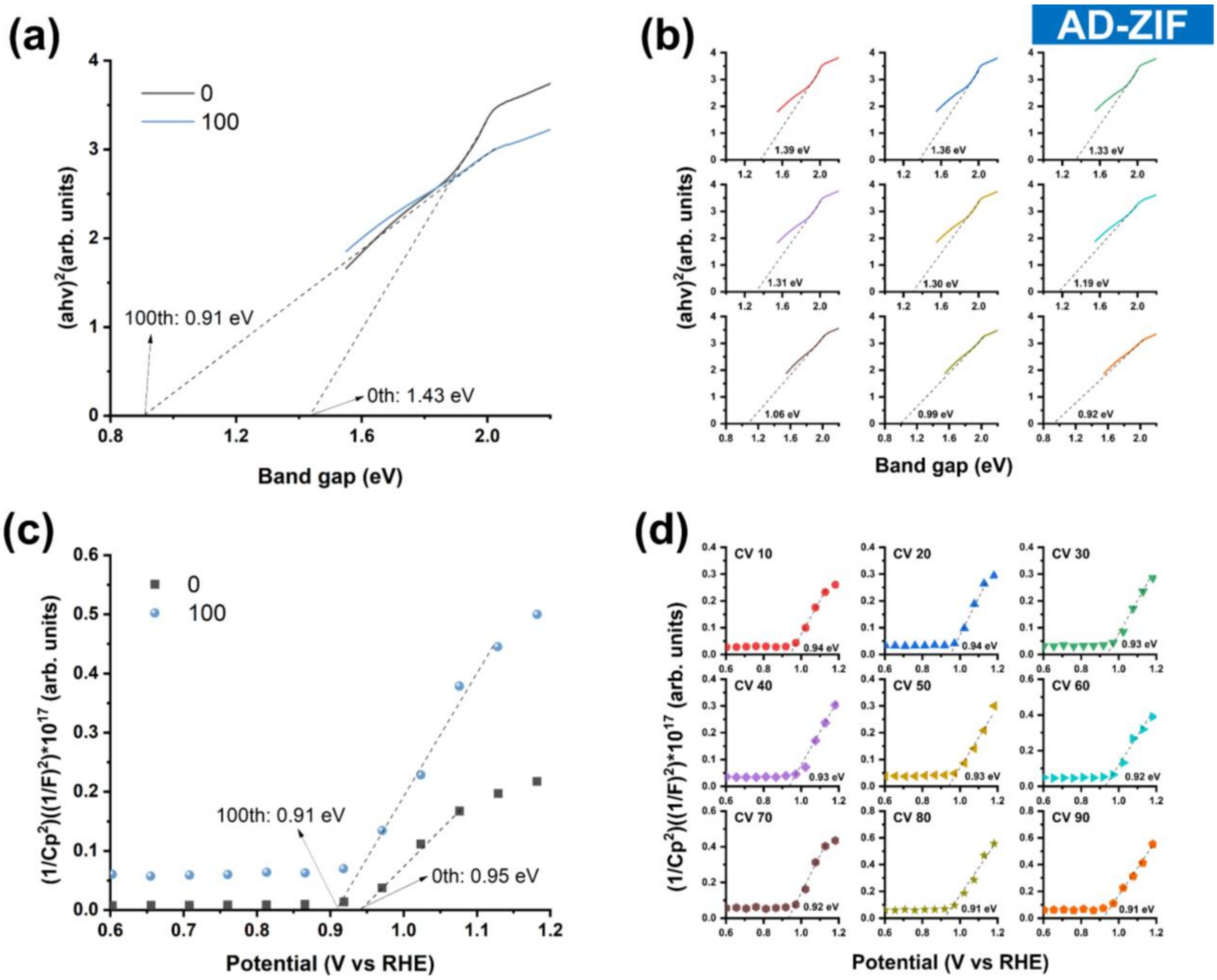

Fig. S44. **a**, **b**, Band gap of AD-ZIF calculated from in-situ UV–Vis absorption spectra from 0 to 100 CV cycles at 0.85-1.55 V. **c**, **d**, Flat band potentials of AD-ZIF calculated from Mott-Schottky plots from 0 to 100 CV cycles at 0.85-1.55 V.

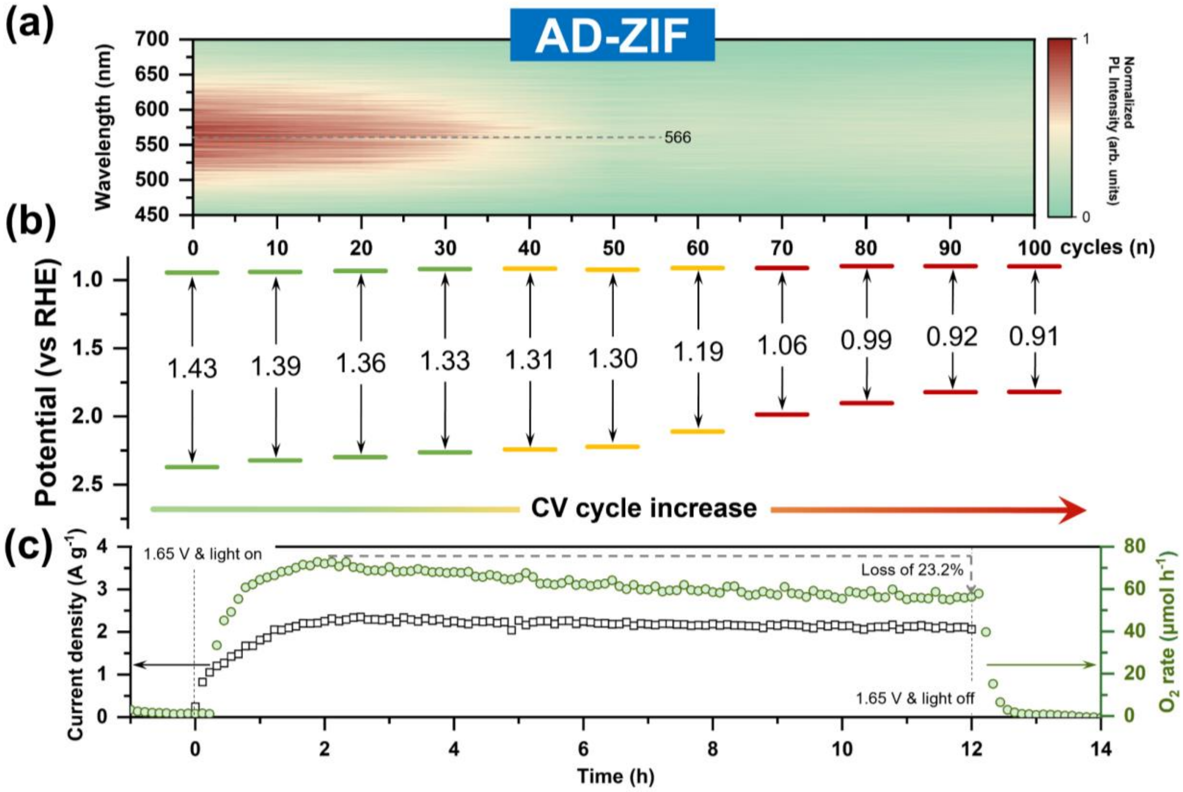

Fig. S45. **a**, **b**, In-situ electrochemical Photoluminescence (PL) spectroscopy (**a**) and band potential diagram (**b**) of AD-ZIF with 100 CV cycles at 0.85-1.55 V. **c**, Amperometric plots and O_2 evolution rates of AD-ZIF at certain potentials of 1.65 V and visible light.

S7. DFT simulation calculations

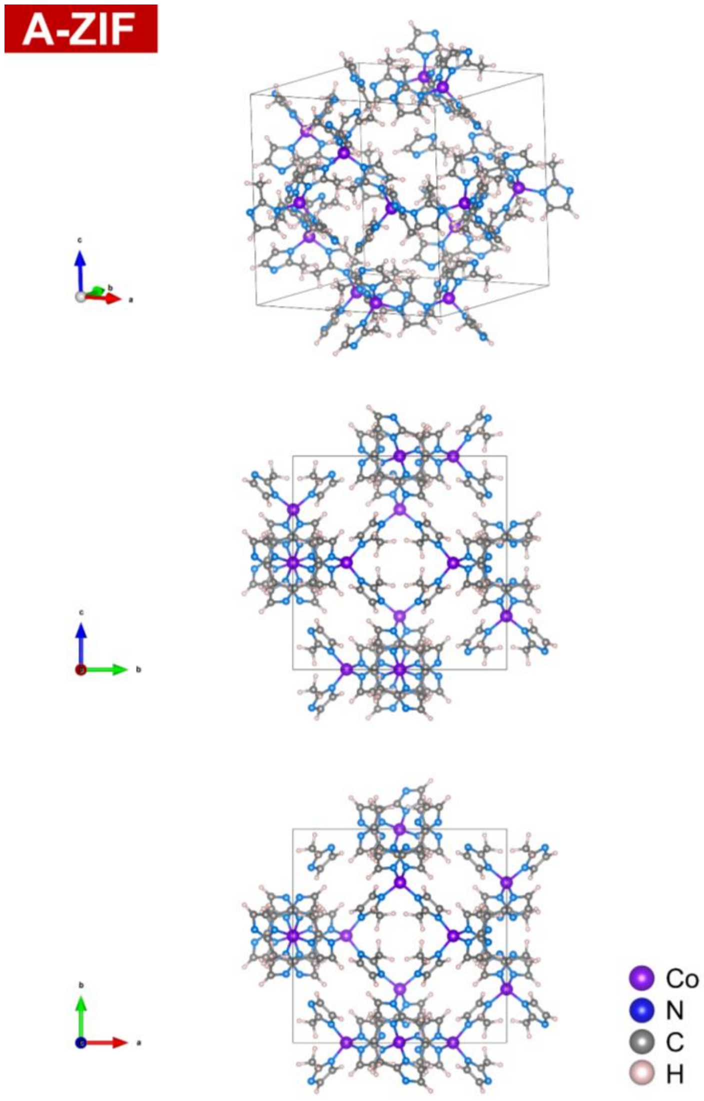

Fig. S46. Models structure of A-ZIF optimized from DFT simulation.

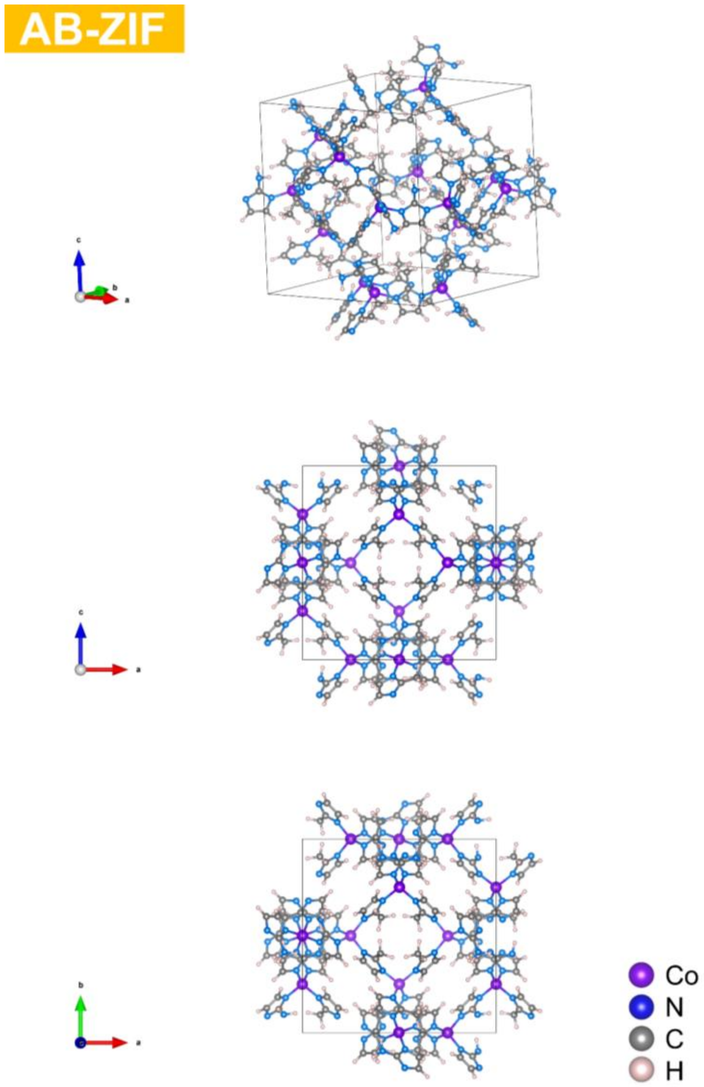

Fig. S47. Models structure of AB-ZIF optimized from DFT simulation.

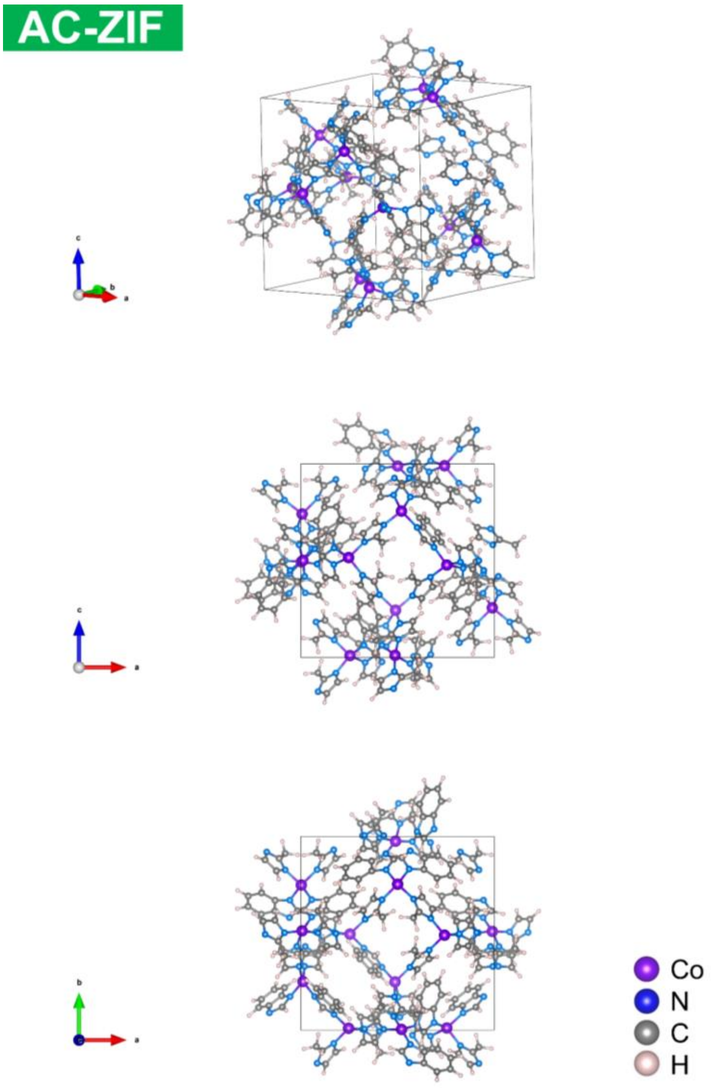

Fig. S48. Models structure of AC-ZIF optimized from DFT simulation.

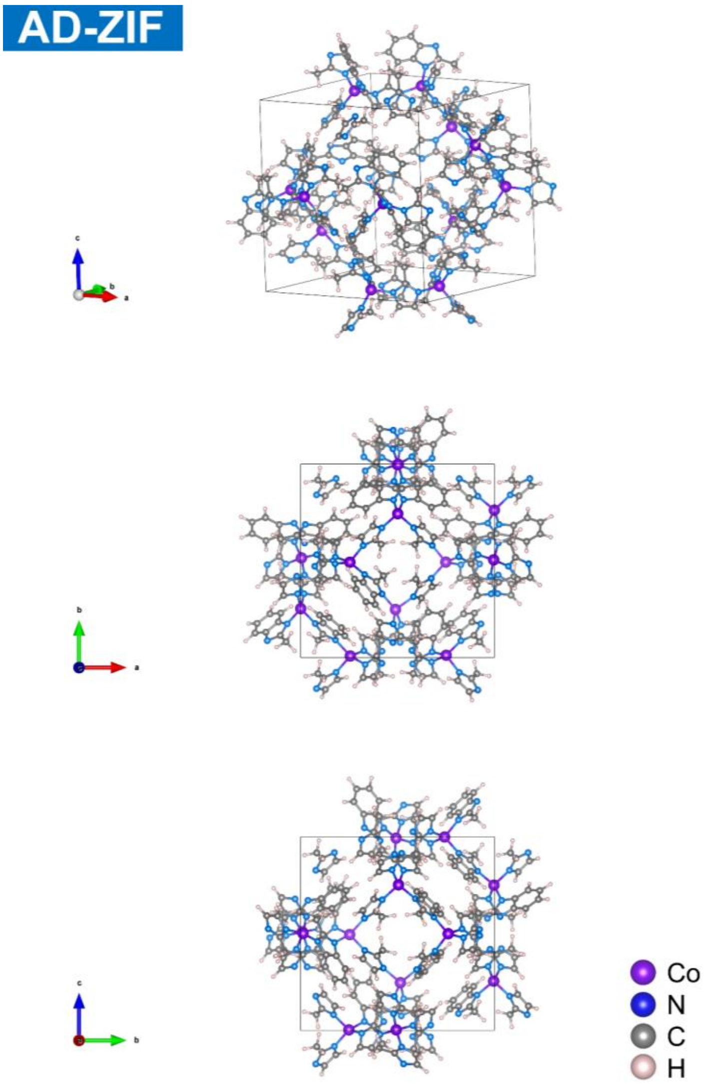

Fig. S49. Models structure of AD-ZIF optimized from DFT simulation.

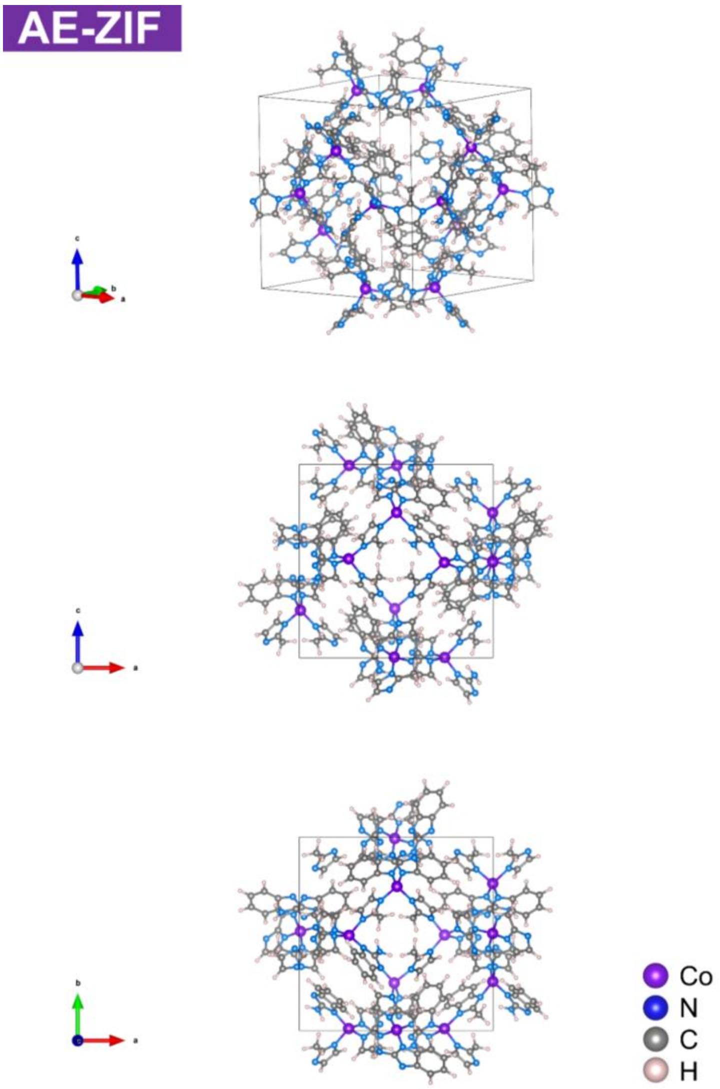

Fig. S50. Models structure of AE-ZIF optimized from DFT simulation.

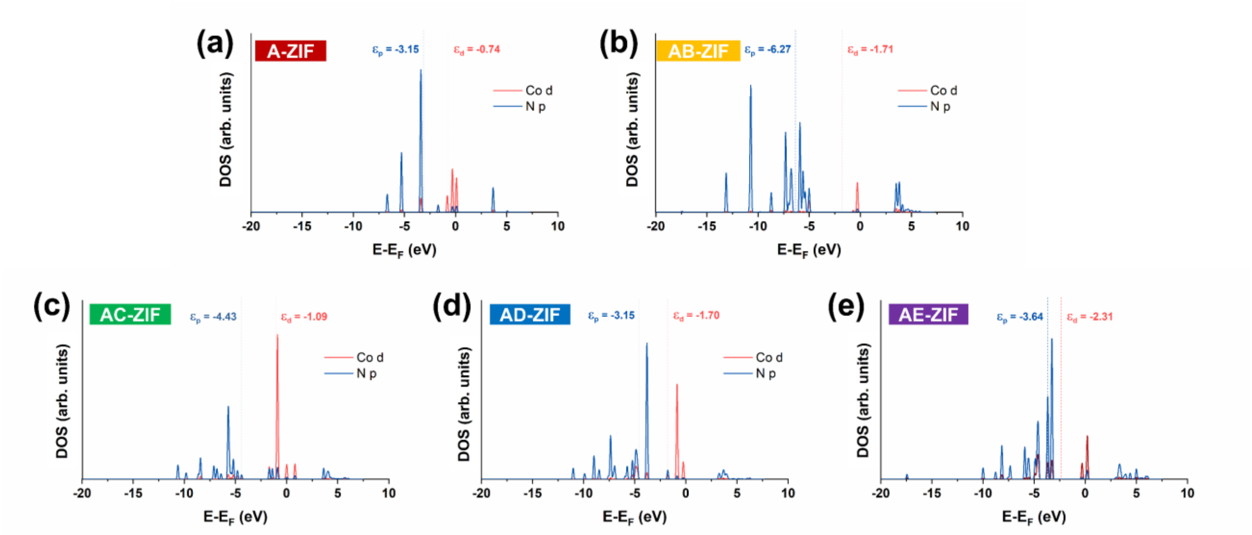

Fig. S51. Calculated DOS of p-state and n-state of A-ZIF (**a**), AB-ZIF (**b**), AC-ZIF (**c**), AD-ZIF (**d**) and AE-ZIF (**e**).

Table S4. Co band center (ε_d), N band center (ε_p) and energy difference (ΔE) between ε_d and ε_p of as-prepared ZIFs.

Samples	**ε_d (eV)**	**ε_p (eV)**	**ΔE ε_d-ε_p (eV)**
A-ZIF	-0.74	-3.15	2.41
AB-ZIF	-1.71	-6.27	4.56
AC-ZIF	-1.09	-4.43	3.34
AD-ZIF	-1.70	-3.15	1.45
AE-ZIF	-2.31	-3.64	1.33

All band center data are from Fig. S51.

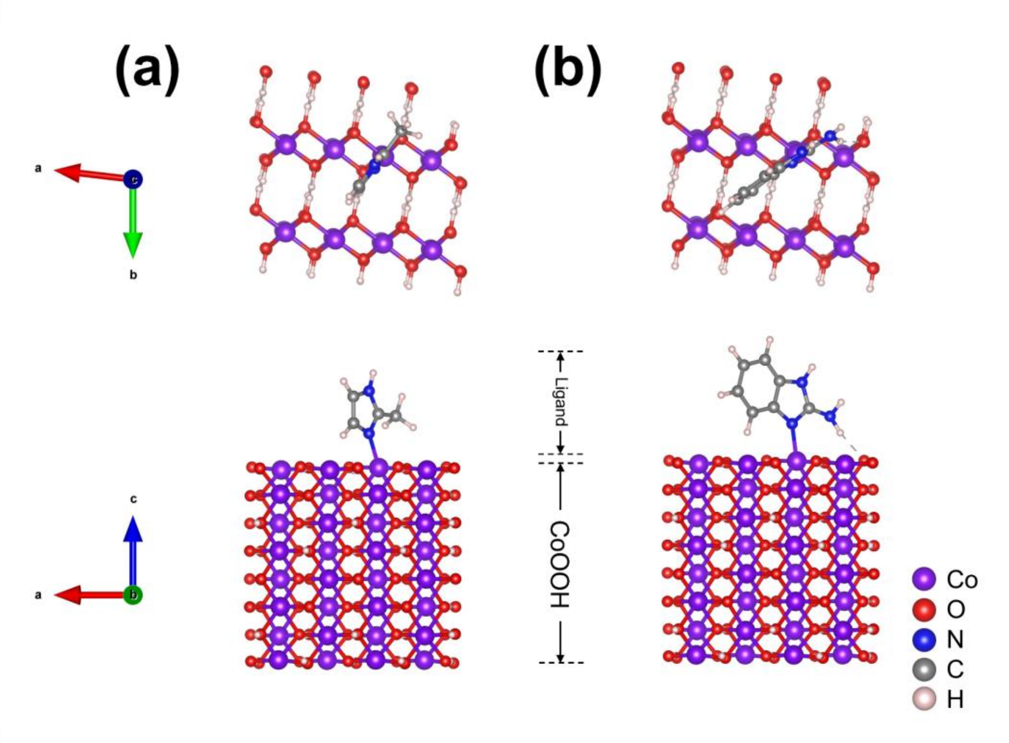

Fig. S52. Models structure of the CoOOH incorporating ligands A (**a**) and E (**b**) optimized from DFT simulation.

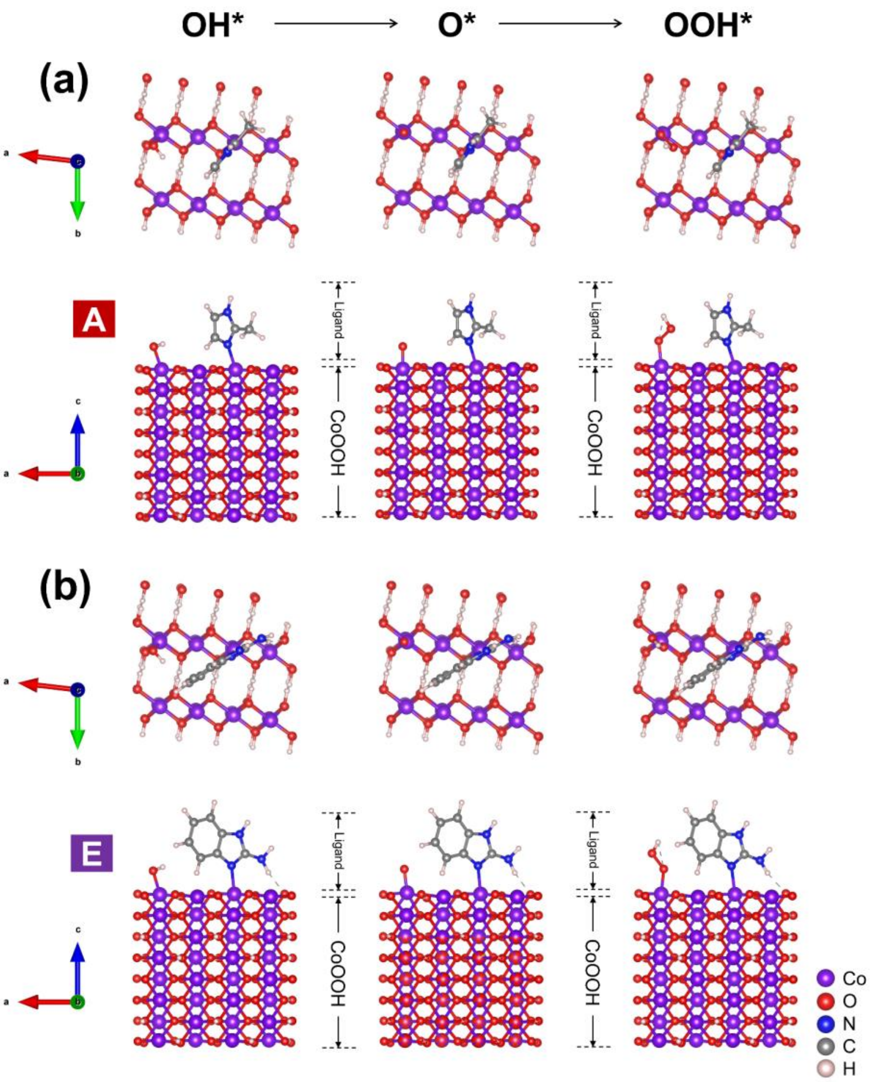

Fig. S53. Calculation steps for OER free energy of A-CoOOH (**a**) and E-CoOOH (**b**).

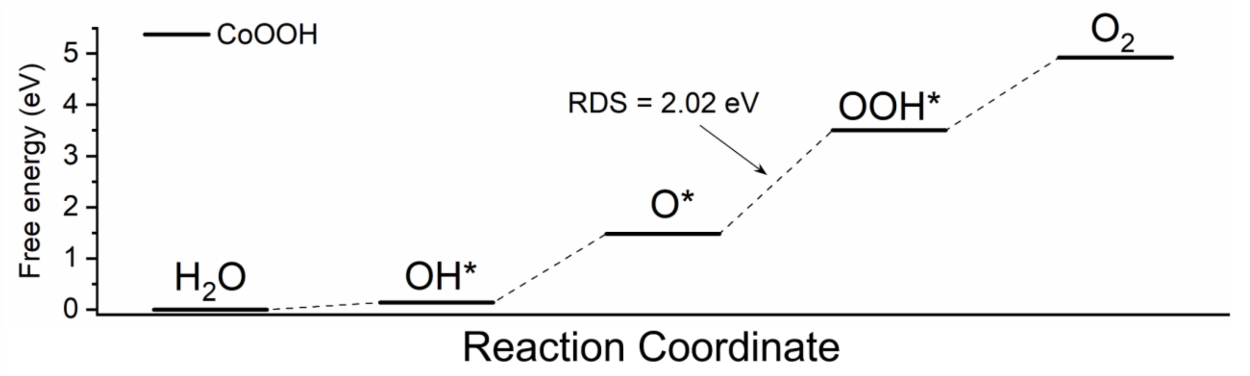

Fig. S54. Free energies diagram of the CoOOH model without ligands.

S8. Characterizations Section

X-ray Diffraction (XRD). Used PANalytical X'Pert Pro multi-purpose diffractometer (MPD) with Bragg Brentano geometry with Cu anode at 45 kV, 40 mA, equipped with a BBHD Mirror and an X-Celerator multichannel detector. The diffraction patterns were tested at a 2θ angle of 5° and 90°. All measurements were performed with Cu sealed tube Kα and Kß radiation (2:1 ratio) with a wavelength of λ=1.54060 Å at a scan rate of 0.5° min^{-1}. Sample holder is a single crystal silicon on which the sample is immobilized by use of a drop of heptane, and rotated every 4 seconds during the test.

X-ray photoelectron spectroscopy (XPS). All XPS measurements were executed using a custom-built SPECS XPS spectrometer equipped with a monochromatized Al-Kα X-ray source (μFocus 350) and a hemispherical WAL-150 analyzer (acceptance angle: 60°). XPS samples were prepared by scratching off the MOF-powder from the FTO substrate and placing it onto In-foil. The In-foil was fixed to the sample holder using double sided carbon tape. For spectral acquisition, pass energies of 100 eV and 30 eV, along with energy resolutions of 1 eV and 100 meV, were employed for survey and detailed spectra, respectively. An excitation energy of 1486.6 eV, beam energy and spot size of 70 W onto 400 μm, an angle of 51° to the sample surface normal were used. The base pressure reached a value of $5x10^{-10}$ mbar, and the pressure throughout the measurement was $5x10^{-9}$ mbar. All reported content values are presented in units of relative atomic percent (at%), with a typical detection limit in survey measurements ranging from 0.1-1 at%, contingent on the specific element. The accuracy of XPS measurements is approximately 10-20% of the reported values.

N_2 Physisorption. Measurements were conducted at temperature of 77 K, on a 3Flex instrument by Micromeritics. Before measuring, the samples were vacuum outgassed at 150°C for 3-12 hours. The apparent surface area was calculated by applying the Brunauer-Emmet-Teller (BET) equation, following the recommended procedure for microporous sorbents [16]. The relevant pore size distributions were determined from the adsorption branch of the isotherms using the kernel of nonlocal density functional theory (NLDFT).

Scanning electron microscope (SEM). Images were recorded on a FEI Quanta 250 (Schottky-)FEG-SEM, facilitated by USTEM (university service center for transmission electron microscopy) at TU Wien, equipped with an ETD Secondary electron detector and an EDAX-AMETEK Octane Elite 55 detector for elemental characterization by energy-dispersive X-ray-spectroscopy. The device was operated at a voltage of 10 kV at a working distance of about 5 mm, providing a maximum resolution of roughly 2 nm. Chemical X-ray microanalysis was performed at 20 kV and 10 mm working distance.

Transmission electron microscope (TEM). All HR-TEM measurements displayed in this paper were performed on a Tecnai F20 FEG-TEM, facilitated by USTEM (university service center for transmission electron microscopy) at TU Wien, equipped with a X-FEG, a Gatan Rio16 CCD-camera, Gatan DigiSTEM II with HAADF detector for STEM imaging, an EDAX-AMETEK Apollo XLTW SDD EDX-detector. The operating voltage was kept at 200 kV for all measurements, providing a maximum lattice resolution of approximately 0.14 nm.

In-situ electrochemical Raman spectroscopy. Measurements were collected on HORIBA LabRAM Spectrometer with a 532 nm laser.

In-situ electrochemical UV–Vis absorption spectroscopy (UV–Vis). Absorbance of each ZIF@FTO glass were obtained at 350-700nm by Jasco V-670. Measurements were carried out using the Jasco V-670 in diffuse reflectance mode with an Ulbricht-sphere.

In-situ electrochemical Photoluminescence spectroscopy. Measurements were carried out with a PicoQuant FluoTime 300 spectrophotometer. The excitation source was a xenon arc lamp (power = 300 W), coupled with a double-grating monochromator. The detection system comprised of a PMA Hybrid 07 detector along with a high-resolution double monochromator. Samples were excited directly at a wavelength of 425 nm with ZIFs@FTO glass.

Nuclear magnetic resonance spectroscopy (^{1}H NMR). Liquid phase ^{1}H spectra were measured using the Bruker ADVANCE 250 (250.13 MHz) instrument, which is equipped with a 5 mm inverse-broad probe head and z-gradient unit. To serve as an internal reference, Acetic Acid with a $\delta = 1.96$ ppm was used. Due to the limited solubility of ZIFs in typical NMR solvents, the sample weighing 2 mg was digested with 0.5 ml of d_4-acetic acid and then sonicated until it was well dispersed in the acid.

S9. References

1. Mor J, Utpalla P, Bahadur J, Sharma SK. Flexibility of Mixed Ligand Zeolitic Imidazolate Frameworks (ZIF-7–8) under CO2 Pressure: An Investigation Using Positron Annihilation Lifetime Spectroscopy. *Langmuir* **38**, 15694-15702 (2022).

2. Hillman F, Zimmerman JM, Paek S-M, Hamid MRA, Lim WT, Jeong H-K. Rapid microwave-assisted synthesis of hybrid zeolitic–imidazolate frameworks with mixed metals and mixed linkers. *J Mater Chem A* **5**, 6090-6099 (2017).

3. Huang Z, Rath J, Zhou Q, Cherevan A, Naghdi S, Eder D. Hierarchically Micro- and Mesoporous Zeolitic Imidazolate Frameworks Through Selective Ligand Removal. *Small* **n/a**, 2307981 (2023).

4. Cho KY*, et al.* Synthesis of amine-functionalized ZIF-8 with 3-amino-1,2,4-triazole by postsynthetic modification for efficient CO2-selective adsorbents and beyond. *J Mater Chem A* **6**, 18912-18919 (2018).

5. Xiang L, Sheng L, Wang C, Zhang L, Pan Y, Li Y. Amino-Functionalized ZIF-7 Nanocrystals: Improved Intrinsic Separation Ability and Interfacial Compatibility in Mixed-Matrix Membranes for CO2/CH4 Separation. *Adv Mater* **29**, 1606999 (2017).

6. Lee YR, Do XH, Cho KY, Jeong K, Baek K-Y. Amine-Functionalized Zeolitic Imidazolate Framework-8 (ZIF-8) Nanocrystals for Adsorption of Radioactive Iodine. *ACS Applied Nano Materials* **3**, 9852-9861 (2020).

7. Schlumberger C, Thommes M. Characterization of Hierarchically Ordered Porous Materials by Physisorption and Mercury Porosimetry—A Tutorial Review. *Adv Mater Interfaces* **8**, 2002181 (2021).

8. Shinagawa T, Garcia-Esparza AT, Takanabe K. Insight on Tafel slopes from a microkinetic analysis of aqueous electrocatalysis for energy conversion. *Scientific Reports* **5**, 13801 (2015).

9. Chen C-L*, et al.* Conductive Lanthanide Metal–Organic Frameworks with Exceptionally High Stability. *J Am Chem Soc* **145**, 16983-16987 (2023).

10. Zhu R*, et al.* Quasi-ZIF-67 for Boosted Oxygen Evolution Reaction Catalytic Activity via a Low Temperature Calcination. *ACS Appl Mater Interfaces* **12**, 25037-25041 (2020).

11. Zuo F*, et al.* Electrochemical interfacial catalysis in Co-based battery electrodes involving spin-polarized electron transfer. *Proc Natl Acad Sci* **120**, e2314362120 (2023).

12. Gao Z, Liu B, Xu X, Peng J, Wu J, Zhang J. Electrochemical oxidation induced in-situ transformation of lamellar cobalt nitrate-hydroxide to oxygen vacancy-rich porous Ce Doped-CoOOH nanosheet for efficient oxygen evolution reaction. *Materials Today Sustainability* **24**, 100601 (2023).

13. El Haskouri J*, et al.* High Cobalt Content Mesoporous Silicas. *Chem Mater* **16**, 2805-2813 (2004).

14. Kamali K, Joseph B, Narayana C. Stability of zeolitic imidazolate frameworks (ZIF-7) under high pressures and its implications on storage applications of ZIFs. *J Solid State Chem* **309**, 122973 (2022).

15. Kamali K, Prasad S, Sahoo MK, Behera JN, Waghmare UV, Narayana C. Unusual CO2 Adsorption in ZIF-7: Insight from Raman Spectroscopy and Computational Studies. *Inorg Chem* **61**, 11571-11580 (2022).

16. Sánchez-Varretti FO, García GD, Ramirez-Pastor AJ, Romá F. A simple model for studying

multilayer adsorption of noninteracting polyatomic species on homogeneous and heterogeneous surfaces. *J Chem Phys* **130**, 194711 (2009).

Conclusions and outlook

This thesis focuses on zeolitic imidazolate frameworks (ZIFs), a subfamily of metal-organic frameworks (MOFs), are constructed by combining organic and inorganic building units to form periodic open porous structures. As described in Section 1.1, compared to traditional porous materials, ZIFs exhibit great potential and advantages as newly porous materials in environmental and energy applications as a novel class of porous materials. However, they still face several challenges, such as the lack of mesoscale cavities, saturated metal sites, low stability in catalytic environments, and poor electrical conductivity.

To address these limitations, Sections 1.2 and 1.3 introduce the mixed-ligand and selective ligand removal (SeLiRe) strategies to enhance the functional properties. These approaches primarily involve modifying sodalite topology ZIFs (ZIF-8 and ZIF-67) by introducing secondary ligands with corresponding functional groups or creating the mesopore cavities with corresponding defects/open active sites. These modifications aim to overcome the existing shortcomings. Considering the current focus on carbon neutrality, Section 1.4 focuses on exploring the advantages and limitations of MOFs/ZIFs in environmental and energy applications, particularly in water purification and water electrolysis, as well as the latest research progress, and exploration and analysis of recent literature.

Based on this analysis, in Chapter 3, I present three of my published articles. SeLiRe ZIF-8 (Zn) is utilized for dye adsorption (Article #1) and electrocatalytic hydrogen evolution reaction (HER, Article #2), while mixed-ligand ZIF-67 (Co) is used for electrocatalytic oxygen evolution reaction (OER, Article #3). The characterization instruments used in these studies are detailed in Chapter 2.

Firstly, I initially synthesized mixed-ligand ML-ZIF-8 using different ratios of two ligands and achieved uniform mesopores through controlled thermal treatment. Benefiting from the additional mesopores provided a larger pore volume, resulting in a 40-fold increase in methylene blue adsorption capacity. This study provided insights into creating hierarchical pores while retaining structural integrity, addressing the issue of limited active sites for adsorption and catalysis in traditional SOD-type ZIFs.

To extend the versatility and broad applicability of the SeLiRe strategy, I further investigated the (photo)electrocatalytic HER capability of the resulting SeLiRe-ZIFs samples. Synchrotron XAS confirmed that SeLiRe strategy effectively transformed saturated Zn–N_4 sites into unsaturated Zn–N_2 sites by breaking the coordination with two secondary ligands. Monitored through in-situ electrochemical spectroscopy, these localized sites spontaneously chemisorb hydroxyl groups from the 1M KOH electrolyte, subsequently forming the high-valence HO–Zn–N_2 as real active sites. At a current density of 10 mA cm^{-2}, these active sites significantly reduced the HER overpotential from 0.31 V to 0.07 V. DFT simulations further validated that these sites facilitated the adsorption and dissociation steps of H_2O molecules, thereby improving overall HER activity. This study emphasized the importance of unsaturated, localized and high-valence metal sites in promoting catalytic efficiency and provided a blueprint for designing advanced HER catalysts.

Finally, I shifted the research focus to ZIF-67 and utilized a mixed ligand strategy to develop a series of mixed-ligand ZIF-67 electrocatalysts for exploring the (photo)electrocatalytic OER mechanism. The most effective sample demonstrated a great increase around 8 times in both O_2 release rate and current density under 1.65 V applied potential. Incorporating a secondary ligand with organic functional groups—π-π stacking aromatic rings and -NH_2 groups—significantly mitigated the electro-oxidation process and promoted the formation of a thin/stable (oxy)hydroxide layer on the particle surface. Theoretical calculations demonstrated that in electrocatalysis, the accelerated electron transfer at the interface of this core-shell structure, along with the reduction in Gibbs free energy, collectively enhanced the oxygen evolution capability under a given applied potential. This study highlighted the synergistic effects of ligand engineering and provided a pathway for addressing the structural reconstruction challenges commonly faced in OER applications.

As a conclusion of this research, combining in-situ characterization methods with ex-situ characterization before and after reactions is particularly critical, especially for the weak stable MOFs/ZIFs. For example, in Article #2 and #3, without in-situ electrochemical Raman spectroscopy, it would be difficult to detect the subtle structural evolution of the samples. Such "minor/slight changes" could lead to incorrect conclusions regarding the stability of ZIFs, which is undesirable. Thus, future research on the catalytic applications of MOFs/ZIFs should reconsider issues of instability and uncertainty, avoiding being overshadowed by numerous reports of long-term "stable" MOFs.

Additionally, the use of atomic-resolution electron microscopy is equally critical for studying MOFs/ZIFs. However, most MOFs/ZIFs are electron-beam-sensitive materials, and the powerful electron beams of HRTEM can significantly damage their structures, making it difficult to obtain accurate atomic arrangements and pore images. Current solutions include using uniquely configured electron microscopes, such as low-electron-dose TEM or cryo-TEM, but these must be tailored to the specific MOFs being analyzed.

Undoubtedly, MOFs/ZIFs, as novel porous materials, hold immense potential in environmental and energy applications. Their controllable porosity and high surface area/reactive sites far surpass traditional materials, making them extensively researched for gas adsorption/separation and water purification. However, as previously mentioned, low catalytic stability and weak electron conductivity prevent most MOFs/ZIFs from being directly used as catalysts. This is particularly true for OER, which requires high potential, leading to structural reconstruction due to electro-oxidation process. Additionally, MOFs/ZIFs have strict requirements for reaction environments, such as high or low pH, or even pure aqueous solutions, where the framework structures are degraded. The 3D framework formed by interconnecting organic ligands inhibits the most electron transfer during reactions, significantly reducing the intrinsic catalytic activity. Furthermore, the high cost/hard-to-synthesize organic ligands significantly reduce the possibility of industrialization of MOFs/ZIFs. Currently, achieving mass production of MOFs/ZIFs for industrial applications, in contrast to the successful catalyst P25 (TiO_2), remains challenging. Therefore, these issues need to be addressed in future research to advance the industrial application of MOFs/ZIFs in environmental and energy fields.

Although ligand engineering strategies, such as mixed-ligand and SeLiRe, are gaining attention in MOF research to address these challenges, most studies are concentrated on common MOFs such as MIL-125, MIL-101, UiO-66/UiO-67, and HKUST-1. Apart from this thesis, few have applied these strategies to the zeolite-like ZIF family, which is known for its superior stability. Given the thousands of MOF types currently available, establishing a robust three-step framework—synthesis, characterization, and mechanism elucidation—is particularly vital for advancing ligand-engineered MOFs/ZIFs. This could extend the versatility and applicability of these strategies to other MOF families, especially for those unpopular and recently reported MOFs/ZIFs, potentially uncovering structures better suited for diverse applications and harsh industrial environments. For instance, before Article #1 reported mixed-ligand ZIFs for the SeLiRe strategy, there were almost no relevant studies, highlighting the importance of this work in paving the way for broader applications of ligand engineering strategies.

Reflecting on the gains and challenges of this work, I have gained a deeper understanding of the synthesis of MOFs/ZIFs and the theoretical basis for ligand selection, particularly in organic chemistry. I also improved my skills in utilizing advanced characterization techniques, such as synchrotron XAS, and grasped the critical importance of in-situ characterization under reaction conditions. However, my research overly focused on modifying and studying ZIFs with SOD topology (ZIF-8 and ZIF-67) and lacked reverse-designed MOFs tailored for specific application needs. This is a direction I aim to pursue in the future. In fact, I have already synthesized a unique MOF with an unprecedented graphene-like layered structure, which has attracted much attention. I am currently dedicated to resolving and characterizing its structure to enable its use in environmental and energy applications.

In summary, this thesis demonstrates that ligand engineering strategy enhances the application potential of ZIFs in environmental and energy fields, partially addressing the shortcomings of single-ligand ZIFs. It provides a feasible approach for designing multifunctional MOFs/ZIFs with different topologies and lays the groundwork for future advancements. The insights gained from this work offer valuable guidance for researchers aiming to overcome the challenges of stability, conductivity, and scalability, driving the development of MOFs/ZIFs toward practical industrial applications.

Curriculum vitae

Zheao Huang

Birth date: 04/02/1996
Phone: -43 067763943543 | -86 15717168020
Email: zheao.huang@tuwien.ac.at | Group Website: www.tuwien.at/tch/mmc
Office Address: Getreidemarkt 9/BC/02 A34, 1060 Vienna, Austria

RESEARCH

Focused on designing hierarchical porous, multivariate, and novel topological **metal-organic frameworks** (**MOFs**) through metal mixing and ligand engineering strategies, aiming to advance efficient **photocatalytic** and **electrocatalytic** water splitting for hydrogen and oxygen production (**HER/OER**), and **water purification** via efficient photodegradation and adsorption of organic pollutants.

EDUCATION

Vienna University of Technology Vienna, Austria
Ph.D. IN Technical Chemistry | GPA: 3.20 / 4.00 *Feb 2022 - present*
Honors: China Scholarship Council scholarship (CSC 4 years)

Central China Normal University Wuhan, China
M.S. IN Condensed Matter Physics | GPA: 3.44 / 4.00 *Sep 2018 - Jul 2021*
Honors: National Academic Scholarship, Excellent master's thesis

Wuhan Institute of Technology University Wuhan, China
Post & Telecommunications and Information Engineering College *Sep 2014 - Jul 2018*
B.S. IN Pharmaceutical Preparation | GPA: 3.32 / 4.00
Honors: Outstanding Student Scholarship

PUBULICATIONS

- **Huang, Z.**; Wang, Z.; Zhou, Q.; Rabl, H.; Naghdi, S.; Yang, Z.; Eder, D. Engineering of HO–Zn–N_2 Active Sites in Zeolitic Imidazolate Frameworks for Enhanced (Photo)Electrocatalytic Hydrogen Evolution. ***Angewandte Chemie International Edition*** 2024, e202419913 (Hot Paper). *Dec 2024*
- **Huang, Z.**; Wang, Z.; Rabl, H.; Naghdi, S.; Zhou, Q.; Schwarz, S.; Apaydin, D. H.; Yu, Y.; Eder, D. Ligand engineering enhances (photo) electrocatalytic activity and stability of zeolitic imidazolate frameworks via in-situ surface reconstruction. ***Nature Communication*** 2024, 15 (1), 9393. *Oct 2024*
- **Huang, Z.**; Rath, J.; Zhou, Q.; Cherevan, A.; Naghdi, S.; Eder, D. Hierarchically Micro- and Mesoporous Zeolitic Imidazolate Frameworks Through Selective Ligand Removal. ***Small*** 2024, 20 (21), 2307981. *Dec 2023*
- **Huang, Z.**; Zhou, Q.; Wang, J.; Yu, Y. Fermi-level-tuned MOF-derived N-ZnO@NC for photocatalysis: A key role of pyridine-N-Zn bond. ***Journal of Materials Science & Technology*** 2022, *112*, 68-76. *Aug 2021*
- **Huang, Z.**; Zhou, J.; Zhao, Y.; Cheng, H.; Lu, G.; Morawski, A. W.; Yu, Y. Stable core–shell ZIF-8@ZIF-67 MOFs photocatalyst for highly efficient degradation of organic pollutant and hydrogen evolution. ***Journal of Materials Research*** 2021, *36* (3), 602-614. *Nov 2020*
- **Huang, Z.**; Zhao, S.; Yu, Y. Experimental method to explore the adaptation degree of type-II and all-solid-state Z-scheme heterojunction structures in the same degradation system. ***Chinese Journal of Catalysis*** 2020, *41* (10), 1522-1534. *Feb 2020*

EXPERIENCE

MOF2024 Conference Singaporean
9th International Conference on Metal-Organic Frameworks and Open Framework Compounds *13 - 19 Jul 2024*
Poster Presentation: Ligand Engineering Enhances (Photo)Electrocatalytic Activity and Stability of Zeolitic Imidazolate Frameworks.

Porous Materials in Energy Science Conference Munich, Germany
Poster Presentation: Hierarchically Micro- and Mesoporous Zeolitic Imidazolate Frameworks for water purification applications. *29 - 31 May 2024*

EURMOF Conference Granada, Spain
5th European Conference on Metal Organic Frameworks and Porous Polymers *24 - 26 Sep 2023*
Poster Presentation: Hierarchically Micro- and Mesoporous Zeolitic Imidazolate Frameworks through Selective Ligand Removal.

Wuhan Polytechnic University Wuhan, China
15th Annual Academic Conference of the Professional Committee of Environmental Chemistry and Chemical Engineering of Hubei Chemical and Chemical Society *30 Sep 2019*
Oral Presentation: Heterojunction semiconductors $TiO_2@C@C_3N_4$, received an Excellent Award in the Graduate Student Report.

University of New South Wales Sydney, Australia
Student of UNSW Global Education *15 - 26 Jul 2019*
Coursework: English for Engineering and Science & Technology, Nanomaterials and Printing, Functional Materials, Quantum Physics, Molecular Semiconductors, 3D printing, and Energy Materials.

SKILLS

Languages: Mandarin (Native); English (Fluent, TOEFL **101/120**); German (Elementary).
Computer: Microsoft Office, Origin, 3ds max, diamond, Origin, Chem Draw, and so on.
Characterization: XRD, SEM, IR, PL, ATR-IR, UV-vis, GC, TGA, BET physisorption, and so on.

Acknowledgement

I would like to first express my deepest gratitude to Univ. **Prof. Dr. Dominik Eder** for his invaluable guidance and support throughout my doctoral journey. His willingness to accept me as a PhD student from China and his assistance in manuscript writing, research discussion, and participation in international conferences have been instrumental to my success. I am also immensely grateful to the China Scholarship Council for providing the scholarship that covered most of my living expenses in Austria.

Special thanks go to my wife, **Siyi Li**, who gave birth to our daughter in China and raised her with the parents during my PhD studies. Their support allowed me to focus on my research with less worry. My daughter, **Yilin Huang**, has been a source of irreplaceable joy and motivation in my scientific endeavors. My parents have provided both financial support and continuous encouragement throughout my PhD journey.

I am equally grateful to my colleagues at the Eder Laboratory. Dr. Shaghayegh Naghdi and Ass. Prof. Dr. Alexey Cherevan offered valuable advice and research discussions when I first joined the lab. Additionally, Dr. Shaghayegh Naghdi was responsible for almost all the N_2 physisorption measurements and analyses. Dr. Dogukan Hazar Apaydin, Hannah Rabl, and Jakob Nils Blaschke guided my manuscript writing and taught me how to use the electrocatalysis lab equipment. Dr. Stephen Nagaraju Myakala and Pablo Ayala provided essential guidance on photocatalysis experiments. Dr. Jakob Rath and Dr. Sabine Schwarz for assisting with numerous electron microscopy tests. I am deeply thankful to all of them.

My heartfelt appreciation extends to my collaborators at Central China Normal University. **Prof. Dr. Ying Yu** provided valuable feedback on my manuscripts and offered her lab's equipment for my tests. Zhouzhou Wang shared his extensive knowledge of electrocatalysis and assisted with Raman tests. Qiancheng Zhou conducted all the computational simulations for my manuscripts. Despite the physical distance, their support has been crucial to my research.

Thank you all for your unwavering support and contributions to my PhD journey.

References

1. Tian, Y.; Zhu, G., Porous Aromatic Frameworks (PAFs). *Chem. Rev.* **2020,** *120* (16), 8934-8986.
2. Chen, L.-H.; Sun, M.-H.; Wang, Z.; Yang, W.; Xie, Z.; Su, B.-L., Hierarchically Structured Zeolites: From Design to Application. *Chem. Rev.* **2020,** *120* (20), 11194-11294.
3. Sun, L.-B.; Liu, X.-Q.; Zhou, H.-C., Design and fabrication of mesoporous heterogeneous basic catalysts. *Chem. Soc. Rev.* **2015,** *44* (15), 5092-5147.
4. Sun, Q.; Dai, Z.; Meng, X.; Xiao, F.-S., Porous polymer catalysts with hierarchical structures. *Chem. Soc. Rev.* **2015,** *44* (17), 6018-6034.
5. Liu, Z.; Zhu, J.; Peng, C.; Wakihara, T.; Okubo, T., Continuous flow synthesis of ordered porous materials: from zeolites to metal–organic frameworks and mesoporous silica. *Reaction Chemistry & Engineering* **2019,** *4* (10), 1699-1720.
6. Liang, J.; Liang, Z.; Zou, R.; Zhao, Y., Heterogeneous Catalysis in Zeolites, Mesoporous Silica, and Metal–Organic Frameworks. *Adv. Mater.* **2017,** *29* (30), 1701139.
7. Eddaoudi, M.; Moler, D. B.; Li, H.; Chen, B.; Reineke, T. M.; O'Keeffe, M.; Yaghi, O. M., Modular Chemistry: Secondary Building Units as a Basis for the Design of Highly Porous and Robust Metal−Organic Carboxylate Frameworks. *Acc. Chem. Res.* **2001,** *34* (4), 319-330.
8. Cai, G.; Yan, P.; Zhang, L.; Zhou, H.-C.; Jiang, H.-L., Metal–Organic Framework-Based Hierarchically Porous Materials: Synthesis and Applications. *Chem. Rev.* **2021,** *121* (20), 12278-12326.
9. Sun, Q.; Qin, L.; Lai, C.; Liu, S.; Chen, W.; Xu, F.; Ma, D.; Li, Y.; Qian, S.; Chen, Z.; Chen, W.; Ye, H., Constructing functional metal-organic frameworks by ligand design for environmental applications. *J. Hazard. Mater.* **2023,** *447*, 130848.
10. Yaghi, O. M.; Li, H., Hydrothermal Synthesis of a Metal-Organic Framework Containing Large Rectangular Channels. *J. Am. Chem. Soc.* **1995,** *117* (41), 10401-10402.
11. Xiong, Q.; Chen, Y.; Yang, D.; Wang, K.; Wang, Y.; Yang, J.; Li, L.; Li, J., Constructing strategies for hierarchically porous MOFs with different pore sizes and applications in adsorption and catalysis. *Mater. Chem. Front.* **2022,** *6* (20), 2944-2967.
12. Wu, C.-D.; Hu, A.; Zhang, L.; Lin, W., A Homochiral Porous Metal−Organic Framework for Highly Enantioselective Heterogeneous Asymmetric Catalysis. *J. Am. Chem. Soc.* **2005,** *127* (25), 8940-8941.

13. Liu, J.; Liu, T.; Du, P.; Zhang, L.; Lei, J., Metal–Organic Framework (MOF) Hybrid as a Tandem Catalyst for Enhanced Therapy against Hypoxic Tumor Cells. *Angew. Chem. Int. Ed.* **2019,** *58* (23), 7808-7812.

14. Li, B.; Wen, H.-M.; Zhou, W.; Chen, B., Porous Metal–Organic Frameworks for Gas Storage and Separation: What, How, and Why? *J. Phys. Chem. Lett.* **2014,** *5* (20), 3468-3479.

15. Hiraide, S.; Sakanaka, Y.; Kajiro, H.; Kawaguchi, S.; Miyahara, M. T.; Tanaka, H., High-throughput gas separation by flexible metal–organic frameworks with fast gating and thermal management capabilities. *Nat. Commun.* **2020,** *11* (1), 3867.

16. Indra, A.; Song, T.; Paik, U., Metal Organic Framework Derived Materials: Progress and Prospects for the Energy Conversion and Storage. *Adv. Mater.* **2018,** *30* (39), 1705146.

17. Mon, M.; Bruno, R.; Tiburcio, E.; Viciano-Chumillas, M.; Kalinke, L. H. G.; Ferrando-Soria, J.; Armentano, D.; Pardo, E., Multivariate Metal–Organic Frameworks for the Simultaneous Capture of Organic and Inorganic Contaminants from Water. *J. Am. Chem. Soc.* **2019,** *141* (34), 13601-13609.

18. Meteku, B. E.; Huang, J.; Zeng, J.; Subhan, F.; Feng, F.; Zhang, Y.; Qiu, Z.; Aslam, S.; Li, G.; Yan, Z., Magnetic metal–organic framework composites for environmental monitoring and remediation. *Coord. Chem. Rev.* **2020,** *413*, 213261.

19. Kreno, L. E.; Leong, K.; Farha, O. K.; Allendorf, M.; Van Duyne, R. P.; Hupp, J. T., Metal–Organic Framework Materials as Chemical Sensors. *Chem. Rev.* **2012,** *112* (2), 1105-1125.

20. Li, Z.-G.; Li, K.; Dong, L.-Y.; Guo, T.-M.; Azeem, M.; Li, W.; Bu, X.-H., Acoustic Properties of Metal-Organic Frameworks. *Research 2021*.

21. Alizadeh Sani, M.; Khezerlou, A.; McClements, D. J., Zeolitic imidazolate frameworks (ZIFs): Advanced nanostructured materials to enhance the functional performance of food packaging materials. *Adv. Colloid Interface Sci.* **2024,** *327*, 103153.

22. Park, K. S.; Ni, Z.; Côté, A. P.; Choi, J. Y.; Huang, R.; Uribe-Romo, F. J.; Chae, H. K.; O'Keeffe, M.; Yaghi, O. M., Exceptional chemical and thermal stability of zeolitic imidazolate frameworks. *Proc. Natl. Acad. Sci.* **2006,** *103* (27), 10186-10191.

23. Banerjee, R.; Phan, A.; Wang, B.; Knobler, C.; Furukawa, H.; O'Keeffe, M.; Yaghi, O. M., High-Throughput Synthesis of Zeolitic Imidazolate Frameworks and Application to CO2 Capture. *Science* **2008,** *319* (5865), 939-943.

24. Liu, Y.; Pang, H.; Wang, X.; Yu, S.; Chen, Z.; Zhang, P.; Chen, L.; Song, G.; Saleh Alharbi, N.; Omar Rabah, S.; Wang, X., Zeolitic imidazolate framework-based nanomaterials for the capture of heavy metal ions and radionuclides: A review. *Chem. Eng. J.* **2021,** *406*, 127139.

25. Furukawa, H.; Cordova, K. E.; O'Keeffe, M.; Yaghi, O. M., The Chemistry and Applications of Metal-Organic Frameworks. *Science* **2013,** *341* (6149), 1230444.

26. Shahzad, A.; Zulfiqar, F.; Arif Nadeem, M., Cobalt containing bimetallic ZIFs and their derivatives as OER electrocatalysts: A critical review. *Coord. Chem. Rev.* **2023,** *477*, 214925.

27. Heuer-Jungemann, A.; Feliu, N.; Bakaimi, I.; Hamaly, M.; Alkilany, A.; Chakraborty, I.; Masood, A.; Casula, M. F.; Kostopoulou, A.; Oh, E.; Susumu, K.; Stewart, M. H.; Medintz, I. L.; Stratakis, E.; Parak, W. J.; Kanaras, A. G., The Role of Ligands in the Chemical Synthesis and Applications of Inorganic Nanoparticles. *Chem. Rev.* **2019,** *119* (8), 4819-4880.

28. Almeida Paz, F. A.; Klinowski, J.; Vilela, S. M. F.; Tomé, J. P. C.; Cavaleiro, J. A. S.; Rocha, J., Ligand design for functional metal–organic frameworks. *Chem. Soc. Rev.* **2012,** *41* (3), 1088-1110.

29. Naghdi, S.; Cherevan, A.; Giesriegl, A.; Guillet-Nicolas, R.; Biswas, S.; Gupta, T.; Wang, J.; Haunold, T.; Bayer, B. C.; Rupprechter, G.; Toroker, M. C.; Kleitz, F.; Eder, D., Selective ligand removal to improve accessibility of active sites in hierarchical MOFs for heterogeneous photocatalysis. *Nat. Commun.* **2022,** *13* (1), 282.

30. Zhang, G.; Yang, H.; Fei, H., Unusual Missing Linkers in an Organosulfonate-Based Primitive–Cubic (pcu)-Type Metal–Organic Framework for CO2 Capture and Conversion under Ambient Conditions. *ACS Catalysis* **2018,** *8* (3), 2519-2525.

31. He, W.; Lv, D.; Guan, Y.; Yu, S., Post-synthesis modification of metal–organic frameworks: synthesis, characteristics, and applications. *J. Mater. Chem. A* **2023,** *11* (45), 24519-24550.

32. Sun, D.; Fu, Y.; Liu, W.; Ye, L.; Wang, D.; Yang, L.; Fu, X.; Li, Z., Studies on Photocatalytic CO2 Reduction over NH2-Uio-66(Zr) and Its Derivatives: Towards a Better Understanding of Photocatalysis on Metal–Organic Frameworks. *Chem. - Eur. J.* **2013,** *19* (42), 14279-14285.

33. Eddaoudi, M.; Kim, J.; Rosi, N.; Vodak, D.; Wachter, J.; O'Keeffe, M.; Yaghi, O. M., Systematic Design of Pore Size and Functionality in Isoreticular MOFs and Their Application in Methane Storage. *Science* **2002,** *295* (5554), 469-472.

34. Deng, H.; Grunder, S.; Cordova, K. E.; Valente, C.; Furukawa, H.; Hmadeh, M.; Gándara, F.; Whalley, A. C.; Liu, Z.; Asahina, S.; Kazumori, H.; O'Keeffe, M.; Terasaki, O.; Stoddart, J. F.; Yaghi, O. M., Large-Pore Apertures in a Series of Metal-Organic Frameworks. *Science* **2012,** *336* (6084), 1018-1023.

35. Endo, K.; Canossa, S.; Heck, F.; Proserpio, D. M.; Istek, M. S.; Stemmler, F.; van Slageren, J.; Hartmann, S.; Hartschuh, A.; Lotsch, B. V., Crystalline porous frameworks based on double extension of metal–organic and covalent organic linkages. *Nature Synthesis* **2025**.

36. Ma, X.; Zheng, D. J.; Hou, S.; Mukherjee, S.; Khare, R.; Gao, G.; Ai, Q.; Garlyyev, B.; Li, W.; Koch, M.; Mink, J.; Shao-Horn, Y.; Warnan, J.; Bandarenka, A. S.; Fischer, R. A., Structure–Activity Relationships in Ni- Carboxylate-Type Metal–Organic Frameworks' Metamorphosis for the Oxygen Evolution Reaction. *ACS Catalysis* **2023,** *13* (11), 7587-7596.

37. Yuan, S.; Peng, J.; Cai, B.; Huang, Z.; Garcia-Esparza, A. T.; Sokaras, D.; Zhang, Y.; Giordano, L.; Akkiraju, K.; Zhu, Y. G.; Hübner, R.; Zou, X.; Román-Leshkov, Y.; Shao-Horn, Y., Tunable metal hydroxide–organic frameworks for catalysing oxygen evolution. *Nature Materials* **2022,** *21* (6), 673-680.

38. Yao, Y.; Zhao, X.; Chang, G.; Yang, X.; Chen, B., Hierarchically Porous Metal–Organic Frameworks: Synthetic Strategies and Applications. *Small Struct.* **2023,** *4* (1), 2200187.

39. Cohen, S. M., Postsynthetic Methods for the Functionalization of Metal–Organic Frameworks. *Chem. Rev.* **2012,** *112* (2), 970-1000.

40. Qin, J.-S.; Yuan, S.; Wang, Q.; Alsalme, A.; Zhou, H.-C., Mixed-linker strategy for the construction of multifunctional metal–organic frameworks. *J. Mater. Chem. A* **2017,** *5* (9), 4280-4291.

41. Lyu, J.; Zhang, X.; Otake, K.-i.; Wang, X.; Li, P.; Li, Z.; Chen, Z.; Zhang, Y.; Wasson, M. C.; Yang, Y.; Bai, P.; Guo, X.; Islamoglu, T.; Farha, O. K., Topology and porosity control of metal–organic frameworks through linker functionalization. *Chem. Sci.* **2019,** *10* (4), 1186-1192.

42. Kong, X.; Deng, H.; Yan, F.; Kim, J.; Swisher, J. A.; Smit, B.; Yaghi, O. M.; Reimer, J. A., Mapping of Functional Groups in Metal-Organic Frameworks. *Science* **2013,** *341* (6148), 882-885.

43. Deng, H.; Doonan, C. J.; Furukawa, H.; Ferreira, R. B.; Towne, J.; Knobler, C. B.; Wang, B.; Yaghi, O. M., Multiple Functional Groups of Varying Ratios in Metal-Organic Frameworks. *Science* **2010,** *327* (5967), 846-850.

44. Frentzel-Beyme, L.; Kloß, M.; Kolodzeiski, P.; Pallach, R.; Henke, S., Meltable Mixed-Linker Zeolitic Imidazolate Frameworks and Their Microporous Glasses: From Melting Point Engineering to Selective Hydrocarbon Sorption. *J. Am. Chem. Soc.* **2019,** *141* (31), 12362-12371.

45. Gao, C.; Jiang, Z.; Qi, S.; Wang, P.; Jensen, L. R.; Johansen, M.; Christensen, C. K.; Zhang, Y.; Ravnsbæk, D. B.; Yue, Y., Metal-Organic Framework Glass Anode with an Exceptional Cycling-Induced Capacity Enhancement for Lithium-Ion Batteries. *Adv. Mater.* **2022,** *34* (10), 2110048.

46. Ma, N.; Horike, S., Metal–Organic Network-Forming Glasses. *Chem. Rev.* **2022,** *122* (3), 4163-4203.

47. Wang, S.; Ai, Z.; Niu, X.; Yang, W.; Kang, R.; Lin, Z.; Waseem, A.; Jiao, L.; Jiang, H.-L., Linker Engineering of Sandwich-Structured Metal–Organic Framework

Composites for Optimized Photocatalytic H2 Production. *Adv. Mater.* **2023,** *35* (39), 2302512.

48. Wu, K.; Liu, X.-Y.; Cheng, P.-W.; Huang, Y.-L.; Zheng, J.; Xie, M.; Lu, W.; Li, D., Linker Engineering for Reactive Oxygen Species Generation Efficiency in Ultra-Stable Nickel-Based Metal–Organic Frameworks. *J. Am. Chem. Soc.* **2023,** *145* (34), 18931-18938.

49. Liu, L.; Zhang, D.; Zhu, Y.; Han, Y., Bulk and local structures of metal–organic frameworks unravelled by high-resolution electron microscopy. *Communications Chemistry* **2020,** *3* (1), 99.

50. Li, Y.; Wang, K.; Zhou, W.; Li, Y.; Vila, R.; Huang, W.; Wang, H.; Chen, G.; Wu, G.-H.; Tsao, Y.; Wang, H.; Sinclair, R.; Chiu, W.; Cui, Y., Cryo-EM Structures of Atomic Surfaces and Host-Guest Chemistry in Metal-Organic Frameworks. *Matter* **2019,** *1* (2), 428-438.

51. Xiang, W.; Zhang, Y.; Chen, Y.; Liu, C.-j.; Tu, X., Synthesis, characterization and application of defective metal–organic frameworks: current status and perspectives. *J. Mater. Chem. A* **2020,** *8* (41), 21526-21546.

52. Khalil, I. E.; Xue, C.; Liu, W.; Li, X.; Shen, Y.; Li, S.; Zhang, W.; Huo, F., The Role of Defects in Metal–Organic Frameworks for Nitrogen Reduction Reaction: When Defects Switch to Features. *Adv. Funct. Mater.* **2021,** *31* (17), 2010052.

53. Feng, L.; Yuan, S.; Zhang, L.-L.; Tan, K.; Li, J.-L.; Kirchon, A.; Liu, L.-M.; Zhang, P.; Han, Y.; Chabal, Y. J.; Zhou, H.-C., Creating Hierarchical Pores by Controlled Linker Thermolysis in Multivariate Metal–Organic Frameworks. *J. Am. Chem. Soc.* **2018,** *140* (6), 2363-2372.

54. Bueken, B.; Van Velthoven, N.; Krajnc, A.; Smolders, S.; Taulelle, F.; Mellot-Draznieks, C.; Mali, G.; Bennett, T. D.; De Vos, D., Tackling the Defect Conundrum in UiO-66: A Mixed-Linker Approach to Engineering Missing Linker Defects. *Chem. Mater.* **2017,** *29* (24), 10478-10486.

55. Yuan, S.; Zou, L.; Qin, J.-S.; Li, J.; Huang, L.; Feng, L.; Wang, X.; Bosch, M.; Alsalme, A.; Cagin, T.; Zhou, H.-C., Construction of hierarchically porous metal–organic frameworks through linker labilization. *Nat. Commun.* **2017,** *8* (1), 15356.

56. Guillerm, V.; Xu, H.; Albalad, J.; Imaz, I.; Maspoch, D., Postsynthetic Selective Ligand Cleavage by Solid–Gas Phase Ozonolysis Fuses Micropores into Mesopores in Metal–Organic Frameworks. *J. Am. Chem. Soc.* **2018,** *140* (44), 15022-15030.

57. Wang, K.-Y.; Feng, L.; Yan, T.-H.; Wu, S.; Joseph, E. A.; Zhou, H.-C., Rapid Generation of Hierarchically Porous Metal–Organic Frameworks through Laser Photolysis. *Angew. Chem. Int. Ed.* **2020,** *59* (28), 11349-11354.

58. Liu, L.; Chen, Z.; Wang, J.; Zhang, D.; Zhu, Y.; Ling, S.; Huang, K.-W.; Belmabkhout, Y.; Adil, K.; Zhang, Y.; Slater, B.; Eddaoudi, M.; Han, Y., Imaging

defects and their evolution in a metal–organic framework at sub-unit-cell resolution. *Nature Chemistry* **2019,** *11* (7), 622-628.

59. Wang, J.; Liu, L.; Chen, C.; Dong, X.; Wang, Q.; Alfilfil, L.; AlAlouni, M. R.; Yao, K.; Huang, J.; Zhang, D.; Han, Y., Engineering effective structural defects of metal–organic frameworks to enhance their catalytic performances. *J. Mater. Chem. A* **2020,** *8* (8), 4464-4472.

60. Xue, Z.; Liu, K.; Liu, Q.; Li, Y.; Li, M.; Su, C.-Y.; Ogiwara, N.; Kobayashi, H.; Kitagawa, H.; Liu, M.; Li, G., Missing-linker metal-organic frameworks for oxygen evolution reaction. *Nat. Commun.* **2019,** *10* (1), 5048.

61. Ji, S.; Chen, Y.; Wang, X.; Zhang, Z.; Wang, D.; Li, Y., Chemical Synthesis of Single Atomic Site Catalysts. *Chem. Rev.* **2020,** *120* (21), 11900-11955.

62. Chen, Y.; Ji, S.; Wang, Y.; Dong, J.; Chen, W.; Li, Z.; Shen, R.; Zheng, L.; Zhuang, Z.; Wang, D.; Li, Y., Isolated Single Iron Atoms Anchored on N-Doped Porous Carbon as an Efficient Electrocatalyst for the Oxygen Reduction Reaction. *Angew. Chem. Int. Ed.* **2017,** *56* (24), 6937-6941.

63. Li, J.; Chen, M.; Cullen, D. A.; Hwang, S.; Wang, M.; Li, B.; Liu, K.; Karakalos, S.; Lucero, M.; Zhang, H.; Lei, C.; Xu, H.; Sterbinsky, G. E.; Feng, Z.; Su, D.; More, K. L.; Wang, G.; Wang, Z.; Wu, G., Atomically dispersed manganese catalysts for oxygen reduction in proton-exchange membrane fuel cells. *Nature Catalysis* **2018,** *1* (12), 935-945.

64. Shan, J.; Liao, J.; Ye, C.; Dong, J.; Zheng, Y.; Qiao, S.-Z., The Dynamic Formation from Metal-Organic Frameworks of High-Density Platinum Single-Atom Catalysts with Metal-Metal Interactions. *Angew. Chem. Int. Ed.* **2022,** *61* (48), e202213412.

65. Lu, Y.; Ke, Z., Strategies for the Preparation of Single-Atom Catalysts Using Low-Dimensional Metal–Organic Frameworks. *Small* **2024,** *20* (42), 2403767.

66. Ahmad, M.; Chen, J.; Liu, J.; Zhang, Y.; Song, Z.; Afzal, S.; Raza, W.; Zeb, L.; Mehmood, A.; Hussain, A.; Zhang, J.; Fu, X.-Z.; Luo, J.-L., Metal-organic framework-based single-atom electro-/photocatalysts: Synthesis, energy applications, and opportunities. *Carbon Energy* **2024,** *6* (1), e382.

67. Yang, Q.; Yang, C.-C.; Lin, C.-H.; Jiang, H.-L., Metal–Organic-Framework-Derived Hollow N-Doped Porous Carbon with Ultrahigh Concentrations of Single Zn Atoms for Efficient Carbon Dioxide Conversion. *Angew. Chem. Int. Ed.* **2019,** *58* (11), 3511-3515.

68. Zhou, Y.; Chen, G.; Wang, Q.; Wang, D.; Tao, X.; Zhang, T.; Feng, X.; Müllen, K., Fe□N□C Electrocatalysts with Densely Accessible Fe□N4 Sites for Efficient Oxygen Reduction Reaction. *Adv. Funct. Mater.* **2021,** *31* (34), 2102420.

69. Yusuf, M.; Kurzina, I.; Voronova, G.; Islam, M. M.; Mohammed, S. D.; Oladoja, N. A., Trends in the energy and environmental applications of metal–organic framework-based materials. *Energy Advances* **2024,** *3* (9), 2079-2135.

70. Li, J.-R.; Kuppler, R. J.; Zhou, H.-C., Selective gas adsorption and separation in metal–organic frameworks. *Chem. Soc. Rev.* **2009,** *38* (5), 1477-1504.

71. Wang, C.; Liu, X.; Yang, T.; Sridhar, D.; Algadi, H.; Bin Xu, B.; El-Bahy, Z. M.; Li, H.; Ma, Y.; Li, T.; Guo, Z., An overview of metal-organic frameworks and their magnetic composites for the removal of pollutants. *Sep. Purif. Technol.* **2023,** *320*, 124144.

72. Gunaseelan, H.; Munde, A. V.; Patel, R.; Sathe, B. R., Metal-organic framework derived carbon-based electrocatalysis for hydrogen evolution reactions: A review. *Materials Today Sustainability* **2023,** *22*, 100371.

73. Ahmad, F.; Rafiq, K.; Najam, T.; Hussain, E.; Sohail, M.; Abid, M. Z.; Mahmood, A.; Javed, M. S.; Shah, S. S. A., Metal-organic frameworks for electrocatalytic water-splitting: Beyond the pyrolysis. *Int. J. Hydrogen Energy* **2023,** *48* (90), 35075-35111.

74. Lu, X. F.; Xia, B. Y.; Zang, S.-Q.; Lou, X. W., Metal–Organic Frameworks Based Electrocatalysts for the Oxygen Reduction Reaction. *Angew. Chem. Int. Ed.* **2020,** *59* (12), 4634-4650.

75. Agarwal, S.; Yu, X.; Manthiram, A., A pair of metal organic framework (MOF)-derived oxygen reduction reaction (ORR) and oxygen evolution reaction (OER) catalysts for zinc-air batteries. *Materials Today Energy* **2020,** *16*, 100405.

76. Liu, X.; Liu, G.; Fu, T.; Ding, K.; Guo, J.; Wang, Z.; Xia, W.; Shangguan, H., Structural Design and Energy and Environmental Applications of Hydrogen-Bonded Organic Frameworks: A Systematic Review. *Advanced Science* **2024,** *11* (22), 2400101.

77. Wu, Y.-L.; Horwitz, N. E.; Chen, K.-S.; Gomez-Gualdron, D. A.; Luu, N. S.; Ma, L.; Wang, T. C.; Hersam, M. C.; Hupp, J. T.; Farha, O. K.; Snurr, R. Q.; Wasielewski, M. R., G-quadruplex organic frameworks. *Nature Chemistry* **2017,** *9* (5), 466-472.

78. Liu, X.; Yang, X.; Wang, H.; Hisaki, I.; Wang, K.; Jiang, J., A robust redox-active hydrogen-bonded organic framework for rechargeable batteries. *J. Mater. Chem. A* **2022,** *10* (4), 1808-1814.

79. He, C.; Liu, Z.; Wu, J.; Pan, X.; Fang, Z.; Li, J.; Bryan, B. A., Future global urban water scarcity and potential solutions. *Nat. Commun.* **2021,** *12* (1), 4667.

80. Chen, C.; Fei, L.; Wang, B.; Xu, J.; Li, B.; Shen, L.; Lin, H., MOF-Based Photocatalytic Membrane for Water Purification: A Review. *Small* **2024,** *20* (1), 2305066.

81. Uddin, M. J.; Ampiaw, R. E.; Lee, W., Adsorptive removal of dyes from wastewater using a metal-organic framework: A review. *Chemosphere* **2021,** *284*, 131314.

82. Haque, E.; Lee, J. E.; Jang, I. T.; Hwang, Y. K.; Chang, J.-S.; Jegal, J.; Jhung, S. H., Adsorptive removal of methyl orange from aqueous solution with metal-organic frameworks, porous chromium-benzenedicarboxylates. *J. Hazard. Mater.* **2010,** *181* (1), 535-542.

83. Jun, B.-M.; Heo, J.; Taheri-Qazvini, N.; Park, C. M.; Yoon, Y., Adsorption of selected dyes on Ti3C2Tx MXene and Al-based metal-organic framework. *Ceram. Int.* **2020,** *46* (3), 2960-2968.

84. Chen, N.; Chen, D.; Wei, F.; Zhao, S.; Luo, Y., Effect of structures on the adsorption performance of Cobalt Metal Organic Framework obtained by microwave-assisted ball milling. *Chem. Phys. Lett.* **2018,** *705*, 23-30.

85. Wang, K.; Li, C.; Liang, Y.; Han, T.; Huang, H.; Yang, Q.; Liu, D.; Zhong, C., Rational construction of defects in a metal–organic framework for highly efficient adsorption and separation of dyes. *Chem. Eng. J.* **2016,** *289*, 486-493.

86. Zhao, C.; Dong, P.; Liu, Z.; Wu, G.; Wang, S.; Wang, Y.; Liu, F., Facile synthesis of Fe3O4/MIL-101 nanocomposite as an efficient heterogeneous catalyst for degradation of pollutants in Fenton-like system. *RSC Advances* **2017,** *7* (39), 24453-24461.

87. Shi, Z.; Xu, C.; Guan, H.; Li, L.; Fan, L.; Wang, Y.; Liu, L.; Meng, Q.; Zhang, R., Magnetic metal organic frameworks (MOFs) composite for removal of lead and malachite green in wastewater. *Colloids Surf., A* **2018,** *539*, 382-390.

88. Lv, S.-W.; Liu, J.-M.; Li, C.-Y.; Zhao, N.; Wang, Z.-H.; Wang, S., A novel and universal metal-organic frameworks sensing platform for selective detection and efficient removal of heavy metal ions. *Chem. Eng. J.* **2019,** *375*, 122111.

89. Yu, J.; Xiong, W.; Li, X.; Yang, Z.; Cao, J.; Jia, M.; Xu, R.; Zhang, Y., Functionalized MIL-53(Fe) as efficient adsorbents for removal of tetracycline antibiotics from aqueous solution. *Microporous Mesoporous Mater.* **2019,** *290*, 109642.

90. Naghdi, S.; Brown, E.; Zendehbad, M.; Duong, A.; Ipsmiller, W.; Biswas, S.; Toroker, M. C.; Kazemian, H.; Eder, D., Glyphosate Adsorption from Water Using Hierarchically Porous Metal–Organic Frameworks. *Adv. Funct. Mater.* **2023,** *33* (20), 2213862.

91. Sarker, M.; Shin, S.; Jeong, J. H.; Jhung, S. H., Mesoporous metal-organic framework PCN-222(Fe): Promising adsorbent for removal of big anionic and cationic dyes from water. *Chem. Eng. J.* **2019,** *371*, 252-259.

92. Simonin, J.-P., On the comparison of pseudo-first order and pseudo-second order rate laws in the modeling of adsorption kinetics. *Chem. Eng. J.* **2016,** *300*, 254-263.

93. Guo, X.; Wang, J., A general kinetic model for adsorption: Theoretical analysis and modeling. *J. Mol. Liq.* **2019,** *288*, 111100.

94. Ezzati, R., Derivation of Pseudo-First-Order, Pseudo-Second-Order and Modified Pseudo-First-Order rate equations from Langmuir and Freundlich isotherms for adsorption. *Chem. Eng. J.* **2020,** *392*, 123705.

95. Lee, Y. R.; Do, X. H.; Cho, K. Y.; Jeong, K.; Baek, K.-Y., Amine-Functionalized Zeolitic Imidazolate Framework-8 (ZIF-8) Nanocrystals for Adsorption of Radioactive Iodine. *ACS Applied Nano Materials* **2020,** *3* (10), 9852-9861.

96. Kaur, R.; Kaur, A.; Umar, A.; Anderson, W. A.; Kansal, S. K., Metal organic framework (MOF) porous octahedral nanocrystals of Cu-BTC: Synthesis, properties and enhanced adsorption properties. *Mater. Res. Bull.* **2019,** *109*, 124-133.

97. Huang, Z.; Zhao, S.; Yu, Y., Experimental method to explore the adaptation degree of type-II and all-solid-state Z-scheme heterojunction structures in the same degradation system. *Chinese Journal of Catalysis* **2020,** *41* (10), 1522-1534.

98. Huang, Z.; Zhou, J.; Zhao, Y.; Cheng, H.; Lu, G.; Morawski, A. W.; Yu, Y., Stable core–shell ZIF-8@ZIF-67 MOFs photocatalyst for highly efficient degradation of organic pollutant and hydrogen evolution. *J. Mater. Res.* **2021,** *36* (3), 602-614.

99. Gopal, G.; Chandrasekaran, N.; Mukherjee, A., Chapter Three - Overview of nanoparticles technology usage for water treatment with an emphasis on the emerging water pollutants. In *Comprehensive Analytical Chemistry*, Turan, N. B.; Engin, G. O.; Bilgili, M. S., Eds. Elsevier: 2022; Vol. 99, pp 87-103.

100. Guan, W.; Gao, X.; Ji, G.; Xing, Y.; Du, C.; Liu, Z., Fabrication of a magnetic nanocomposite photocatalysts Fe3O4@ZIF-67 for degradation of dyes in water under visible light irradiation. *J. Solid State Chem.* **2017,** *255*, 150-156.

101. Xia, T.; Lin, Y.; Li, W.; Ju, M., Photocatalytic degradation of organic pollutants by MOFs based materials: A review. *Chin. Chem. Lett.* **2021,** *32* (10), 2975-2984.

102. Ali, A.; Muslim, M.; Neogi, I.; Afzal, M.; Alarifi, A.; Ahmad, M., Construction of a 3D Metal–Organic Framework and Its Composite for Water Remediation via Selective Adsorption and Photocatalytic Degradation of Hazardous Dye. *ACS Omega* **2022,** *7* (28), 24438-24451.

103. Lu, X.-F.; Liao, P.-Q.; Wang, J.-W.; Wu, J.-X.; Chen, X.-W.; He, C.-T.; Zhang, J.-P.; Li, G.-R.; Chen, X.-M., An Alkaline-Stable, Metal Hydroxide Mimicking Metal–Organic Framework for Efficient Electrocatalytic Oxygen Evolution. *J. Am. Chem. Soc.* **2016,** *138* (27), 8336-8339.

104. Sun, H.; Yan, Z.; Liu, F.; Xu, W.; Cheng, F.; Chen, J., Self-Supported Transition-Metal-Based Electrocatalysts for Hydrogen and Oxygen Evolution. *Adv. Mater.* **2020,** *32* (3), 1806326.

105. Cui, W.-G.; Gao, F.; Na, G.; Wang, X.; Li, Z.; Yang, Y.; Niu, Z.; Qu, Y.; Wang, D.; Pan, H., Insights into the pH effect on hydrogen electrocatalysis. *Chem. Soc. Rev.* **2024,** *53* (20), 10253-10311.

106. Xu, J.; Shao, G.; Tang, X.; Lv, F.; Xiang, H.; Jing, C.; Liu, S.; Dai, S.; Li, Y.; Luo, J.; Zhou, Z., Frenkel-defected monolayer MoS2 catalysts for efficient hydrogen evolution. *Nat. Commun.* **2022,** *13* (1), 2193.

107. Hansen, J. N.; Prats, H.; Toudahl, K. K.; Mørch Secher, N.; Chan, K.; Kibsgaard, J.; Chorkendorff, I., Is There Anything Better than Pt for HER? *ACS Energy Letters* **2021,** *6* (4), 1175-1180.

108. Zheng, W.; Lee, L. Y. S., Metal–Organic Frameworks for Electrocatalysis: Catalyst or Precatalyst? *ACS Energy Letters* **2021,** *6* (8), 2838-2843.

109. Walter, C.; Menezes, P. W.; Driess, M., Perspective on intermetallics towards efficient electrocatalytic water-splitting. *Chem. Sci.* **2021,** *12* (25), 8603-8631.

110. Chen, R.; Hung, S.-F.; Zhou, D.; Gao, J.; Yang, C.; Tao, H.; Yang, H. B.; Zhang, L.; Zhang, L.; Xiong, Q.; Chen, H. M.; Liu, B., Layered Structure Causes Bulk NiFe Layered Double Hydroxide Unstable in Alkaline Oxygen Evolution Reaction. *Adv. Mater.* **2019,** *31* (41), 1903909.

111. Qin, Y.; Yu, T.; Deng, S.; Zhou, X.-Y.; Lin, D.; Zhang, Q.; Jin, Z.; Zhang, D.; He, Y.-B.; Qiu, H.-J.; He, L.; Kang, F.; Li, K.; Zhang, T.-Y., RuO2 electronic structure and lattice strain dual engineering for enhanced acidic oxygen evolution reaction performance. *Nat. Commun.* **2022,** *13* (1), 3784.

112. Zheng, W.; Liu, M.; Lee, L. Y. S., Electrochemical Instability of Metal–Organic Frameworks: In Situ Spectroelectrochemical Investigation of the Real Active Sites. *ACS Catalysis* **2020,** *10* (1), 81-92.

113. Tian, J.; Jiang, F.; Yuan, D.; Zhang, L.; Chen, Q.; Hong, M., Electric-Field Assisted In Situ Hydrolysis of Bulk Metal–Organic Frameworks (MOFs) into Ultrathin Metal Oxyhydroxide Nanosheets for Efficient Oxygen Evolution. *Angew. Chem. Int. Ed.* **2020,** *59* (31), 13101-13108.

114. Song, X. Z.; Zhang, N.; Wang, X. F.; Tan, Z., Recent advances of metal-organic frameworks and their composites toward oxygen evolution electrocatalysis. *Materials Today Energy* **2021,** *19*, 100597.

115. Feng, K.; Zhang, D.; Liu, F.; Li, H.; Xu, J.; Xia, Y.; Li, Y.; Lin, H.; Wang, S.; Shao, M.; Kang, Z.; Zhong, J., Highly Efficient Oxygen Evolution by a Thermocatalytic Process Cascaded Electrocatalysis Over Sulfur-Treated Fe-Based Metal–Organic-Frameworks. *Advanced Energy Materials* **2020,** *10* (16), 2000184.

116. Huang, Z.; Rath, J.; Zhou, Q.; Cherevan, A.; Naghdi, S.; Eder, D., Hierarchically Micro- and Mesoporous Zeolitic Imidazolate Frameworks Through Selective Ligand Removal. *Small* **2024,** *20* (21), 2307981.

117. Huang, Z.; Wang, Z.; Zhou, Q.; Rabl, H.; Naghdi, S.; Yang, Z.; Eder, D., Engineering of HO−Zn−N2 Active Sites in Zeolitic Imidazolate Frameworks for Enhanced (Photo)Electrocatalytic Hydrogen Evolution. *Angew. Chem. Int. Ed.* **2024,** *n/a* (n/a), e202419913.

118. Huang, Z.; Wang, Z.; Rabl, H.; Naghdi, S.; Zhou, Q.; Schwarz, S.; Apaydin, D. H.; Yu, Y.; Eder, D., Ligand engineering enhances (photo) electrocatalytic activity and stability of zeolitic imidazolate frameworks via in-situ surface reconstruction. *Nat. Commun.* **2024,** *15* (1), 9393.